

# **Mechanical properties and structural evaluation of diamond structure Ti6Al4V lattices made by Electron Beam Melting**

Sarah Nield Morrish Jenkins

A thesis presented for the degree of  
Doctor of Philosophy



Department of Materials Science and Engineering  
The University of Sheffield  
United Kingdom

December 2017



## Abstract

Additive manufacturing allows a new approach to the creation of porous metals, in the form of regular lattice structures. These lattices have the potential to reduce the weight of parts, for example structures in aircraft, by replacing heavy, solid components with porous structures. To utilise this opportunity, a full understanding of a range of mechanical properties is required. While there have been reports regarding mechanical properties of metallic lattices, there is a large variation in the precise manufacturing methods, conditions, and design of the structures. To assess the suitability of such materials for the use in aircraft, a systematic investigation of the strength and failure properties is needed.

To work towards this ambitious goal, the additive manufacturing method of electron beam melting has been used to produce sets of Ti6Al4V diamond structure lattices (of various dimensions, dependent on the investigation).

Through tests in compression, tension, and by fatigue, the mechanical properties of the structures were determined, compared, and detailed in this piece of work.

A series of investigations was completed: A study to investigate the minimum number of unit cells required to ensure reliable mechanical properties; a study to determine whether lattices are anisotropic by nature; a study to determine if post processing the lattices could improve their mechanical properties; and a study to investigate fatigue life of the lattices.

It was discovered that due to their high porosity, lattice properties are highly dependent on density. Contrary to previous reports, however, there appears to be no anisotropy in lattices. Reasons for why this is the case, and why previous reports suggested otherwise are explored. Hot isostatic pressing and surface improvement through etching led to minor improvements in strength, however these also led to reduced ductility, at a high monetary and time cost. These post processes alone led to no improvements in strength, and HIP alone led to a reduction in fatigue life.

As a principal conclusion, it is seen that it is critically important to control process parameters in the EBM method to produce lattices to suit the application, as post processing is a costly option providing minimal improvement.



Contents	
Chapter 1	Introduction ..... 10
Chapter 2	Literature review ..... 12
2.1	Titanium..... 12
2.1.1	Production ..... 12
2.1.2	Powder production ..... 15
2.1.3	Titanium alloys ..... 16
2.1.4	Ti6Al4V ..... 18
2.2	Additive Manufacturing..... 24
2.2.1	AM Processes..... 25
2.2.2	Electron Beam Melting ..... 27
2.2.3	Influence of processing on the properties of AM parts ..... 34
2.3	Lattices..... 38
2.3.1	Metal foams and the emergence of lattices ..... 38
2.3.2	Lattice geometry ..... 42
2.3.3	General properties of AM lattices ..... 47
2.4	Fatigue ..... 53
2.4.1	Fundamentals of fatigue..... 55
2.4.2	Fatigue in Ti6Al4V ..... 57
2.4.3	Fatigue in lattices ..... 62
Chapter 3	Procedures ..... 67
3.1	Lattice choice..... 67
3.2	Building in EBM..... 68
3.2.1	Size effect builds..... 70
I.	Size effect builds 1 and 2 ..... 71
II.	Size effect builds 3 and 4 ..... 72
3.2.2	Anisotropy investigation ..... 74
I.	Anisotropy investigation build 1 ..... 75
II.	Anisotropy investigation builds 2a, 2b and 2c ..... 76

3.2.3	Lattice modification builds .....	77
I.	Lattice modification build 1 .....	77
II.	Lattice modification build 2 .....	78
3.2.4	Fatigue samples .....	79
I.	Fatigue build 1 .....	80
II.	Fatigue builds 2 and 3.....	81
3.3	Post processing .....	82
3.3.1	Hot Isostatic Press (HIP) .....	82
3.3.2	Surface enhancing using an etching agent.....	82
3.4	Measurements.....	83
3.4.1	Classical methods .....	83
3.4.2	SEM method.....	84
3.5	Compression test .....	85
3.6	Tensile test.....	87
3.7	Fatigue test .....	88
3.7.1	Statistics.....	89
I.	Weibull distribution.....	89
II.	Null hypothesis .....	90
III.	t test .....	90
IV.	Generalised Likelihood Ratio test .....	90
V.	Log-rank test.....	91
3.8	Additional methods .....	91
3.8.1	Standard deviation .....	91
3.8.2	Density correction factors.....	92
3.8.3	Anisotropy determination.....	93
3.8.4	Microscopy .....	94
3.9	Chemical composition.....	94
Chapter 4	Results and Discussion.....	95
4.1	Building EBM lattices .....	95

4.2	Minimum number of unit cells required for reliable mechanical properties.....	97
4.3	Effect of build direction on mechanical properties of asymmetrical lattices.....	103
4.4	Post processing lattice modification .....	110
4.4.1	Determination of ideal etching time.....	110
4.4.2	Compression tests of etched lattices compared to as-built lattices .....	114
4.4.3	Microstructural analysis of as-built and post processed lattices .....	123
I.	Solid cubes.....	124
II.	As-built lattices .....	126
III.	Etched lattices .....	130
IV.	HIP lattices.....	133
V.	HIP+etch lattices.....	136
4.4.4	Summary .....	140
4.5	Fatigue testing of as-built and further processed lattices .....	142
4.5.1	Determination of viability of the fatigue test.....	142
4.5.2	Effect of position on the build plate on mechanical properties of samples.....	143
4.5.3	Fatigue analysis to determine SN and EN curves .....	145
4.5.4	Fracture analysis .....	146
4.5.5	Fatigue analysis of HIP to as-built samples.....	148
Chapter 5	Conclusions and future work .....	152
5.1	Conclusions.....	152
5.2	Future work.....	154
Chapter 6	References .....	156
Chapter 7	Appendix .....	171



## Acknowledgements

I sincerely thank the EPSRC, and GKN Aerospace, for their financial support, without which this research would not have been possible.

With thanks to the staff at Vikings plc. and the staff at The University of Sheffield. To those in the Metallic Systems CDT, the Materials Science and Engineering department, the Mathematics and Statistics department, Mechanical Engineering department, the Medical School, and staff at the Diamond and the Sorby centre, for being always willing to help with both this work, and my personal development. This Ph.D. has been a truly interdisciplinary task.

With thanks to my husband, Nick Jenkins, for his love, support and patience during the past four years. With thanks to my Mum, Jenny Morrish, for tirelessly reading all my work, and with thanks to my Dad, Mark Morrish, for his continued interest and enthusiasm. I thank my colleagues, and my friends, for their ideas and advice, and for the love and laughter that kept me going.

Finally, I thank my supervisory team, both at GKN Aerospace and The University of Sheffield. In particular, I thank Iain Todd, for always helping to fill the gaps in my knowledge, Mikkel Pedersen, whose willingness to strive for more pushed the limits of the project, Lampros Kourtis, who helped to tie up the loose ends, and I thank Russell Goodall, for going above and beyond to inform, encourage, and inspire.

Thank you.

# Chapter 1 Introduction

This thesis presents a body of work on Ti6Al4V alloy lattices produced by the Additive Manufacturing (AM) method of Electron Beam Melting (EBM).

Reducing the weight in aircraft can lead to fuel savings, which directly translates to cost savings. By considering the forces on aerospace components in service, optimised structures can be designed to render the best mechanical properties, while minimising solid material. The overall aim of this research was to investigate the mechanical properties of the lattices produced, with the view of eventually incorporating lattice structures into aerospace components, as a filler to replace particular solid volumes in bulk parts. This was conducted in association with GKN Aerospace. There are some key areas of importance where gaps were identified.

As lattices are a relatively new occurrence, a not insignificant number of studies base their work on metal foams. When building lattice samples, the minimum number of unit cells for testing had been established from data on foams. When measuring mechanical properties, it is important to know that size effects will not be a factor in the data.

In many AM methods, bulk parts have a characteristic microstructure, arising from the highly directional heat flow. This occurs across a range of materials, and provides an inherent anisotropy in mechanical properties. As lattices are highly porous, and bear more of a resemblance to foams than their bulk material counterparts, anisotropy may not occur in lattices.

After the build is complete, some AM methods require post processing to relieve internal stresses, refine the microstructure, close porosity and improve surface quality. The EBM process boasts several key factors that make many post processing steps unnecessary, however it is important to investigate processes that may produce higher quality lattices through improvements to mechanical properties.

While static tests provide a lot of useful information, for aerospace, fatigue life is a very important factor. Throughout the use of an aerospace component, a great many forces will act on the part, which require validation through fatigue tests. As the lattice is a novel structure, little is known about the fatigue life, therefore this is an important area to advance.

From these key areas, a number of individual studies were proposed:

- ) An investigation into the minimum number of unit cells required to produce reliable mechanical properties.
- ) An investigation to determine whether there is anisotropy within the lattices arising due to build direction during manufacture.
- ) An investigation into how post processing (Hot Isostatic Pressing and surface etching) of EBM lattices affects their mechanical properties through static and dynamic tests.
- ) An investigation into the fatigue life of EBM lattices when subjected to cyclic loading through the use of force-controlled and position-controlled dynamic tests.

Chapter 1 presents the aims of the study, and gives an outline of the thesis.

Chapter 2 discusses the literature surrounding this piece of work. Titanium as a metal is discussed, focusing on the Ti6Al4V alloy. AM methods are discussed, with particular emphasis on EBM. The development of lattice structures is discussed, with comparisons to metal foams. Following this, mechanical properties of lattices produced by AM are explored, with the difficulties surrounding obtaining mechanical properties discussed. Finally the mechanism of fatigue is discussed, focusing on studies based on the fatigue life of lattices built by AM.

Chapter 3 gives a detailed account of the procedures used in this thesis. Every build utilised is listed, with details surrounding the manufacture of each lattice. The mechanical tests carried out are discussed, as is the equipment used for each test, and how the data was analysed following these tests. The calculations used in data analysis are given, including basic mechanical equations and statistical analysis.

Chapter 4 displays the results of the tests in various charts, tables and images, along with an analysis and discussion. These results are grouped by their experimental process, as laid out in the list of investigations.

Chapter 5 summarises the results through a concise series of conclusions, and considers where further work could answer questions raised in this piece of research.

References are listed, and additional information is provided in the appendix

## Chapter 2 Literature review

This chapter gives a brief review of titanium and its alloys, looking more closely at the grade 5 alloy, Ti6Al4V. Material properties of Ti6Al4V, and its uses in various applications are considered. The methods of Additive Manufacturing (AM) are discussed, with specific attention given to the Electron Beam Melting (EBM) method utilised in this thesis. The next section contains information on metallic lattices, with consideration given to the material properties of lattices and related structures within scientific literature, and a particular focus on Ti6Al4V EBM produced lattices. Finally, an overview of fatigue is given, with a review on the fatigue related literature of Ti6Al4V and AM lattices.

### 2.1 Titanium

Titanium is a transition metal, in position 22 on the periodic table. It is a high strength, lightweight material, and is used in many industries as a heat proof alternative to aluminium and a lighter alternative to steel [1].

Titanium is the fourth most abundant structural element, and makes up around 0.6% of the Earth's crust [2]. Despite this, there have been difficulties obtaining pure titanium metal due to its affinity to bind with other elements. Titanium ore can refer to a number of different titanium minerals. Ilmenite,  $\text{FeTiO}_3$ , is currently the most common source of titanium, accounting for 91% of the world consumption of titanium minerals, with 94% of all titanium mineral concentrates supplying  $\text{TiO}_2$  pigment production [3]. Deposits of  $\text{TiO}_2$  can be found naturally in various structural forms in titanium rich minerals such as rutile (tetragonal, twinned), anatase (tetragonal, near octahedral), and brookite (orthorhombic) [4].

#### 2.1.1 Production

Most titanium is commercially manufactured using the Kroll process [5]–[7]. Coke is mixed with titanium ore at high temperature to reduce the ore to rutile ( $\text{TiO}_2$ ). Chlorine gas is passed through the rutile to produce titanium tetrachloride ( $\text{TiCl}_4$ ), which produces other volatile chlorides as a waste product.  $\text{TiCl}_4$  is reduced using molten magnesium to produce a titanium metal sponge and magnesium chloride. To refine the titanium, the sponge is compressed to remove the magnesium chloride, and purified by acid leaching or vacuum distillation techniques. The resulting sponge is melted down, with any alloying additions combined at this stage, then cooled to form an ingot. For AM methods, the ingot must be taken for further processing steps to form the metal powder required (as discussed in 2.1.4).

There are concerns associated with the Kroll process. Due to the high affinity for titanium to react with oxygen, parts of the process that are conducted at elevated

temperatures must be completed in an inert atmosphere or vacuum. This is a large expense for any production method, and as such, titanium is still a high commodity material. As it is a batch process, there are many high energy, labour intensive steps. The use of chlorine, a highly toxic gas, leads to the production of volatile compounds. These compounds are removed by fractional distillation, however, due to its high toxicity, the use and disposal of chlorine and its by-products must be closely monitored by processing plants. If the conditions are not perfect, there can be incomplete reduction of  $\text{TiCl}_4$ , to  $\text{TiCl}_3$  or  $\text{TiCl}_2$ , leading to further processing steps.

Prior to the Kroll process, the Hunter process was the only other commercially viable option for producing titanium [7]. The Hunter process produced an excess of  $\text{TiCl}_4$  by the addition of molten sodium (Na) to produce sodium chloride (NaCl) and titanium. The NaCl salt and titanium metal were separated through the leeching of the salt through addition of hydrochloric acid (HCl). The brine would be discarded, and a fresh quantity of sodium would be required for the next batch of titanium. This method was mostly abandoned in favour of the more efficient Kroll process.

The Armstrong process is a method by which gaseous titanium tetrachloride is passed through liquid sodium. This produces coarse titanium powder of a “coral like” structure, and sodium chloride [8]. The crystalline product is then washed in water to dissolve the salt and leave the solid titanium. Other metal chlorides can be added to the reaction to provide alloying additions, however post processing of the powder to form homogenous spheres is required.

The Fray, Farthing and Chen (FFC) process, developed at the University of Cambridge in the 1990s, can produce titanium powder from the reduction of titanium oxides and dioxides to titanium by electrochemistry [9]. The intellectual rights to the process were acquired by Metalysis, who at the time of writing are working on developing and marketing the process as commercially viable [10]. The FFC process takes titanium dioxide, and uses electrolysis with carbon anodes in a bath of calcium chloride at 800-1000°C, to form carbon dioxide and titanium. Once the reaction is complete, the titanium is encapsulated in solid calcium chloride to avoid oxidation upon removal. The mass is washed with water to reveal the titanium powder, and light pressure is applied to break up larger pieces. This has fewer process steps from ore to product, and fewer toxic by-products than the Kroll process, with the benefit of no post processing steps to manufacture powder, as the product is in a spherical powder form. However, like the Kroll process, the FCC process is a batch process, which is time consuming, and requires very careful considerations to ensure consistent quality.

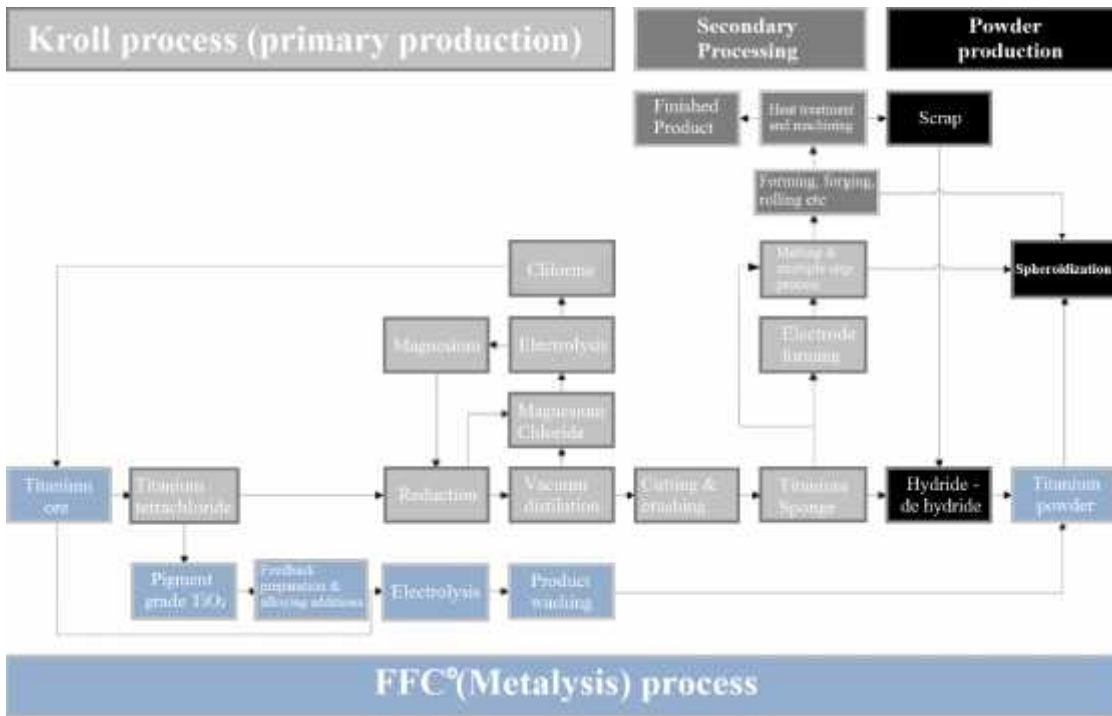


Figure 1: FFC process as developed by Metalysis to produce titanium powder compared to the Kroll process (Mellor et al. 2015)

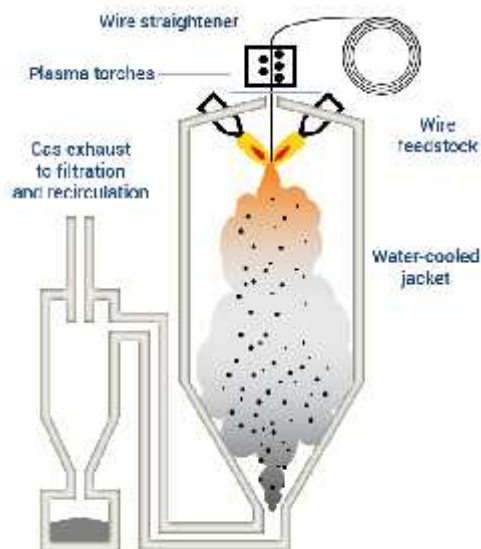
In addition to these production methods, various direct electrolytic methods have been proposed, which utilise carbon. Through use of a graphite anode, calcium oxide can reduce  $TiO_2$  to a solid titanium granular sponge [11]. By dissolving  $TiO_2$  in a fluoride electrolyte, and conducting the electrolysis in a graphite vessel with a graphite anode, liquid titanium can be produced [12]. By reacting  $TiO_2$  with carbon powders and solidifying the mixture, a  $Ti_2CO$  anode can be formed, which reduces to a titanium crystalline solid in the presence of a  $NaCl:KCl$  electrolytic mixture [13]. Common problems with these electrolytic methods are the level of contamination within the titanium, the incomplete reaction of titanium, and the large expense for the small amounts of titanium obtained. Despite these concerns, the results are promising, however at the time of writing these methods remain in the experimental stages.

<sup>1</sup> Reprinted from Titanium Powder Metallurgy, edited by M Quian and F H Froes, Chapter 4 “Titanium powder production via the Metalysis process”, I Mellor, L Grainger, K Rao, J Deane, M Conti, G Doughty, and D Vaughan, p51-67, © 2015, with permission from Elsevier

### 2.1.2 Powder production

Titanium ingots produced by classical manufacturing methods require a post processing step to produce metal powder. The most common methods at the time of writing involve some form of gas atomisation. The standard technique involves a pool of molten metal, which falls through a high speed inert gas stream as it is forced through a nozzle. On leaving the nozzle, the atomised molten metal is solidified as it falls through a cooled chamber [14].

The method of powder production employed for the powder in this project is Plasma Atomisation (Figure 2). This can produce powders of 0-250 $\mu$ m in size [15]. The process feeds a wire into a chamber, where three plasma jets of superheated argon gas atomise the metal. The powder cools as it falls, and it is collected at the bottom of the chamber where it is removed for filtering to separate powder sizes. Using a wire has some advantages over standard gas atomisation. As the wire is fed into the chamber, the solid metal is suspended in the gas as it travels through the plasma jets. The molten metal does not come into contact with the cold surfaces of the machine, which would lead to rough powders with impurities. By controlling the feed speed of the wire, the particle size can be controlled, and as the powder particles fall through cooled gas, highly spherical powder is produced. Sieving can be employed to separate the required powder sizes.



2

Figure 2: Plasma atomization process for manufacturing powdered metal (AP&C 2017)

<sup>2</sup>Image reproduced with permission from “<http://advancedpowders.com/plasma-atomization-technology/our-technology>”, date accessed 25/08/2017, © 2017, Advanced Powders and Coatings Inc.

### 2.1.3 Titanium alloys

Titanium has a high strength to weight ratio, and is often utilised as a stronger alternative to aluminium, and a lighter alternative to steel. Pure titanium has a Hexagonal Close-Packed (HCP) structure at room temperature in its alpha (  $\alpha$  ) phase, with a phase transformation at 882.5°C into a Body Centred Cubic (BCC) structure as its beta (  $\beta$  ) phase, and a melting point of 1668°C [2]. The abundance of these phases influence material properties, and titanium can be alloyed with other elements to act as phase stabilisers.

Titanium alloys are grouped into grades, and defined by their constituent elements. Grades 1-4 describe unalloyed, or “commercially pure” (CP) titanium, with the highest purity unalloyed titanium being grade 1, and grades 2-4 allowing for minimal additions and varying amounts of impurities [16].

From here, a great many titanium alloys are available with varying amounts of alloying additions. These alloys can be categorised into alpha, beta, or alpha-beta alloys, although some alloys are further referred to as “near alpha” or “near beta” alloys.

As titanium in its basic form has an HCP structure, stabilisers, such as aluminium, can be alloyed with titanium to stabilise and strengthen the  $\alpha$  phase, by raising the transition temperature to inhibit the allotropic transformation (see Figure 3). Common alloying elements which stabilise the  $\alpha$  phase in titanium are aluminium, carbon, nitrogen and oxygen. For most titanium alloys, however, to avoid the retention of  $Ti_3Al$  precipitates in the microstructure, the aluminium content is limited to around 6% [17]. If these alloying additions are present, they form the alpha (or near alpha) group. By having a pure HCP structure, the importance of alpha alloys is in their lack of ductile-brittle transition, meaning they are very useful for cryogenic applications [18]. This group has a satisfactory fracture toughness, weldability and creep resistance, however alpha alloys have a low-medium strength, in the context of titanium alloys, and are not heat treatable [16].

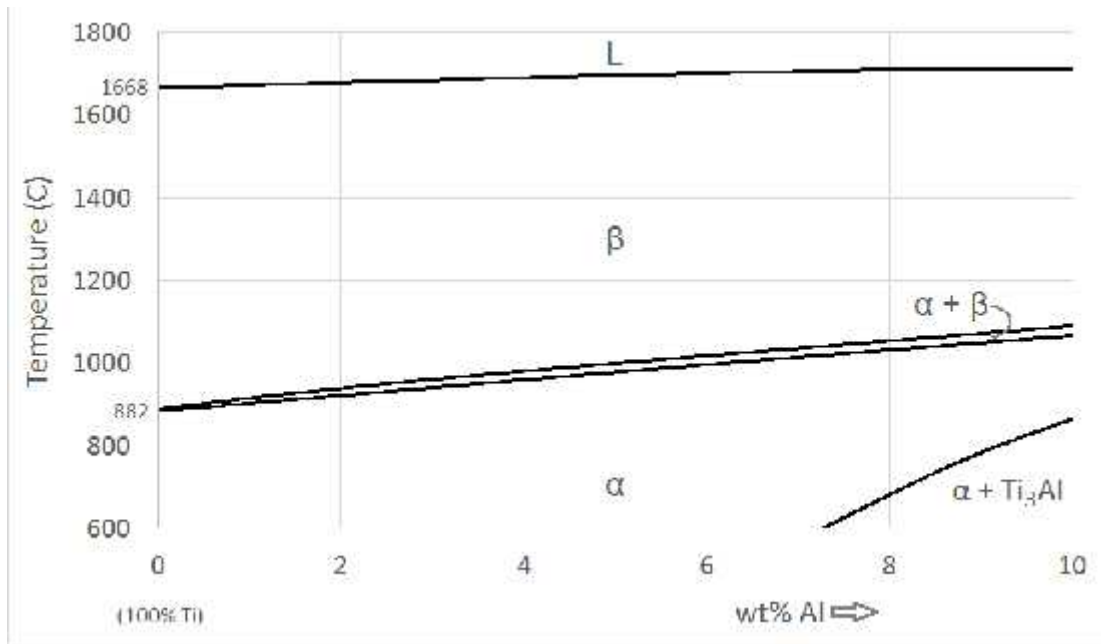


Figure 3: Titanium aluminium phase diagram (redrawn from Calphad 2017)

[19]

Common alloying additions which stabilise the  $\beta$  phase are vanadium, molybdenum, tantalum and niobium. If these are added to titanium, they form the beta (or near beta) group. The BCC structure of the  $\beta$  phase is introduced to pure titanium at 882.5°C. By the introduction of  $\beta$  stabilisers, this temperature can be reduced, leading to more  $\beta$  phase at room temperature (see Figure 4). Typically, compared to other titanium alloys,  $\beta$  titanium alloys have the highest strength to weight ratios, are generally weldable and heat treatable, with good formability and hardenability [2].  $\alpha$  alloys also have the highest density, can have issues with segregation, and their low elasticity and high strength can cause problems with tooling design [20].

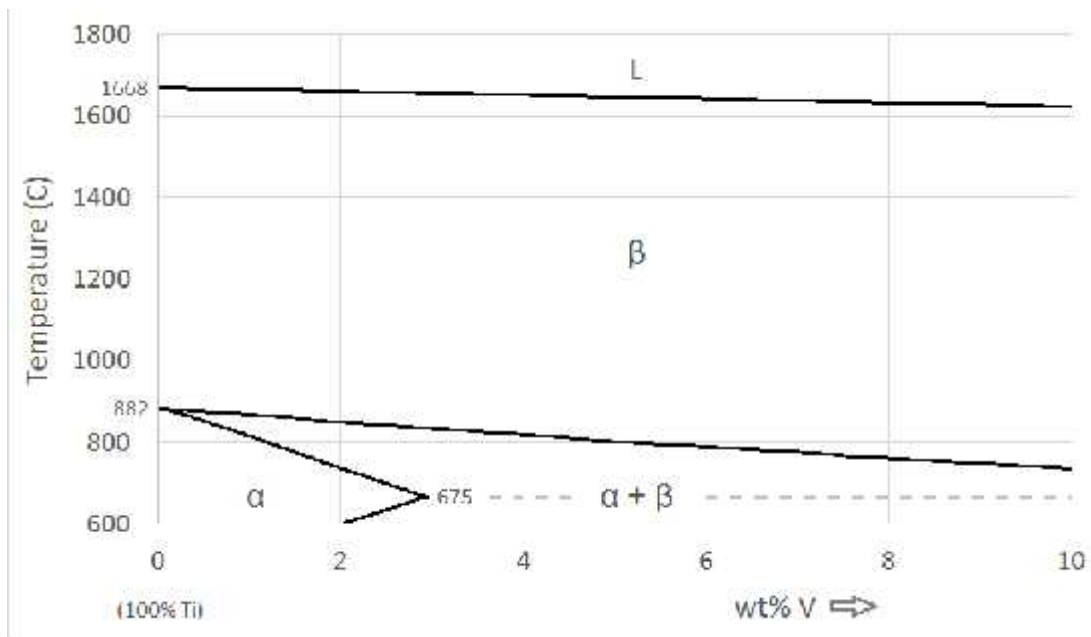


Figure 4: Titanium vanadium phase diagram (redrawn from Predel, 1998)

[21]

#### 2.1.4 Ti6Al4V

Ti6Al4V is a titanium alloy with main alloying additions being aluminium and vanadium, at 6wt% and 4wt% respectively. Depending on the application, aluminium additions could be anywhere between 5.5-6.75wt%, and vanadium additions between 3.5-4.5wt% [22]. The aluminium and vanadium in Ti6Al4V respectively stabilise the  $\alpha$  and  $\beta$  regions in titanium at room temperature, therefore Ti6Al4V is an alpha-beta alloy. Ti6Al4V has a good balance of corrosion resistance, high temperature capability and a significantly higher strength than commercially pure (CP) titanium [18]. Currently, there are two common grades which Ti6Al4V could refer to: grade 5 or grade 23.

Grade 5 may contain a maximum 0.3% iron, 0.2% oxygen, 0.08% carbon, 0.05% nitrogen, 0.015% hydrogen and 0.005% yttrium. Other individual elements must be no larger than 0.1%, and total less than 0.4%, with titanium making up the balance. Although it is beneficial to keep all impurities to a minimum, the particular named impurities can drastically affect the mechanical properties, despite their small quantities. For example, oxygen content increases the strength of titanium alloys, but reduces the ductility [23], and as hydrogen embrittlement is a common concern (for many metals including titanium alloys) hydrogen should be kept to a minimum [24][25].

Grade 23 is an extra-low interstitial (ELI) grade, meaning the powder contains fewer amounts of impurities (in particular oxygen, nitrogen and iron) which work to alter the  $\alpha$  and  $\beta$  phases.

Other than these, Ti6Al4V alloys for advanced corrosion resistance are available. Grades 24 and 25 both contain 0.04-0.08wt% palladium, with grade 25 also containing

0.3-0.8wt% nickel [26]. Grade 29 is an ELI alloy, containing 0.08-0.14 ruthenium, a cost effective alternative to palladium.

Ti6Al4V, as an alpha beta alloy, retains both HCP and BCC phases at room temperature. At raised temperatures, the  $\beta$  transus lies at  $\sim 1000^{\circ}\text{C}$ , with the liquidus at  $\sim 1650^{\circ}\text{C}$  [27]. Controlling the alloying additions, time at raised temperatures and the cooling rate can determine how much of these phases remains at room temperature, and what form they take. In Ti6Al4V, three main microstructures can be expected, bimodal, equiaxed, and lamellar (Figure 7). The continuous cooling transformation (CCT) diagram (Figure 6) shows that  $\beta$  martensite can be formed during the diffusionless transformation temperatures, to give an orthorhombic structure. If the Ti6Al4V is fast cooled from the melt (such as a room temperature weld, or a water quench from high temperatures) a bimodal microstructure would be expected [28][29]. As time to cool increases,  $\beta$  is transformed to retain  $\alpha + \beta$  phases, in their respective HCP and BCC structures. Holding the material in the  $\beta \rightarrow \alpha + \beta$  region and slow cooling from here leads to an equiaxed microstructure [30][31]. If cooling from high temperatures is slow,  $\beta$  phase can transform straight to  $\alpha + \beta$ , which leads to a distribution of  $\alpha$  and  $\beta$  phases into a lamellar structure [32].

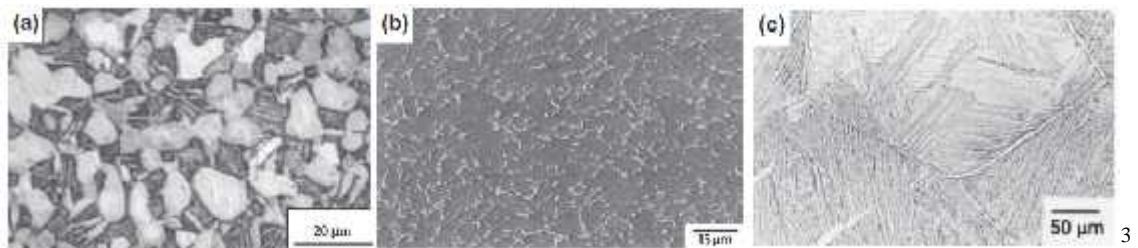


Figure 5: Ti6Al4V microstructures available: a) bimodal, b) equiaxed, c) lamellar (Wu et al. 2013)

<sup>3</sup> Reprinted from Materials & Design, 46, G.Q.Wu, C.L.Shi, W.Sha, A.X.Sha, H.R.Jiang, “Effect of microstructure on the fatigue properties of Ti–6Al–4V titanium alloys”, p668-674, © 2013 with permission from Elsevier

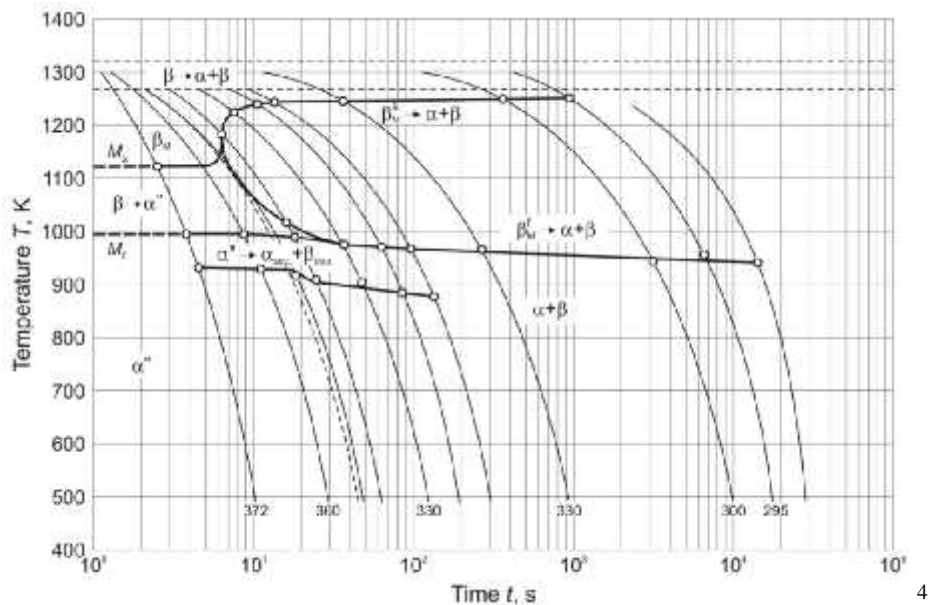
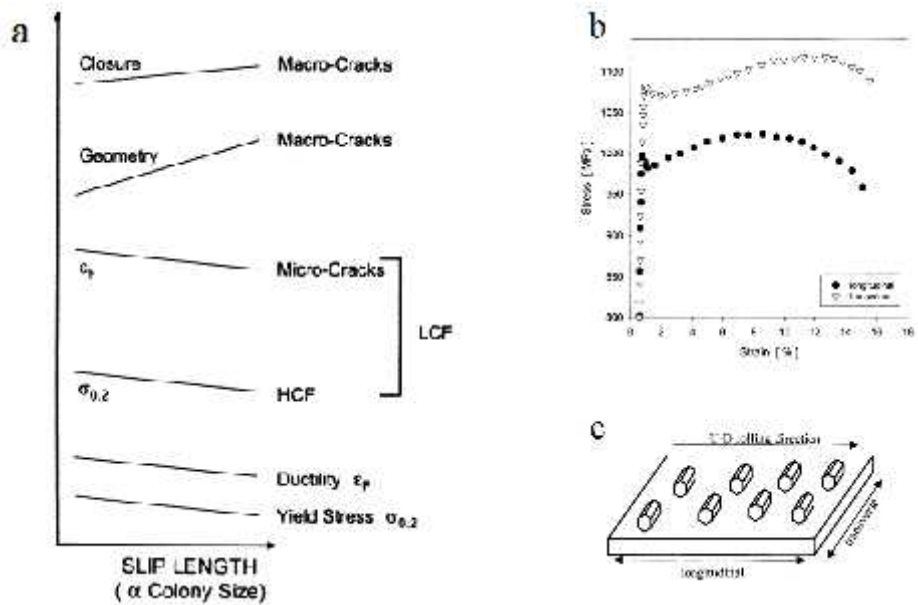


Figure 6: CCT diagram for Ti6Al4V (Sieniawski et al. 2013)

As well as the available phases, grain sizes, thicknesses, and texture are important considerations when designing for optimal mechanical properties. By controlling the cooling rates of titanium alloys, different microstructures can be produced from the same constituent elements. The specifics can be estimated by using CCT diagrams as a guide (see Figure 6).

In 1998, Lütjering generalised the effects of colony size on the mechanical properties (Figure 7), by determining that an increasing colony size provided an increasing slip length, which improves ductility and fracture toughness [33]. As well as this, the orientation distribution of the grains (texture) plays an important role in the mechanical properties. As titanium has a primary HCP structure, the orientation of this can affect the strength depending on the test direction, and titanium alloys can display anisotropy (see Figure 7) [34]. This is not just limited to the titanium alloys, however, as anisotropy is recorded in alloys [35].

<sup>4</sup> Reproduced from fig 1, © 2013. Sieniawski, W. Ziaja, K. Kubiak and M. Motyka. Originally published in InTech, reproduced under CC BY-NC-SA 3.0 license. Available from: DOI:10.5772/56197



5

Figure 7: Microstructural features affecting mechanical properties: a) colony size in fully lamellar microstructures (Lütjering 1998); b) textural anisotropy observed in a rolled Ti6Al4V plate, with c) defining textural directions (Bache et al. 2001)

Table 1: Simplification of how microstructure affects mechanical properties, where > means better than, and < means worse than. Information from Lütjering 2007

<b>Property</b> →	<b>0.2 Yield stress</b>	<b>Elastic modulus</b>	<b>High cycle fatigue</b>	
Microstructural feature ↓				Microstructural feature ↓
Small $\alpha$ colonies	>	>	>	Coarse lamellar
Small $\alpha$ lamellae	>	>	<	Fully lamellar
Bi-modal structure				
Small $\alpha$ grain size	>	>	>	Large $\alpha$ or fully equiaxed
More oxygen	>	<	>	Less oxygen
Secondary $\alpha$ in $\beta$	>	<	>	No secondary $\alpha$ in $\beta$
Stress // to 0001 dirn in HCP	>	N/A	> in vacuum < in air	Stress $\perp$ to 0001 dirn in HCP

<sup>5</sup> Reprinted from Materials Science and Engineering: A with permission from Elsevier:

a) Vol 243(1-2), G.Lütjering, "Influence of processing on microstructure and mechanical properties of (+) titanium alloys", 32-45, © 1998

b and c) Vol 319, M.R.Bache, W.J.Evans, "Impact of texture on the mechanical properties in an advanced titanium alloy", 409-414, © 2001

When analysing microstructural images of Ti6Al4V, characteristic basket weave (or Widmanstätten patterns) are one available microstructure. The main composition of this structure is lath, where retained rods can be seen between the colonies. Figure 8 demonstrates that despite the different manufacturing methods used to produce these Ti6Al4V samples, all display the characteristic Widmanstätten pattern. Despite the similarities of these microstructures, there is clear contrast between them, the most obvious of which is how fine or coarse the grains are.

In general, ultra-fine equiaxed grains are of higher strength than coarse equiaxed grains [2][36]. This is logical considering ultra-fine grains will provide barriers to the many slip systems in the HCP structure, limit twinning, and resist movement on a microstructural level to increase strength. In the case of grain sizes of lamellar arrangement (Figure 9), larger plates lead to higher yield strength [37]. How this is controlled, however, can be a delicate balancing act, as heat treatments and cooling rates can have adverse effects on other aspects of microstructure [38][39]. Due to variations in microstructure, it is difficult to generalise when it comes to mechanical properties of metals.

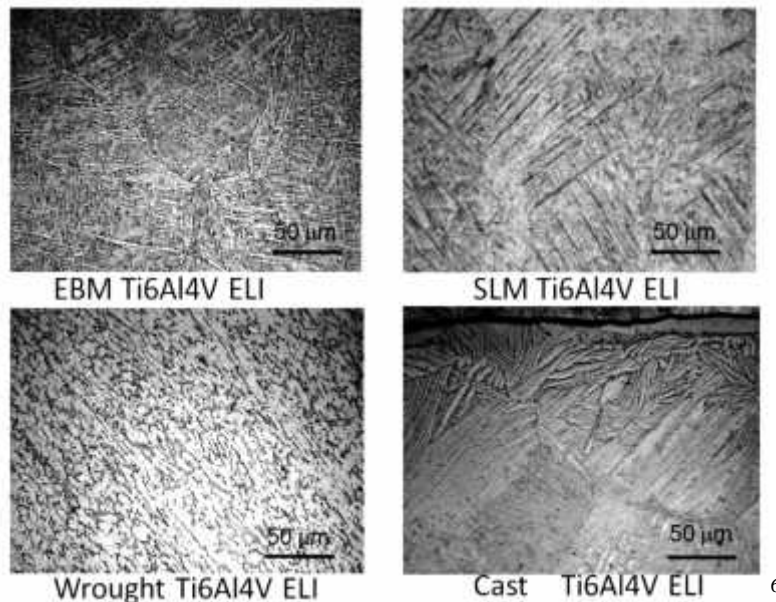


Figure 8: Ti6Al4V extra low interstitial (ELI) microstructures from various manufacturing methods (Koike et al. 2011)

---

<sup>6</sup> Reproduced from fig. 5 © 2011 M. Koike, P. Greer, K. Owen, G. Lilly, L.E. Murr, S.M. Gaytan, E. Martinez, and T. Okabe, Originally published in Materials 4, reproduced under CC BY-NC-SA 3.0 license. Available from DOI:10.3390/ma4101776

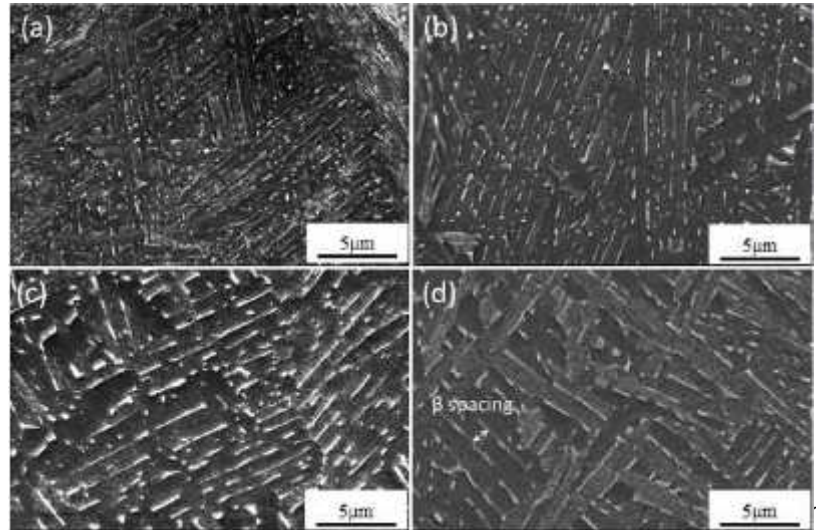


Figure 9: Microstructure of solid EBM Ti6Al4V rods of varying thicknesses: (a) 1mm, (b) 5mm, (c) 10mm and (d) 20mm (Tan et al. 2015)

The actual mechanical property values of Ti6Al4V are highly dependent on the microstructure, therefore although the literature gives a range of values for mechanical properties of Ti6Al4V, the exact values of a part will depend on its history. Compared to other titanium alloys, the elastic modulus of Ti6Al4V is mid-range, with a higher compressive value than tensile, and a stiffness to weight ratio which is comparable to aluminium alloys [40]. Where Ti6Al4V excels is its good corrosion resistance and high strength, which is retained up to 400°C.

Table 2: Range of typical mechanical properties available for Ti6Al4V

	UTS (MPa)	Yield Strength (MPa)	Elastic Modulus (GPa)
Value	895-930	825-869	100-130
Reference	[40]	[40]	[18]

The high costs associated with titanium production prevents widespread use, with the majority of Ti6Al4V consumed by the aerospace sector, as a lightweight alternative to steel for components, such as landing gear mounts and wing attachments [41][42]. Recent advances in high performance alloys and carbon based composites provide competition for Ti6Al4V within aerospace [43]. Other than aerospace, the medical industry utilise titanium alloys due to its biocompatibility and corrosion resistance

<sup>7</sup> Reprinted from Journal of Alloys and Compounds, 646, X.Tan, Y.Kok, Y. Tan, G. Vastola, Q. Pei, G. Zhang, Y Zhang, S. Tor, K. Leong, C. Chua, “An experimental and simulation study on build thickness dependent microstructure for electron beam melted Ti–6Al–4V”, p303-309, © 2015, with permission from Elsevier

(often in the form of surgical tools and implants), and the weight savings that can be obtained by replacing steel with titanium alloys make titanium alloys an attractive proposition for the automotive industry [44][45].

## 2.2 Additive Manufacturing

The origins of Additive Manufacturing (AM) begin with Charles W Hull, who filed a US patent in 1986 describing a method of producing objects by stereolithography [46]. Since then, the concept has gone from strength to strength by various methodologies, as industry has recognised the many advantages AM can provide.

AM can be broadly defined as the building of products by the specific addition of a base material in layers. This is in contrast to the traditional “subtractive manufacturing”, where a block of material is machined away to reveal the required part. AM is often colloquially referred to as “3D printing”, and contains many different methods, with the ability to utilise a range of materials. AM offers building solutions for plastics, ceramics, and materials of other types, however this section will be mainly considering processes which utilise metal.

Despite their individual characteristics, all additive manufacture methods begin with the design of the object, which is created using Computer Aided Design (CAD) software. The CAD model must then be converted to a format that is readable by the AM machine in question, and then transferred to the AM machine for the build begin.

This occurs through the layering and forming of the desired material in the x-y plane, and through movement in the z direction of either the platform the object stands on, the depositing mechanism, or both. The material deposited is fused by a direct heat source, common current mechanisms being laser, electron beam, or plasma.

Once the build is complete, the object can be removed from the machine for inspection, and post processing. The post processing of the object is often manual work in finishing the piece, perhaps removal of supports if necessary, or polishing to improve the surface finish. The number of post processing steps necessary after the build is very specific to the AM method, as each method has its advantages and challenges.

From this, although AM can be defined as a generic process from idea to application, the specifics of each step vary between methods [47]. A range of AM processes are discussed in the next sub-section, with a closer look at powder bed fusion. The final sub-section concentrates on the particular method utilised in this project, Electron Beam Melting (EBM).

### 2.2.1 AM Processes

Additive manufacturing (AM) has several main advantages over traditional methods. Complex designs can be realised quickly and efficiently, through minimal machining and material wastage. This drives down the cost in tooling and time. Parts which previously would have only been possible by combining many individual components can now be made as a whole single part, leading to a reduction in time, cost and weight [48][49]. Complex parts which would not have been feasible to produce traditionally, such as lattice structures and custom made medical parts, can now be realised due to advances in AM processes [50]–[52]. As with traditional manufacturing routes, the AM methods available provide variation in mechanical properties (see Figure 10).

As well as the EBM process utilised for this project (discussed in 2.2.2), other processes for metal AM are commercially available. Several of these process families are described here.

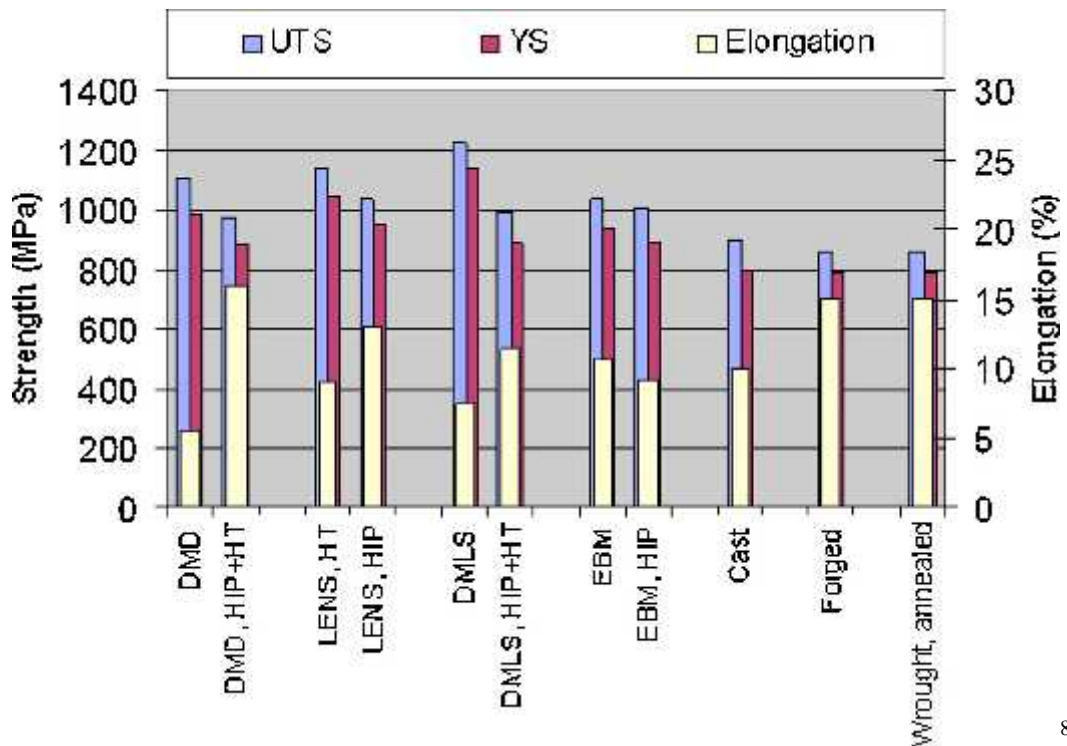


Figure 10: Comparison of mechanical properties of Ti6Al4V samples manufactured by various processes. In lieu of elastic modulus, elongation prior to fracture is provided (Dutta et al. 2017)

<sup>8</sup> Reprinted from Metal Powder Report, 72(2), B.Dutta, F.Froes, “The Additive Manufacturing (AM) of titanium alloys, p96-106”, © 2017, with permission from Elsevier

### Sheet Lamination

One of the earliest AM techniques was that of the sheet lamination process [53]. This involved the cutting and bonding of thin sheets, each representing a cross sectional area of a layered CAD model. Although this layering process is possible for metals, as AM techniques have advanced, more time and cost effective methods for metal manufacturing are available.

### Binder Jetting

Binder jetting is an AM process utilising a binding agent to hold the powdered material in its structure, before heating the part to incorporate or evaporate the binder. Traditionally this has been highly effective for polymers with low melting points, however ExOne (USA) is one company utilising the method for powdered metal, using techniques developed at the Massachusetts Institute of Technology [54]. As well as metals and metal alloys, sand, ceramics, glass, and composite materials can all be 3D printed in this method.

### Direct Metal Deposition

Direct energy deposition processes (or direct metal deposition, DMD) use a focused heat source to melt the material, as the material is being deposited onto the build surface. Three different heat sources have been utilised in this AM process: laser, electron beam, or plasma arc welding system [47]. Two main feed systems supplying the metal to be deposited are available, wire or powder fed.

The Rapid Plasma Deposition™ system by Norsk Titanium (Norway), builds up near net shapes using titanium wire [55]. In general, wire fed processes have a higher feedstock efficiency than powder bed technologies, as during the process the entire volume of wire is used to build the part. Using a solid wire as the source of the material means that the user is not exposed to the hazards surrounding metal powders. However, wire processes are restricted by the thickness of the wire, which limits the geometries available for manufacture. As such, although wire fed AM processes are a low material wastage and highly time effective process, as the complexity of the part increases, the wire fed AM process becomes less feasible.

Alternatives to wire fed direct energy deposition exist in the form of powder fed methods. One such company belonging to this AM family is BeAM S.A.S (France). The Laser Metal Deposition (LMD) technology from BeAM deposits metal powder from a nozzle, which intersects with a laser to melt the powder onto the surface of the part [56]. As well as having all the usual advantages of AM technology, LMD is not restricted by the size of a build chamber, and has the ability to not only build new parts, but the potential to repair worn or defective parts manufactured by any other process. Due to the small deposition area, innovative repairs can be performed without welding defects. However, this highly innovative technology means this method is currently one of the more expensive AM processes.

### Laser Powder Bed

Laser powder bed (LPB) processes work by depositing a layer of powder onto a build platform with a rake or blade, and using a laser beam to selectively melt areas to form the part. LPB systems can work in an inert atmosphere, which is a cost effective alternative to a vacuum, however the energy efficiency of a laser is significantly less than that of an electron beam [57][58]. LPB is a cold process, in that the only areas of the build subjected to heat, are the melt areas where solidification is required. Due to the high temperature gradient between the melt and the powder, internal stresses accumulate within the part during manufacture. From this, hot post processing is often required to relieve these internal stresses, although recent studies have been investigating steps to reduce residual stresses during the build [59]–[62]. The build chamber is of a simpler design than EBM, meaning it is less time consuming to clean, therefore, turnaround time is lessened, and different metal alloys can be used in the same machine more often.

The LPB based systems have been commercialised by a range of different companies, each preferring different terms to describe very similar systems. Selective laser melting (SLM), direct metal laser sintering (DMLS), and Laser Engineered Net Shaping (LENS® Sandia National Laboratories) are all variations of the system [63]. Such equipment is available from various companies, such as 3D systems (USA), Renishaw (UK), SLM solutions (Germany), and Concept laser (Germany) among others.

### *2.2.2 Electron Beam Melting*

The EBM process is a powder bed method first made commercially viable for 3D printing purposes by Arcam AB, based in Mölndal, Sweden. The first patent submitted in 1993 describes how a beam of electrons can be utilised to melt particles on a vertically moving platform [64]. From there, further research and development was investigated with Chalmers University of Technology, Gothenburg, before Arcam AB became fully established in 1997. In 2002, the S series of EBM machines was launched, followed by the A series in 2007 and the Q series in 2013. Over this time period, EBM technology has predominantly been used for medical and aerospace applications, due to the advantages of high precision engineering. Unfortunately, the high costs of installation, upkeep, and consumable costs means EBM is only available to a niche market.

EBM follows the same general steps as every other AM method, however there are some key features which can influence the parts produced. Arcam provides a series of recommended settings, however the settings can be altered at the discretion of the user.

The builds within this project had three areas where selections were made, which due to their complexity can contribute significantly to variations in properties. These three are the layer thickness, the preheat theme, and the beam pattern. The reasons behind

choosing these will be discussed in the relevant build sections, however the basis of these processes will be discussed here.

For EBM, the user builds their part using CAD software and saves the file in an stl format. Sometimes the part may need the addition of supports to ensure a successful build. Supports are thin metal solids which can be used to connect the part to the base plate, to quickly and effectively reduce the heat in the part. These supports act to transfer the heat to the base plate, to prevent swelling. Swelling is an undesirable effect occurring from the build-up of excess heat in the part [65]. This can happen particularly with negative surfaces (which occur when the beam melts a new layer on top of a previous layer of sintered powder) as opposed to building on top of the solidifying melt from the previous layer (see Figure 11). Such surfaces can warp upward with an excess of heat, and supports can act to dissipate this heat [66]. Despite their name, supports are not load bearing. There are many support structures available, and studies have suggested some support structures are advantageous over others [67].

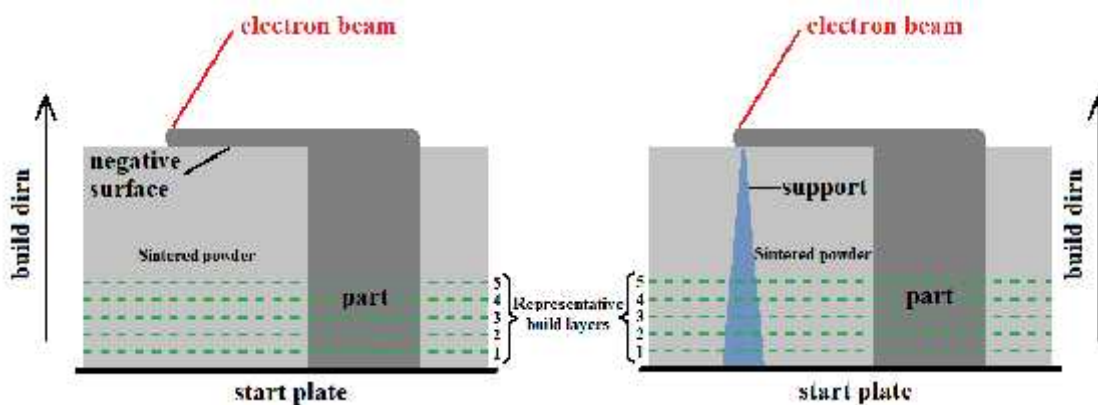


Figure 11: negative surfaces occur when melt occurs on top of sintered powder (light grey). Supports (blue) are generated to avoid generating negative surfaces, and are melted using the “support” setting

The stl files are loaded into Arcam AB Build Assembler to prepare the models for the build. Here, no further editing can occur, and any problems with the design must be identified and resolved before this point. In this software, the build envelope size (the volume in the EBM machine in which the objects will be built), and the size of the start plate are selected. The stl files are loaded, and the user defines the layer thickness (typically either 50 $\mu$ m or 70 $\mu$ m).

The advantage of 50 $\mu$ m layers is that they will give a closer representation of the model than the 70 $\mu$ m layers, through higher resolution achieved through a greater number of layers. As well as this, Algardh et al. report that 25 $\mu$ m layer thicknesses provide a better surface quality than the 50 $\mu$ m layers, therefore it is probable that the 50 $\mu$ m layers would provide a better surface quality than the 70 $\mu$ m layer thickness [68]. There are advantages in selecting 70 $\mu$ m layer thickness over 50 $\mu$ m layers, in that the build time is

shorter for the 70  $\mu\text{m}$  layers, due to there being fewer physical layers to build. This increases productivity of the equipment and reduces the risk that a build may be interrupted by a filament failure (the filaments used in this project had an advised lifetime of 80 hours). Furthermore, with a 50 $\mu\text{m}$  layer thickness, less powder is deposited on the powder bed after each rake pass, with more powder being swept off the build area, therefore the user must have enough powder available to complete a 50 $\mu\text{m}$  build. It is therefore important to consider the risk versus reward with regards to choosing layer thickness.

Following this, the user can define whether the parts within the stl files need to be melted under one of the three “themes”, solids, netts, or supports; a selection which defines pre-set conditions for the build. The solid setting is for standard bulk material parts, traditionally manufactured by subtractive machining from solid metal. The nett setting is for porous materials, such as lattices and foams, which range from difficult to impossible for traditional manufacturing methods. If the part has areas where the beam would melt material on top of layers sintered powder, a support may be required to fill the negative space (see Figure 11). The support setting provides less beam power to the melt, leading to less consolidation of the material. This combined with the CAD model design gives minimal connection to the part, therefore the supports should be able to be removed from the solid part with ease.

Once the user has selected the layer thickness, the program slices the part into layers. This provides a stack of surfaces for the machine to melt layer by layer. This file is saved in an abf format, and transferred to EBM control (the user interface for the Arcam EBM machine). The software is accessible on either the EBM machine or a computing device. The build is loaded, and further build specific settings are activated by selecting themes and related models.

To prepare the machine for a build, the user follows a protocol to inspect and replace any consumables that may have reached the end of their life. For example, if the rake teeth are bent, they will need to be replaced, if metallization is present on the heat shields, they will need to be replaced, and if the build plate is not uniform following thermal expansion and cooling, it will need to be replaced.

Once the machine has been thoroughly cleaned, the user fills the hoppers with metal powder and locks the door. A vacuum is induced, and once the pressure is low enough, the build can begin. Figure 12 shows a schematic of the build process.

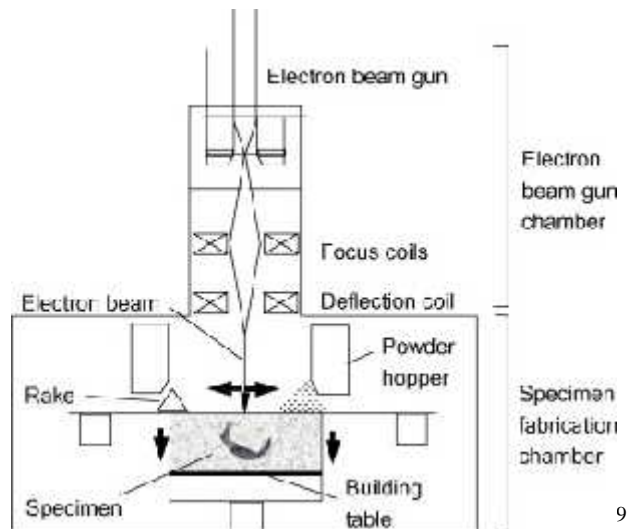


Figure 12: Schematic of EBM system (Koike et al. 2011)

A rake sweeps the powder across the build chamber, leaving a layer of powder on the build plate. A voltage is induced across the filament, liberating electrons into an electron beam gun. A stream of high energy electrons is directed down the column, and is focused using magnetic coils to a high precision onto the build plate. The electron beam sweeps over the powder surface in a preheat step, sintering the powder. The next step is the melt. During the melt, the beam speed and energy input at different points of the build are controlled, to attempt to maintain a constant temperature.

When the beam melts the powder, it can be completed by contouring or hatching. Hatching sweeps the beam across the entire melt area, turning on when the object is in the beam area, and off when the beam is over the sintered powder. Contouring is the method by which the beam is guided around the edge of the part, melting the powder around the parts as it passes over. Figure 13 is a simplified illustration of the three possible methods used in this project.

<sup>9</sup> Reprinted from Journal of Materials Processing Technology, 211, M. Koike, K. Martinez, L. Guo, G. Chahine, R. Kovacevic, and T. Okabe, "Evaluation of titanium alloy fabricated using electron beam melting system for dental applications", p1400-1408, © 2011, with permission from Elsevier

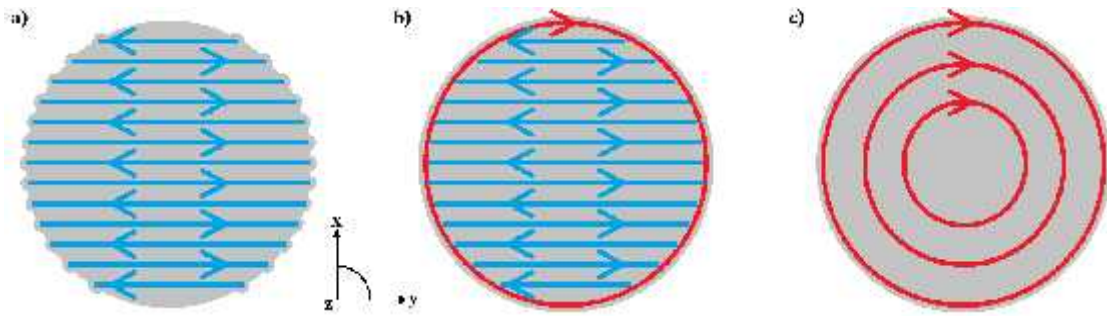


Figure 13: Schematic of the melting of a lattice strut. Not to scale. a) Blue line shows hatching alone. b) Red line shows contouring, and hatching in the blue line. c) Red lines show three contour passes

a) shows the hatching theme alone, where, although the beam stops at the outer edge, it is suspected that the surface roughness is greater due to the path the beam takes. If solid builds are to be fully machined, hatching can be used alone to speed up the build, as the surface will be removed in post processing. It is not advised by manufacturers to use the hatching theme alone if the parts are to be used straight out of the machine.

b) shows one contour trace for simplicity, even though in this project, when contouring was used, the minimum number of contour traces would be three. The contour melt would occur first, followed by hatching. As illustrated, the contour line contains the melt pool, created during the hatching process. As contouring moves from area to area, the layer time is greatly increased by including it in lattice builds. This is due to the need to melt each individual strut in this circular fashion. The result of contour and hatching themes on the build layer can be seen in image c in Figure 14. The third strut down is designed as a 1mm diameter strut, like those used within this project. In solid builds, contouring can be very effective in improving the surface finish, and is particularly important if parts are to be used straight out of the build.

c) shows the contour theme alone, with three contour traces. The number of contour traces can be chosen in the settings. In this project, if contours were used, three traces were chosen as a minimum. The beam melts the powder from outside to inside, at a beam spacing set within the settings. The result of contour only theme on the build layer can be seen in image b in Figure 14. The third strut down is designed as a 1mm diameter strut, like those used within this project.

In Hernandez-Nava et al. (Figure 14), a series of weld tracks were obtained for a single contour pass, three contour passes, and three contour passes and a hatch [69]. These weld tracks were based on octagonal struts of increasing width. This work demonstrated the actual melt area in relation to the beam. From Figure 14a, it can be seen that one contour pass comfortably covers the areas where strut diameter is  $500\mu\text{m}$  and  $650\mu\text{m}$ ,

however for traces above this size, there emerges a clear, central, untouched region. In b, three contour passes cover the area up to strut diameter of 1.3mm, above this size three contour passes would not fully melt the strut. In c, it can be seen that the hatch setting is required to fully melt the strut area, for struts of all widths.

Comparing the first three weld tracks in b and c, it is difficult to see whether the addition of the hatching step has any influence on the melt pool. As the machine has no way to identify the melt pool, the hatch setting will run the beam over the melt area, even if the contouring step has already fully melted the region. Therefore, when building lattices of strut diameter 1mm, it is questionable whether a hatch step in addition to a contour step is required.

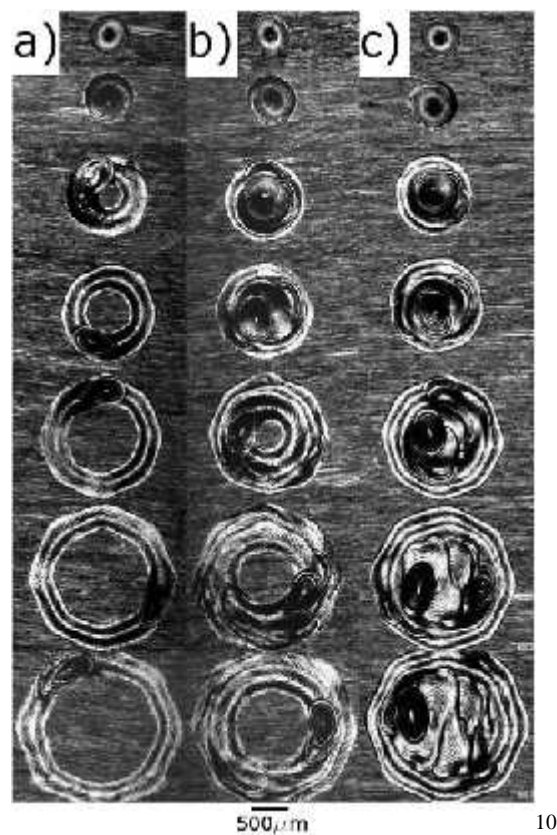


Figure 14: Comparison of melted zones with differing strut diameter: a) one contour pass, b) full contouring region, c) contouring and hatching stages (Hernandez-Nava et al. 2016)

Once the melt step is complete, the build plate lowers by one layer thickness. Another layer of powder is deposited by the rake and the process repeats until the build is complete. The build is left to cool, and once the temperature is below 100°C, the door is

<sup>10</sup> Image reproduced under Creative Commons Attribution Licence from fig.14, p290 in E. Hernandez-Nava et al., “The effect of defects on the mechanical response of Ti-6Al-4V cubic lattice structures fabricated by electron beam melting,” *Acta Mater.*, vol. 108, pp. 279–292, 2016.

opened to remove the build. The build platform is raised, and loose powder vacuumed out. The part is removed within a sinter cake, and put into the powder recovery system (PRS). The PRS uses the same powder composition to blast the sinter away and reveal the solid part within the cake. The excess powder falls through a grate and is processed by the PRS to remove powder particles below 45 $\mu$ m. Once all the powder has been removed from the EBM machine and processed by the PRS, the powder is transferred to an airtight barrel for storage, through a sieve to remove particles above 100 $\mu$ m. The powder can then be reused many times, as long as the composition remains within specification [70]. The part is then ready for use, however a polishing step can be performed to improve the surface finish.

As well as all the advantages of AM methods, the Arcam EBM system has many advantages due to its design. A high energy density is achieved through the use of a high power electron beam. This means high melting temperatures can be obtained and sustained at high melting speeds. One disadvantage to using an electron beam is the requirement of a vacuum, however the presence of a vacuum eliminates the possibility of introducing impurities to the part from the atmosphere, which is highly advantageous. The electron beam performs a preheating step, whereby the beam sweeps over the entire build area prior to melting the part model. This preheating step means there are little to no residual stresses in EBM parts [71]. The inherent design of the EBM system means that once the build has started, the chamber must remain closed. This can be seen as an advantage, as after the user has set up the machine, no further input is required from the operator to perform the build. Equally, this could be a disadvantage, as if anything goes wrong during the build, no steps can be taken to manually rectify the problem, the build would fail, and need to be started from scratch. After the build is complete, sintered powder can be removed from the, now solid, part, by the powder recovery system. This metal powder can be removed, filtered, sieved and reused, which is a huge reduction in potential waste.

Unfortunately, the EBM method as currently implemented is high cost, with not only the initial purchase price of equipment, installation costs and training of users, but also the continuous need for consumables, running costs and maintenance to consider. The build chamber of the EBM is very complex, with many intricate parts and tiny spaces for metal powder to fall into. It is very difficult to thoroughly clean the machine, and therefore it is strongly advised that each machine should be exclusive to one metal alloy, to avoid cross contamination of powder.

This method is also a batch process, with no current feasible method to achieve a continuous process. Arcam have, however, been working on making larger machines to yield larger parts and have a higher volume build envelope, therefore future machines may become more cost effective with the physical space and further technology required to build more parts per batch [72].

### 2.2.3 Influence of processing on the properties of AM parts

Due to the nature of powder processes, the surfaces of AM parts have a high surface roughness. The surface roughness of as built parts differs between processes and powder size. When looking at AM parts, the most obvious surface roughness occurs as cold powder particles next to the melt are incorporated into the part. As the melt cools, the powder particles are solidified into the part. In EBM, for example, the powder particles are between 45-100 $\mu\text{m}$ . These particles will have been sintered, changing the morphology of the powder when particles accumulate at the edges of the melt.

Surface finish is an important consideration for many applications, as rough surfaces can lead to stress concentration points, and places where cracks can nucleate (or propagate if they are already present) which causes problems for mechanical properties, particularly fatigue life (further details in section 2.4).

In the medical industry, studies have suggested the rough surfaces of as-built parts may enhance bone ingrowths, with other studies attempting to further this effect with innovative surface coatings [73]–[75]. Where a rough surface is undesirable, traditional grinding and polishing steps are available [76]. For parts with complex geometries, improving the surface finish requires more creative ideas, such as chemical etching [77] (further details in see 2.3.3).

Depending on the method of AM, post processing may or may not be required. For hot processes, such as EBM, a major advantage is that a stress relief post process step is not needed. For cold processes, a stress relief is usually required, due to the build-up of internal stresses caused by the large temperature gradient between the melt and the part.

Hot isostatic pressing (HIP) is an effective stress relief, and can lead to the reduction of porosity, however the times and temperatures involved are likely to act to alter the microstructure, therefore HIP is not always seen as beneficial. Indeed, Kahlin et al. determined that HIP had a negligible effect on fatigue life of solid EBM and LPB solid Ti6Al4V specimens with as-built surfaces [78], with De Formanoir et al. suggesting that applying a HIP treatment to EBM solid parts with as-built surfaces did not bring considerable improvement to the mechanical properties [79]. Contrary to this, Benedetti et al. investigated SLM Ti6Al4V solid samples and found the HIP improved high-cycle fatigue resistance through changes to the microstructure [80], and a study by Galarraga et al. who tailored mechanical properties of EBM samples using heat treatment, made improvements to strength with no reduction in porosity [81]. In summary, whether heat treatments and HIP have a desirable effect on additive manufactured parts depends on the conditions of the treatment, and requirements of the investigators.

As previously discussed, different AM methods have advantages and disadvantages, with the biggest effects of manufacturing method translating to the parts. In 2013, a comprehensive study by Rafi et al. compared the EBM and SLM processes [82]. They found significant differences in surface conditions and microstructure, which could

explain their findings that SLM had superior tensile and fatigue properties than EBM. As well as this, the study also found differences between mechanical properties if the samples were tested parallel, or perpendicular to the build direction.

Table 3: Comparison of mechanical properties of tensile samples build by EBM and SLM, tested parallel (//) and perpendicular (⊥) to their build directions (Rafi et al. 2013)

AM process with test dirn. in relation to the build dirn.	YS <sub>0.2</sub> (MPa)	UTS (MPa)
EBM //	869 (±7.2)	928 (±9.8)
EBM ⊥	899 (±4.7)	978 (±3.2)
SLM //	1143 (±30)	1219 (±20)
SLM ⊥	1195 (±19)	1269 (±9)
Cast and Annealed (ASTM standard)	885	930

Other studies have suggested anisotropy in the mechanical properties is linked to the anisotropic microstructure that arises from the highly directional heat flow in the process. With the layer by layer process inputting heat on the top of the part, heat flows downwards through the solidifying material, to be distributed through the start plate, cooling the part. This heat flow encourages grain growth in this direction, which has been widely reported. It is this characteristic directional growth, present in many AM processes, that provides great interest with regards to anisotropy in mechanical properties.

In 2007, Gong et al. found that anisotropy in the microstructure led to better corrosion resistance for Ti6Al4V columnar samples built parallel to the build direction, as opposed to lying perpendicular to the build direction [83]. This was attributed to a lower density of grain boundaries, and less  $\beta$  phase present in the microstructure of the parallel samples, compared to the perpendicular samples.

A 2013 study on samples cut horizontally and vertically from Ti6Al4V walls made by Wire Arc Additive Manufactured (WAAM) determined anisotropy in the results, with samples tested perpendicular to the build direction having a higher UTS and YS than samples tested parallel to the build direction [84]. This is in contrast to a study on Ti6Al4V tensile samples built by DMLS, where samples tested parallel to the build direction had a statistically significant higher UTS than samples build perpendicular to the build direction [85].

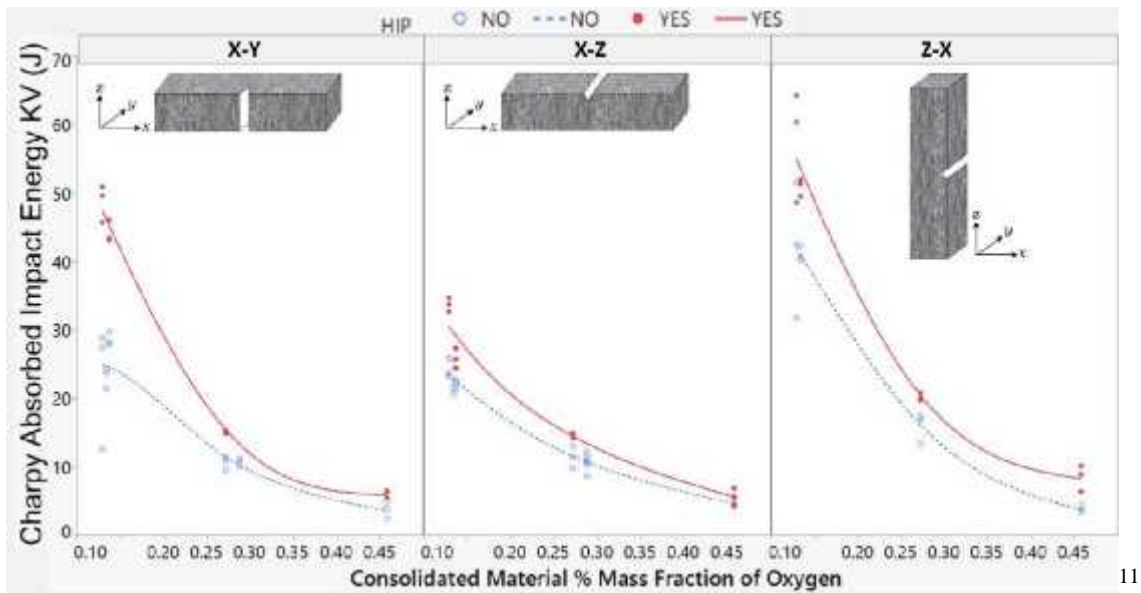


Figure 15: Charpy impact energies for samples tested in differing orientations to the build direction (Grell et al. 2017)

Other materials built by EBM can produce columnar microstructures in the build direction. Zhong et al. observed columnar grains in 316L stainless steel in the build direction [86], Sun et al. observed precipitate alignment along the build direction in Co-Cr-Mo alloy [87], and Deng et al. found anisotropy in mechanical properties of Inconel 718 tensile samples, which were attributed to columnar grain growth in the build direction [88].

With regards to Ti6Al4V, Antonysamy et al. observed columnar grain growth in samples built by EBM through a systematic study utilising EBSD maps [89]. A “base” was built to allow the microstructure to become established, before walls of different thicknesses were built from the base (see Figure 16). This is supported by Tan et al. whose investigation revealed a graded microstructure depending on distance from the build plate (schematic in Figure 16) [90]. In addition, Zhai et al. compared EBM, LENS and wrought Ti6Al4V samples, and found evidence of columnar grains, with fine morphologies in the AM samples arising from the directional heat flow during manufacture [91]. They concluded that these led to higher fracture toughness, but lower yield strength than wrought samples. From this, it is clear to see where anisotropy arises, as the columnar grains will behave differently when tested parallel or perpendicular to their growth.

<sup>11</sup> Reprinted from Additive Manufacturing, 17, W. A. Grell, E.Solis-Ramos, E.Clark, E.Lucon, E.J.Garboczi, P.K.Predecki, Z.Loftus, M.Kumosa, “Effect of powder oxidation on the impact toughness of electron beam melting Ti-6Al-4V”, p123-134 © 2017 with permission from Elsevier

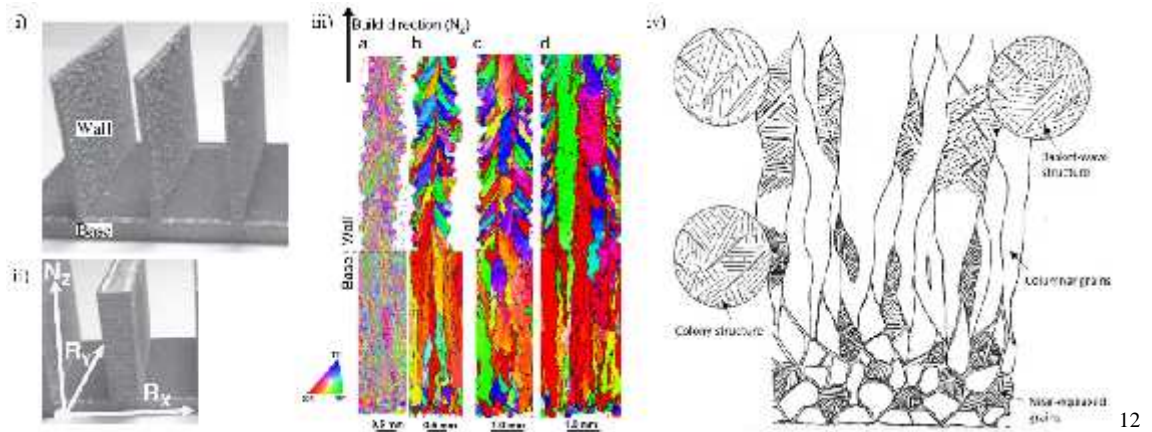


Figure 16: Samples built by EB to conduct microstructural analysis. i) wall samples built on a base, in ii) defined directions. iii) EBSD maps of a) phase map, b-d) reconstructed grain structures for 1mm, 1.5mm and 2mm walls (Antony et al.). iv) graded microstructure (Tan et al. 2015)

In 2012, Rafi et al. built cylindrical samples in EBM for tensile and fatigue testing [92]. The paper concluded that parts built horizontally had a slightly higher tensile strength than the parts tested in the build direction. There is a clear spread in the data, therefore how statistically significant this is remains to be seen. With regards to fatigue testing, the paper concluded that samples tested parallel to the build direction had had a greater fatigue life to those tested perpendicular, however due to the low number of samples, the spread in the data, and lack of statistical supporting evidence, it would be difficult to determine this conclusively.

In summary, recent studies suggest that AM parts can perform as well as traditionally manufactured parts. At the time of writing, there is no general consensus as to whether AM samples have a higher UTS and YS parallel or perpendicular to the build direction. Ti6Al4V parts built by AM methods are expected to display anisotropy, from the presence of columnar grains which grow in the build direction. Although this is often using post processes, in particular surface improvement, it can be argued as the AM process cuts out most of the manufacturing steps, even with these post processes, the number of processing steps is still reduced.

<sup>12</sup> Fig i-iii, © 2013 .Antony et al., Meyer, Prangnell. Originally published in *Materials Characterization*, 84, reproduced under CC BY 3.0 license. Available from: DOI: 10.1016/J.MATCHAR.2013.07.012

Fig iv Reprinted from *Acta Materialia*, 97, X. Tan, Y. Kok, Y. J. Tan, M. Descroins, D. Mangelinck, S. B. Tor, K. F. Leong, C. K. Chua, "Graded microstructure and mechanical properties of additive manufactured Ti-6Al-4V via electron beam melting", p1-16, © 2015, with permission from Elsevier

## 2.3 Lattices

Metal lattices have come a long way since their first description as sets of plaited wire [93]. In the present day, metal lattices can be used to describe many structures, both on large engineering scales in structural design, and on the smaller scales where the lattice can be treated as a material in its own right, which is the focus of this work. It could be said that the specific interest of this work, EBM Ti6Al4V lattices, have more in common with metal foams than their wire twisted cousins, therefore the account of their history will begin here. Following this, the evolution into structured porous materials is discussed with the development of metal lattices. Different lattice geometries are available, and these are covered in the next section. Finally, mechanical properties that have been obtained by metal lattices are discussed in the final section.

### 2.3.1 *Metal foams and the emergence of lattices*<sup>13</sup>

The term “metal foams” can be loosely attributed to any porous metal structure, however the earliest mention of a deliberate foaming of molten metal by a gas was a 1925 French patent [94]. According to a review paper by Banhart [93], the patent describes the process as one of two things: “(i) *the injection of inert gas into a molten metal, or, (ii) the addition of a blowing agent such as a carbonate to a molten metal, during which the melt is stirred*”.

Further patents were filed in the USA throughout the 1940’s and 1950’s, describing various methods of metal foaming, however the stability of these foams while in the liquid state is temperamental [95][96]. In 1957, a short, but continuous process of foaming metal to produce a solid foam was patented [97]. In the 1960’s, the Ethyl Corporation became the research centre for metallic foams, and from this, very slowly, foam technology advanced to industrial processes in the late 1980’s [98][99].

At the time of writing, there are various methods available for the production of metal foams, but all types of metal foam can be divided into two categories: either closed or open cell foams.

Closed cell foams contain independent, unconnected pores. These pores can be formed by the stabilising of gases within a molten mixture, usually involving the addition of high-temperature resistant particles to increase the viscosity and retain the gas bubbles in the liquid up to the point of solidification [100]. The bubbles are formed by the introduction of gas, either by blowing gases into the mixture, causing dissolved gases to be liberated from the solution, or by the release of gases from the breakdown of foaming agents, compounds which generate gases from particles distributed within the mixture [101]–[103]. The selection of the gas product can be very important, as the properties of

---

<sup>13</sup> This sub-section contains text adapted from Morrish et al 2017

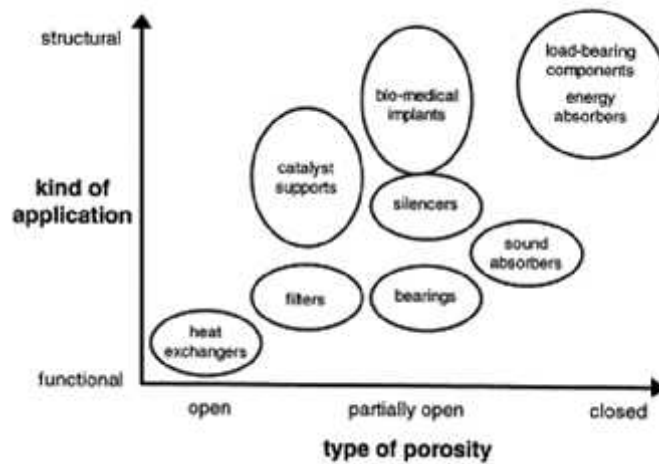
the trapped gas within closed pores will affect the formation and mechanical properties of the foam.

Open celled foams contain channels which are formed from connecting pores. These pores can be formed from solid spacers within the mix, which can tolerate high temperatures of the molten metal, and can later be removed in order to form the channels in the open celled foam [104]–[106]. Direct foaming processes that utilise liquid metals are advantageous, as they can be manufactured by a continuous process [101]. Continuous processes have a huge time saving advantage over batch processes, and therefore these are desirable for the metallic foam industry.

Metal foams can be either stochastic (having a random porosity size and distribution) or regular. Most foams are stochastic as it is technically challenging to control the gases or space holders in the metals. The individual pore sizes within the foam may vary, however methods are often used to restrict the range of pore sizes as much as possible. Regular foams have been traditionally produced by careful selection of solid spacers combined with casting methods, however ensuring an even mix presents difficulties for commercial production [101][107].

With regards to regular foams, AM techniques could be applied with great success here. CAD files would make light work of complex foams, to produce structured foams, as opposed to the randomised nature of current production methods. At the time of writing no such commercial production is in place. The expense of using AM techniques for such foams would be a hindrance, considering the continuous foaming techniques that exist, however perhaps in the future this will be a financially viable option.

There are many potential uses for metal foams, with their varying levels of porosity making them effective for the given application (Figure 17). Open celled foams can be useful as heat exchangers, where the high surface area of an open celled foam can effectively transfer heat between the metal and the medium flowing through the structure [108]–[110]. The high surface area can be advantageous for catalytic applications, where chemical reactions occur within the foam as liquids and/or gases flow through it [111]–[113]. Similarly, foam can be effective for filtration systems where impurities can be removed via reactions with the metal foam, such as in automotive exhausts [114], or by the impregnation of a chemical within the foam, as in the purification of metal alloys [115][116]. Foams with a more closed cell structure can be used to absorb pressure waves as in the case of automotive silencers and firearm suppressors [117][118], and at the furthest end of the energy absorbing spectrum, closed cell foams can be highly proficient in impacts such as bumpers in motor vehicles, and armoured panels for military vehicles [119][120].



14

Figure 17: Applications of metal foams relating to their porosity (Banhart 2001)

Foams have many functional applications, but the difficulty in controlling the structure of foams is a problem which could be solved by the use of AM. One such area where structure is crucial is within the medical industry, for implants in orthopaedics and dentistry [121]–[123]. If structured foams can be produced, the next logical step is to look at geometries beyond spherical pores. Interest surrounding the potential of lattices as an alternative to foams is growing, therefore it is important to consider the differences between foams and lattices, as will be discussed further in the next sections [124]–[126].

When generalising the mechanical properties of foams and lattices, there are many variables to consider. The metal itself has an inherent effect on the mechanical properties (see section 3.8.1 for relationship between strength and density of foams and their constituent metal). Within the foam, the size of pores, distribution of pores, and the level of porosity are important considerations. These must be carefully controlled when manufacturing metal foams to ensure reproducibility, and therefore consistency within the product.

When mechanical properties of stochastic metal foams are investigated, the minimum number of pores in each direction is widely accepted to be six; a value which is often used as a lower limit to the size of samples in designing experiments [127]–[130]. This idea originates from work where metal foams of different average pore size were mechanically tested, and a convergence of mechanical property values was seen over increasing numbers of pores [131]. This led to the conclusion that 6 pores was the minimum required to ensure reliable mechanical properties. This conclusion has been carried over into lattice technology, which is discussed further in the next section.

<sup>14</sup> Reprinted from Progress in Materials Science, 46(6), J.Banhart, “Manufacture, characterisation and application of cellular metals and metal foams”, p559-632, © 2001, with permission from Elsevier

Metal lattices such as those within this thesis are a relatively recent occurrence, as a product of AM methods. As such, research on metal foams has been used as a basis for setting standards, such as that of size dependent properties. On a macroscopic scale, inherent mechanical properties of materials are not size dependent, however when the specimen size approaches the size of the structures, this can change. For most materials small dimensions are acceptable, however the applications that require porous solids often have a structure that is much closer in size to typical test pieces.

As the ability to manufacture large samples of regular structured lattices only came about recently with the widespread introduction of additive manufacturing methods, this ideal number was applied to lattice technology [132]. It was assumed that as a minimum of six pores were required for foams, six unit cells in every direction for lattices would be needed, although this was yet to be confirmed experimentally.

Some exploration of size effects in lattices has been performed by Ahmadi et al. who used finite element modelling to predict the properties of lattices of different sample cell size ratios [133]. They found convergence with larger sizes, with the difference in predicted properties dropping to below 1% for the change from 14 to 15 cells across the sample. Therefore they interpreted 14 as being the minimum number of unit cells for consistency. Nevertheless, experimentally they produced samples with 6 unit cells across the diameter, and found good agreement between the results. From this, a size-independent predictive model developed, indicating that the value of 14 cells may be a feature of the finite element model only.

### 2.3.2 *Lattice geometry*

As previously discussed, there are many areas where metal foams are useful. Lattices are an optimised design and can use their optimised structure to be better planned versions of foams. Due to the high costs associated with lattices, two particular industry areas have invested in the optimised lattice, medical and aerospace. These will be discussed here.

One particular area of interest within the medical industry is in dentistry and orthopaedics. Considering the structure of bone, which is a porous natural material, there is a qualitative (though potentially misleading, from a materials properties perspective) match with foams. Solid metal parts can be used to replace bones in the form of implants, however there are problems with using bulk metals in the body. Solid load bearing implants which are more resistant to forces than their natural bone counterparts, can cause problems due to the difference in stiffness between metal and bone, in a process known as stress shielding [134]. As such, investigations are underway into metallic foams and lattices being used as a compromise, to retain an appropriate degree of strength, but reduce the stiffness [135]–[139].

With regards to aerospace, the more weight in an aircraft, the more fuel is required to get it off the ground, therefore weight reduction directly leads to cost reduction in fuel savings [140]. Utilising lattices as a filler structure to replace solid volumes in bulky parts is an attractive prospect for the aerospace sector [141][142]. Such parts are likely to be complex part shapes, of integrated lattice and dense parts, for example in the manner of a sandwich panel [143]–[147]. More research into the structure is required before the lattice can be considered as a standalone replacement.

As a highly porous material, the lattice cannot be expected to behave as its constituent metal, therefore consideration must be given to the geometry of the structure in order to maximise desirable mechanical properties. This is due to the inherent nature of a geometric structure to behave in either a bending or stretching dominated mode [148][149]. Structures that deform by bending do so by deformation of the struts, where failure can occur through buckling of the edges, plastic hinging at the corners, or for the case of brittle materials, with fracture of struts at the nodes (Figure 18). Rigid structures with no nodes where flexibility can occur (such as those of triangular geometries) deform by stretching, where the struts are forced to deform parallel to their length. This causes the structure to elongate elastically when in tension, however in compression the structure is more liable to fracture as there is no flexibility at the nodes within the structure.

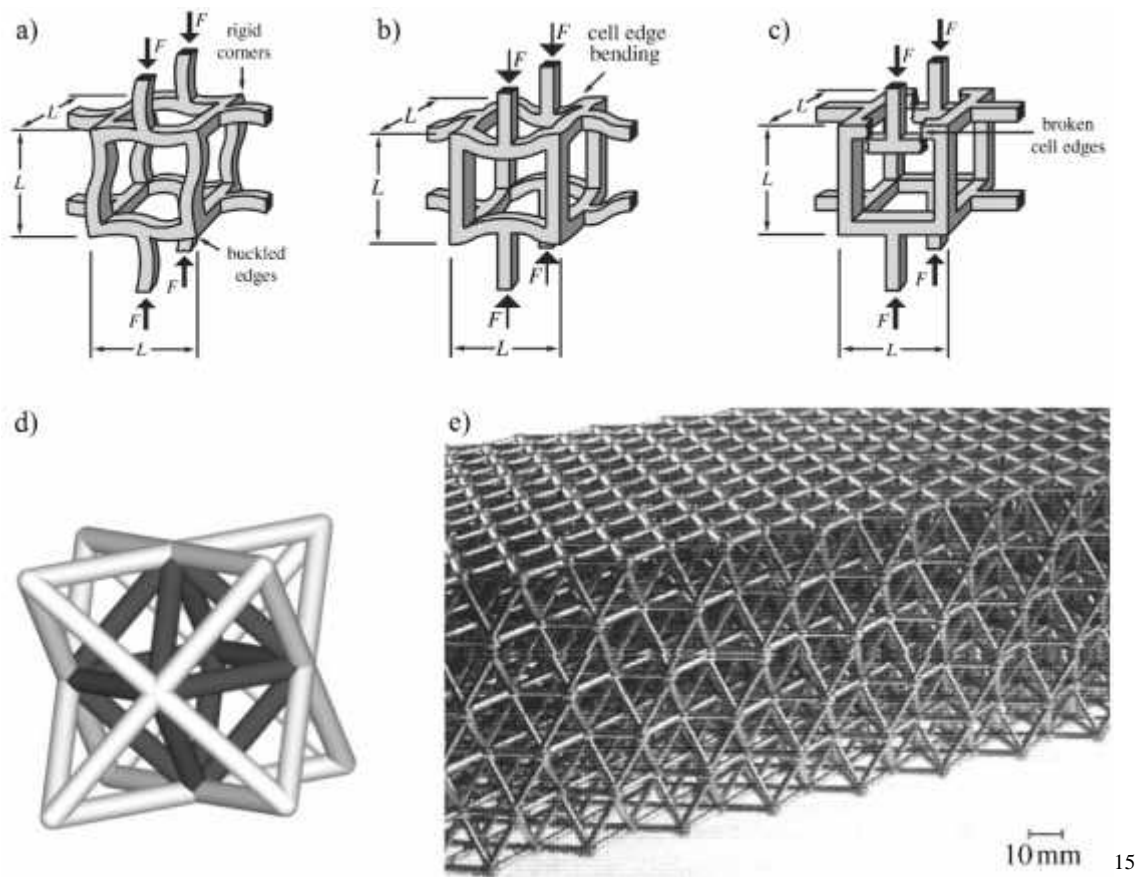


Figure 18: Visual representations of two available lattice geometries dominated by different deformation mechanisms: a, b, c) bending dominated deformation in cube structures with different final points of failure, and: d, e) octet structures which display stretching dominated deformation (Ashby 2006)

A study of SLM lattice structures by Rahmin Rashid et al. looked at how different geometries fared in 3 point bend tests, with the lattice structure “filling” a solid outer shell [150]. Circular, triangular, and hexagonal cells were tested, and it was determined that some geometries are better than others in the flexural bend test (Figure 19). An interesting point in this study was the solid test specimen, and circular and triangular celled specimens all suffered a sudden decrease in stress, suggesting sudden catastrophic failure occurred. With regards to the hexagonal structure, there were a series of steps to catastrophic failure, suggesting the links fractured strut to strut. All these lattice structures had lower strengths than the solid, however were more flexible in terms of flexural modulus.

<sup>15</sup> Licensed content reproduced from Philosophical Transactions A, 364(1838), M.F.Ashby, “The properties of foams and lattices”, ©2006 The Royal Society

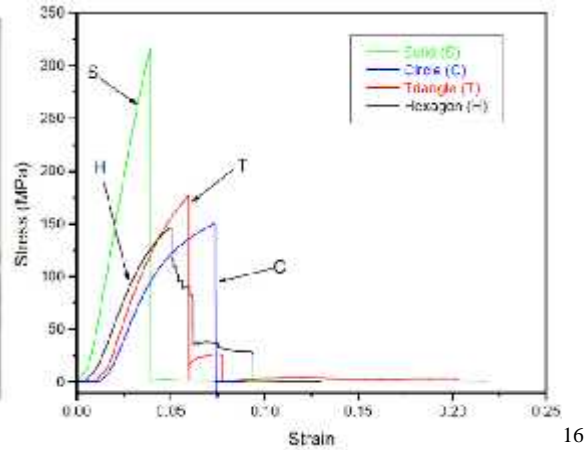
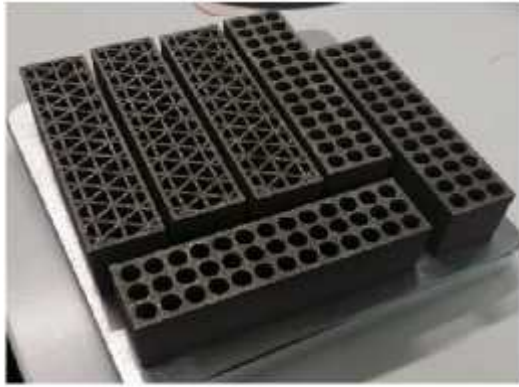


Figure 19: SLM built circular and triangular specimens on build plate (Rahman Rashid et al. 2017)

A similar study on the flexural properties of lattices was conducted by Horn et al. on Ti6Al4V cellular structures [136]. These were of rhombic dodecahedron geometry, and made by EBM to investigate how altering numbers of unit cells and diameters of the struts affected the flexural properties (Figure 20). The main focus of this study was to investigate the actual relative density produced by EBM, compared to the designed relative density of the CAD model, for orthopaedic applications. During the study, four point bend tests were performed, which found that higher densities led to higher strengths, with thinner struts providing greater flexibility.

<sup>16</sup> Reprinted from Materials Today: Proceedings, 8(8), R.A. Rahman Rashid, J. Mallavarapu, S.Palanisamy, S.H.Masood, "A comparative study of flexural properties of additively manufactured aluminium lattice structures", p8597-8604, © 2017, with permission from Elsevier

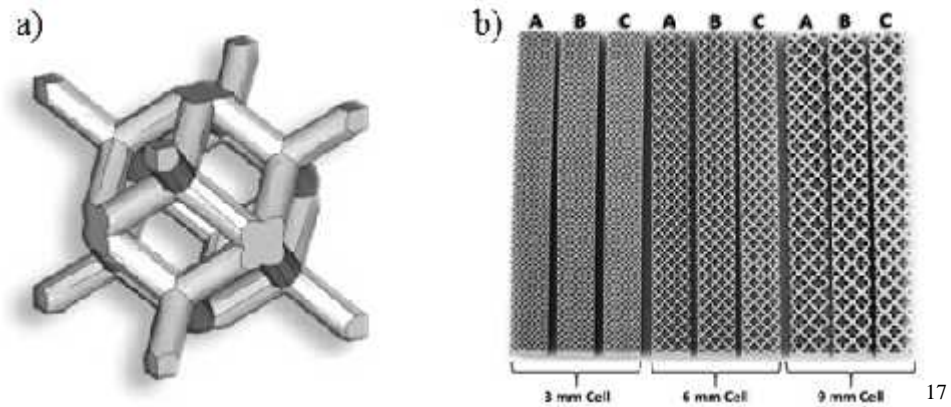


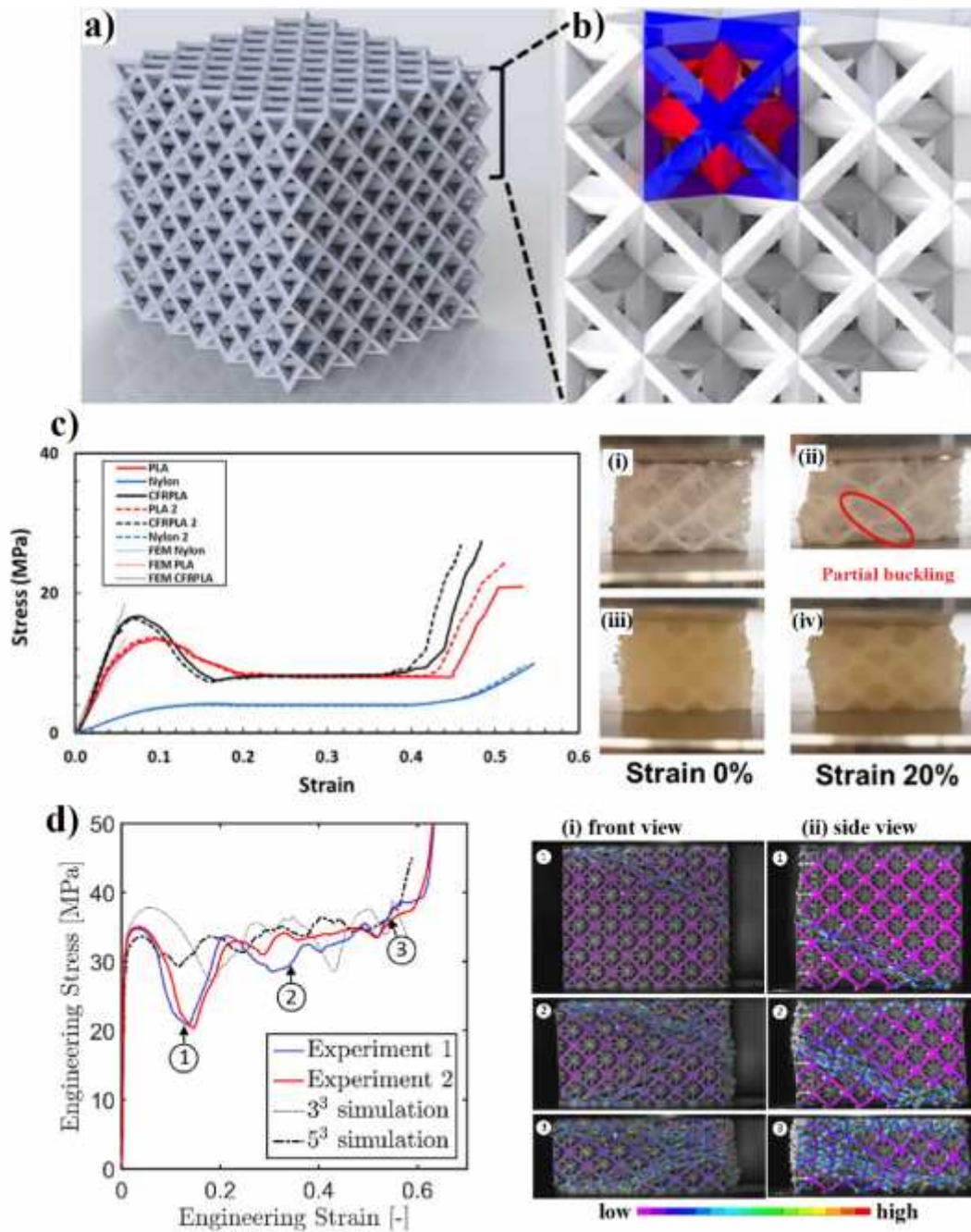
Figure 20 a) rhombic dodecahedron unit cell, and b) samples with differing numbers of unit cells and strut widths (Horn et al. 2014)

Due to the higher stiffness of metal compared to polymers, there are significantly more recent studies on bending dominated failure in metal lattices than stretching dominated deformation (consider various example studies in Figure 21). Hernandez-Nava et al. investigated the effect of defects on Ti6Al4V cubic lattice structures and found the deformation mechanism was more in line with that of a uniform bending dominated model than that of a sudden buckling or shearing.

Kaur et al. investigated micro-truss octet (and octahedral) lattices made from various polymers utilising fused deposition modelling, and observed predominantly stretching dominated behaviour in compressive tests, (with some partial buckling observed for some failures) [151]. Bonatti and Mohr modelled the behaviour of several lattices, including the octet lattice, which were then made from stainless steel 316 using SLM [152]. In this study, initially the stress/strain curves suggest stretching dominated behaviour, however looking at the trend of the graph alongside the samples, the deformation mode for the solid octet struts was bending dominated. Buckling was observed, with fracture occurring both normal, and 45° to the applied force. These two studies both used octet lattices, however due to the materials used to build the lattices, different behaviour was observed.

Considering these studies, it is clear that while choosing an appropriate geometry for the application influences the structural performance, material selection is still very relevant with regards to deformation modes. The following section discusses other important considerations when predicting the behaviour of the part.

<sup>17</sup> Reprinted from Additive Manufacturing, 1-4, T. J. Horn, O. L. A. Harrysson, D. J. Marcellin-Little, H.A. West, B. D. X. Lascelles, R. Aman, “Flexural properties of Ti6Al4V rhombic dodecahedron open cellular structures fabricated with electron beam melting”, p2-11, © 2014, with permission from Elsevier



18

Figure 21: a) CAD model of octet, with b) single unit cell highlighted within the structure. c) stress strain curves of polymer lattices, with (i-iv) deformation at 0% and 20% strain for (i)(ii) polylactide (PLA) and (iii)(iv) nylon (Kuar et al. 2017)

d) stress/strain curves obtained from simulations and experiments, with (i,ii) photograph of deforming specimen from front and side respectively. Colour indicates deformation intensity obtained by planar DIC (Bonatti, Mohr 2017)

<sup>18</sup> a,b,c) Reprinted from Materials and Design, 134, M.Kaur, T.G.Yun, S.M.Han, E.L.Thomas, W.S.Kim, “3D printed stretching-dominated micro-trusses”,272-280, © 2017, with permission from Elsevier  
d) Reprinted from International Journal of Plasticity, 92, C.Bonatti, D.Mohr, “Large deformation response of additively-manufactured FCC metamaterials: From octet truss lattices towards continuous shell mesostructures”, 122-147, © 2017, with permission from Elsevier

### 2.3.3 *General properties of AM lattices*

Although there is extensive research regarding the mechanical properties that can be achieved in solids using AM methods, less information is available on lattice technology. As such, solid AM properties often form the basis of publications on lattices. This comparison is not the most appropriate due to the high porosity of lattices, as the rules that govern the mechanical properties are quite different. For lattices, when a force is applied, the initial deformation mechanism is bending and flexing of the structure, as there is far less rigidity compared to solids. This mechanism has been investigated both by mechanical property evaluation, and by computational modelling, which has the advantage of being able to isolate the deformation mechanism [142], [153]–[158]. Due to this, when considering the elastic modulus of the structure, for example, it is not appropriate to quote the value of the constituent metal, as the entire structure has elasticity due to its geometry.

As further deformation occurs, macro defects have a predominant role in structural failure. In a solid, the negative effects of cracks and internal porosity can take some time to cause failure in the metal, due to the cracks having to travel through the bulk. In lattices, the majority of the volume is empty space, leading to a high surface to volume ratio, therefore the effects of cracks and internal porosity become apparent more quickly (see 2.4.3). Finally, effects on the microstructural level can be realised, where the reduction of micro defects and optimisation of the microstructure can act to improve the mechanical properties of lattices. This could be done by optimising process parameters, or through post processing, however further investigations are required to fully explore these possibilities [159].

The bending and flexing which is inherent to mechanical properties of lattices can be controlled by the geometry, as discussed in section 2.3.2. A 2016 study by Zargarian et.al found that lattice geometry had a large effect on fatigue life, when three different structures were plotted for the same relative density (see Figure 22) [160]. This was accounted for by referring to an “ $r/l$  ratio”, the ratio of strut radius over strut length. Here, the authors state a larger value corresponds to higher inertia within the cross section of the struts, and a lower bending stress. As the truncated cuboctahedron had the highest  $r/l$  ratio, followed by the diamond structure, with the rhombic dodecahedron of the lowest  $r/l$  value, this could explain the differences in lifetimes, despite the relative density being the same. This study is an excellent example of how geometry alone can affect mechanical properties, with this case considering fatigue life.

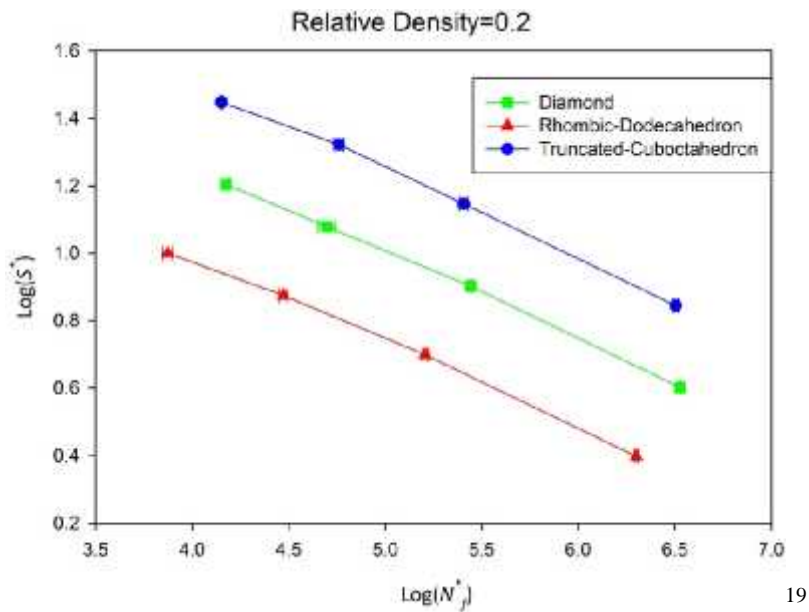


Figure 22: Predicted SN curve of different lattice structures at relative density of 0.2 (Zargarian et al. 2016)

When considering macro features, it is important to control internal porosity of the lattice struts. Studies have looked at optimising the AM process in order to improve features of solid parts, however as this often means deviating from the recommended machine settings, which can introduce other areas for concern, optimising settings for lattices is not well investigated at this time [159], [161]–[163].

Post processing AM lattices to reduce porosity is another possibility, however there is limited literature on how this could be done effectively. Traditionally, porosity can be reduced in solid parts by the application of a hot isostatic press (HIP) treatment, which is effective for reducing porosity in AM solid parts [164][165]. Here, high pressure is applied at elevated temperatures to compress the solid part in order to reduce porosity. For lattices, it is possible that this could be effective, however it is also possible that the high pressure gases will flow through the structure, without reaching high enough pressures to affect the internal porosity of the metal structure. At the time of writing, most of the literature focuses on HIP as an AM lattice post process for fatigue testing, as discussed in 2.4.3, however whether the observed improvements are down to reducing porosity, or due to the heat treatment is an area where further research is needed.

<sup>19</sup> Reprinted from Materials Science and Engineering: C, 60, A.Zargarian, M.Esfahanian, J.Kadkhodapour, S.Ziaei-Rad, “Numerical simulation of the fatigue behavior of additive manufactured titanium porous lattice structures”, p339-347, © 2016, with permission from Elsevier

Surface quality is another important consideration. For AM surfaces, there are two components to consider: the powder sintered to the surface, and the surface produced by the step function inherent to layer manufacturing processes.

When parts are removed from the EBM in their sintered cake, most of the sintered powder is loose, and therefore removed in the PRS step of the process. Some of the sintered powder remains attached to the part, bonded to the surface of the part as un-melted powder binds to the melt during the build. Figure 24 from Cansizoglu et al. demonstrates how partially melted powder is incorporated into the melt as the struts are built [166]. It can be seen that surface quality changes with increasing strut angle.

Recent studies have considered methods for improving the surface finish of complex parts. Atae et al. attempted to remove the un-melted powder particles by bombarding the surface of Ti6Al4V gyroid lattices made by EBM with ceramic beads [167]. The authors suggest the lattice surfaces were improved, although not all powder particles were removed using this method.

Lhuissier et al. characterised the surface improvement of 1.66mm struts within octet lattice structures of Ti6Al4V made by EBM by chemical etching, as seen in Figure 23 [77]. They determined there were two types of surface roughness, partially melted powder stuck to the sides of the strut (type I), and stacked plate-like defects (type II). It was found that the etchant swiftly removed type I defects, however type II defects took longer to remove. The effect of this surface improvement on mechanical properties requires further investigation.

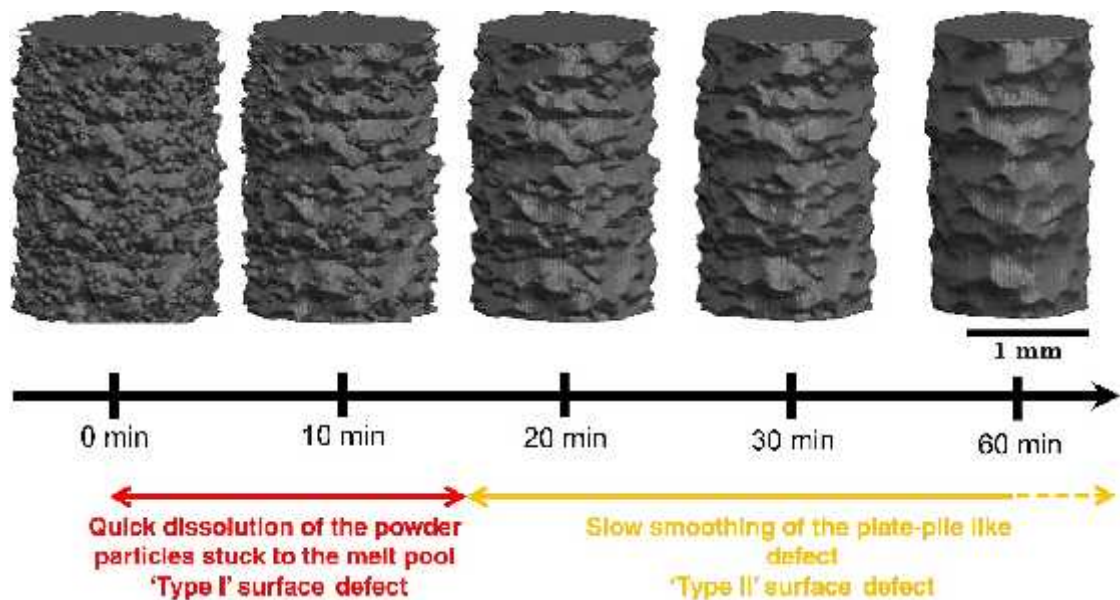
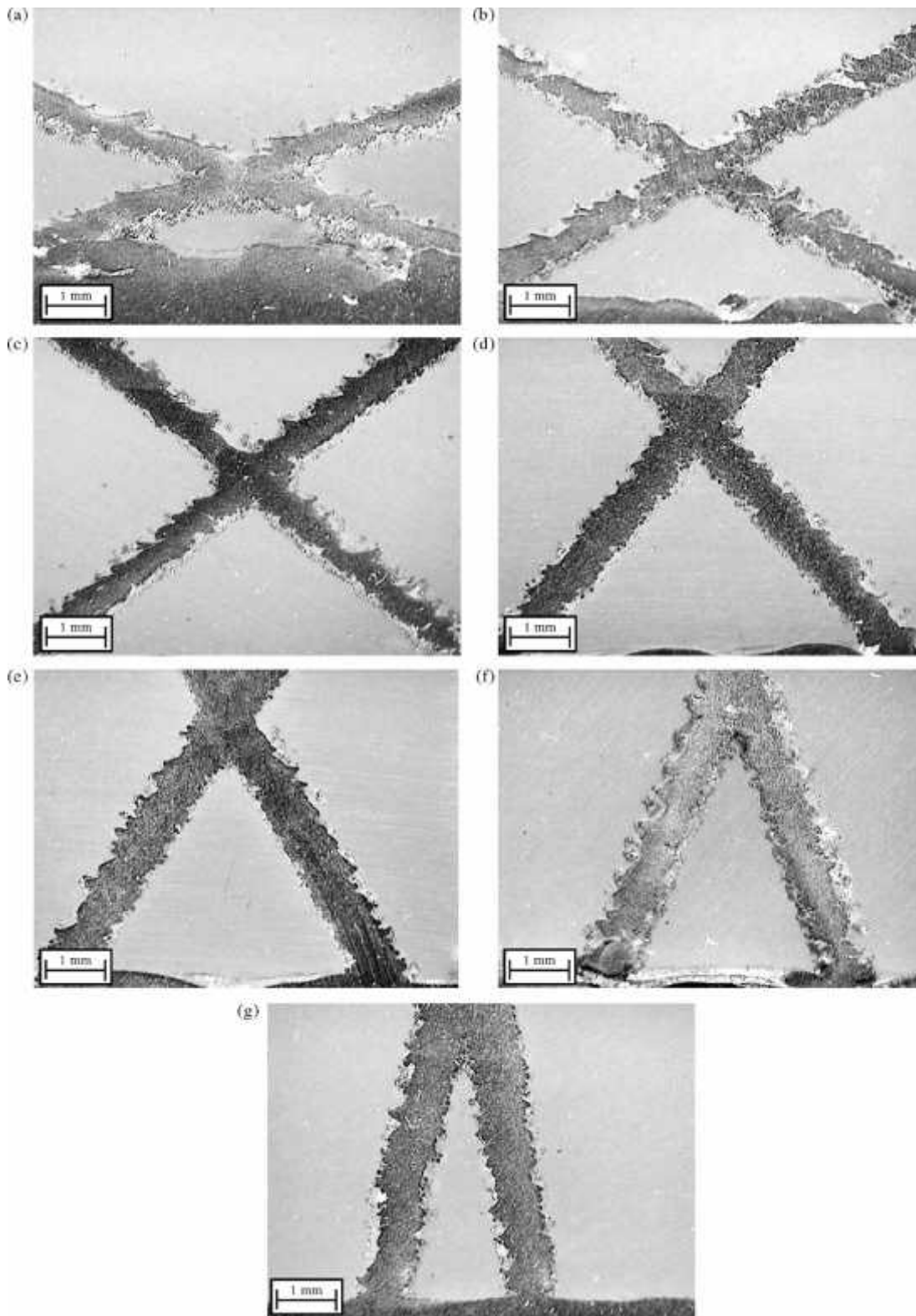


Figure 23: Effect on strut surface quality from etching agent, where type I defects are swiftly removed, and type II are slowly eroded (Lhuissier et al. 2016)

<sup>20</sup> Reprinted from Materials & Design, 110, P.Lhuissier, C.de Formanoir, G.M.Rémy, D.S.Godet, “Geometrical control of lattice structures produced by EBM through chemical etching: Investigations at the scale of individual struts”, p485-493, © 2016, with permission from Elsevier



21

Figure 24: Lattice micrographs with struts at: a) 20°, b) 30°, c) 40°, d) 50°, e) 60°, f) 70°, g) 80°, to the build platform (Cansizoglu et al. 2008)

<sup>21</sup> Reprinted from Materials Science and Engineering:A, 492(1-2) O. Cansizoglu, O. Harrysson, D. Cormier, H. West, and T. Mahale, "Properties of Ti-6Al-4V non-stochastic lattice structures fabricated via electron beam melting", p468-474, © 2008, with permission from Elsevier.

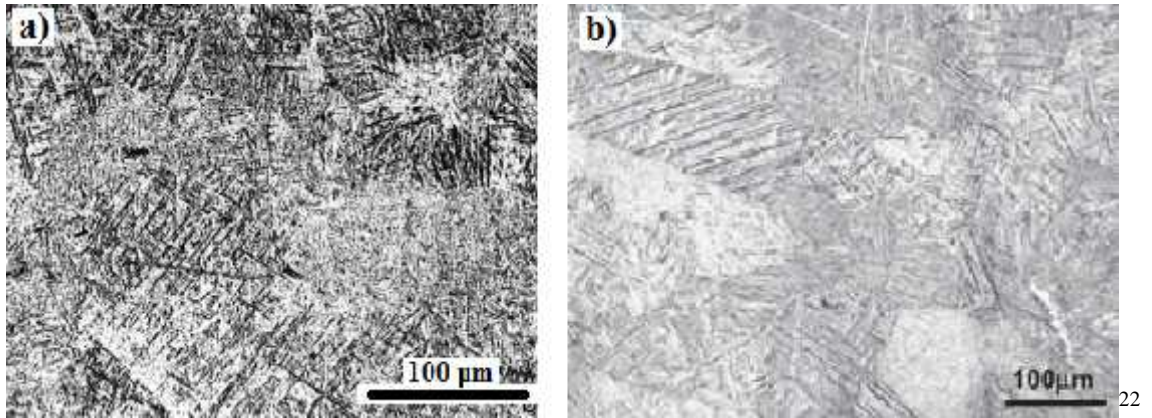


Figure 25: EBM cellular structure microstructures a) open cellular foam (Murr et al 2010), and b) lattice (Li et al. 2012)

The microstructure of Ti6Al4V lattices is similar to that of solids. Figure 25 shows two microstructures obtained from Ti6Al4V porous structures made by EBM, with both structures displaying the characteristic Widmanstätten patterns.

While some studies have looked at mechanical properties of lattices and foams, due to many variations between studies, it is difficult to compare the results. One comparison of two in depth studies on Ti6Al4V cubic lattices (Table 4) shows that SLM lattices have an ultimate compressive strength of almost twice as much as comparable EBM lattices of similar porosity [132][168]. When trying to compare between lattice studies, variations can come in many forms, for example: geometry, manufacturing method, and post processing. Without extensive manipulation of the data and through the introduction of normalising parameters, it would be inappropriate to comment on whether these properties are beneficial or detrimental. As such, when considering results across studies, it is best to try and ensure as many identical variables as possible. What can be said, however, is that for porous structures, there is a strong correlation between mechanical properties and density. This is to be expected, as more material would lead to more resistance to deformation. Where studies compare porosity of the structures, or their density, in general, higher densities lead to higher strengths and stiffer structures, therefore a density correction can be applied to normalise mechanical properties for the relative density (quantified by Gibson and Ashby [169], see section 3.8.2) [170]–[173].

<sup>22</sup> Reprinted from *Materials Science and Engineering: A*, 527(7-8), L.E.Murr, S.M.Gaytan, F.Medina, E.Martinez, J.L.Martinez, D.H.Hernandez, B.I.Machado, D.A.Ramirez, R.B.Wicker, “Characterization of Ti–6Al–4V open cellular foams fabricated by additive manufacturing using electron beam melting”, p1861-1868, © 2010, with permission from Elsevier

Reprinted from *Acta Materialia*, 60(3), S.J.Li, L.E.Murr, X.Y.Cheng, Z.B.Zhang, Y.L.Hao, R.Yang, F.Medina, R.B.Wicker, “Compression fatigue behavior of Ti–6Al–4V mesh arrays fabricated by electron beam melting”, p793-802, © 2012, with permission from Elsevier

Table 4: Table comparing UCS values of SLM and EBM porous cube lattices compiled with data from table 6 in [168] and table 5 in [132].

AM method	Porosity	UCS	Reference
EBM	60.41 ( $\pm 0.81$ )	117.05 ( $\pm 5.54$ )	Table 6 [132]
SLM	63.8	219 ( $\pm 4$ )	Table 5 [168]
EBM	70.32 ( $\pm 0.63$ )	83.13 ( $\pm 10.25$ )	Table 6 [132]
SLM	70.7	163 ( $\pm 2$ )	Table 5 [168]

Asymmetry of properties is apparent in solid AM parts, as discussed in section 2.2.3. In solid EBM samples, it is known that the orientation of samples within the build can affect the mechanical properties of the final products when tested along, or perpendicular to the build direction [174]. With regards to lattices, it is not clear whether anisotropy is a concern. In 2008, Heintl et al. investigated the mechanical properties of diamond and hatched structure lattices made by EBM when tested parallel and perpendicular to their build direction [175]. It was found that lattices tested parallel to the build direction had a greater strength and higher elastic modulus than those tested perpendicular to the build direction. This is in direct contradiction to a 2015 study by Wauthle et al., who investigated the effects of heat treatment and build orientation on mechanical properties of diamond structure Ti6Al4V lattices made by SLM [176]. Here, there was no statistically significant difference between samples that were tested parallel or perpendicular to their build direction. This was true for comparing orientations of the as-built samples, and comparing orientations of heat treated samples, despite clear differences in microstructure. Here, prior grains were observed in all conditions, aligned with not only the build direction, but also the strut direction. This is due to higher conductivity of solid metal compared to the powder, causing the heat to travel preferentially through the solid lattice structure, rather than directly downward through the powder. It is clear further studies are required to investigate this possible effect.

## 2.4 Fatigue

Fatigue is a failure mechanism brought about by the interactions between load, time and environment. Changing any of these things can contribute to the effect of fatigue, and engineers work to improve fatigue life by considering how the component design will interact with these three inherent factors.

Fatigue occurs when a part is subjected to a repeating cyclic load. When a load is applied, stress concentrates at small defects and cracks within the part. These local stress concentration points can cause crack growth, which causes large cracks to propagate through the material. If left unchecked, the progressive crack growth can result in the failure of the part. This can be avoided by limiting the amount of stress the part is subjected to. If limiting the stress is not possible, by predicting the number of cycles a part can undergo before failure, catastrophic failure can be avoided.

In order to understand the behaviour of the part during application, fatigue tests can be performed. Although the compression and tensile tests provide important mechanical property information, very rarely are parts used for a single application, subjected to their ultimate strength, and then discarded. The fatigue test indicates how the part will perform for the given application, which will be dynamic in nature, and cause the part to undergo cyclic stresses (such as temperature changes, vibrations, or movement of attached components). Often these will be well below the ultimate strength of the particular material, however the cyclic nature of the applied load means the part can still fail.

The first extensive investigation on fatigue was conducted by Wöhler in the late 1800's, who characterised fatigue behaviour by plotting the stress against a logarithmic scale of the number of cycles (SN curve) [177]. The SN curve is obtained through the application of a constant force, and can be said to be force controlled. This causes the elongation to increase over increasing cycles. For parts in service, often the forces do not act to elongate the part in one exclusive direction. Indeed, the movement of the part is restricted by its proximity to, or contact with, other parts. A position controlled test can be performed, to obtain a strain cycle curve (EN curve) where the cyclic deformation is fixed and the force required to elongate the part decreases over increasing cycles.

In general, SN curves contain three regions, a plastic region, an elastic region, and an infinite life region. During the fatigue test, varying degrees of deformation occur that are a combination of plastic and elastic deformation (see Figure 26). When a material is subjected to a stress or strain above its yield strength but before its UTS, the fatigue life is dominated by plastic strain. If a material is being subjected to forces within its plastic region, failure will occur at a low number of cycles, as each cycle causes plastic deformation to inherently change the internal microstructure of the material. This is low cycle fatigue. When a material is subjected to a stress or strain below its yield strength, the material is dominated by elastic deformation, which is where high cycle fatigue can be investigated.

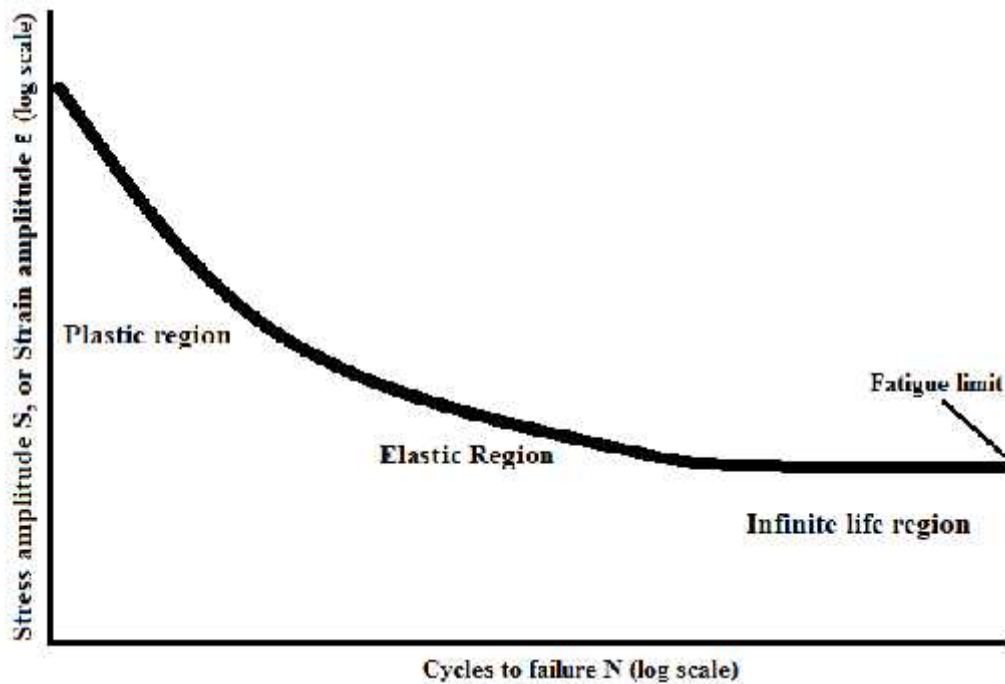


Figure 26: Generalisation of SN/EN curve, showing regions influenced by plastic and elastic deformation

If the stress or strain is low enough that no plastic deformation occurs, the material is said to have reached a fatigue limit, a point where, theoretically, the part could have an infinite life. In reality, this fatigue limit is reached if the part has survived after a very high number of cycles, and saying that the part will never fail is a dangerous assumption.

It is at the point the fatigue limit is reached where designing for fatigue becomes important. This can be done by implementing either a safe life approach, or fail safe design [178]. A safe life approach is the removal of the part before failure is expected to occur. For example, if a part has survived a million cycles in testing, it may be decided that during application, the part will be taken out of service after every 500,000 cycles. This can lead to a large amount of wastage as parts are removed and replaced long before their time, however this is a safety conscious method for safety critical systems. A fail safe design accepts that failure will occur, and compensates for this with a design such that failure of the part will not lead to failure of the whole system. If failure of the part occurs, the part can be removed and replaced without catastrophic consequences. A refinement of this philosophy is the damage tolerant design, where the part is inspected after a number of cycles. It is then decided if the part needs to be removed from service, or can be put back into service and inspected after so many more cycles. This inspection often involves examining crack lengths to determine if the cracks are large enough to cause structural failure before the next inspection point. Cracks cannot be repaired, however steps can be taken to reduce the likelihood of cracks nucleating and propagating.

Fatigue testing is destructive and time consuming, both of which are major factors when considering cost. Fatigue by nature gives highly variable results, due to a number of features regarding the material and the part. This gives rise to a large scatter within the data set, therefore a great number of samples are needed for reliable results. In the 1950's, Weibull produced a series of statistical models for the SN curve to try to quantify this scatter. One of which in particular interest to this project, is the reliability of a fatigue result, considering the number of samples tested (see section 3.7.1). Since Weibull, a branch of statistics known as survival analysis has evolved. As well as engineering fatigue, survival analysis is particularly useful in the medical field when looking at patient data in clinical studies [179][180].

### *2.4.1 Fundamentals of fatigue*

The key feature of fatigue is failure through some cyclic behaviour. For parts in service, the persistent loading and unloading through the constant application and release of stress causes the material to fail well below its theoretical strength for static tests [178].

Fatigue begins with crack nucleation at a defect within the material [181]. Alternatively, cracks may already be present following manufacture. Non-destructive inspection (NDI) techniques are important after production, to identify any potential issues before they arise. Surface roughness is a common site for crack initiation, as the surface is exposed to the environment and vulnerable to any corrosion. Parts can be polished to give smooth surfaces to increase the fatigue life, by removing the cracks before they have a chance to penetrate deeper into the material.

There are many possible crack nucleation sites within the material where stresses are raised due to stress concentrations. Internal porosity is an important area when considering fatigue [182]. Cracks take the route that is most energetically favourable, and therefore take the path of least resistance. If pores are present, cracks can propagate faster through the material, as there is less material to physically resist deformation. As well as this, the pore itself can act as a crack nucleation site, as stress concentrates around the surface of the pore. Some other examples of possible defects present are corrosion pits and pores, however as these are not problems for the samples covered in this work, these issues will not be discussed further here.

One microstructural defect is dislocations, where the atoms are out of alignment from the general crystal structure. When the material is subjected to stress, the dislocation moves within the atomic lattice, causing the atomic planes to slip over one another. Dislocation motion could, theoretically, allow the part to undergo cyclic fatigue without permanent deformation leading to an infinite life, as if the dislocation motion is unhindered, dislocations could repeatedly glide over each other in a “reversible state” [183][184]. In reality, dislocation motion leads to interlocking, a plastic deformation mechanism which accumulates to form persistent slip bands (PSBs). PSBs can act as

areas for crack initiation if no external factors are at play, can be locations for fatigue cracks to run along, and can also be found accumulating in the plastic zones ahead of the cracks [185]. For in depth fatigue studies, PSBs are an important feature when considering plastic deformation leading to failure in fatigue, however due to limitations of this project, the topic will not be discussed further in this work.

During fatigue initiation, micro-plasticity causes the dislocations to move through the grains, and accumulate at the grain boundaries [178]. This accumulation leads to stress concentrations, and eventually cracks. Cracks can then propagate easily along grain boundaries, particularly when segregation or residual stresses are present. Some examples of often desirable features to prevent crack initiation in the material are grain boundaries and second phase particles, which can act to inhibit dislocation motion.

As mentioned previously, the stress cycle curve is a useful tool, whereby obtaining lifetime values for a given stress or strain, once the part survives for a long time, the fatigue limit can be said to have been reached. Furthermore, if the curve appears to be levelling off, it can be extended to demonstrate how staying below the line can lead to longer lifetimes.

Miner's rule builds on a theory originally proposed by Palmgren, which links the number of stress magnitudes applied to the sample, and uses an experimentally determined constant to predict the lifetime based on the number of cycles each stress magnitude contributes [181]. Although this provides a neat ratio, it doesn't take into account the probabilistic nature of fatigue, or the changing mechanisms between low cycle and high cycle fatigue.

Paris' law considers the physical characteristics of the part itself, by using fracture mechanics to consider a relationship between the size of crack growth over a number of cycles, and relating this to a stress intensity factor [186]. This is very useful when designing for safe life parts, as they can be inspected periodically to see the size and number of cracks, in order to determine if the part is safe to re-enter service, or if it should be removed.

For high cycle fatigue, where parts survive many cycles at low stresses and strains, the parts deform elastically. Basquinn's law is applied where a constant stress or strain amplitude is maintained throughout the life of the component, in order to predict the number of cycles at which failure will occur [177]. Considering it is better for parts to survive for as long as possible, many studies focus on high cycle fatigue (as discussed in the next sections). This is typically lifetimes over  $10^4$  cycles, where survival is possible due to low stresses and strains, and where the material can deform in its elastic region for as long as possible.

When parts undergo large stresses and strains, plastic deformation occurs, whereby failure processes have commenced and the lifetime of the part is limited. This leads to fast failure in the form of low cycle fatigue. This can be characterised by Coffin-Manson law, which states that at low cycle fatigue, the part fails at high stresses and strains from undergoing plastic deformation [187][188]. This relates the plastic strain

amplitude to values relating to the ductility in the material during fatigue testing, to predict the number of cycles before failure.

In summary, there are a number of improvement techniques that can be put into place to design for fatigue, with two main areas specific to this project. By improving the surface finish of a part, surface cracks can be removed before they have a chance to penetrate further into the material. Internal defects within the material should be eliminated so as to not provide areas for stress concentration cracks to nucleate. As discussed, there are many factors influencing fatigue life that makes it very difficult to predict. It is possible to estimate the survival of the part in fatigue by looking at related studies and conducting fatigue tests, however to most accurately predict the behaviour of the part, destructive tests are required. The next section considers studies on fatigue of the titanium alloy utilised in this project, Ti6Al4V.

#### *2.4.2 Fatigue in Ti6Al4V*

For Ti6Al4V, variations in microstructure lead to differences in fatigue life. In general, finer microstructures lead to longer lives at higher stress amplitudes, while coarse microstructures lead to fatigue limits at lower stress amplitudes [2]. For high cycle fatigue (HCF), Wu et al. (2013) compiled a comprehensive review of the HCF values of Ti6Al4V in the literature, to determine that the fatigue strength in Ti6Al4V is strongest for bimodal structure, then lamellar, then equiaxed microstructure [189]. There is a large variation in the actual literature values due to the high number of variables that cause fatigue failure, which makes predicting fatigue behaviour difficult. For Ti6Al4V specimens, there are a large number of production methods available which produce microstructural difference, introduce potential defects, and have varying levels of surface roughness. All of these factors can influence the fatigue life, therefore in order to understand the fatigue properties, extensive testing is required.

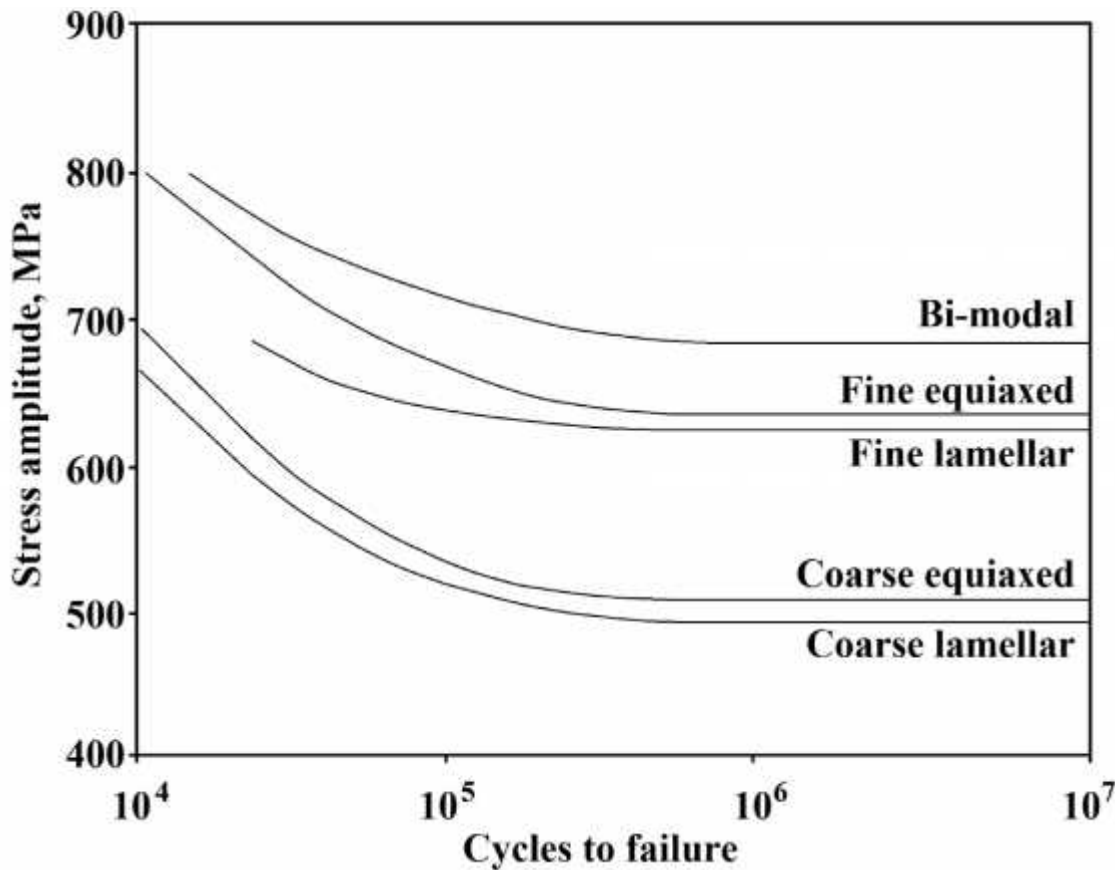
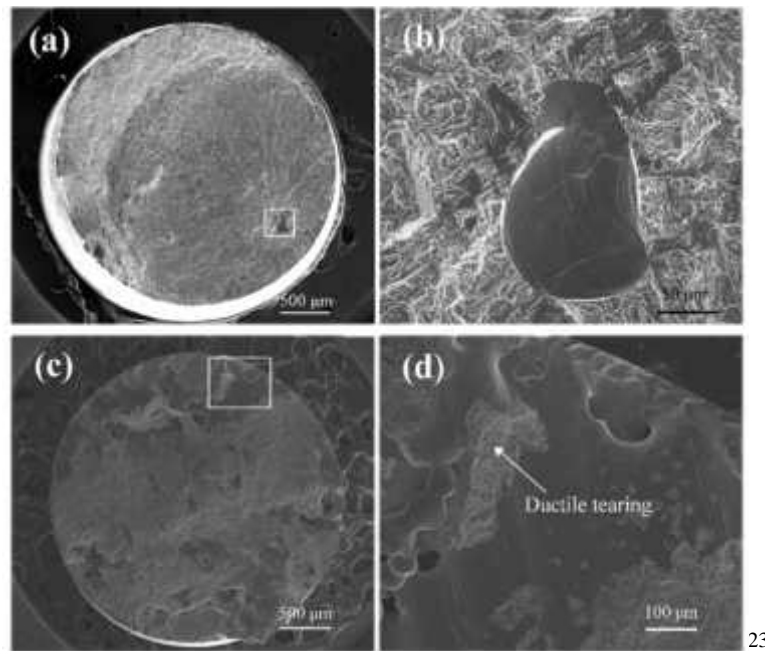


Figure 27: SN curve for Ti6Al4V annealed at 800°C for 1hr, water quenched, aged at 500°C for 24hrs, and fatigue tested at RT in air. Redrawn from Materials Properties Handbook on Titanium Alloys [18]

Due to the large number of variables affecting fatigue lifetimes, it is difficult to categorically state which metals survive for longer times than others. In general, high fatigue strength can be categorized by having a high endurance limit (a stress at which the material can survive over 10<sup>7</sup> cycles), which can correlate to high tensile strength, however this is not for all cases, and is not directly proportional [177].

In general, Ti6Al4V fatigue life benefits from small slip lengths, as in fine grain microstructures, whereas the  $\alpha$  colony or Widmanstätten microstructure provides a poorer fatigue strength (see Figure 27) [18]. Ti6Al4V typically undergoes ductile fracture at room temperature, with some examples of ductile fracture given in Figure 28 [2][190]. In 2016, Konecny et al. considered the propagation of fatigue cracks in DMLS Ti6Al4V [191]. In the microstructure, columnar  $\alpha$  grains were observed to have grown in the build direction, before transforming to needle-like  $\beta$  martensite. It was at these very fine needles where the cracks propagated, as opposed to the boundaries of the prior  $\alpha$  grains.



23

Figure 28: Fracture surfaces of Ti6Al4V fatigue samples made by EBM, where a & b are one specimen, and c & d are another. The images on the left show the fracture surface, with the images on the right displaying the fracture features at a higher magnification (Gong et al. 2015)

Zhai et al. compared EBM, LENS and wrought Ti6Al4V samples to consider the fatigue crack growth properties. The authors observed initial crack growth behaviour of the AM parts was similar to that of wrought samples, in that crack initiation was more closely determined by the location of the grains, however as an increased driving force on the crack tip, propagation was not hindered by grain boundaries. This is supported by Edwards et al. who evaluated the fatigue crack properties of EBM Ti6Al4V, and found that fracture toughness and fatigue crack growth were comparable to wrought specimens [192].

In 2016, an extensive review of the literature by Li et al. brought together fatigue results for Ti6Al4V from various AM processes, and compared these to traditional manufacturing routes [193]. There was a huge variability in the data, dependent on the surface quality, post process (or lack of), and heat treatment (or lack of).

The comparison of fatigue performance of SLM Ti6Al4V compiled from papers from 2010-2015 showed that parts fatigue tested all failed at lower stresses than wrought, aged and machine polished parts (see Figure 29). The only exception to this was parts made by Rafi et al., where the SLM parts were heat treated for 4 hours at 650°C, to provide a similar lifetime to wrought products [82]. A similar comparison of lifetimes of Ti6Al4V samples built by EBM, compiled from papers between 2010-2013, shows

<sup>23</sup> Reprinted from Materials and Design, 86, H.Gong, K.Rafi, H.Gu, G.D.Janaki Ram, T.Starr, B.Stucker, "Influence of defects on mechanical properties of Ti-6Al-4V components produced by selective laser melting and electron beam melting", p545-554, © 2015 with permission from Elsevier

that as-built samples have very poor fatigue life, however there are two instances where similar lifetimes to wrought, aged and machine polished Ti6Al4V can be achieved using EBM. Brandl et al. HIP treated for 4 hours at 843°C, and then electropolished the surface [194], and Ackelid & Svensson HIP treated for 2 hours at 920°C before machining the surface [195], and both of these methods provided samples with similar or better performance than traditionally produced parts. In 2017, Persenot et al. compared EBM as-built fatigue samples to those which had been etched, in order to improve the surface quality [196]. Parts with the etched surface had a higher fatigue strength of some 60% compared to those in the as-built condition. In studying the fracture surface, it was seen that for all parts, the critical defects originated from lack of fusion during the EBM process.

In 2012, Rafi et al. fabricated Ti6Al4V test specimens by EBM in vertical and horizontal orientations, with as built and machine polished surfaces [92]. This paper concluded that the fatigue strength of lattices with a machined surface survived longer in fatigue tests than their as built counterparts, which is supported by failure at  $10^7$  cycles at 100-250MPa for as built samples, with 300-350MPa for samples with a machined surface.

In 2017, Kahlin et al. discovered that EBM Ti6AL4V specimens with an as built surface, had similar lifetimes whether or not they were in the as built condition, or had been HIP treated [197]. In this study, although no samples in the as build condition with machined and polished surfaces were tested, HIP treated parts with machined and polished surfaces were able to withstand stresses almost three times higher than their as built counterparts, and had lifetimes comparable to samples from a wrought bar. This is reinforced by Beretta et al. who support the adoption of defect tolerant design to reduce defects and improve surface quality in order to produce EBM parts with mechanical properties comparable to those of traditionally manufactured parts [198].

In general, it is important to consider that fatigue studies must be compared “like for like”, and so comparing fatigue data across different studies should be treated with caution due to the potential variability in the details. Therefore, exactly how much the microstructure of a certain sample or part will vary the fatigue limit is difficult to predict without destructive testing. Equally, solid Ti6Al4V parts may be a good starting point for research into porous metal structures, however the porous structures must be considered as structures in their own right. The following section discusses findings from studies on fatigue of lattices.

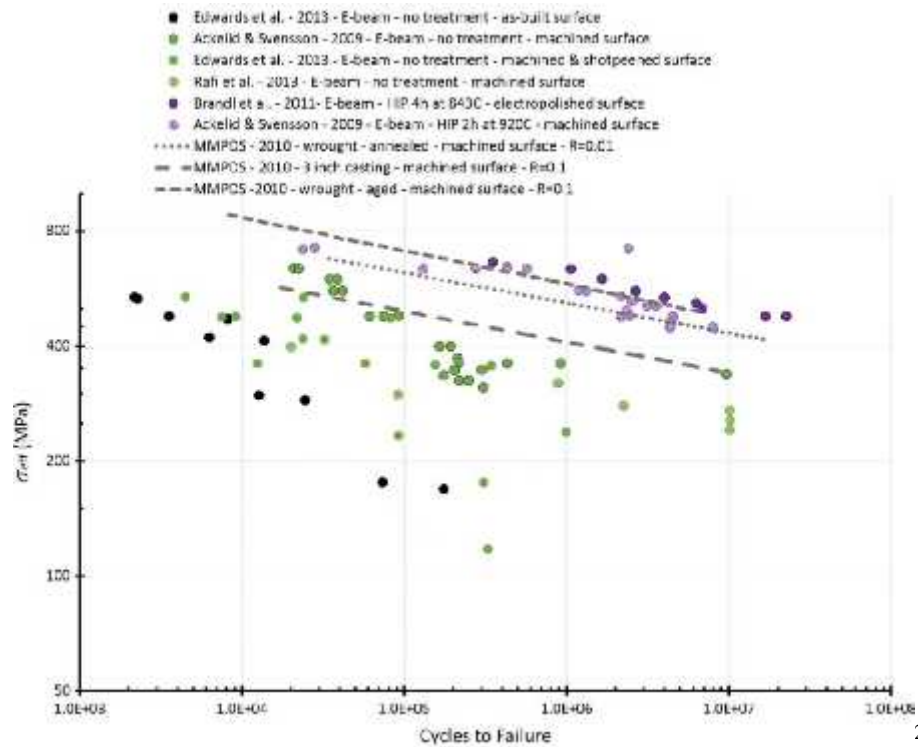
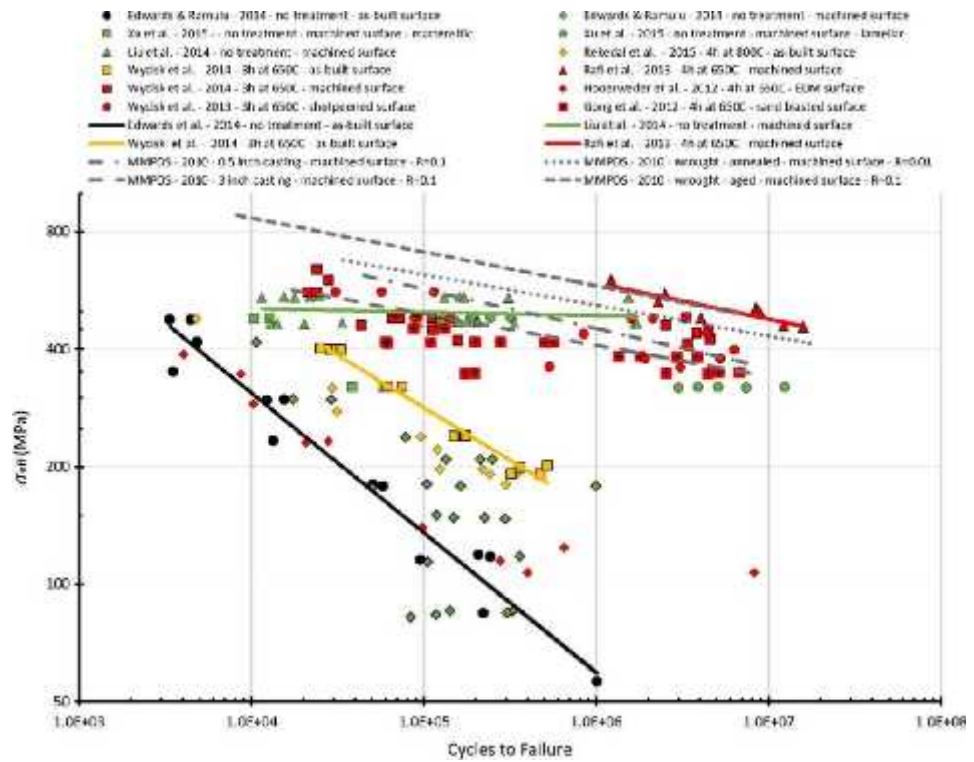


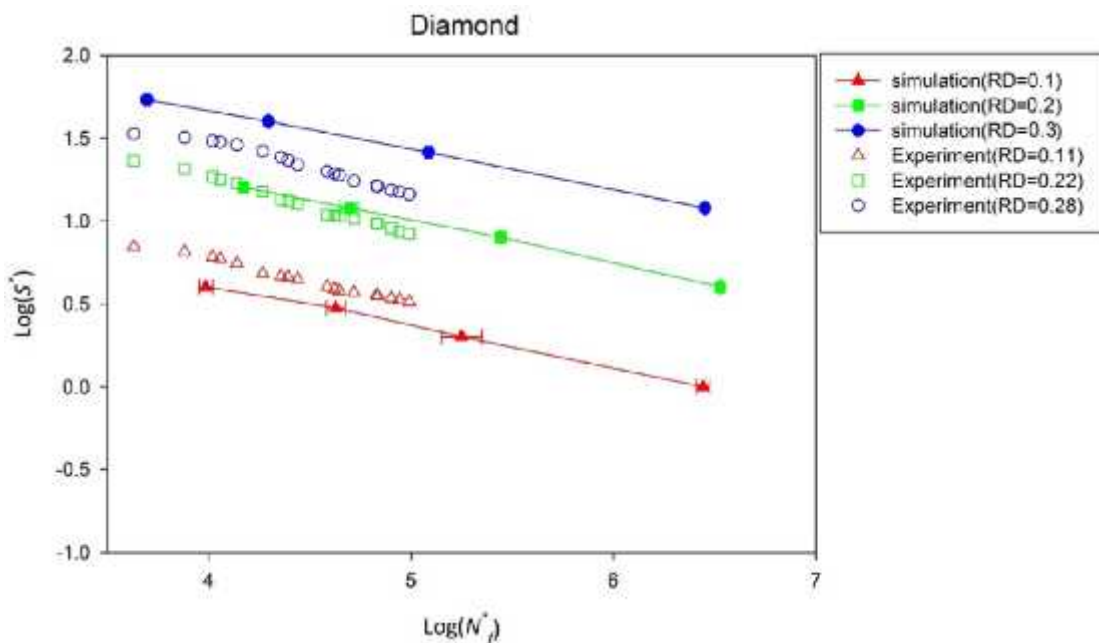
Figure 29: Compiled fatigue data for traditionally manufactured samples, compared to a) LPB and b) EBM manufactured parts (Li et al. 2016)

<sup>24</sup> Reprinted from International Journal of Fatigue, 85, P. Li, D. H. Warner, A. Fatemi, and N. N.Phan, "Critical assessment of the fatigue performance of additively manufactured Ti-6Al-4V and perspective for future research", p. 130-143, © 2016 with permission from Elsevier.

### 2.4.3 Fatigue in lattices

Considering the huge variation in AM solid Ti6Al4V, there will obviously be huge variation in fatigue life of lattice structures. This section gives a broad overview of reported considerations in lattice design, and processes that aim to improve fatigue characteristics of lattices, based on what is known about fatigue in solids.

At the present time, fatigue of lattices is a new concept, therefore the majority of the literature focuses on fatigue damage on the macroscale, rather than tracking damage on the microscale. In 2016, however, Zargarian et al. simulated fatigue behaviour of titanium lattice structures of various geometries to investigate the possible deformation mechanisms [160]. Through finite element analysis (FEA), the authors compared their findings to literature to determine fatigue behaviour of lattices was in agreement with Basquin's power law. The authors linked the fatigue strength to the fatigue life, through use of a constant which depend on the fatigue properties of the metal, the relative density and the lattice geometry. The results of their models were compared to published experimental data, as shown in Figure 30. Although the relative densities are not exactly the same for the FEA and experimental lattices, there is good agreement between the two data sets. While it can be seen that the general trend of the SN curves follow the FEA closely, there is some work to be done regarding the accuracy of the actual values.



25

Figure 30: S-N curve of diamond structure Ti6Al4V scaffold comparing FEA with differing relative densities (Zargarian et al. 2016)

<sup>25</sup> Reprinted from Materials Science and Engineering: C, 60, A.Zargarian, M.Esfahanian, J.Kadkhodapour, S.Ziaei-Rad, "Numerical simulation of the fatigue behavior of additive manufactured titanium porous lattice structures", p339-347, © 2016, with permission from Elsevier

As with solids, fatigue in foams typically begins with a surface defect, which leads to an inward growing crack [169]. Work by Zhao et al. determined four categories where fracture mechanisms originated, all of which occur either at cell wall surfaces, or internally, at sites of defects, such as internal pores [199]. Hedayati et al. investigated the crack pathway of ELI Ti6Al4V lattice structures made by SLM, when tested in tension-tension fatigue tests [200]. It was found that the crack propagated at 45° to the notch, where the notch is perpendicular to the test direction. This was said to be due to the fact that this particular lattice structure (rhombic dodecahedron unit cell, page 45) the weakest struts in the unit cell are those at 45° to the loading direction.

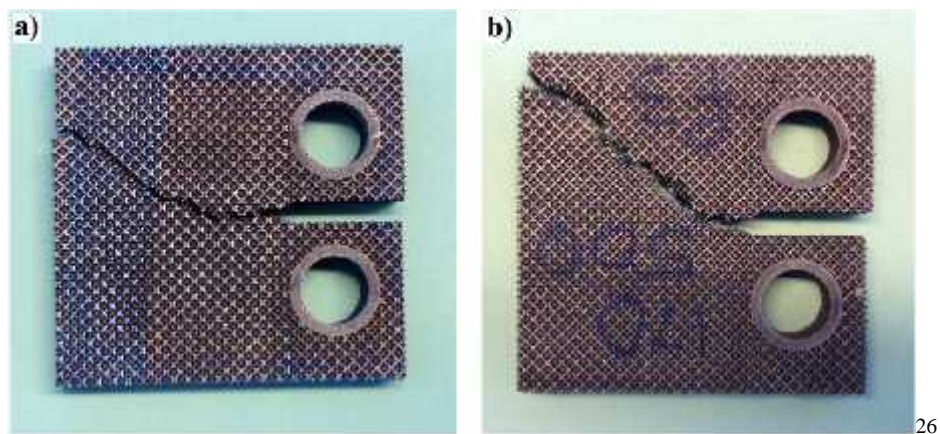


Figure 31: Comparison of crack pathways in lattices of two different porosities of a) 66.4%, and b) 77.1%. (Hedayati et al. 2017)

As is with solid Ti6Al4V, Ti6Al4V lattice fracture surfaces display ductile failure (see Figure 32). This was seen in Zhao et al. who compared the fatigue properties of three Ti6Al4V EBM manufactured lattice structures: cubic, “G7” (a unit cell from the Materialise/Magics software) and a rhombic dodecahedron structures [201]. Despite their differing geometries, all lattices were dominated by bending deformation, with the primary fatigue mechanism being cyclic ratcheting, where the accumulation of plastic strain over each cycle leads to catastrophic failure. The study concluded that the fatigue crack growth was closely related to surface quality, presence of defects and cumulative damage through bending and buckling of struts.

<sup>26</sup> Reprinted from Materials Science and Engineering: C, 76, R.Hedayati, S.Amin Yavari, A.A.Zadpoor, “Fatigue crack propagation in additively manufactured porous biomaterials”, p457-463, © 2017, with permission from Elsevier

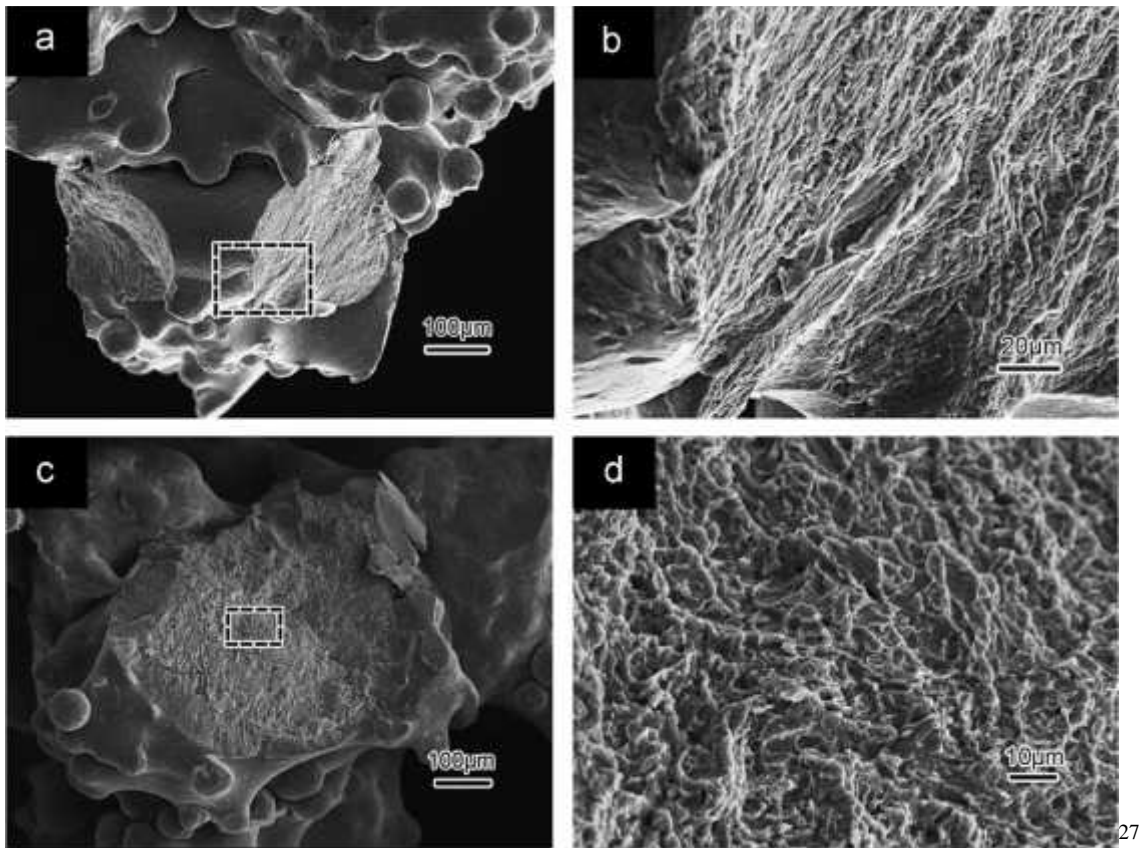
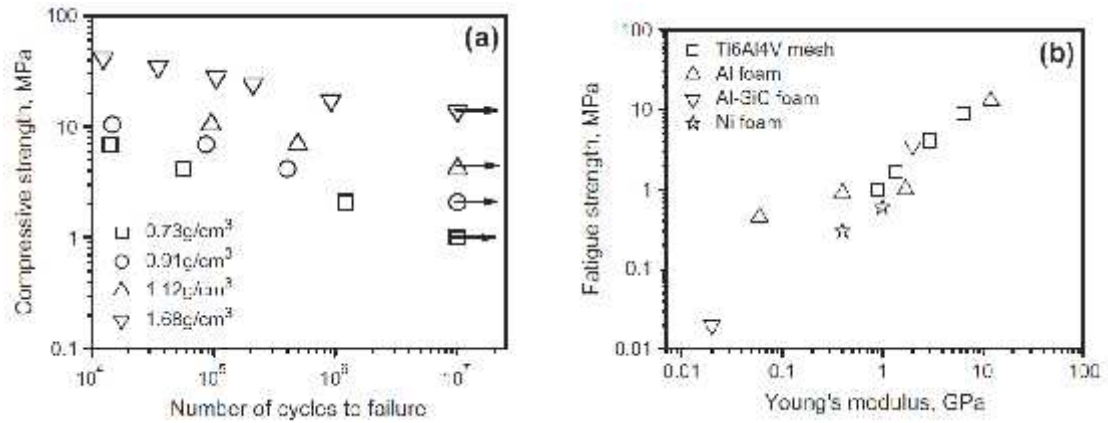


Figure 32: SEM images of Ti6Al4V lattice fracture surfaces, with a, b) G7 and c,d) cubic cells (Zhao et al. 2016)

A 2012 study by Li et al. uses “cube orientated” arrays of ~60-85% porosity determined higher porosity led to a shorter fatigue life [202]. The S-N curve produced has fatigue life plotted against compressive strength, and it is not clear in the text whether this is the applied stress or Ultimate Compressive Stress (UCS), therefore it is difficult to compare these curves to other work. The number of samples tested to determine these curves is not given, and there is no statistical analysis to suggest the reliability of these results. The study does suggest that the mechanism of fatigue in these meshes is an interaction between the fatigue cracks and cyclic ratcheting. It is suspected that: “*dislocations are generated along the a interface, and may contribute towards retardation of cyclic ratcheting and improve fatigue strength*” Li et al. 2012 [202].

<sup>27</sup> Reprinted from Journal of the Mechanical Behaviour of Biomedical Materials, 59, S.Zhao, S.J.Li, W.T.Hou, Y.L.Hao, R.Yang, R.D.K.Misra, “The influence of cell morphology on the compressive fatigue behavior of Ti-6Al-4V meshes fabricated by electron beam melting”, p251-264, © 2016, with permission from Elsevier



28

Figure 33: “S-N curve” of mesh arrays of variable densities, with a) compression strength vs N, and b) fatigue strength vs elastic modulus (Li et al. 2012)

It is clear that defect free surfaces lead to a longer fatigue life, however the traditional methods of grinding and polishing are not applicable for the complex nature of lattice structures, and chemical etching has been applied in some cases (see section 2.3.3).

Hooreweder and Kruth investigated the fatigue life of diamond structure lattices produced by SLM [204]. A set of Ti6Al4V lattices were built and fatigue tests were conducted after various post processes had been completed. These were compared to lattices with a high relative density, and a low relative density, which were labelled “as-built”. Some high relative density lattices underwent a HIP treatment, and some of those were chemically etched for surface improvement. It was observed that the fatigue life when comparing the as-built lattices was similar despite the differences in density. Lattices that underwent the HIP treatment, however, had a greater fatigue life, and lattices with a HIP treatment and chemical etching had the greatest fatigue life (Figure 34).

<sup>28</sup> Reprinted from Acta Materialia, 60(3), S.J. Li, L.E. Murr, X.Y. Cheng, Z.B. Zhang, Y.L. Hao, R. Yang, F. Medina, R.B. Wicker, “Compression fatigue behavior of Ti-6Al-4V mesh arrays fabricated by electron beam melting”, p793-802, © 2012, with permission from Elsevier.

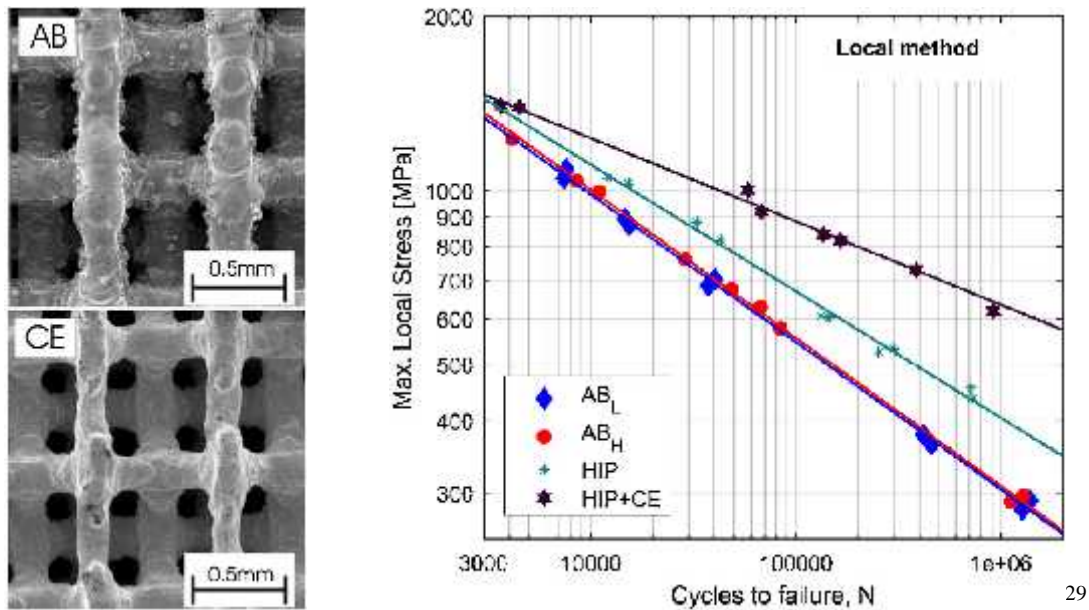


Figure 34: SEM images of the as-built (AB) and chemically etched (CE) surfaces of the diamond structure lattices, with representative SN curve of lattice fatigue tests (Hooreweder and Kruth, 2017)

As SLM is a cold process, there would be internal stresses present in the part immediately after production. In this paper, a stress relief was not conducted. It would be expected, therefore that due to internal stresses, there would be a reduction in ductility and a lower fatigue life. Some might argue that, for lattices, the internal stresses are very small, however it could also be argued that the struts themselves are small, therefore due to their comparative size, internal stresses could have a large effect on the mechanical properties. Indeed, Wauthle et al. found stress relief significantly improved yield stress for SLM diamond structure lattices compared to as-built SLM lattices in static tests, with HIP treatment providing similar yield stresses to as-built lattices, such that the differences between the two were not statistically significant either way [176]. Due to this, and a lack of microstructural images, it is not clear if the reason for the increase in fatigue life in the Hooreweder and Kruth study was due to the changing of the lattice microstructure, the stress relief effect, or both, from the HIP.

As discussed, there are many influencing factors before microstructural effects take effect, however further studies on whether lattices require stress relief would be beneficial.

<sup>29</sup> Reprinted from CIRP Annals - Manufacturing Technology, 66(1), B.V.Hooreweder, J.P.Kruth, "Advanced fatigue analysis of metal lattice structures produced by Selective Laser Melting", p221-224, © 2017, with permission from Elsevier

## Chapter 3 Procedures

This chapter details the procedures undertaken in this work. Lattices are briefly discussed, and EBM as the method of manufacture detailed. Each build where samples were manufactured is detailed here, with any deviation from the standard build stated. Some lattices were post processed prior to testing, and these methods are identified. The methods of measurements are stated, and the mechanical testing procedures are discussed. How the data was collected and analysed is covered, and the various mathematics applied in this work are specified.

### 3.1 Lattice choice

A diamond tetrahedral structure was chosen, as this a commonly assessed metallic lattice structure. Each node was attached to four struts at  $109.5^\circ$  angles to one another. This gives rise to a tetrahedral structure, which, when repeated, creates the diamond unit cell.

One unit cell is the simplest structure that can be repeated to build a specimen. Four tetrahedral structures, with four struts each, were required to build one diamond unit cell. This is shown in Figure 35.

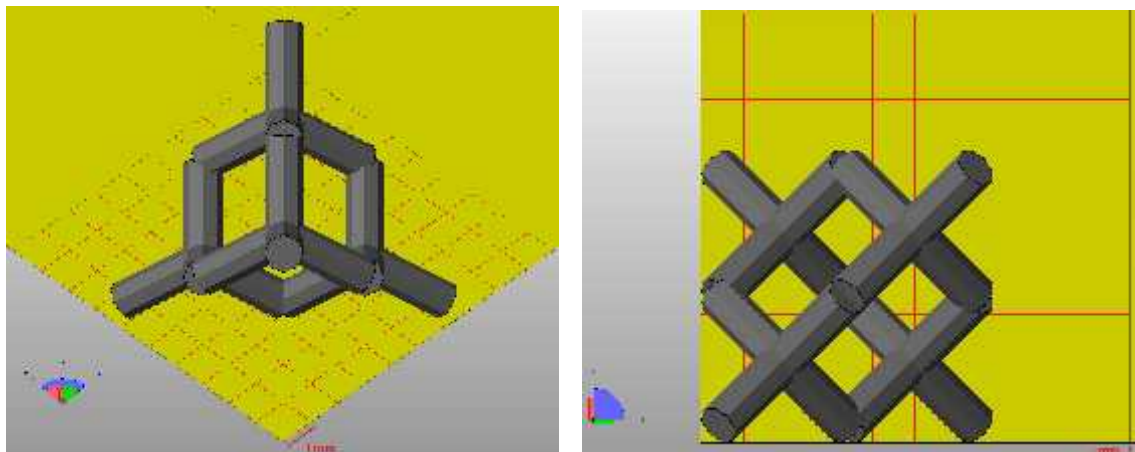


Figure 35: Single unit cell of the diamond structure. a) (111) plane, b) (100) plane

Typically, compression testing of metals utilises cylindrical samples, however, in this study, cubic samples were made for compression testing. It was decided that for simplicity, whole unit cells would be kept in cube and cuboid shapes, as is common in the literature (section 2.3.2).

## 3.2 Building in EBM

The following description applies to all parts in this section, unless explicitly stated otherwise.

Each build began as a computer aided design model, created using Autodesk® Netfabb®, or Materialise Magics software. In general, the lattices were based on a diamond structure formation, with a unit cell size of 6mm×6mm×6mm. The struts were designed to be 1mm diameter and 6mm in length unless otherwise specified. For struts of this size, the individual struts were designed as octagonal prisms, however, due to the beam resolution, these are cylindrical upon melting (see 2<sup>nd</sup> strut down, Figure 14, page 32). If larger struts are required, the software recommends shapes with more vertices to produce struts that more closely resemble cylinders.

All samples were made with standard Arcam Titanium Ti6Al4V grade 5 powder, of a particle size between 45 and 100 microns. “In specification” powder refers to Ti6Al4V with an oxygen content of less than 0.2wt%, with “out of specification” powder having more than 0.2wt% oxygen.

Parts processed at the Department of Materials Science and Engineering, The University of Sheffield, were built either with a 50µm or 70µm layer thickness, as specified in the particular build section. The machines available were either an Arcam A2 machine, or a modified Arcam S12. The A2 machine was a standard A2 machine with no alterations. The modified S12 was an earlier model, which had had internal parts replaced with A2 technology over the years with standard wear and tear, to bring it up to A2 standard.

All parts made by GKN Aerospace, Filton, were built with a 50µm layer thickness on a standard A2 machine. All machines utilised a tungsten filament with a maximum current of 11A, and a maximum applied voltage of 60kV.

All machines ran Arcam software version 3.2.121. Unless otherwise specified, the standard Arcam preheat theme was used prior to building, followed by the standard nett theme for lattices (with standard melt theme for solids where appropriate). All builds were started once the chamber pressure was below 10<sup>-5</sup> mbar, and after the build plate had been preheated to 730°C.

The standard Arcam theme for lattices and solids recommends three contour passes and a hatch, however this was not always the case for the parts in this work. During the creation of the builds in this project, some builds were made with contour passes switched off, some had both contour and hatch steps, and some used contours alone. Where this is the case, the changes to settings are brought to the attention of the reader during the specific build.

The lattices could not be built directly onto the start plate, as due to their delicate nature, removal would prove problematic. For most builds, support struts were not appropriate, despite the presence of negative surfaces between unit cells (Figure 36). As the support struts are of similar size to lattice struts, removal of the supports after the build could lead to damage of the struts. As an alternative to supports, “dummy solids” were sometimes placed at areas of the build where swelling could be an issue. As discussed

in section 2.2.2, swelling occurs when heat builds up during the build, and the melted part swells to a height which interferes with the building of layers and causes the build to fail. Further discussion on the mechanism of dummy solids is expanded on in 4.1.

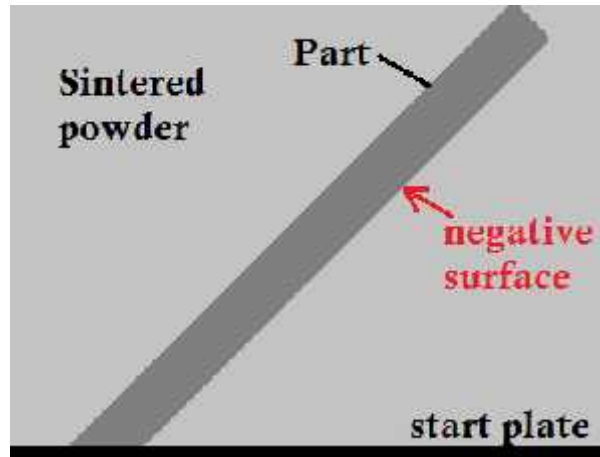


Figure 36: Diagram of negative surface which arises in lattice builds. Occurring when solid part is built on top of sintered powder

### 3.2.1 Size effect builds

This section details the samples produced for the size effect investigation (SE).

Sets of lattices were manufactured, with each build containing cube lattices of minimum  $2 \times 2 \times 2$  unit cells up to maximum  $10 \times 10 \times 10$  unit cells. These samples would go on to be compression tested in order to investigate whether there was a size effect affecting mechanical properties.



Figure 37: Lattices produced from SE builds, of  $2 \times 2 \times 2$  unit cells up to  $10 \times 10 \times 10$  unit cells for compression testing (Morrish et al 2017)

[205]

---

<sup>30</sup> “Size effects in compression in Electron Beam Melted Ti6Al4V diamond structure lattices” by Morrish et al. is licensed under CC BY 4.0, doi.org/10.1016/j.matlet.2016.12.130

I. *Size effect builds 1 and 2*

Two identical files of lattices were built at Sheffield University. The powder was “out of specification” (i.e. it had been cycled through a number of builds and contamination levels exceeded the tolerances of the supplier).

The 1<sup>st</sup> build (SE1) was completed on an altered S12 Arcam machine, using the standard Arcam 70 micron themes for preheat, nett and melt. There were no changes made to these settings.

The 2<sup>nd</sup> build (SE2) was completed on an A2 Arcam machine, with an altered preheat theme. The nett and melt settings were the Arcam standard 70 micron themes. There were no further changes made to these settings.

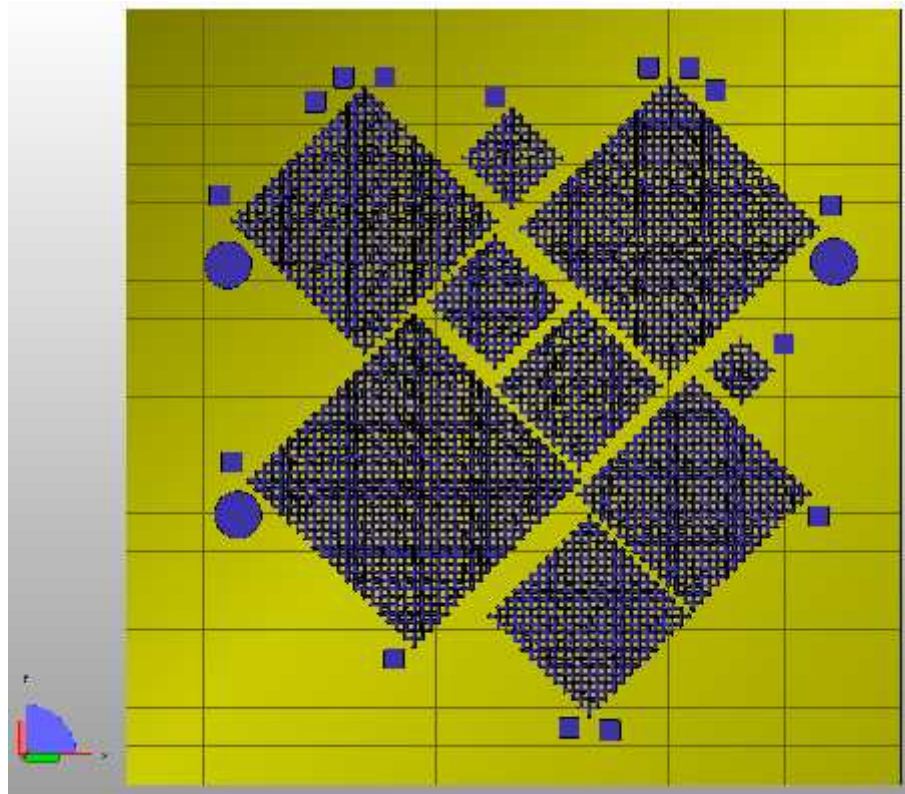


Figure 38: SE 1 and SE2. Lattices and their arrangement for the determination of the minimum number of unit cells required to ensure universal mechanical properties

## II. *Size effect builds 3 and 4*

These lattices were built by GKN Aerospace. In previous builds, solid parts had been included as heat sinks to avoid swelling. For this build, GKN reported that this was unnecessary due to their heat themes, therefore the solid parts were omitted in these builds. In total, a minimum of four sets of lattices with  $2 \times 2 \times 2$  unit cells to  $9 \times 9 \times 9$  unit cells were built (the  $10 \times 10 \times 10$  unit celled lattices were removed, as tests on SE1 and SE2 had determined that these exceeded the limits of the testing equipment).

Both builds were manufactured at GKN Aerospace, to ensure the builds could be manufactured consecutively utilising the same machine with the same batch of powder. The machine was an Arcam A2, using the standard Arcam settings, with 50 micron themes for preheat and nett. There were no changes made to these settings.

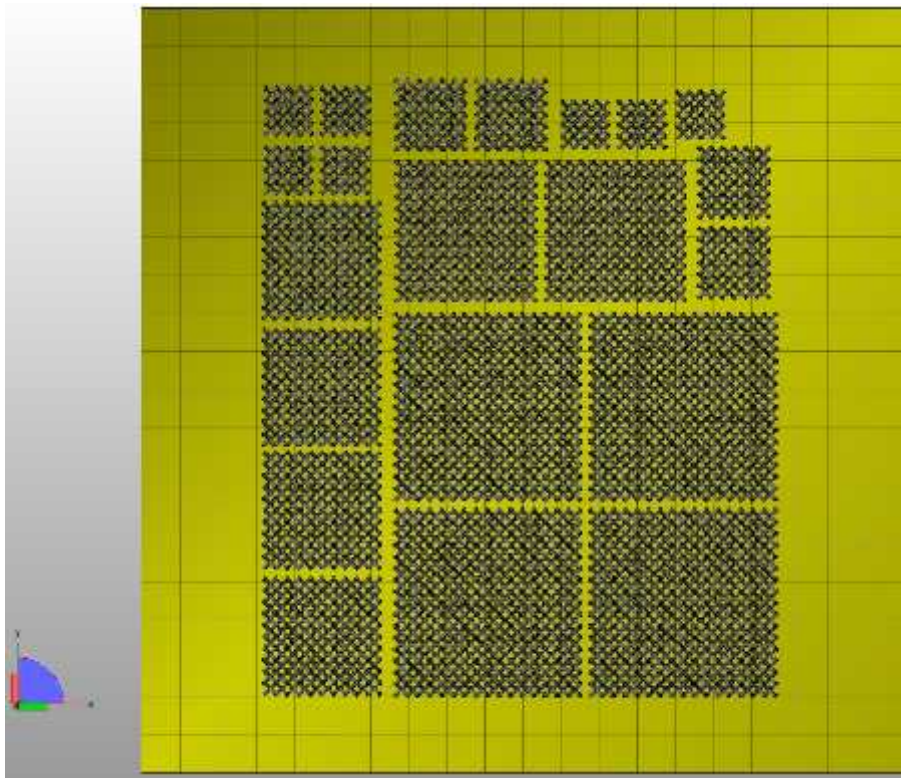


Figure 39: SE3: Lattices and their arrangement in the build for the compression tests. Four lots of 3, 5 and 8 unit celled lattices, with two 6 unit celled lattices and seven 2 unit celled lattices

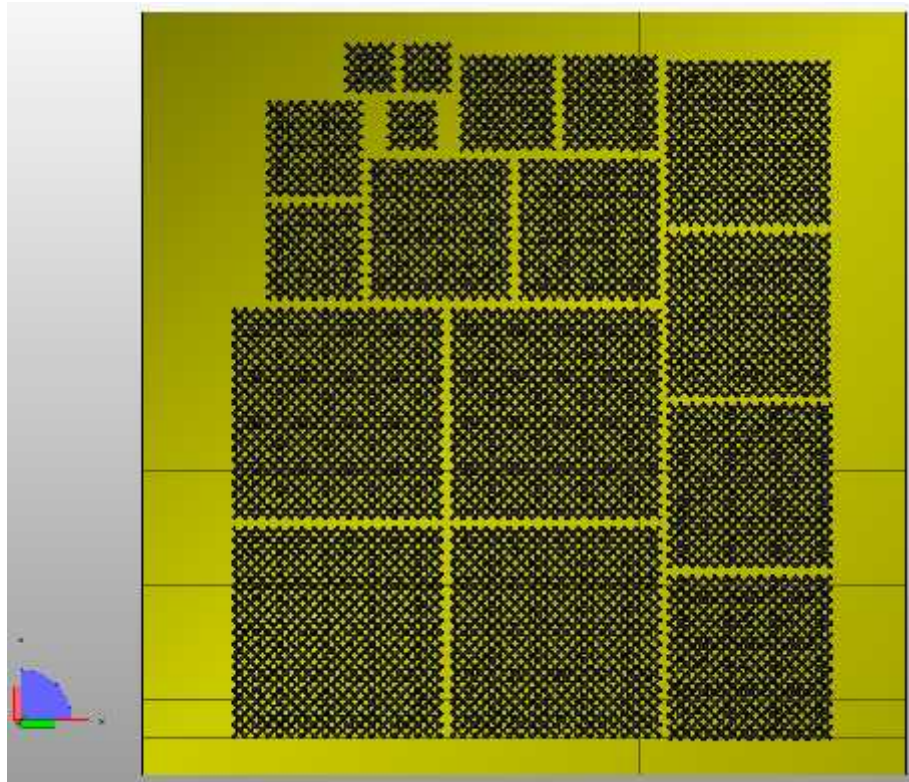


Figure 40: SE4: Lattices and their arrangement in the build for the compression tests. Four lots of 4, 7 and 9 unit celled lattices, with two 6 unit celled lattices and three 2 unit celled lattices

### 3.2.2 Anisotropy investigation

This section details the samples produced for the anisotropy investigation (AI).

A set of asymmetrical lattices was designed by stretching the standard diamond lattice cube CAD models in the z direction, by doubling the height of the lattices. All other dimensions remained the same. Four standard diamond lattice samples of  $6\times 6\times 6$  unit cells were produced for comparison.

Also included in this build were four tensile samples of  $4\times 4\times 6$  unit celled lattices with solids at each end, measuring  $24\times 24\times 10$ mm, and a number of solid lattice cubes for another investigation (these models can be seen in Figure 41-Figure 43, however results regarding these samples are not detailed in this work).

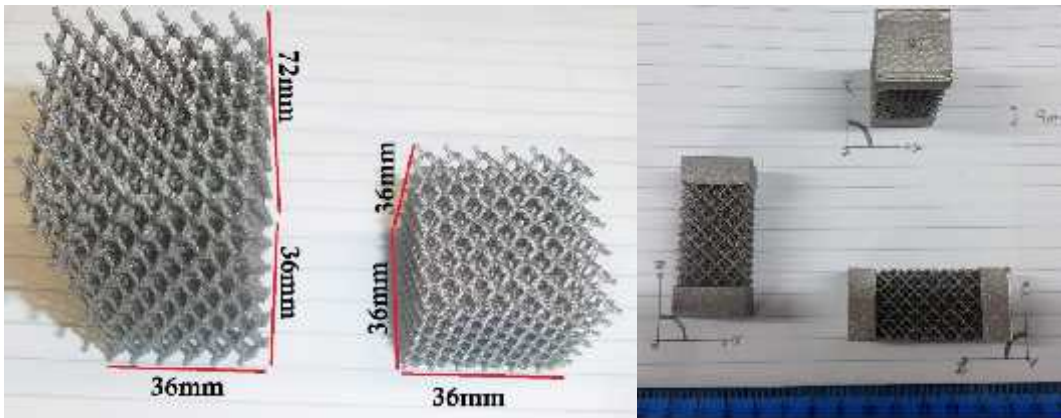


Figure 41: Samples from AI builds, a)  $6\times 6\times 6$  asymmetrical lattice, and  $6\times 6\times 6$  standard diamond lattice. All asymmetrical lattices were tested in the orientation that can be seen in the image, whatever their build orientation, and b)  $4\times 4\times 6$  lattices with solid ends for tensile testing

I. *Anisotropy investigation build 1*

The 1<sup>st</sup> build (AI1) was manufactured at The University of Sheffield for proof of concept and preliminary testing. The powder was “in specification” grade 5, manufactured on an altered S12 Arcam machine, using the standard Arcam 70 micron themes for preheat, nett and melt. There were no changes made to these settings.

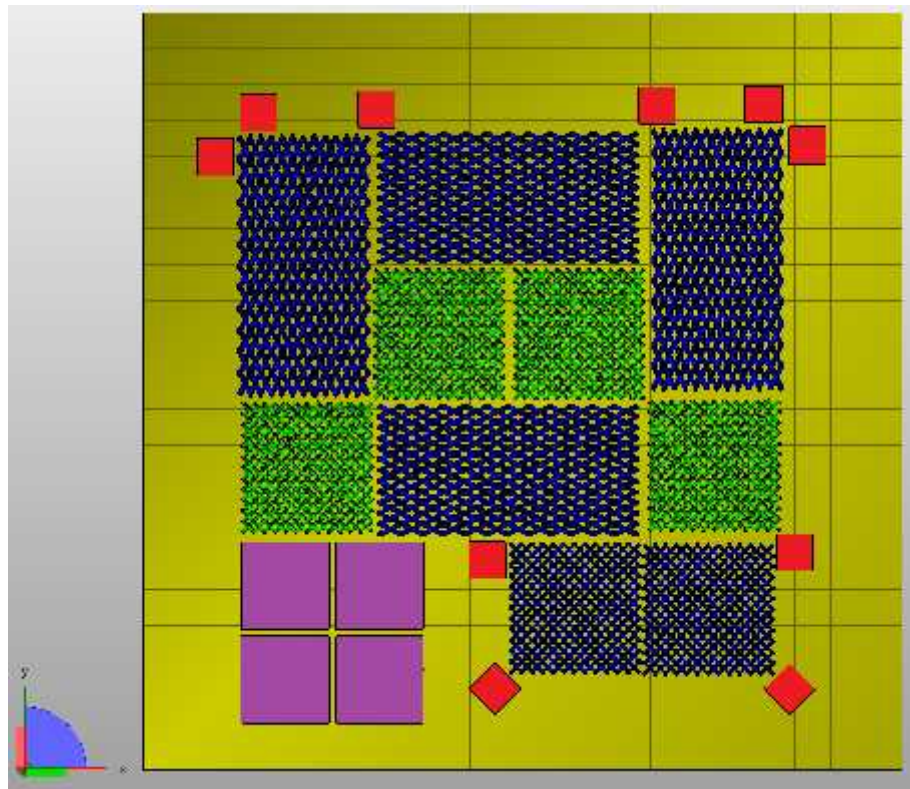


Figure 42: AI1: Lattices, solids, and their arrangement in the build for the compression and tensile tests. With dark blue asymmetrical lattices, green lattice cubes, purple tensile samples, and red solid cubes

## II. Anisotropy investigation builds 2a, 2b and 2c

Three anisotropy investigation (AI) builds were run consecutively, and numbered 2a, 2b and 2c respectively. These were built at GKN Aerospace to ensure all builds could be manufactured consecutively using the same machine and with the same batch of in specification, grade 5 powder, for consistency. The machine was an Arcam A2, using the standard Arcam settings, with 50 micron themes for preheat, melt and nett. Contours were turned off to decrease the build time.

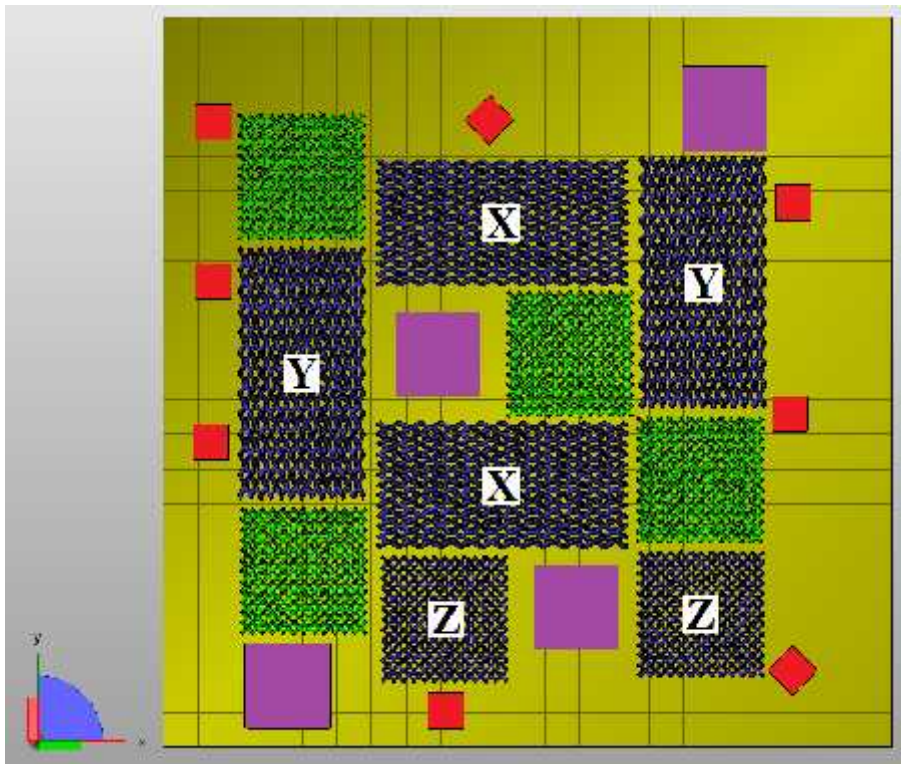


Figure 43: AI 2a, 2b and 2c. Lattices, solids, and their arrangement in the build for the compression and tensile tests. With dark blue asymmetrical lattices, green lattice cubes, purple tensile samples, and red solid cubes. Asymmetrical lattices labelled X, Y or Z denote their build orientation in relation to mechanical property results

### 3.2.3 Lattice modification builds

This section on lattice modification (LM) details the manufacture of lattices for the purpose of altering the samples, by post processes of hot isostatic press (HIP) treatment or surface alteration by etching agent.

#### I. Lattice modification build 1

The 1<sup>st</sup> build (LM1) was produced at The University of Sheffield using an Arcam A2 machine.

Within this build were three solid cubes, one would be melted using the contour only theme, one would be melted using hatch only theme, and one would be melted using the standard three contours and a hatch. This was to investigate whether the microstructure varied depending on the setting chosen (see section 4.4.3I).

For the lattice models, it was suspected that due to the melt pattern of the themes, contours would produce smoother surfaces than the hatch, therefore these lattices were completed using a contour only theme, set to 99 to ensure complete melting of the lattice cross sectional area. The hatching mode of the beam movement was turned off, and the build set to 50 $\mu$ m layer thickness, with a standard preheat theme. This build initially failed due to the heat of a 50 $\mu$ m melt leading to swelling of the first layer of lattices, therefore supports were put in between the lattices and the base plate, rather than edit the heat settings, which would be complex and difficult to recreate for other builds.

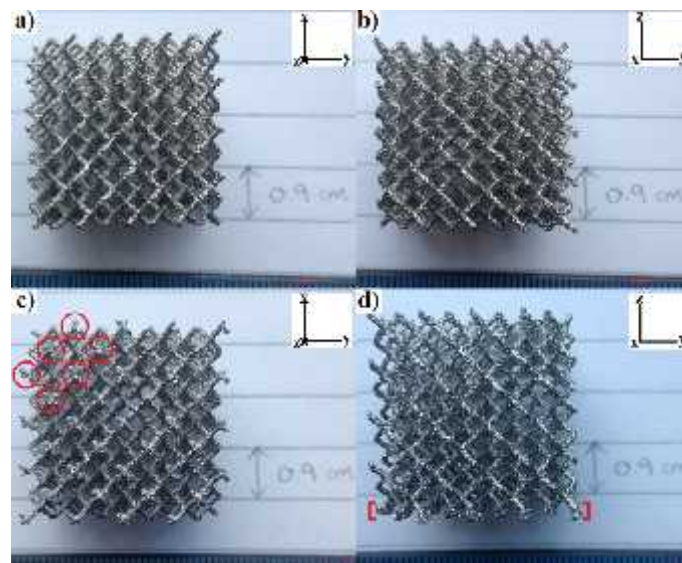


Figure 44: 4 $\times$ 4 $\times$ 4 lattices. a & c are the base of the lattices, with build direction into the plane, and b & d show the side, with the arrows indicating build direction. a, b) Lattices without supports, c,d) lattices with supports, highlighted in red

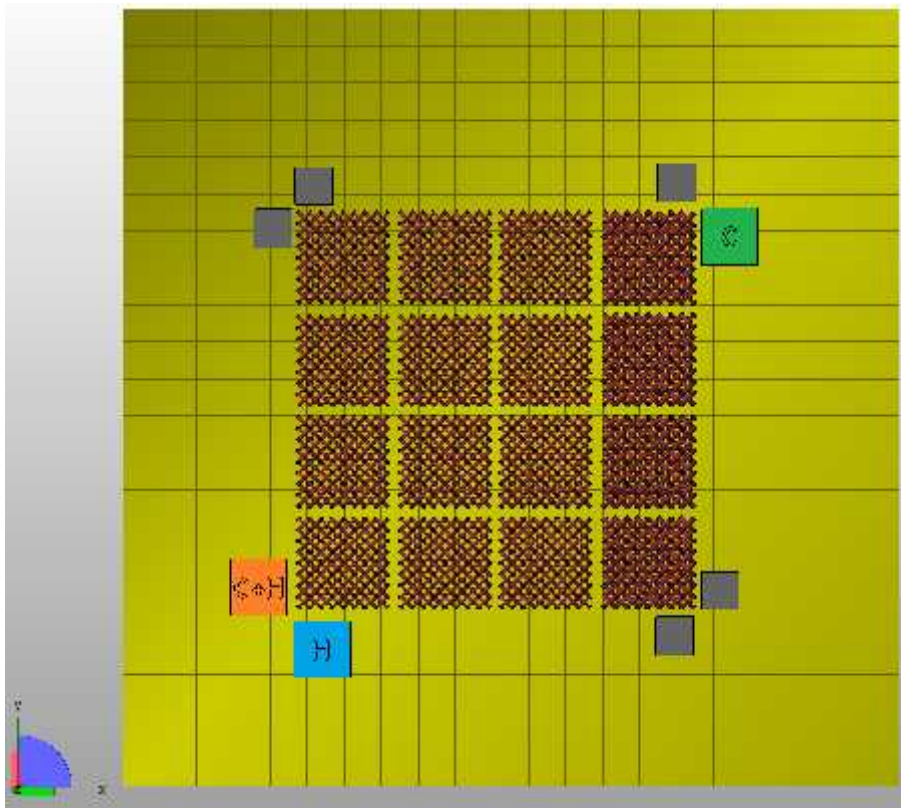


Figure 45: LM builds. Lattices and solids, and their arrangement in the build for HIP and/or etch post processing, and microstructural analysis. The labelled solid cubes built at the corners were produced with different build settings: C by contours only, H by hatch only, and C+H by 3 contours and a hatch, for microstructural analysis

## II. *Lattice modification build 2*

The 2<sup>nd</sup> build (LM2) was completed at GKN Aerospace.

4×4×4 lattices were produced, where four with 1mm strut diameters and four with 1.25mm strut diameters were selected for testing. The four lattices with 1.25 mm strut diameters would be sent for surface alteration by etching (section 3.3.2).

These lattices were completed using a contour only theme, set to 99 to ensure complete melting of the lattice cross-sectional area, with no hatch theme. The layer thickness was set to 50µm.

### 3.2.4 Fatigue samples

This section details the manufacture of samples for fatigue testing.

The design was a  $4 \times 4 \times 16$  unit celled lattice, with solid ends, however the CAD model of the lattice struts at the solid interface, were designed to penetrate the solid end (see Figure 46). This was to reduce the likelihood of the struts breaking at the ends, due to the increased surface area of the strut cross section, compared to the pointed ends of the nodes, it was decided that this design would hold the lattice more securely, due to the higher contact area.

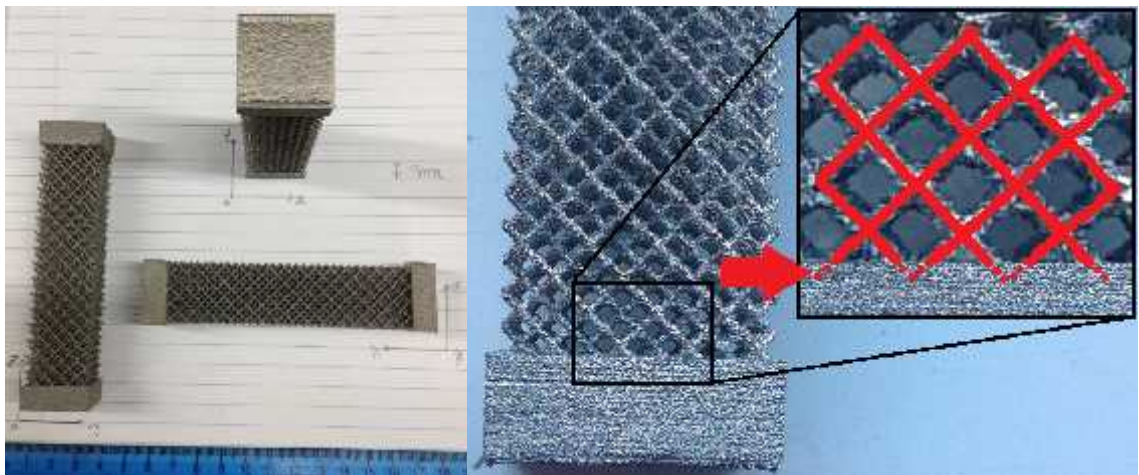


Figure 46: Fatigue samples. Solid ends with  $4 \times 4 \times 16$  unit celled lattices. a) viewing samples from all sides, b) demonstration of how the lattice CAD model is designed to penetrate the solid end

I. *Fatigue build 1*

The first set (F1) of fatigue samples were built at The University of Sheffield. These samples were built to address two questions. The first was to investigate whether position within the build had any discernible effect on the mechanical properties. Each lattice had a number on the side of the solid to identify position on the build plate, which can be seen in Figure 47 as the dark blue protrusion from the solids. The second reason was to establish whether collecting data from fatigue testing was viable, or if it was too advanced a test for such a novel structure.

The machine was an S12, the build settings were standard Arcam settings for preheat, nets and solids at 70µm layer thickness. There were no alterations made to these settings. The powder was in specification grade 5.

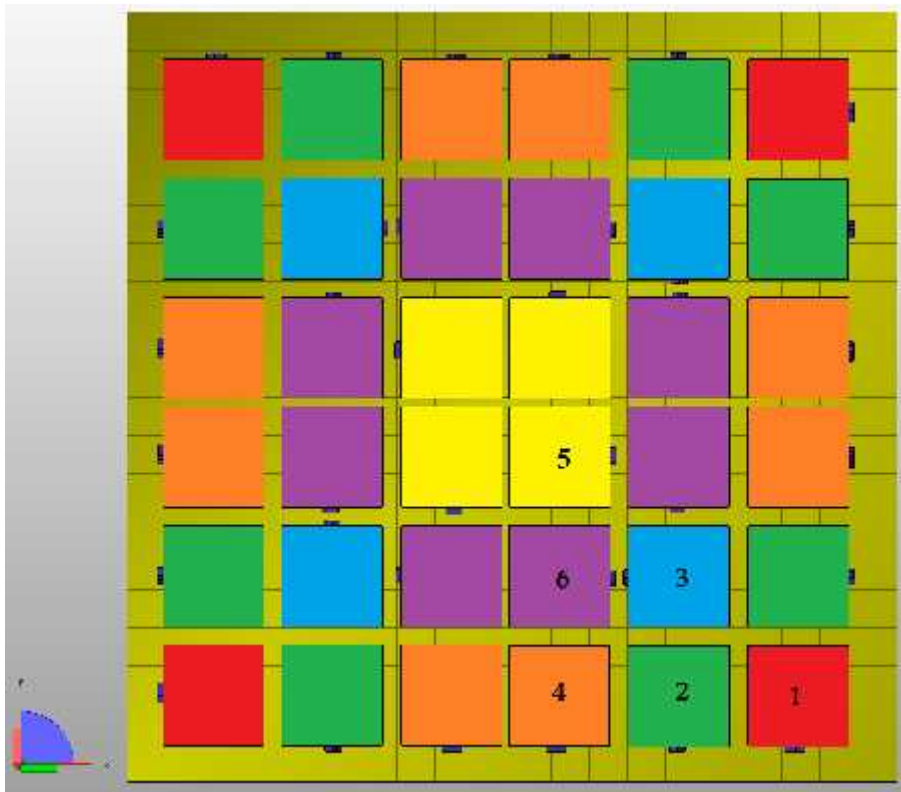


Figure 47: F1 samples. Colour coded fatigue sample arrangement in build. All samples were numbered from 1-6 according to their place on the start plate. The colours correspond to samples with the same numbers

## II. *Fatigue builds 2 and 3*

Following the preliminary tests from F1, seventy two samples were prepared from two consecutive builds for fatigue testing, built with in specification grade 5 powder at The University of Sheffield. These lattices were identical in appearance to Figure 46, without the numbers on the sides of the solid ends.

These samples were completed using a contour only theme, set to 99 to ensure complete melting of the lattice cross-sectional area, with no hatch theme. The layer thickness was set to 50 $\mu$ m, with a standard preheat theme.

The 36 samples from F2 were utilised for testing to determine EN and SN curves (section 4.5.3, page 145).

Of the 36 samples from F3, 18 were sent for HIP treatment. These were fatigue tested with the 18 lattices that were not HIP treated, to determine any differences in fatigue life due to heat treatment (section 4.5.5, page 148).

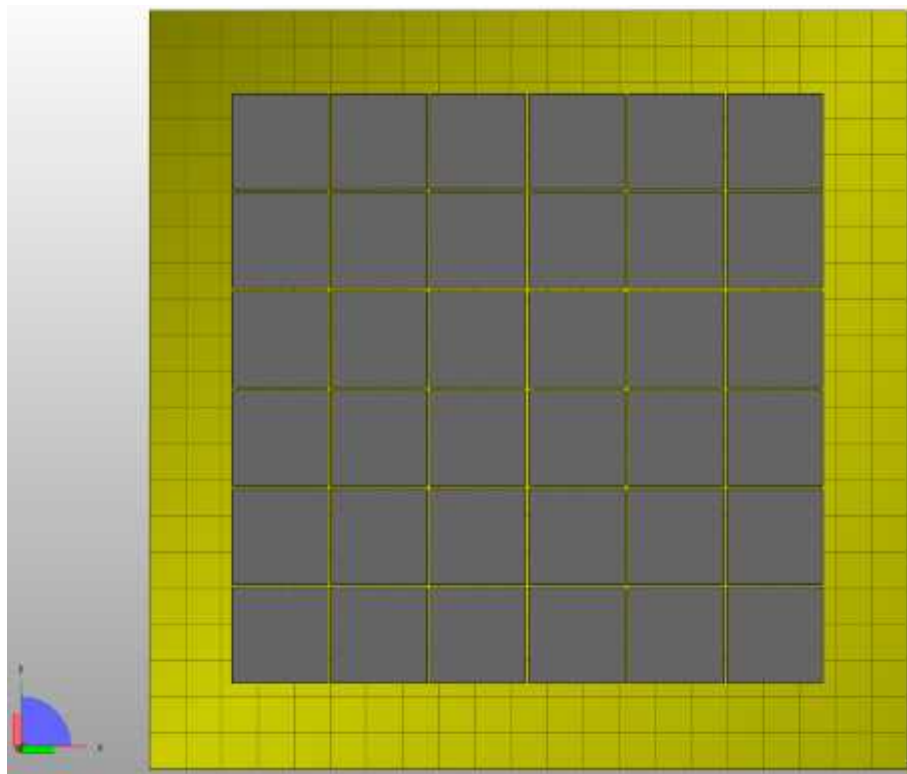


Figure 48: The arrangement of fatigue samples in the builds F2 and F3

### 3.3 Post processing

Most EBM parts in this project were tested in the as-built condition, however some EBM parts were subjected to post processing techniques that were not standard, as defined in this section.

#### *3.3.1 Hot Isostatic Press (HIP)*

Due to the porosity identified within some lattice struts, a number of EBM parts were sent for hot isostatic pressing (HIP) to attempt to improve the mechanical properties. Eighteen fatigue samples from the F3 build, and eight compression samples from LM2 build, were sent by GKN Aerospace to a GKN external contractor for HIP treatment.

The exact details of the HIP conditions are export controlled, and therefore cannot be published in this work, however it is possible to speculate on the HIP conditions by obtaining the known stress relief method for laser lattices. Unfortunately, the exact details of this cannot be published either, however it can be said that when Ti6Al4V LPB manufactured lattices are stress relieved, this is by using a method similar to a HIP treatment. For stress relief, the temperature is gradually raised from room temperature to just under the transus, and held for a length of time, before fast cooling back to room temperature. It is suspected that this method is similar to the HIP, which has the addition of the high pressure atmosphere to the heat treatment in this temperature range.

#### *3.3.2 Surface enhancing using an etching agent*

Two batches of four EBM compression test lattice samples were sent to a GKN external contractor for a polishing step utilising an etching agent. The process is an industry standard for improving the surface finish of AM parts. Although the exact details of the process are commercially sensitive, the process immerses the samples in a corrosive solution, at a raised temperature, for a time that is dependent on the needs of the customer, for the part that is being treated.

The first set of four samples were placed in the solution for different lengths of time, to determine the ideal amount of time to produce smooth lattice struts, without removing too much material to significantly weaken the structure. Each sample was subjected to the process for 4 minutes, 8 minutes, 12 minutes or 16 minutes.

From these preliminary tests, a steady removal rate was observed (given in section 4.4.1, page 110). A new batch of Ti6Al4V lattices was obtained, four of ~0.85mm strut diameter, and four of ~1.05mm strut diameter<sup>31</sup>.

---

<sup>31</sup> The lattices were designed to have 1mm and 1.25mm struts, however when the lattice struts were measured, it was found the struts were actually 0.7-1mm, and 0.9-1.2mm

It was determined that in order to remove 0.2mm of material to give lattices with ~1mm struts, 10 minutes in the etching solution was required. Therefore four of the ~1.05mm strut lattices were sent away to repeat the process. After this, four as-built ~0.85mm strut lattices and four ~0.85mm strut lattices that had been etched from ~1.05mm strut lattices were compression tested to determine what effect the etching process had on the mechanical properties.

### 3.4 Measurements

When taking physical properties, various methods were employed to obtain measurements, as discussed here.

#### 3.4.1 Classical methods

Once the samples were ready, they were measured and weighed, and their dimensions and masses recorded on an excel spreadsheet.

This was conducted by taking a series of measurements using electronic vernier callipers in every direction around the lattice cube (see Figure 49).

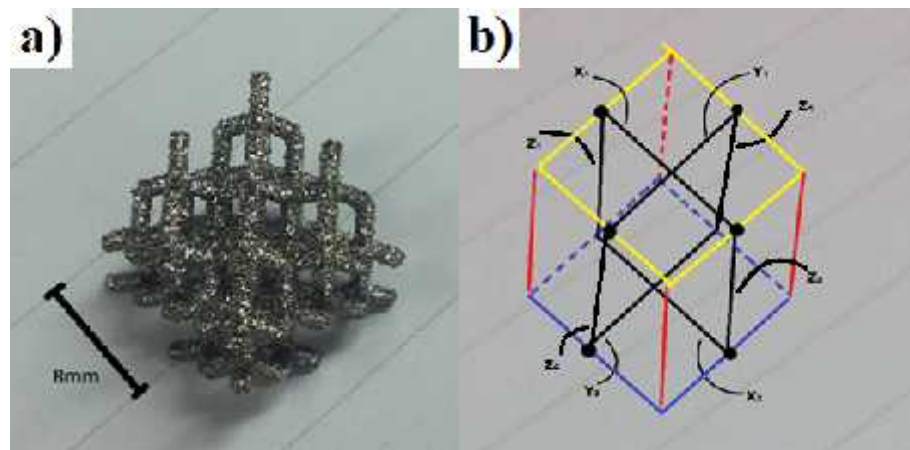


Figure 49: a) shows a 2 unit cell lattice, and b) shows the direction of the measurements taken from the lattices, using vernier callipers. Subscript 1 on X and Y is the top of the build, and subscript 2 on X and Y is the base of the build. All subscripts of X, Y and Z values were averaged, and the product of these averages was used to calculate volume

The mass was found by using a standard scientific balance accurate to  $\pm 5 \times 10^{-6}$  kg.

The density value used in correction calculations for solid EBM Ti6Al4V was not calculated from the measurements. To improve the accuracy of the density result, an Archimedes balance was used to determine the density.

All lattice measurements were obtained from these methods, and were recorded as accurately as the instruments available allowed.

### 3.4.2 SEM method

For more accurate strut width measurements, the measure function in the SEM was used to measure strut diameters. Some problems arose here, as the perspective of the unit cells was not accurately depicted in the 2D image captured in the SEM. Considering Figure 50, the struts labelled A appear to be thicker than the struts labelled B. This was an observation, which persisted after many measurements, however was unusual as all lattice struts should have been the same size. It was decided that this is probably due to perspective, caused by the measurement function on the SEM measuring across a 2D image, and therefore having no depth perception. To try and negate this effect, only measurements taken from struts closest to the detector were used.

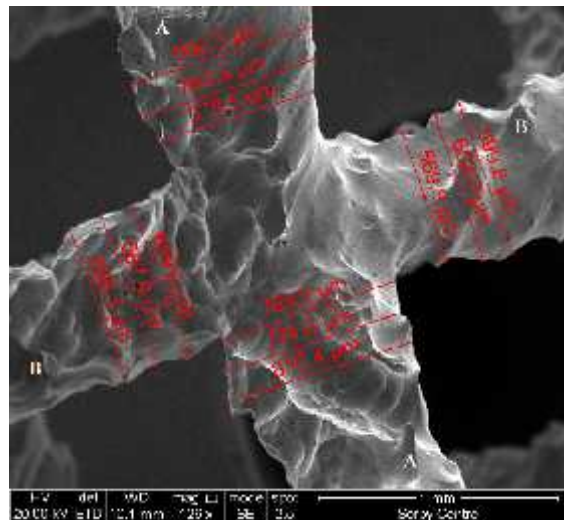


Figure 50: Top of a lattice, where A struts appear larger due to their proximity to the detector than B struts. When measured manually, the struts were statistically the same size

### 3.5 Compression test

A Zwick Roell Z050 testing machine with a 50 kN load cell was used to compress each cubic lattice at varying speeds, determined by the lattice height, to ensure a strain rate of  $10^{-3} \text{ s}^{-1}$ .

The force applied to the lattice was recorded automatically by the machine, alongside the distance travelled by the crosshead.

The data was removed from the testing machines in a file format compatible with Microsoft Excel. Some calculations and charts were produced using SigmaPlot by Systat Software Inc. All compression (and tensile) data collected was in standard force versus deformation, with the following equations used to plot the data in a suitable format:

Engineering strain was calculated using the standard equation:

$$\varepsilon = \frac{\Delta l}{l}$$

*Equation 1*

where:  $\varepsilon$  = strain,  $\Delta l$  = deformation,  $l$  = original overall height.

Engineering stress was calculated using the standard equation:

$$\sigma = \frac{F}{A}$$

*Equation 2*

where:  $\sigma$  = stress,  $F$  = force,  $A$  = original nominal area of cube in XY plane

Conventionally, compliance correction to account for deformation of the test machine should be applied when using the crosshead values, by conducting a plate to plate compression test at a very low force. This is to account for deformation in the test frame. In addition to this, at low strain stages of the test curves, there is an uptake of stress, as contact between the specimens and the platen is established.

This was not possible in this study, therefore to correct for this, during the data analysis stage, the elastic modulus was used to extrapolate the curve back to zero and shift the curve to the left to find accurate strain values.

A standard MS Excel spreadsheet was designed to be used as a basis for calculating results. The new data was input into the spreadsheet for each data set. As standard, the elastic modulus, ultimate compressive stress and offset yield stress were determined from the curve, as demonstrated in Figure 51.

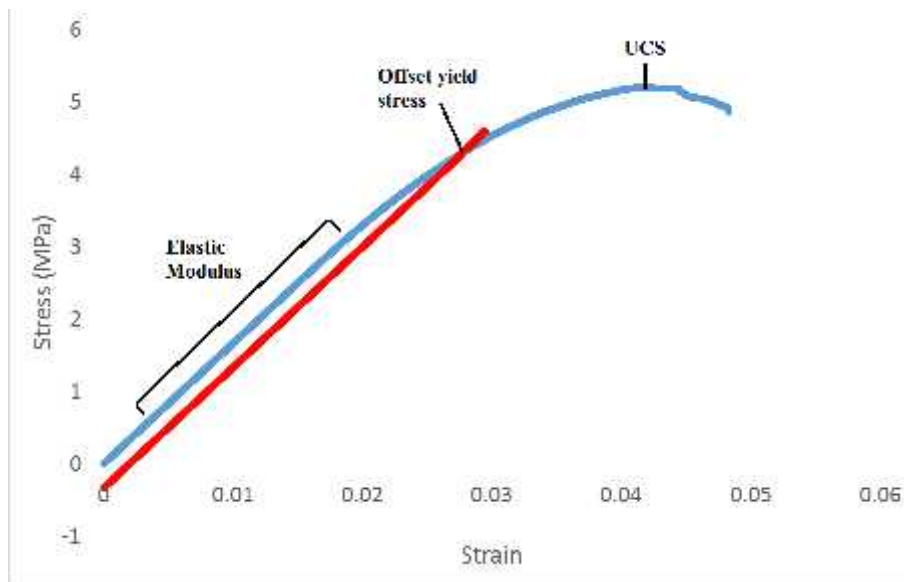


Figure 51: Representative stress/strain curve, showing elastic modulus, ultimate compressive strength (UCS) and offset yield stress

Using a straight edge for guidance, a straight line was plotted parallel to the straightest part of the curve, and the two values furthest along the curve, while remaining on the straight line, were selected. This data set was plotted on a graph, and a trend line drawn with the equation displayed. The gradient of this stress versus strain curve gives the elastic modulus, and was recorded on the spreadsheet.

The yield stress (YS) was found by drawing an offset line with the same slope as defined by the elastic modulus. This was extended until the intercept point between the extended elastic modulus and the stress/strain curve was found.

Usually, a 0.2% yield stress was satisfactory, however, in some cases, this was not possible. In some cases it was found that a 0.2% shift did not intercept the curve, as catastrophic failure would occur before a substantial plastic region could be established. Alternatively, single struts might break leading to load drops in the elastic region. In these cases, a 0.02% proof strength was used, and obtained for all the data within that investigation, instead of 0.2% proof strength. This was found using the same method, but using the 0.02 value in place of the 0.2 value.

### 3.6 Tensile test

A Zwick Roell Z050 testing machine was used to test lattice bars in tension. Due to size restrictions within the tensile clamps, a custom set of steel clamps was made to fit the samples in the machine (see Figure 52). These were designed based on the dimensions of the tensile clamps and manufactured by Viking Precision Engineering Ltd, Perivale.

The clamp consisted of steel base (red), with a moving slider (yellow), which held the sample in place by tightening a bolt (blue) with a nut (purple). To prevent the slider from moving in the z direction during testing, a screw (green) was in place to hold the slider neat against the base. Grooves were scored into the flat contact surfaces in order to hold the sample securely.

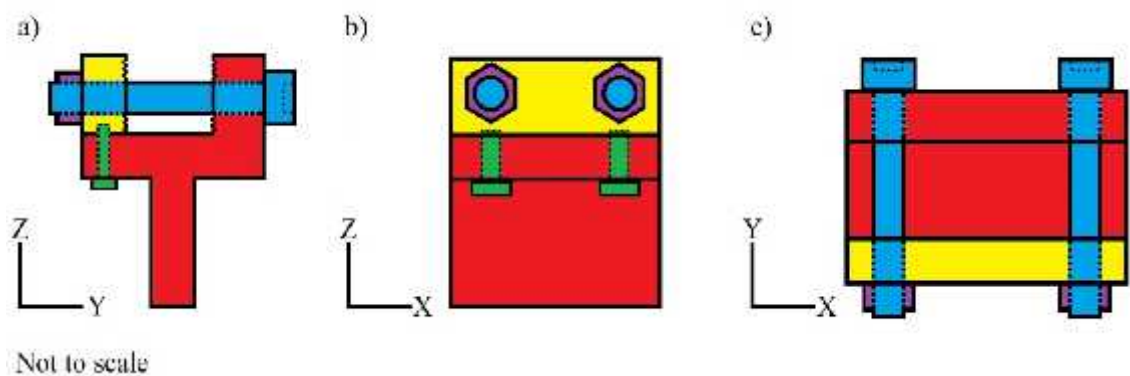


Figure 52: Schematic of custom clamps, redrawn from technical drawings. a) shows the side view, b) shows the head on view when looking at the fatigue setup, and c) shows a birds eye view of the custom built clamp

To ensure a good grip between the sample and the clamps, the clamps were attached to the machine first, and top and bottom clamps carefully aligned. The clamps were then set to a large distance apart, and the sample placed in the bottom clamp. The top clamp was lowered slowly to the top of the sample, until the distance between the clamps was approximately equal to the height of the sample. The clamp jaws were tightened with two 6mm hex headed, partially threaded bolts, by use of a torque wrench. The jaws were tightened alternately to avoid twisting the sample and introducing strain.

Engineering stress and strain were calculated using Equation 1 and Equation 2 respectively, with effective elastic modulus, offset yield strength and UTS found using the graphical method detailed in 3.5.

### 3.7 Fatigue test

The fatigue tests were carried out on a Nene hydraulic testing frame, refurbished with a Parker system actuator (see Figure 53). The load cell was an interface 1010AF, with a maximum load of 12.5 kN. All fatigue tests were compression/tension, with amplitude, A, and maximum displacement, 2A.

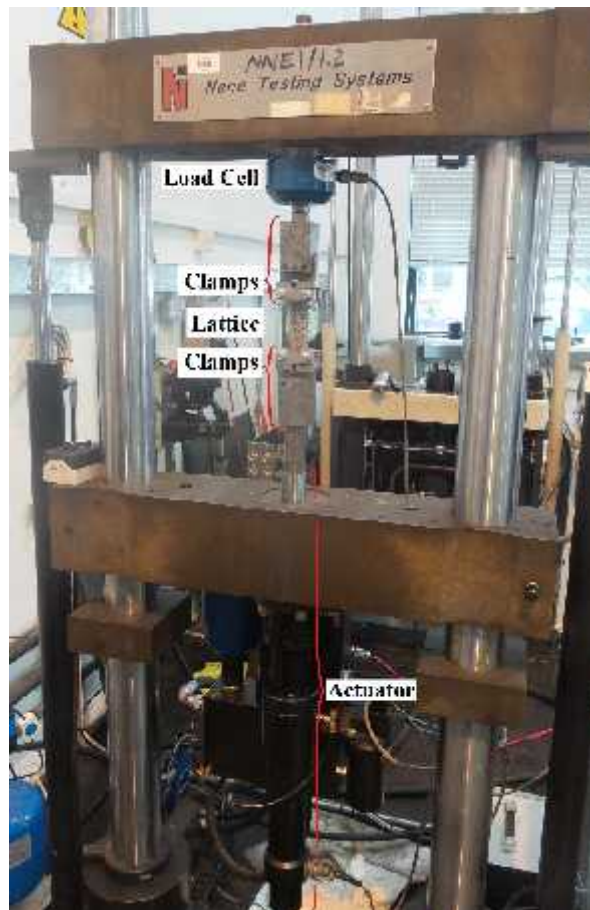


Figure 53: Fatigue test setup. The Parker actuators contain the moving silver coloured pistons in black casing. The Nene test rig contains the experiment within it, and holds the actuators. The test rig can be seen in the image, comprising of two large silver coloured pillars, and the darker grey solid areas

Test speeds were calculated using chosen strain rates through the simple equation:

$$v = l\epsilon$$

*Equation 3*

where:  $v$  = velocity,  $l$  = length,  $\epsilon$  = strain rate

During the fatigue testing, the speed from the strain rate had to be converted to frequency by the following equation:

$$f = \frac{v}{2\pi}$$

*Equation 4*

where:  $f$  = frequency,  $v$  = velocity,  $A$  = amplitude of force or displacement, depending on the test

The initial experiment to determine whether sample position on the build plate affected mechanical properties was conducted using an amplitude of 2.350mm to provide a maximum displacement equating to a 5% change in length and a frequency of 6.370 Hz. This rate was chosen to save time as there were many samples to test. The strain rate of  $10^{-3} \text{ s}^{-1}$  had been used for every previous test, however for fatigue, this strain rate would result in a very lengthy testing time. A strain rate of  $5 \text{ s}^{-1}$  was chosen for efficiency. The frequency of the experiment was determined using Equation 4, where amplitude was half of 5% of the lattice length, as determined in prior testing.

The obtaining of the stress life curve utilised the force controlled function, with increasing force amplitude (kN) applied at a frequency of 7.95Hz. The obtaining of the strain life curve utilised the position controlled function, with increasing displacement amplitude (mm) applied at frequencies of 3.18Hz for high strains and 9.54Hz for low strains, due to time constraints.

### *3.7.1 Statistics*

#### *I. Weibull distribution*

The Weibull distribution is a method for generating a probability function, where there is a small data set. It is always best to test many samples in order to secure a high confidence in the result, however due to the high variability in fatigue results, there is a point where data collection must stop.

The Weibull distribution is a cumulative probability that a specimen fails before a certain lifetime [206]. This can be estimated graphically by ranking the data in the series from lowest to highest, and using a natural logarithmic plot of the number of cycles against the proportion surviving. The gradient of the line gives the Weibull modulus, a numerical value which gives a measure of the reliability of results.

## II. *Null hypothesis*

A null hypothesis is the default position in science and engineering until evidence suggests otherwise. Typically, a null hypothesis will state that there is no difference between two or more data sets. Three analysis methods were employed in this work to assess evidence for the null hypothesis to be rejected, in favour of a hypothesis which believes there is a difference between data sets. For this, a “p value” must be found, which measures the strength of the evidence against the null hypothesis. In general, if a p value is less than 0.05, further investigation can be justified. This corresponds to a confidence value of 95% or higher.

Three statistical analyses were performed: a t test, a Generalised Likelihood Ratio Test (GLRT) and a log-rank test, as discussed in the following sections<sup>32</sup>.

## III. *t test*

The t test acts to determine if two data sets are statistically different from each other by comparing the mean average values. In a two sample t test, the two means are compared and a p value found based on how different the means are. How far each data point deviates from the mean is taken into account by performing the 2-sample t test for unequal variances (where variance is standard deviation squared).

Therefore, the t test was run using the statistical analysis function in MS Excel “two sample assuming unequal variances”.

## IV. *Generalised Likelihood Ratio test*

The Generalised Likelihood Ratio Test (GLRT) is used to assess the evidence against a null hypothesis, by considering that the two data sets come from a common specified distribution, as opposed to different, distinct distributions. It is a powerful test in that it is strengthened by the assumed distribution, however it is important that the correct distribution is chosen. Within this project, a Weibull distribution was assumed based on the shape of the Kaplan-Meier plot produced from the data (Figure 86, page 149). This test, therefore, assessed whether the data sets came from two distinct Weibull distributions, or a common one.

With high cycle fatigue, sometimes the test must be suspended before catastrophic failure can occur. In statistics, this is known as a “censored” result. If the samples fail catastrophically, ending the test, this is an “observed” result. The GLRT takes the test

---

<sup>32</sup> The scripts to run the GLRT and the log-rank test were written by Dr Timothy Heaton, and run in the computer package R by Dr Eleanor Stillman of the department of Mathematics and Statistics at the University of Sheffield (see Appendix 3)

status into account, as an observed test can be considered more reliable statistically than a censored test. In the case of fatigue results in this study, all results were observed.

## V. *Log-rank test*

The log-rank test compares the data sets, by finding a hazard function for both data sets, which sets an expectation of failure for certain numbers of cycles. The hazard functions are compared, and how similar they are is stated. This method assumes no specific distribution, therefore it can be said to be non-parametric. In this way, it is a less powerful test than the GLRT, however it is advantageous in that it runs without the need for assumptions, which could arise from user bias. This test can allow for censored data if required, however, in this work, all results were observed.

## 3.8 Additional methods

### 3.8.1 *Standard deviation*

Where the results have been displayed graphically, the sample standard deviation formula was used to indicate the error in the results. The use of this formula was appropriate, as it was anticipated that all results would be concentrated around the mean value, as is the case for a standard distribution. The “stdev” function in excel was often utilised, which equates to:

$$s_D = \sqrt{\frac{\sum(x - \bar{x})^2}{n - 1}}$$

*Equation 5*

where:  $s_D$  = standard deviation,  $x$  = value,  $\bar{x}$  = sample mean,  $n$  = number of values, and all other symbols have their standard mathematical functions.

### 3.8.2 Density correction factors

Where samples had a significant density difference, a correction factor was applied to account for the difference. The following formulae were adapted from Gibson and Ashby equations based on coefficients of proportionality [169]. The correction factor was calculated using experimental values.

To obtain the correction factor for elastic modulus, Equation 6 was used:

$$\frac{E_t}{E_s} = C \left( \frac{\rho_t}{\rho_s} \right)^2$$

*Equation 6*

where:  $E$  = elastic modulus,  $\rho$  = density, subscript  $l$  = of lattice, subscript  $s$  = of solid,  $C$  = correction factor

To obtain the correction factor for yield strength, Equation 7 was used:

$$\frac{\sigma_Y}{\sigma_Y} = C \left( \frac{\rho_t}{\rho_s} \right)^{3/2}$$

*Equation 7*

where:  $\sigma$  = stress,  $\rho$  = density, subscript  $Yl$  = yield strength for lattice, subscript  $Ys$  = yield strength for solid,  $C$  = correction factor

To obtain the correction factor for ultimate compressive strength (UCS), Equation 8 was used:

$$\frac{\sigma_U}{\sigma_U} = C \left( \frac{\rho_t}{\rho_s} \right)^{3/2}$$

*Equation 8*

where:  $\sigma$  = stress,  $\rho$  = density, subscript  $Ul$  = UCS for lattice, subscript  $Us$  = UCS for solid,  $C$  = correction factor.

All these equations can be simplified to:

$$\frac{X_t}{X_s} = C \left( \frac{\rho_t}{\rho_s} \right)^n$$

*Equation 9*

where:  $X$  = mechanical property,  $\rho$  = density, subscript  $l$  = lattice, subscript  $s$  = solid,  $C$  = correction factor,  $n$  = numerical power

To find the correction value,  $C$ , for an individual sample, the equation was rearranged to:

$$\frac{1}{C} = \frac{X_s}{X_l} \left( \frac{\rho_l}{\rho_s} \right)^n$$

*Equation 10*

To compare across data sets, an expected value of  $X_l$  was required, using the  $C$  value obtained for that data set, and the average density of the data set to be compared:

$$X_l = X_s C \left( \frac{\rho_l}{\rho_s} \right)^n$$

*Equation 11*

A correction factor was obtained for each result using the experimental value of mechanical property at its corresponding experimentally obtained density. This  $C$  value was then used to obtain theoretical values for mechanical properties, for a theoretical density, which was selected based on the average density. This allowed mechanical properties to be directly compared, as differences in density had been eliminated.

The values of  $n$  used were taken from Gibson and Ashby, where a value of  $3/2$  for  $Y_s$  and UCS, and a value of  $2$  for  $E$ . It is worth noting that Gibson and Ashby obtained these values for cellular solids that were not diamond structure lattices. Due to geometrical differences, it is possible that these values for  $n$  are not the most appropriate when considering effects of geometry on mechanical properties. However, obtaining more appropriate values for  $n$  was beyond the scope of this project, therefore these are the values that were used throughout this work.

### *3.8.3 Anisotropy determination*

When comparing anisotropy in mechanical properties, a ratio can be obtained from:

$$A = \sqrt{\left( \frac{P_{\parallel} - P_{\perp}}{P_{\parallel}} \right)^2}$$

*Equation 12*

where:  $P$  = mechanical property, subscript // = part tested parallel to its build direction, subscript  $\perp$  = part tested perpendicular to its build direction

The closer the value is to 0, the more isotropic the structure, and the closer the value is to 1, the more the structure could be considered anisotropic.

### 3.8.4 Microscopy

Samples were mounted in conductive Bakelite by hot mounting for two minutes and being water cooled for 4 minutes, at a temperature of 150°C and a pressure of 290bar. Under these conditions, the microstructure of titanium would not be affected, however, it became apparent that the pressure of the hot mounting acted to deform some struts in some samples. It is therefore recommended that in future work, cold mounting should be used to avoid this issue.

Following mounting, the samples were ground and polished using graded polishing plates and polishing suspensions obtained from Struers. The method involved grinding with MD Plano 600 with water for 10 minutes, followed by MD Plano 1200 with water for 6 minutes, MD Largo with 9 $\mu$ m Diamet solution for 10 minutes, with a final polish using MD Chem with colloidal silica for 6 minutes.

For optical microscopy, the polarised light function was used on the optical microscope to see the microstructure. For SEM work, the ground and polished samples were sent to GKN to be etched with HF, and returned to The University of Sheffield for microstructural analysis.

## 3.9 Chemical composition

Some lattices were sent to AMG Analytical Services, Rotherham, for compositional analysis. Compositions were obtained for some builds using the XRF FETI technique to obtain compositions of Ti, Al, V and Fe, and the LECO<sup>®</sup> technique to obtain composition values of C, N and O.

XRF emits a beam of X-rays at a wide range of wavelengths through the sample, and the intensity of the output radiation is detected. This produces a characteristic pattern, unique to the constituent element.

LECO<sup>®</sup> elemental analysers introduce elements to the sample, and utilise heating methods to cause the elements within the sample to react, and become gaseous. An infrared detector is utilised for the detection of C and O in the sample, and a thermal conductivity cell is utilised to determine N content.

## Chapter 4 Results and Discussion

This chapter provides the results and discusses possible interpretations from the data.

This section begins with an overview of the issues encountered regarding manufacture of the lattices.

Following this, a discussion of the minimum number of unit cells required to ensure reliable mechanical properties from mechanical property data, is displayed with microstructural images.

As discussed in the literature review, previous research has indicated anisotropy in additively manufactured parts, therefore this was investigated for lattice structures. The investigation considered anisotropy in mechanical properties by comparing mechanical property data obtained from two designs of diamond lattice, built in differing orientations.

After this, trials into the effect of two major alterations to the as-built diamond lattice structure were conducted. Some lattices underwent a HIP procedure, others used an etchant to reduce the surface roughness of the lattices, and some had both post processes applied. These were compared to as-built lattices through mechanical properties obtained by compression testing, and by microstructural analysis.

The final section considers the fatigue life of the lattices, and aims to draw stress cycle and strain cycle curves to find a fatigue limit. Following this, further investigation considers whether HIP treatment has any effect on the life compared to as-built lattices.

### 4.1 Building EBM lattices

When building parts directly attached to the steel start plate, leeching of the steel alloy into the base of the part can occur [207]. For solids, this layer can be ground and polished away, however for lattices, this is not possible. In addition to this, due to the relatively small size of lattices, a 50 $\mu$ m layer of steel contaminated Ti6Al4V could play a detrimental role to the mechanical properties of the lattices. To avoid this, the lattices were built “floating”, where the lattices were not built directly onto the build plate, and had a number of sintered, un-melted powder layers between the lattice and the build plate. It is known that building on powder leads to negative surfaces, which leads to difficulties with drawing heat away from the part (see Figure 36). For solids that are built floating, the solution to this is the use of supports, which link the part to the build plate, and act as a heat sink. Supports that attach to solids are easily removed with the turning moment of the support, where twisting the support leads to separation from the solid easily. In the case of lattices, due to the similar size of the supports to the struts, it is difficult to remove supports from the lattice without damaging the struts, as the supports break preferentially at the base plate, and remain attached to the lattices (Figure 44, page 77).

When building the lattices at The University of Sheffield, building floating lattices alone led to failed builds. The corner struts of the lattices at the outer edges would swell, causing the build to fail as the rake contacted with these raised, protruding struts, damaging the rake and sweeping the build across the layer. From the experience of colleagues who have made lattices, putting solid models in the build near these problem areas led to more successful builds (these were known as “dummy solids” and are seen in the build layout). While the exact mechanism is currently unknown, reasons for this can be speculated.

When more models are in the build, it takes more time to complete the build, therefore there is more time between layers for the parts to cool before the next layer. This can reduce the residual heat in that layer, before the building of the next layer. While the exact algorithms of the EBM system are, at the time of writing, commercially sensitive, it was noted that with longer build times, the electron beam compensated for this with an increased power on the beam, therefore it is possible that this theory of “a greater time to cool” is not accurate.

Another idea is that the presence of the solids acts as a heat sink. Even though the solids are not directly attached to the lattices, they are in close proximity. As the heat radiates from the melted lattice struts and across the sintered powder, solid parts will have a better conductivity than the sintered powder, in order to draw the heat down to the cooling base plate. A counter argument to this is that the lattices are actually closer to the base plate despite the powder layer (ten 50  $\mu\text{m}$  build layers, totalling 0.5mm of sintered powder), than the solid parts are to the lattices (more than 5mm between parts). As well as this, upon closer inspection of the CAD files, the solid models were also floating, meaning the solids themselves would have a heat sink problem, and therefore if this mechanism were correct, none of the builds should have succeeded.

A final idea is that the algorithm of the EBM means that when the electron beam determines it is reaching a corner or an edge, the beam speeds up to “get around” the corner more quickly, to ensure a constant speed when building the part. To compensate for the shorter dwell time, the beam puts more power in to attempt to keep a homogenous heat input. For solids, this is necessary for a homogeneous microstructure to ensure a steady cooling rate as heat distributes throughout the part easily. For lattices, which are built as independent points, the increased speed does not affect the cooling rate, whereas the increased beam power leads to an overload of heat which cannot be distributed away quickly enough. By putting dummy solids at the corners and edges, the beam does not consider the corners and edges of lattices to require the increased heat input, and therefore the solids get the increase in heat, as the programme commands, due to the decreased dwell time. Unfortunately, as the exact details of the algorithms are unknown, this cannot be confirmed. For future work, a thermal camera could be set up in the build chamber to monitor the actual heat input to the part and compare to the beam power and speed directed from the algorithm.

## 4.2 Minimum number of unit cells required for reliable mechanical properties

When considering tests on lattices in the literature, a six unit cell minimum appeared to have been established, originating from a study on metal foams. This had not been shown to apply to lattices, therefore, it was decided that this should be tested experimentally. A set of lattices between 2-10 unit cells in side length was produced, and these were compression tested to find their mechanical properties. A convergence was expected, and this value would be the minimum number of unit cells required for lattices to give reliable mechanical properties.

For this, SE1 and SE2 were utilised, each build containing one set of lattices from 2-10 unit cells. Following data collection, SE3 and SE4 were manufactured at GKN, who built four sets of 2-9 unit celled lattices, and these were delivered to The University of Sheffield for testing.

The results of these tests are given on the following pages.

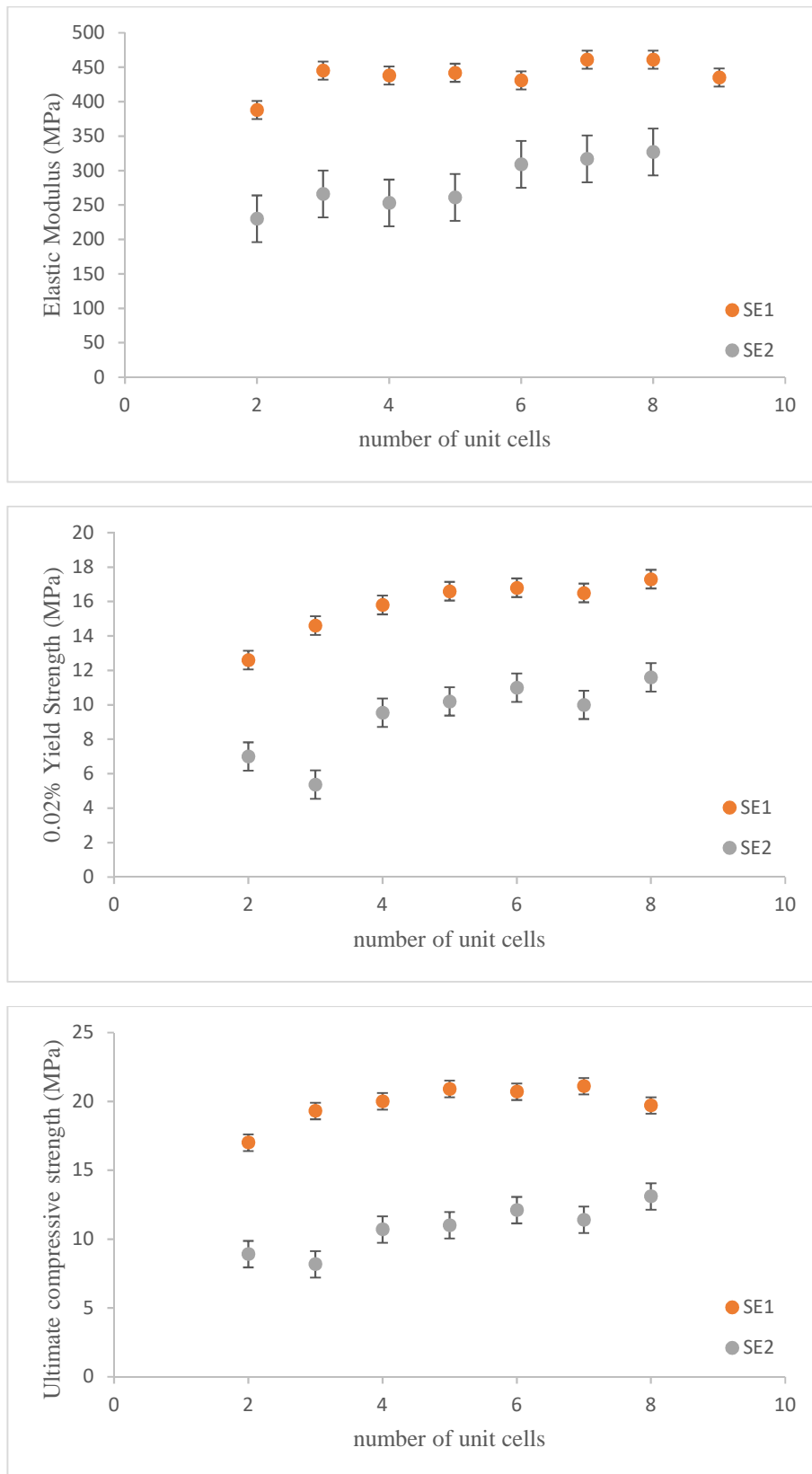


Figure 54: Graphs showing various mechanical properties against number of unit cells, n, for SE1 and SE2 builds. a) Elastic modulus, b) 0.02 Yield strength, c) Ultimate compressive strength, UCS.

During the tests, the 9 and 10 unit celled lattices exceeded the safe load capacity of the machine, and the tests for these two lattice sizes were suspended. As limited data was collected for these lattices, these two unit cell sizes are not included in the graphs.

Considering the SE1 and SE2 build data, there is a large difference between the mechanical properties across the sets. It was considered that the relative density could be causing this difference. The SE1 data set had a relative density of 9.4%, corresponding to a porosity of 90.6%, and the SE2 data set had a relative density of 10.7%, corresponding to a porosity of 89.3%. Intuitively, a lower porosity and higher density should correspond to a higher strength. This was not the case here, with SE1 producing higher strength lattices despite a lower density.

It is known that in titanium alloys the oxygen content should be minimised in order to preserve the desired mechanical properties, as discussed in section 2.1.4. The Ti6Al4V powder used in the production of these parts was out of specification, meaning the oxygen content was over 0.2wt%, with the SE2 build manufactured a month after SE1. Therefore the 2 unit cell lattice from each SE1 and SE2 build were sent for chemical analysis (Table 5).

Table 5: Chemical composition for size effect builds SE1 and SE2 (wt. %). Accuracy in Appendix 1

Build	Ti	Al	V	O	Fe	N	C
SE1	balance	5.8	4.1	0.23	0.2	0.03	0.03
SE2	balance	6.0	3.9	0.35	0.3	0.05	0.05

Higher oxygen content leads to higher strength and lower ductility. The oxygen content of SE1 was 0.234%, and SE2 was 0.352%. The samples with higher strength were not the same samples that had higher oxygen content, therefore it was decided that this was probably not the source of the difference.

The method of manufacture was considered as a potential source of the difference. Build SE1 was manufactured on an altered S12 machine, where the outer casing was of the S series; however, the inner components had been updated and replaced with wear and tear. The build settings used the standard Arcam 70 micron themes for preheat, nett and melt. The SE2 build was completed on an A2 machine, with an altered preheat theme. The theme was a steel preheat, which was entered in error, and although the exact temperature of the preheat is unknown, it would be a lower temperature than the standard Ti6Al4V preheat theme (~800°C) due to the lower melting point of steel (~1500°C) compared to titanium (~1700°C). The nett and melt settings were the Arcam standard 70 micron themes for Ti6Al4V.

To explore the possibility that these differences caused the mechanical property difference, microstructural images were obtained from optical microscopy using polarised light, and shown in Figure 55, where all images on the left are taken from the SE1 and all images on the right are taken from SE2.

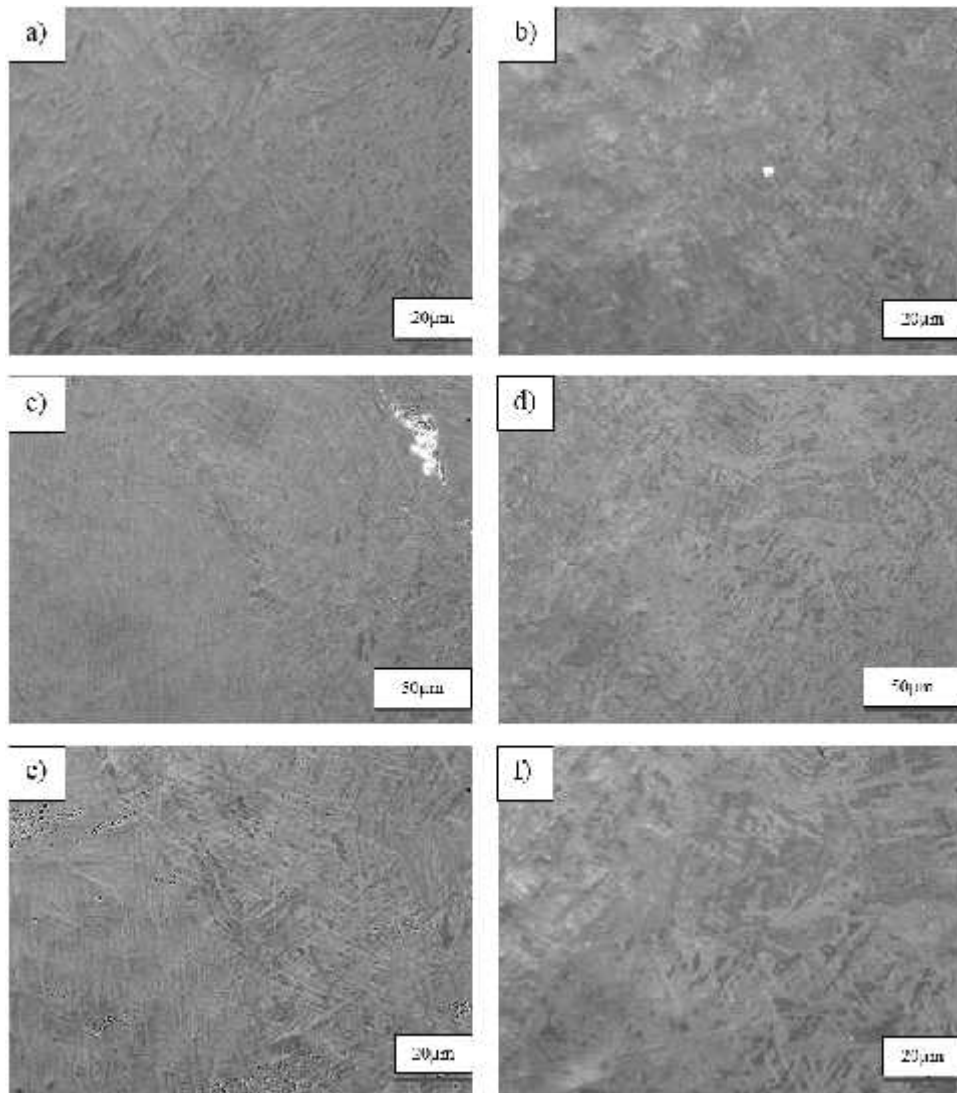


Figure 55: Optical microscopy from the top of the lattices, from the same areas of builds SE1 and SE2, where: a, c, e) build SE1, and b, d f) build SE2

It can be seen that the SE1 microstructure has a more disordered appearance than the SE2, which has more organised areas of a basket weave structure. Considering that build SE1 had the standard Ti6Al4V preheat with the standard melt, whereas SE2 had a lower temperature preheat, followed by the standard Ti6Al4V melt, SE2 would be subjected to a steeper temperature gradient between preheat and melt. This would lead to more extreme temperature cycles throughout the build, compared to the standard settings of SE1. This could explain the differences between microstructural images.

Looking at the individual data sets, it is difficult to draw an absolute conclusion for the minimum number of unit cells required to ensure reliable mechanical properties, therefore builds SE3 and SE4 were manufactured and tested, with results in Figure 56.

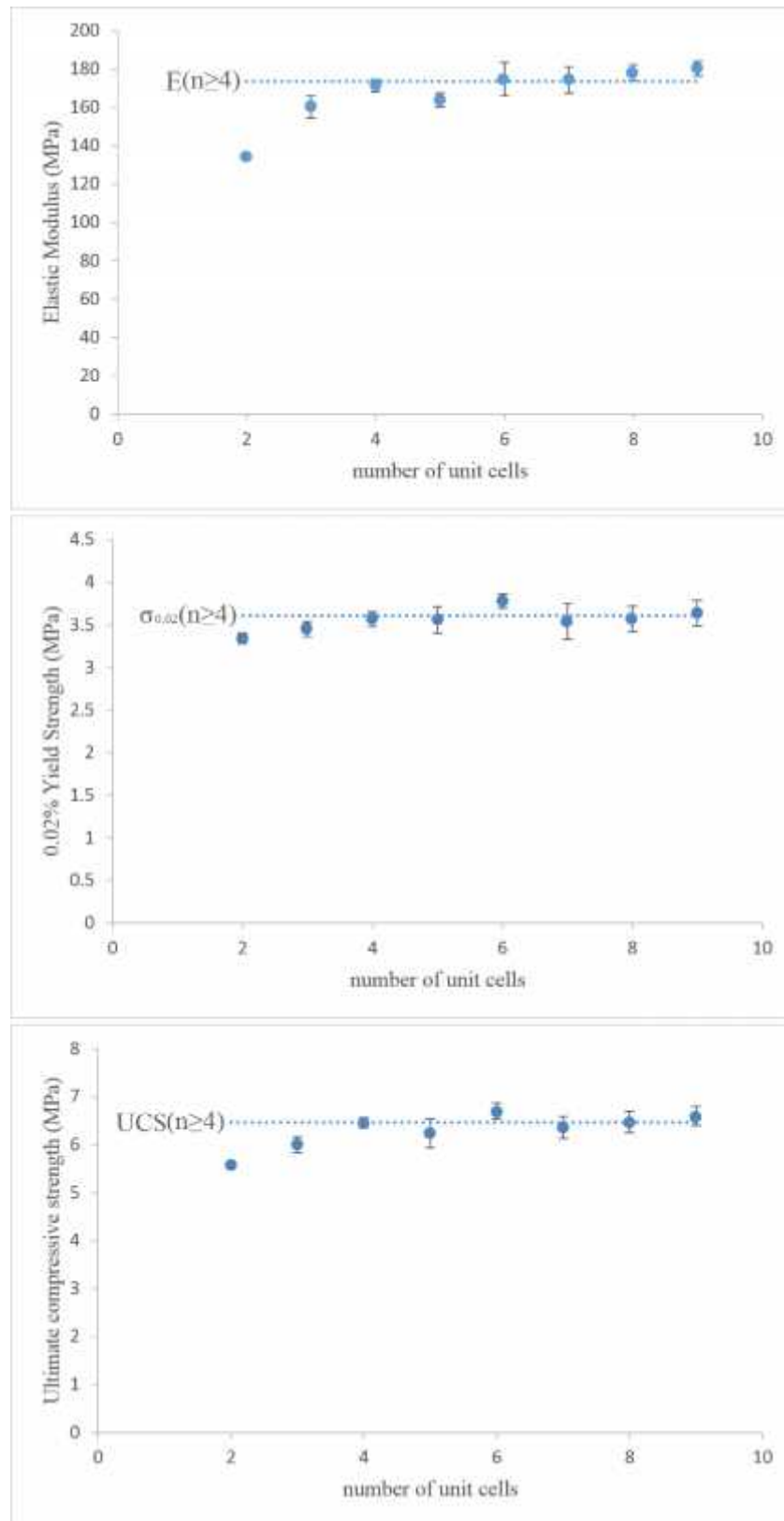


Figure 56: Graphs showing various mechanical properties against number of unit cells,  $n$ , with a straight line through average of  $n \geq 4$ . a) Elastic modulus  $E = 174$  MPa at  $n = 4$ , b) 0.02 Yield strength  $\sigma_{0.02} = 3.61$  MPa at  $n = 4$ , c) Ultimate compressive strength,  $UCS = 6.48$  MPa at  $n = 4$

These results show a clearer picture, with the data points converging on a horizontal line. These results indicate that the 6 unit cell minimum recommended by Andrews et al. would be suitable, however the data shows that samples of 4 unit cells could give reliable mechanical properties.

This difference between lattices and foams could come from the regular structure of lattices compared to the randomised nature of foams. Unlike foams, there is no need for the larger number of unit cells to account for random pore size, shape or position. Increasing the number of unit cells in lattices does nothing to statistically reduce the size effect of these randomisations found in foams, as the randomness does not exist in lattices. Saying that, there is a factor affecting the properties, perhaps a constraint of neighbouring cells, otherwise there should be no reason why 2 unit cells could not be used.

The EBM method produces struts with high surface roughness as a feature of the process. One source of surface roughness comes from the powder distribution when the electron beam melts the strut cross sectional area, and un-melted powder particles that become sintered to the lattice structure (see 2.3.3). Due to the powder size, the rough strut surface causes an inherent  $\pm 50\mu\text{m}$  error when measuring lattice size, therefore it is logical that the surface roughness would have a greater effect on smaller lattices with unit cells in the mm range, than the same unit cells in lattices in the cm range.

The parts of the lattice in contact with the platens in the test play a part in the physical stability of the lattice. For the 2 unit celled lattice, there were 11 contact points on each surface, for 3 unit cells, 23 contact points, and for 4 unit cells, 39 contact points, with the number of contact points increasing proportionally to the number of unit cells. If the lattice is not stable when the force is applied, the force will be unevenly distributed across the lattice area leading to premature failure as some struts take a greater load than others. The surface area as a whole is accounted for in the calculation of stress, and the instability of the lattices is accounted for in the compliance of the machine, however any uneven distribution of force, or damage caused by the force during this time is not.

With a greater number of contact points comes greater stability, and any defects in random surface struts matter less when there are more surface struts with fewer defects. Therefore, the effect could be that the strut surface roughness affects the points of contact, by giving a  $\pm 50\mu\text{m}$  variation across the struts. In order to negate this surface effect, a minimum of 39 points of contact are required, which here equates to a  $4\times 4\times 4$  unit cell.

The question of how much influence the surface roughness has on the mechanical properties is discussed later, however due to these findings, the lattices tested all had a minimum of four unit cells in every direction.

### 4.3 Effect of build direction on mechanical properties of asymmetrical lattices

Based on the growing body of work supporting anisotropy in the structure, and properties, of AM parts, an investigation into whether lattices were influenced by build direction as strongly as solid parts was conducted. 18 lattices in three different orientations were built over three consecutive builds. The models were an elongated diamond structure, of 36mm×36mm×72mm, from AI builds 1, 2 and 3. All lattices were tested in the “tallest” direction, under a strain rate of  $10^{-3} \text{ s}^{-1}$ .

Following manufacture of the anisotropic lattices (for build orientations of X, Y and Z lattices given on page 74), it was noticed that the Z lattices (which were tested in their build direction) were 2mm wider in the directions perpendicular to the build direction, and 0.7mm shorter in the build direction. This led to a slightly more porous structure on average for the Z lattices, then the X and Y lattices (which were tested perpendicular to their build directions, due to their orientation within the build). Therefore, within the data analysis, a density correction was applied to all the asymmetrical lattice data (section 3.8.2). As a basis, standard diamond structure lattices were also tested in the build direction and perpendicular to the build direction, to compare to the asymmetrical data.

Table 6: Mean values (with standard deviation) of elastic modulus, 0.02% yield strength and ultimate compressive strength for asymmetric lattices, and standard diamond lattices

<b>Lattice</b>	<b>Orientation tested</b>	<b>Elastic Modulus [MPa]</b>	<b>0.02% Yield Strength [MPa]</b>	<b>Ultimate Compressive Strength [MPa]</b>
Asymmetric	X	734.6 (35.1)	11.9 (0.5)	16.9 (0.8)
	Y	720.4 (23.4)	12.0 (0.7)	16.5 (0.8)
	Z	734.8 (14.1)	12.0 (0.8)	16.3 (0.5)
Standard diamond	⊥	173.7 (15.3)	6.2 (0.3)	6.9 (0.4)
	∥	181.0 (3.46)	5.5 (1.1)	7.1 (0.3)

Considering the asymmetrical lattices, the mechanical properties are all very similar across the given orientations, with only the elastic modulus for the Y lattices having a significantly different value. Considering the error, all values lie within one standard deviation of each other.

For the standard diamond lattice tests, those tested parallel to their build direction have a higher elastic modulus and UCS, but a lower yield strength than the lattices tested perpendicular to their build direction. Again, considering the calculated errors, the data lies within one standard deviation of each other.

Therefore, it can be said that there is no substantial difference in mechanical properties in the samples examined here, whether these lattice structures are tested parallel or perpendicular to the build direction.

Taken at face value, the asymmetrical lattices are at least twice as strong as the standard diamond lattices. Making a direct comparison, however, between the mechanical properties of the standard diamond lattices and the asymmetrical lattice is difficult for a number of reasons. Although the computational design of the asymmetrical lattices began with the original 6 unit cell diamond structure, the asymmetrical lattices are clearly of a different geometry. The six unit cells occupy a larger volume, by keeping the x and y lengths the same, but doubling the length in z. This means the lattices contain longer struts, with different angles than their standard counterparts. As well as this, due to the translation of an stl file to a manufactured part, the actual density of the parts post build differed slightly. The average porosity value for asymmetrical lattices was 90.9%, and for the standard diamond structure lattices 91.4%. This gave the actual percentage of metal contained within the lattice to be 9.1% and 8.6% respectively. This seems like a minimal difference, but translates to an almost 9.5% increase of metal in the asymmetrical compared to the standard diamond structure lattice. This difference in density along with the aforementioned geometry difference are likely to be major factors behind the large differences in mechanical properties observed.

The main argument for anisotropy exists in the literature of Ti6Al4V solids, where columnar structures have been demonstrated (see 2.2.3). Recalling one such study, in 2013, Antonysamy et al. discussed coarse, columnar -grain growth in the build direction of EBM Ti6Al4V solid bars [89]. Within this paper, EBSD maps were generated, which showed different microstructures at the edges compared to the centre of the bars.

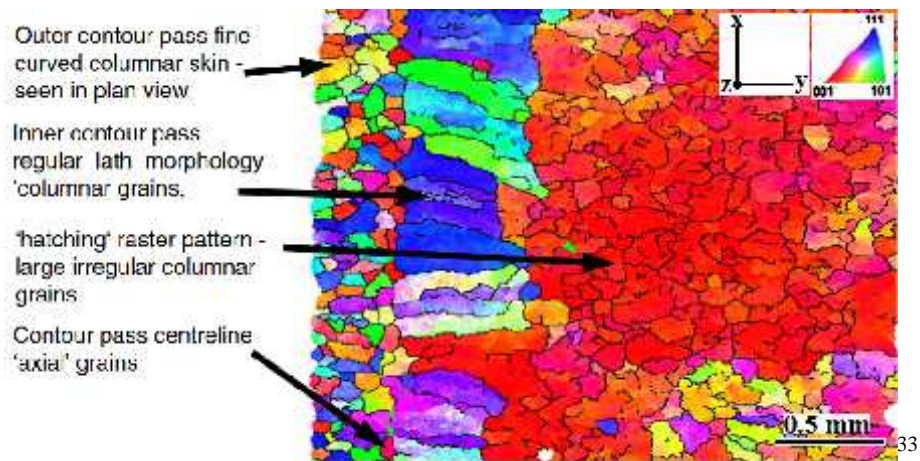


Figure 57: Textural differences depending on distance from edge of the part. Build direction is out of the page

Considering the microstructural differences here are explained by the use of a contour and hatch setting in the Arcam, it is possible that the lattice struts are not thick enough to produce the columnar structure common in AM Ti6Al4V parts. The columnar structure in AM Ti6Al4V solids arises from the highly directional heat flow, parallel to the build direction. As the lattice struts are angled, and not in line with the build direction, it is possible that the heat flow within the lattices does not act to produce the characteristic columnar grain structure. Considering Figure 57, it is possible that the microstructure of the “skin” described in the work of Antonysamy et al. is the microstructure of the entire lattice strut in this work.

To investigate whether this lack of columnar structure is a viable theory, Table 7 compares the anisotropy of the mechanical properties from other lattice work. This was measured using a ratio of the properties,  $P$ , obtained when testing perpendicular ( $\perp$ ) and parallel ( $\parallel$ ) to the build direction, as denoted in Equation 12, page 93. The closer the value of anisotropy is to 1, the more the structure could be considered anisotropic, with values close to 0 indicating isotropic properties.

In Table 7, the calculated anisotropy values obtained from comparing perpendicular and parallel tests are given. The table contains the comparison of the standard diamond lattices, and the asymmetrical diamond lattices from the results obtained in this work. To relate to the wider literature, anisotropy values have been obtained for two other studies on diamond lattices, where results included a compression test on lattices perpendicular and parallel to the build direction. Although these studies did not calculate anisotropy in the same way as Equation 12, the calculation has been applied to their data.

<sup>33</sup> Fig.4d, © 2013 .Antonysamy, Meyer, Prangnell. Originally published in Materials Characterization, reproduced under CC BY 3.0 license. Available from: DOI: 10.1016/J.MATCHAR.2013.07.012

Table 7: the anisotropy in various properties for additively manufactured diamond lattices from this work and the literature (Wauthle et al. 2015 and Heintl et al. 2008)

Lattice and method of manufacture	Anisotropy in property			Source
	Elastic Modulus	Yield Strength	First compressive maxima	
Asymmetric Diamond EBM	0.01	0.0003	0.03	This work
Diamond EBM	0.04	0.13	0.03	
Diamond EBM	0.44	0.27	0.28	Heintl et al. 2008
Diamond SLM	0.03	0.01	0.08	Wauthle et al. 2015

Using Equation 12, it can be said that the closer the value of anisotropy is to 1, the more the structure could be considered anisotropic. In this work, the values of anisotropy are never more than 0.13, which would suggest a very weak argument for the structure having anisotropy.

This is interesting, as, by definition, the HCP structure of titanium, means the + alloy leans towards anisotropy (see 2.1.4 Ti6Al4V). With the added effects of the layer by layer AM building process, anisotropy would be expected, as has been recorded in the literature (see 2.2.3 Influence of processing on the properties of AM parts).

These findings of no anisotropy are supported by the data from Wauthle et al., where the data for diamond SLM lattices tested parallel and perpendicular to their build direction have mechanical properties that are very similar.

This does not agree with the results of Heintl et al., whose findings for diamond EBM lattices suggest that there is a large anisotropy.

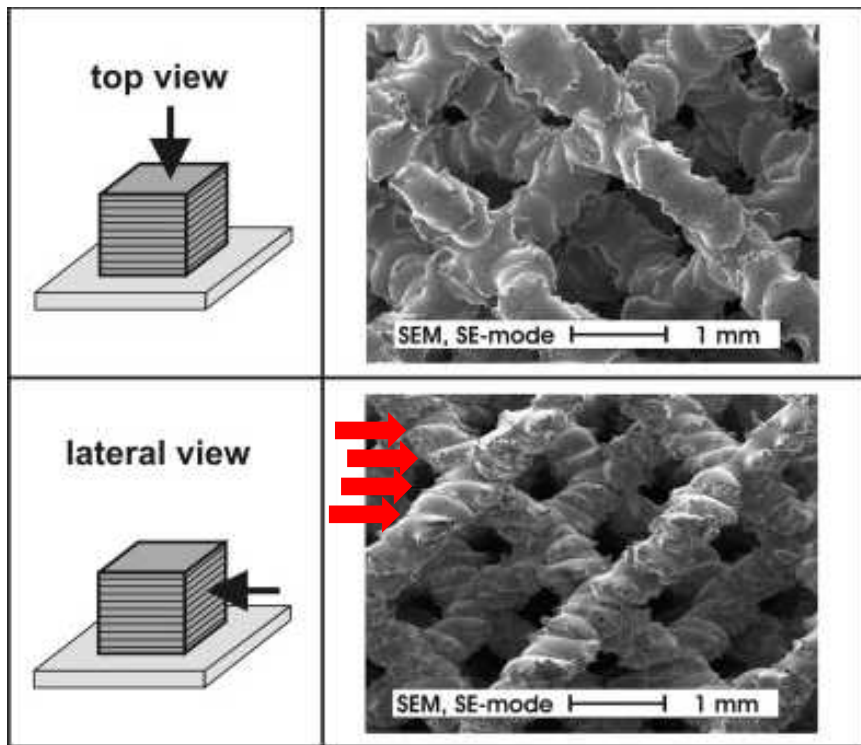
There are a few speculations as to why this might be the case. Since Heintl et al.'s work was published in 2008, a great many changes have been implemented by Arcam to the equipment to resolve various issues. The machine used in Heintl's study was an S series machine, with the related software. The software used in this study is that specified for the next generation of machines, the A series, although at the time of writing, Arcam EBM machines are currently in the Q series.

Other than the evolution in technology, the specific difference between Heintl's work and this study is the layer thickness. The Heintl paper states that the samples were fabricated using a nominal layer thickness of 100µm. As discussed in section 2.2.2 on

page 27, layer thickness is a setting which can significantly change the time taken to complete a build, with all the knock on effects that arise from this.

With larger layer thicknesses, the microstructure will be affected. A higher layer thickness means a longer dwell time at each melt point. A higher power is recommended to try to combat this, but with higher powers other issues arise with the inability for heat to dissipate. The only solution is time, however the longer it takes for the next layer to get underway, the more solidification will be occurring. This means each layer may not be sufficiently bonded to the previous layer, as the melt lies on top of the cooling solid, as opposed to the melt integrating with a cooling melt. This could be an additional potential cause of anisotropy in the part. This would be due to the inherent weakness in the direction perpendicular to the build, caused by the stacking effect in the build direction of each build layer, as opposed to the successful melting of the layers, solidifying into a fully bonded structure.

Current standard A series themes used in this study, provide layer thicknesses of 50 $\mu$ m or 70 $\mu$ m. If surface finish is a priority, 50 $\mu$ m layer thickness is recommended as less power is input into the melt pools, to produce a “tighter” melt. 70 $\mu$ m is used when time is of higher importance, where the finished parts will undergo a post processing step to improve the surface finish. A 70 $\mu$ m layer is more likely to have areas of unmelted powder, due to stacking and settling of powder particles during the rake pass, which may not be adequately melted. This is particularly true for lattices, where each lattice layer is melted in a spot pattern, as opposed to the sweeping beam pass applied in solid parts. To avoid areas of unmelted powder, a higher beam power is applied for 70 $\mu$ m themes, otherwise a 50 $\mu$ m theme is recommended.



34

Figure 58: a) SEM image of top, and b) side of diamond lattice structure, used in the study by Heidl et al. [175]

In Figure 58b, the 100 $\mu$ m layers can be very clearly seen. This apparent stacking of layers suggests that the anisotropy in the material could arise here. The clear differences in surface due to step features and this may reflect a difference in microstructural fusion that could be a basis for increased anisotropy for lattices explored in the Heidl paper.

If true, this could suggest that when testing perpendicular to the build direction, the struts would be a source of weakness as forces accumulate to cause failure between the layers. This could lead to micro-cracking, which may not be perceived as sudden failure on the scale of the material as a whole. The mechanism of fracture testing parallel to the test direction would be different, as the load compresses the layers within the lattice struts.

In the case of the lattices in this study, mechanism of failure was when the struts fractured at the nodes. This was true for both parallel and perpendicular test directions. Although the Heidl paper does not specify fracture mechanism, the theory that thicker build layers lead to anisotropy could be supported if the perpendicular direction is weaker than the parallel. This was the case, with Heidl reporting a parallel 0.2 yield strength of 22 MPa, and a perpendicular 0.2 yield strength of 16.1 MPa ( $\pm 1.1$  and 0.4 MPa respectively).

<sup>34</sup> Reprinted from Acta Biomaterialia, 4, "Cellular Ti-6Al-4V structures with interconnected macro porosity for bone implants fabricated by selective electron beam melting", P. Heidl, L. Muller, C. Korner, R. F. Singer, A. Muller, p1536-1544, © 2008, with permission from Elsevier



If it is assumed that the measurements taken are reliable, and the authors took these measurement errors into account with their stated  $\pm 0.4\%$  error, this still gives lattice structures that are significantly more dense (81% porosity in the Heigl paper) than those presented in this work (91% porosity in this work). As discussed in section 2.2.3, EBM solids have displayed anisotropy, therefore if it is true that low porosity lattices are also anisotropic, and it is true that high porosity lattices are isotropic, that there is a transition point where lattices shift from anisotropy to isotropy. At some point, the behaviour becomes more dominated by the structure than by the microstructure, and this point may lie between 81-91% porosity.

In summary, the 100 $\mu\text{m}$  layer thickness is a plausible cause regarding the problems identified here. It is probable that anisotropy in lattices was seen when 100 $\mu\text{m}$  layer thickness was common, as in Heigl's case, and this may no longer be an issue with the lesser layer thickness achieved in the EBM, as in this case. As EBM has many features that mean heat treatments and post processes are not conducted, where settings exist to reduce porosity and avoid delamination, it is strongly recommended that these settings be used. Studies that occurred before these settings existed should be carefully considered when making comparisons with recent data.

## 4.4 Post processing lattice modification

This section discusses the surface alteration of lattices through use of an etchant, and how this translates to changes in mechanical properties. Initially, a set of lattices was etched at different times to determine at which point surface improvement becomes detrimental surface degradation. From this, a set of as-built lattices and a set of lattices that had undergone a HIP post process was etched and their mechanical properties obtained.

### *4.4.1 Determination of ideal etching time*

The following images show the surfaces of as-built, un-etched lattices, followed by the surfaces of lattices which were submerged in etching agent for 4, 8, 12 and 16 minutes.

The set of lattices used for this initial stage were recovered from a failed build, to be used in this determination. A perfect set of lattices was produced for the mechanical tests discussed in 4.4.2. It was decided that as this test was for a surface determination, the lattices did not need to be as robust as lattices required for mechanical testing. Due to this less than perfect build, defects can be seen in some of the images, in the form of large pores. The problems arising from these are discussed further at the end of this section.

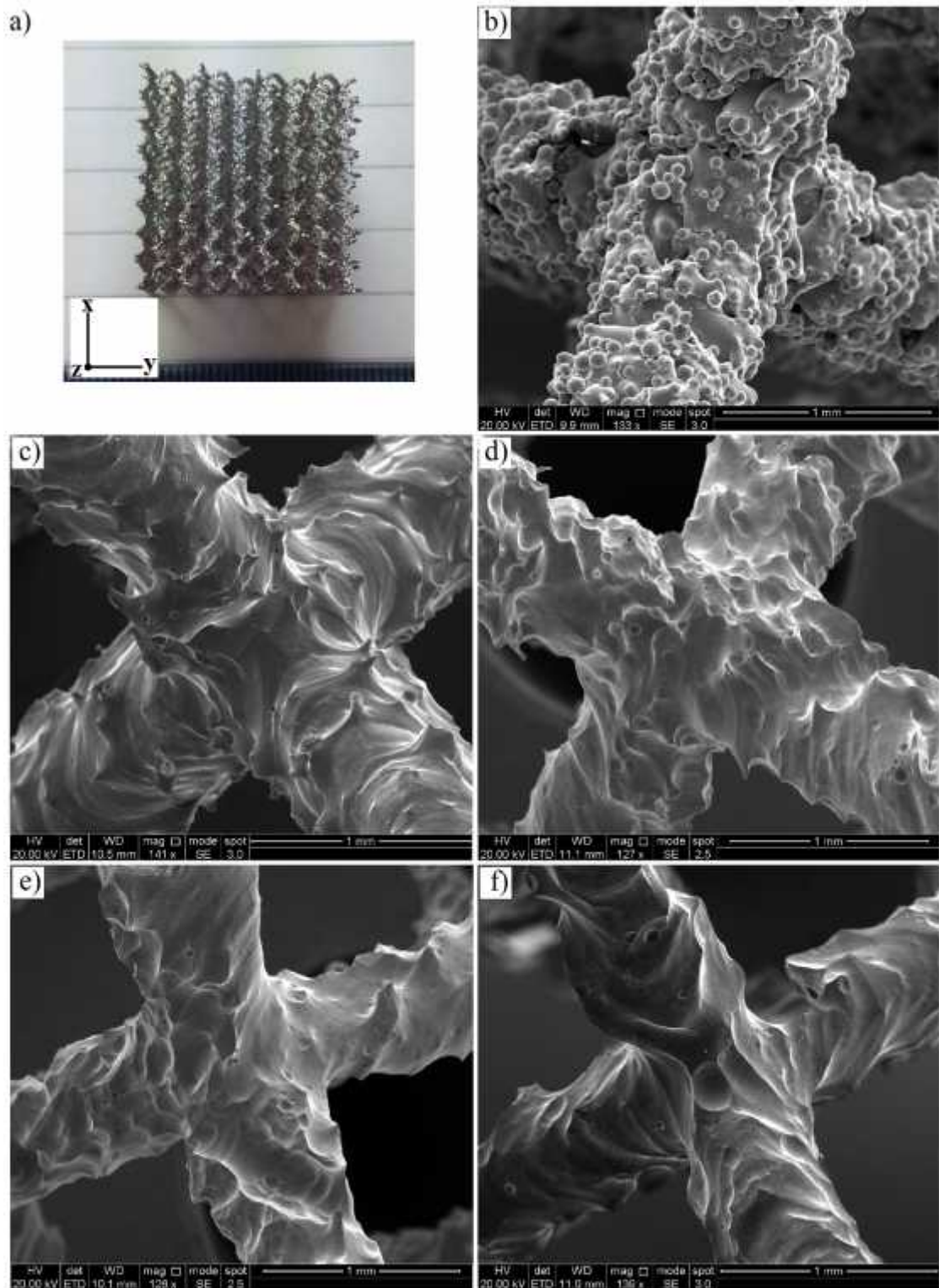


Figure 60: The build direction of all lattices is out of the plane.  
 a) 4×4×4 lattice etched for 10 minutes. SEM images of lattice surfaces:  
 b) As-built surface, un-etched lattice, average strut size 958 $\mu\text{m}$ ,  
 c) after 4 minutes in etching solution, average strut size 867 $\mu\text{m}$ ,  
 d) after 8 minutes in etching solution, average strut size 739 $\mu\text{m}$ ,  
 e) after 12 minutes in etching solution, average strut size 712 $\mu\text{m}$   
 f) after 16 minutes in etching solution, average strut size 625 $\mu\text{m}$

Figure 60b shows an un-etched, as-built lattice strut surface. Sintered powder particles that have merged with the melt are very clear, fused to a flake-like scale that makes up the surface of the lattice. Looking closely at this image, large pores can be seen on the strut to the left and right of centre. These pores were present due to a computational error at the design stage, which was fixed for the lattices made for compression tests in this section. Due to this, it must be considered that the severe erosion of the struts seen in the later images could be from the infiltration of the etchant into the lattices and eroding from the inside out. This could cause premature surface removal, and was considered when choosing a suitable etching time for the perfect lattices. To consider the effect of the etchant, we look at the images in Figure 60 in order:

c) shows the four minute etch, where the etching solution works to first remove large powder particles which are sintered to the structure. This leaves smaller sintered powder attached to the strut, and exposes fully melted, sharp features that jut out from the strut.

d) shows the 8 minute etch, where the complete removal of smaller powder particles leaves pits, however the sharp features seen after four minutes begin to soften, though they still remain. It was expected that the etching solution would erode these features to smoothen the struts, however this was only partially the case.

e) shows the surface at 12 minutes, where the general strut is appears smoother as the pores left by sintered powder are removed, however the mountainous features are becoming more defined, with the valleys between the features increasing in depth.

f) shows after 16 minutes, where these valleys become full crevices, with the etchant carving out sections of the strut. It appears, therefore, that different parts of the strut etch at different rates. This could be due to underlying features, such as grain boundaries, that etch along grains to reveal these features. It is also possible that there are certain features within the lattice microstructure that may be accentuated if certain crystal planes etch before others. Due to the undisclosed process, however, these suggestions remain speculation.

Taken at face value, the 12 minute etched lattices have the smoothest appearance, however a more scientific approach was needed. As “smoothness” is a qualitative measure, it was decided that it was important to remove the sharp features, whose valleys could act as areas of stress concentration, however not to the extent that erosion deepens the valleys to act as crack initiation sites.

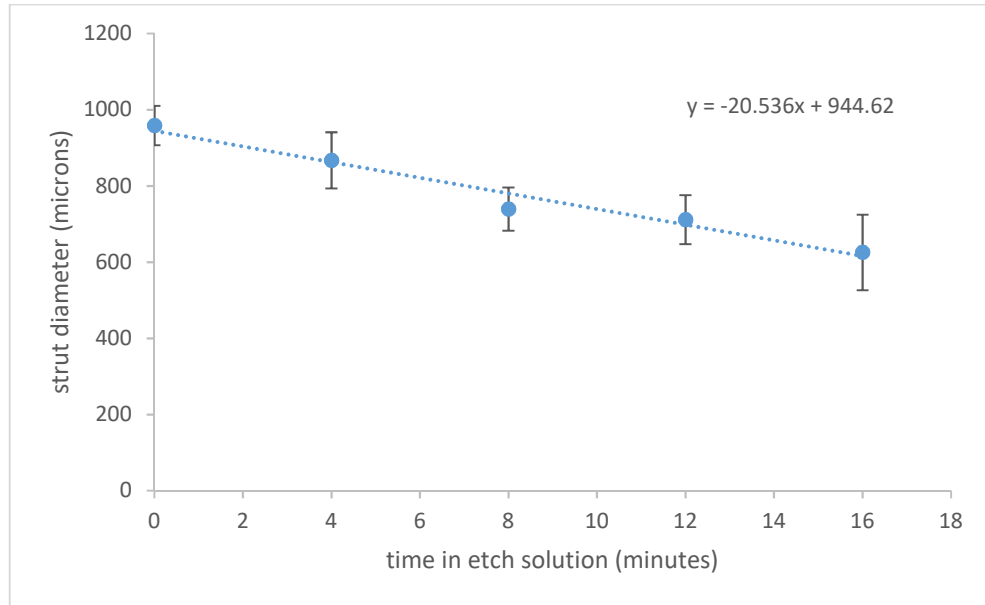


Figure 61: charts to determine the removal rate of material by etching agent through measuring diameter of the struts after etching

The lattice strut widths were measured using the SEM, and the average strut width determined for each etchant time, to determine the rate of removal. From this graph, it was determined that the lattice struts would need to be “scaled up” in order to end up with lattices of a similar strut size for testing.

Considering 1mm designed struts yielded an average 958 $\mu$ m strut, from these results, it was decided that diamond lattices of 1.25mm diameter struts would be designed and built. These would be etched for 10 minutes to remove 200 $\mu$ m of surface, in order to be tested alongside as-built lattices with designed 1mm struts. One such lattice can be seen in Figure 60a.

#### 4.4.2 Compression tests of etched lattices compared to as-built lattices

Four EBM samples of strut diameter  $n$  were produced alongside four EBM samples of strut diameter  $n+0.2n$ , at GKN Aerospace. The same lattice set was produced at The University of Sheffield to produce sixteen lattices in total. The Sheffield set of eight lattices underwent a HIP post process via a GKN Aerospace sub-contractor.

On their return, dimensions were taken of the eight  $n+0.2n$  EBM lattices, which were sent to a GKN Aerospace sub-contractor for etching for 10 minutes. Their physical properties were recorded and compared to the physical properties obtained prior to etching. The reduction effect of etching is given in Table 8<sup>35</sup>.

Table 8: Effect of etching on physical properties of the lattices

	Etch	HIP+etch
Reduction in strut width (mm)	0.25-0.26	0.25-0.26
Reduction in overall size (%)	4.2	3.9
Reduction in mass (%)	39.4	40.3

The strut widths decreased at the same proportion, which would be expected, however the overall lattice size decreased in different proportions.

The etched lattices all had more material removed than predicted with ~40% of the metal mass removed in both cases. Despite slightly less mass being removed, the etched lattices had a greater reduction in volume than the HIP+etch lattices.

In general, these differences are very small, so although important to note, may not be relevant.

The lattices were compression tested at a strain rate of  $10^{-3} \text{ s}^{-1}$  as is consistent with previous compression tests. The raw data is given over the following pages.

---

<sup>35</sup> Size reduction =  $1 - (\text{final volume} / \text{initial volume})$ , mass reduction =  $1 - (\text{final mass} / \text{initial mass})$

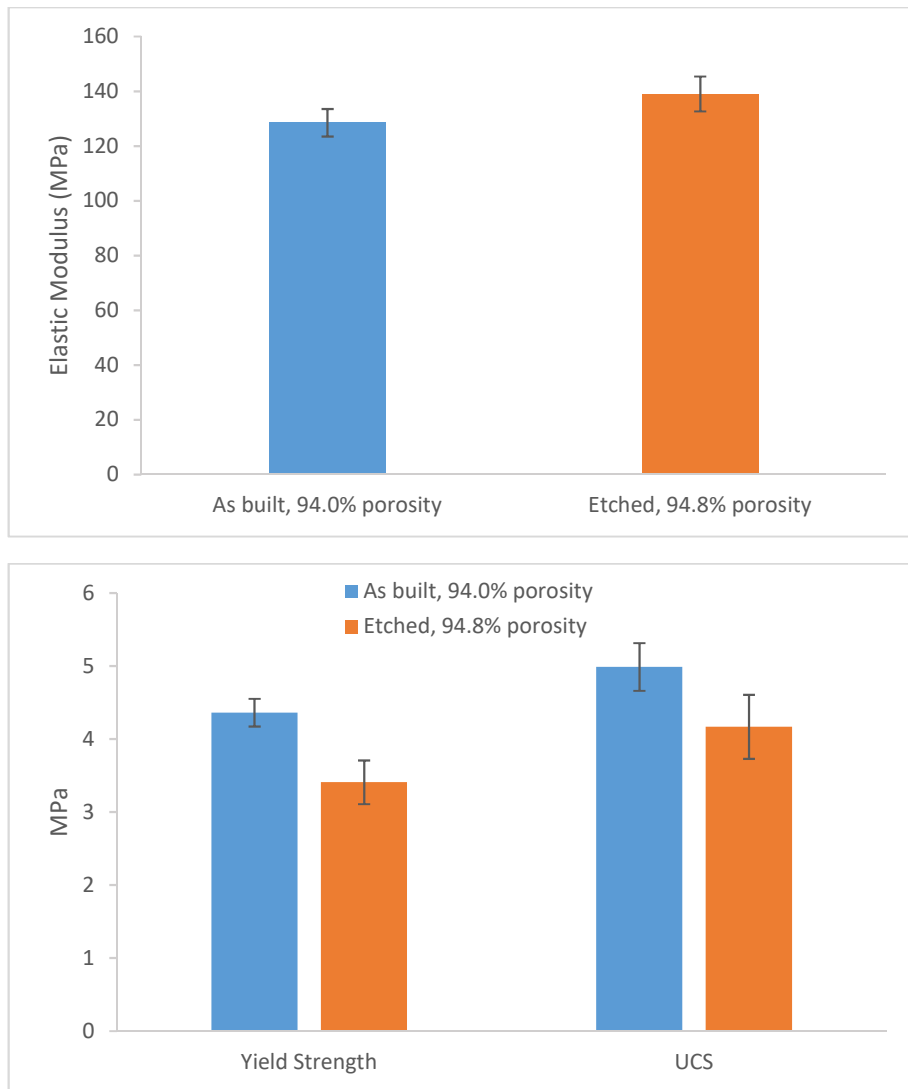


Figure 62: Average of mechanical properties obtained through compression testing for as built and etched lattices for a) Elastic modulus, and b) 0.02% offset Yield Strength and Ultimate Compressive Strength (UCS)

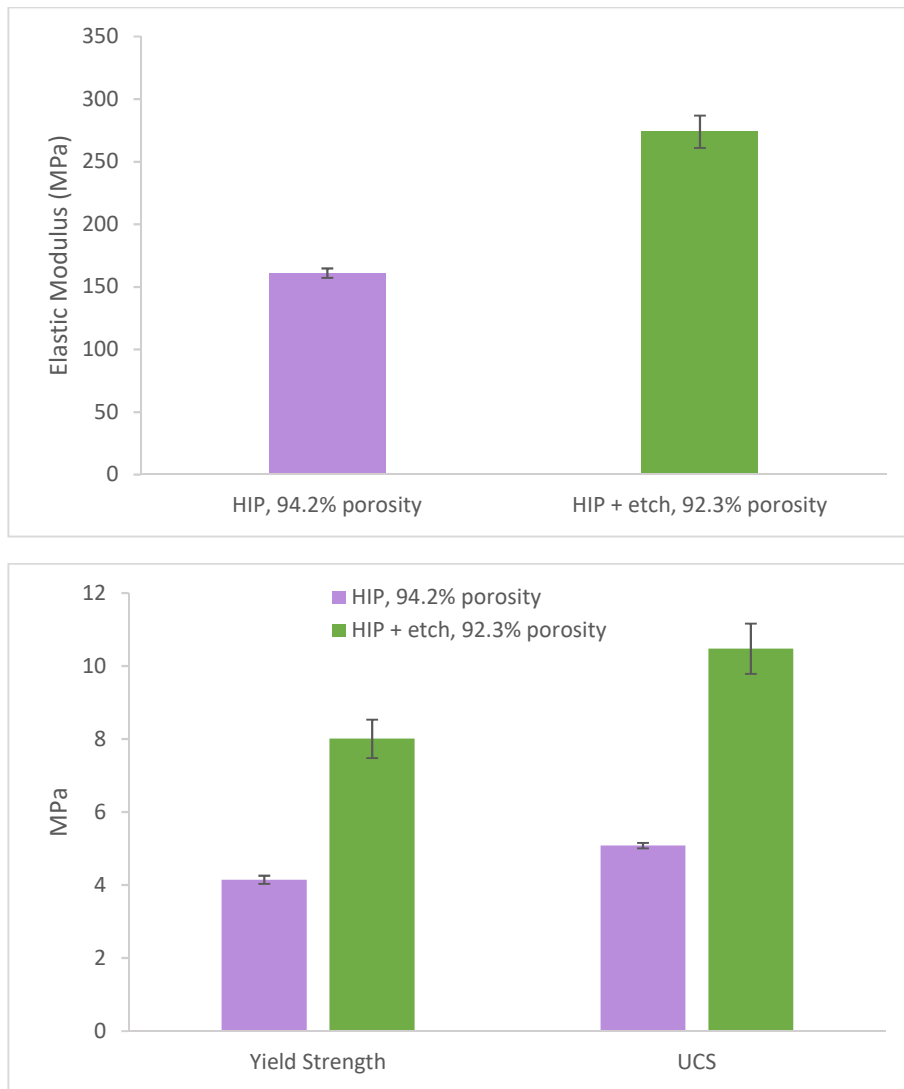


Figure 63: Average of mechanical properties obtained through compression testing for lattices having undergone HIP post process, and HIP lattices with an additional etching step, a) Elastic modulus, and b) 0.02% offset Yield Strength and Ultimate Compressive Strength (UCS)

It is clear that density plays a large role in the mechanical properties measured in the compression tests for all lattices.

Looking at the as-built and etched lattices in Figure 62, as would be expected, the etched lattices with a lower density of  $229 \text{ kg/m}^3$  have lower strengths than the as-built lattice with its higher density of  $266 \text{ kg/m}^3$ . These lattices have a porosity of 94.7% and 93.9% respectively, and with a reduction in metal content comes a reduction in strength.

The elastic modulus, however, appears to be higher for the etched lattice despite having the lower density. Taking a closer look, the error bars lead to an overlap in the data, therefore it is possible the elastic modulus is the same for both lattices, despite the etching step.

Considering the HIP and HIP+etch lattices in Figure 63, again, the lattices of lower density have lower strength, with the HIP lattices of  $225 \text{ kg/m}^3$  having a lower strength than the HIP+etch lattices of density  $340 \text{ kg/m}^3$ . These lattices have porosity of 94.2% and 92.3% respectively, with the higher metal content of the HIP+etch lattices leading to a higher strength.

The elastic modulus here is of particular interest. The results show that the HIP+etch has a much higher elastic modulus than the HIP lattice. This is different to the finding of the elastic modulus for as-built and etched lattices. As well as this, the error bars contain no overlap here, as the ~2% porosity difference in HIP and HIP+etch lattices leads to a greater gap in elastic modulus values, compared to the <1% porosity difference for the as-built and etched lattices. Considering the metallurgy, it would be expected that etching would have little to no effect on the elastic modulus, therefore this difference must be accounted for elsewhere.

Looking at the physical properties of the lattices, each lattice has a different density. As density has an effect on lattice properties, a correction factor was applied (see 3.8.1), and the results after the correction factor are given in the following charts. When using the Archimedes balance to determine density of solid EBM Ti6Al4V, the values fluctuated between  $4350 \text{ kg/m}^3$  and  $4415 \text{ kg/m}^3$ . Therefore a value of  $4400 \text{ kg/m}^3$  was used, as this value is similar to reported literature values of solid EBM Ti6Al4V as  $\sim 4400 \text{ kg/m}^3$  [208].

The average density across all lattice values was  $\sim 272 \text{ kg/m}^3$ , therefore the corrected values are for a lattice with a density of  $275 \text{ kg/m}^3$  for simplicity and continuity.

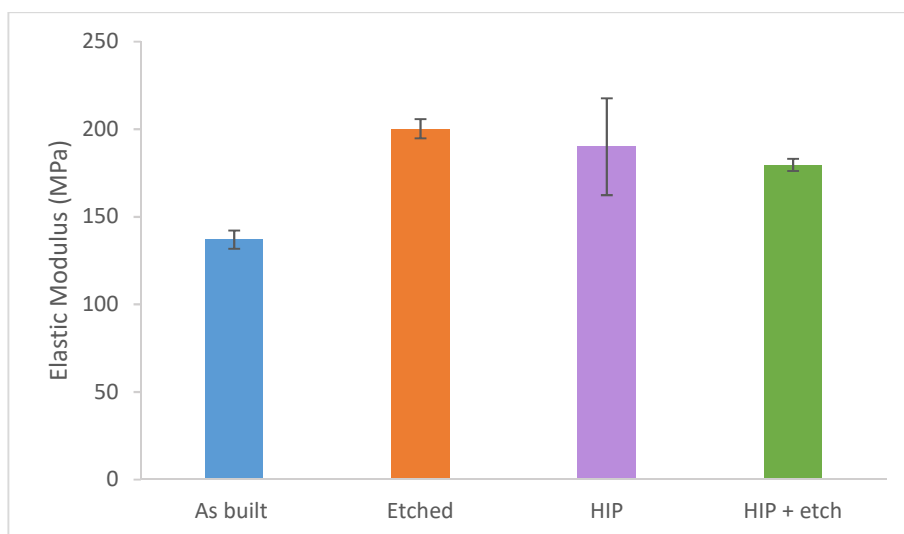


Figure 64: Average elastic modulus for all lattices, after correction applied for a density of  $275 \text{ kg/m}^3$ , translating to a porosity of 93.8%

When considering the effective elastic modulus of the structures, the as-built samples stand out as the most pliant, while the etched lattices are the least elastic. The HIP+etch samples lie somewhere in the middle, however the lattices with the HIP alone overlap both etched lattices. Therefore, the order from most compliant to most stiff could be considered to be: as-built, HIP+etch, then etched, with HIP lattices lying anywhere after the as-built lattices.

Despite the correction factor to account for the density differences, there is still a difference between the original samples and their etched counterparts. From a metallurgical point of view, the etchant should not alter the elastic modulus.

Recalling builds LM1 and LM2, the lattices to be etched were built with struts 25% thicker than those that would not be etched. This increase in strut width could lead to a difference in microstructure between the two lattices. Recalling the two different types of surface defects from Lhuissier et al. [77]: if the 1mm struts were mostly composed of the “skin” of sintered powder incorporated into the melt (“type 1” defects) whereas if the 1.25mm struts were mostly composed of a core solid metal, (bearing a closer resemblance to the “type 2” plate pile defects) these would have a different microstructure and different characteristics. This could explain the difference between the “As built” and “etched” lattices, however if this were the case, the HIP post process would act to give both lattices an identical microstructure prior to the etching. To further investigate this, microstructural images were required, as is discussed in the next section.

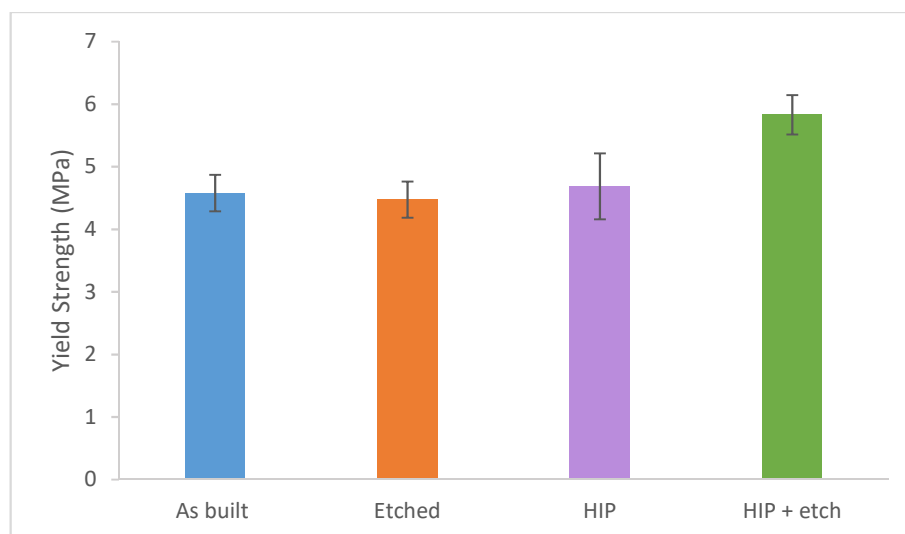


Figure 65: Average Yield Strength for all lattices, after correction applied for a density of  $275 \text{ kg/m}^3$ , translating to a porosity of 93.8%

Here there is a large overlap in the data, with the as-built, etched and HIP lattices having a similar yield strength (when considering the error). The HIP+etch lattices, however, display a larger yield strength out of the error range of the other lattices. Therefore, the order from highest to lowest yield strength could be considered to be HIP+etch, followed by as built, etched and HIP lattices.

This could arise from the HIP providing a preferable microstructure, however the effects of surface roughness could mask this. As surface roughness is improved with the etchant, the microstructure could then become the dominant factor with regards to mechanical properties, however microstructural images are required to confirm this.

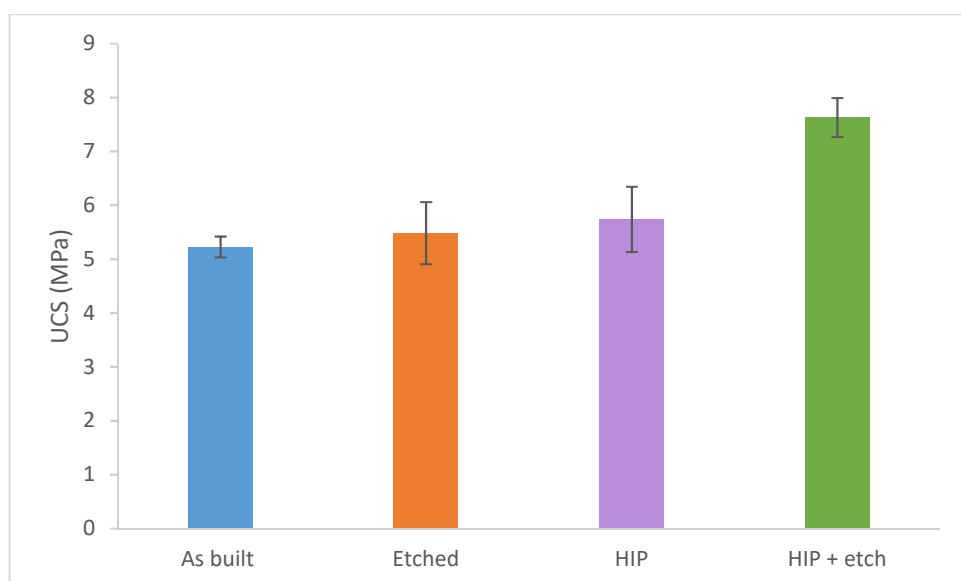


Figure 66: Average Ultimate Compressive Strength (UCS) for all lattices, after correction applied for a density of  $275 \text{ kg/m}^3$ , translating to a porosity of 93.8%

Like the yield strength, the as-built, etched, and HIP lattices all have similar values for Ultimate Compressive Strength with overlap within the error. Again, the HIP+etch lattices have a higher strength value than the other lattices, therefore the order from highest to lowest ultimate compressive strength could be considered to be HIP+etch, followed by as built, etched and HIP lattices.

Considering the experiment as a whole, up until this point, all lattices had been built with dummy solids and without supports (see 3.2). In this build, however, use of the contour only setting puts more heat into the system, therefore the heat did not dissipate quickly enough by using the usual provisions. The builds failed repeatedly despite adding, moving, and taking away dummy solids, and in order to get the build to work at all, supports were required. GKN had no such issues when building the same model. The reason why Sheffield lattices required supports and GKN lattices did not is unclear. The machine settings, at face value, were identical, with all controllable parameters set the same. By speculating, it could be that there are differences inaccessible to the users (for example in the machine hardware or software updates) between the GKN Arcam machines and those at The University of Sheffield. Therefore, unfortunately, there is no clear reason why GKN could build the lattice set with no problems, and The University of Sheffield could not.

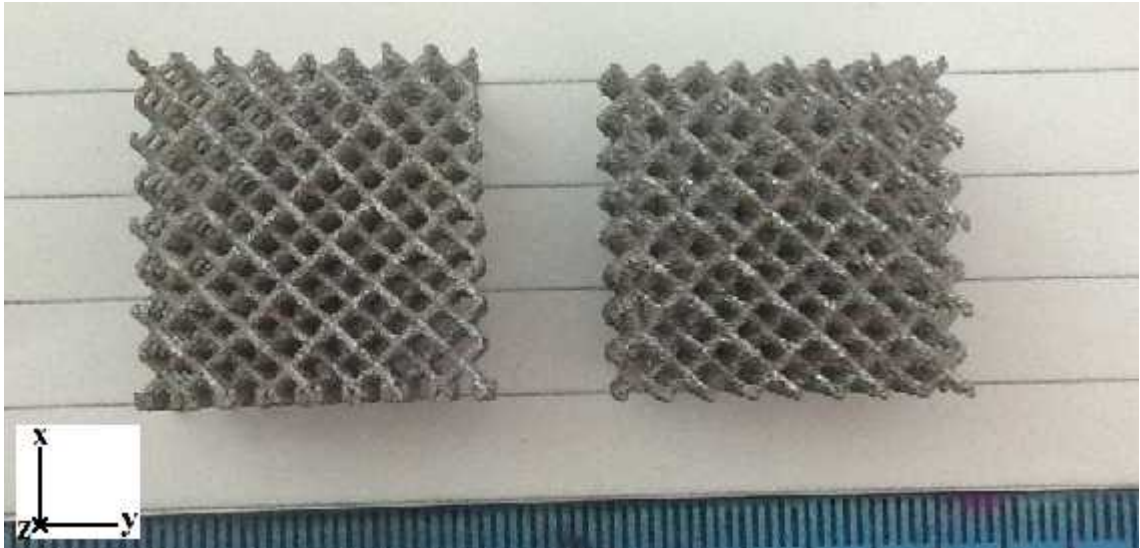


Figure 67: 4×4×4 lattices, left lattice made at the University of Sheffield with supports, and right lattice made at GKN Aerospace without supports

As discussed, in order to complete the build, the Sheffield lattices (HIP and HIP+etch) had supports added prior to building, whereas the GKN specimens (AB and etch) did not. When initially trying to remove the supports from one lattice after the build, some of the struts were damaged, therefore of the Sheffield lattices that were tested, supports remained attached to all of the lattices, to avoid damaging the struts.

Admittedly, this could have influenced the results during mechanical testing. As the supports remained attached, the contact area between the lattice and the platen in the Zwick is dependent on the support. This was confirmed, as when placing the lattices in the machine, a few were unstable when light pressure was applied by the fingertips to test their steadiness.

When taking measurements, although the increased height of the lattice from the addition of supports can be taken into account, the support may be a weak point in the structure, and therefore a source of apparent premature lattice failure. The machine would not be able to determine whether sudden drops in the force data were due to the breaking lattice struts, or supports, therefore the results would be skewed. This was confirmed when, after the test appeared to be over, some supports remained on the platen having fractured from the lattices, despite the lattices appearing otherwise whole.

To counteract these issues, data analysis was conducted with particular care. Considering the incomplete contact area, as long as the supports remained intact by the end of the test, this instability would be accounted for in the initial extrapolation back to zero (which was performed preferentially to the compliance correction). If supports were seen on the platens post-test, this was noted next to that data. In analysis, if this data appeared to be an outlier, this was not assumed to be the case, and the result was assumed to be unreliable and removed from the final results. Ultimately, very few lattices had completely separated supports, and although a minimum of four lattices

were tested for each result, each data point given in this work had a minimum of three lattices contributing to its result.

It is unlikely that surviving supports contributed any strength to the lattices. Indeed, the themes used to produce the supports are intended to weaken the metal contact, to allow easy removal from the part. When comparing the mechanical property values obtained here to other lattices tested over the course of this project, there is no significant deviation from the expected results. Therefore, any contribution to, or deduction of strength by the supports is not large enough to be significant, and assumed to be accounted for within the standard error.

Considering the samples themselves, it would be expected that every lattice would contain a different microstructure. The HIP process changes the microstructure, but the etch process removes the sintered surface structure to leave the microstructure of the pure melt underneath. The original lattices for the etched samples were built with thicker struts, therefore after etching, the lattice leftover may more closely resemble the metal produced in solid EBM parts (which are polished to bring the part up to standard). To support this, elastic modulus is affected by microstructure, with strength of lattices more dependent on macro features. As seen here, the elastic modulus is different for each lattice, however the error is too large to say for sure whether the difference is statistically significant. To investigate the potential differences in microstructure, SEM images were obtained, as discussed in the following section.

#### *4.4.3 Microstructural analysis of as-built and post processed lattices*

Following mechanical testing, one lattice from each set was sectioned, to display the xy plane. These were mounted, polished and etched (section 3.8.4) in order to view the microstructure, as presented here. Due to the angle of the struts within the mount, what is seen in the microstructural images in this section is not a cross sectional area perpendicular to the strut, it is a cross sectional area parallel to the (100) plane of the lattice cube, which is perpendicular to the build direction . Therefore, the struts seen in the microstructural images more closely correspond to one layer built in the EBM as opposed to the approximate 1mm diameter of a lattice strut.

Unfortunately, parts of the lattice collapsed during the mounting process, therefore the struts visible were not only cross sections of struts, but also nodes from within the unit cell. When choosing the struts for imaging, “floating” struts were chosen, which corresponded to single struts, all of a similar size of around 0.8mm. In future, only cold mounting processes should be used to prevent this from occurring.

The images in this section begin with solid cubes, followed by the lattices in the order: as-built, etched, HIP, and HIP+etch. Each set of images is discussed, followed by a summary discussing the differences seen between them. A minimum of four struts from each lattice were imaged, as given in the following figures.

## I. Solid cubes

Within the Sheffield build, solid cubes were built for comparison to lattice structures. One cube was by contour only with contours set to 99 (like the lattice structures within this section), and one cube was built by hatch only.

With regards to the contour only build (Figure 68), towards the centre of the solids, there are large grains with a homogeneous microstructure. Internal porosity can be seen, and smaller grains accumulate around these pores, within the areas of larger grains. One particular concern is the apparent presence of segregation over  $500\mu\text{m}$  from the edge. Here, large grains can be seen next to small grains, with the Widmanstätten pattern evident. As this is present over  $500\mu\text{m}$  from the edge of the cube, it is possible that this can occur due to the extra heat put into the build when using the contour only setting.

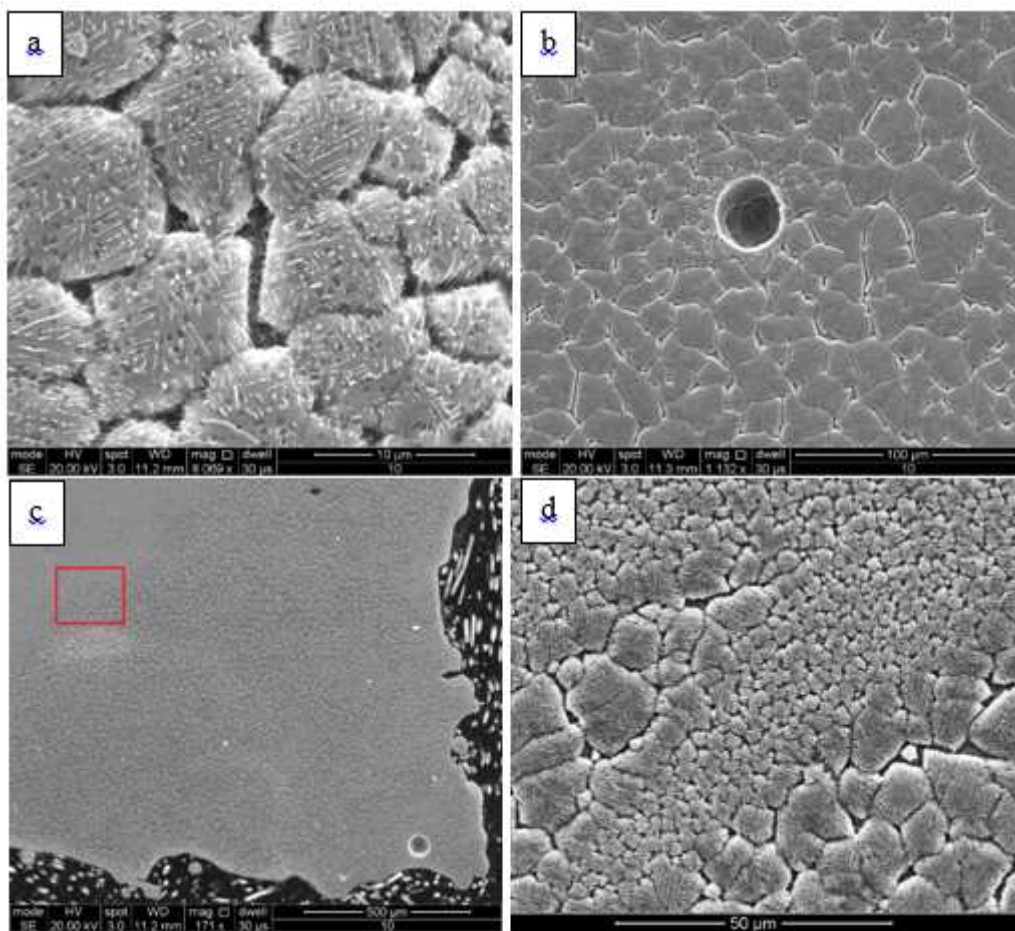


Figure 68: SEM images of contour only solid cube in the xy plane. a) clear Widmanstätten microstructure, b) a pore, c) segregation over  $500\mu\text{m}$  from the edge, d) higher resolution of segregated grains

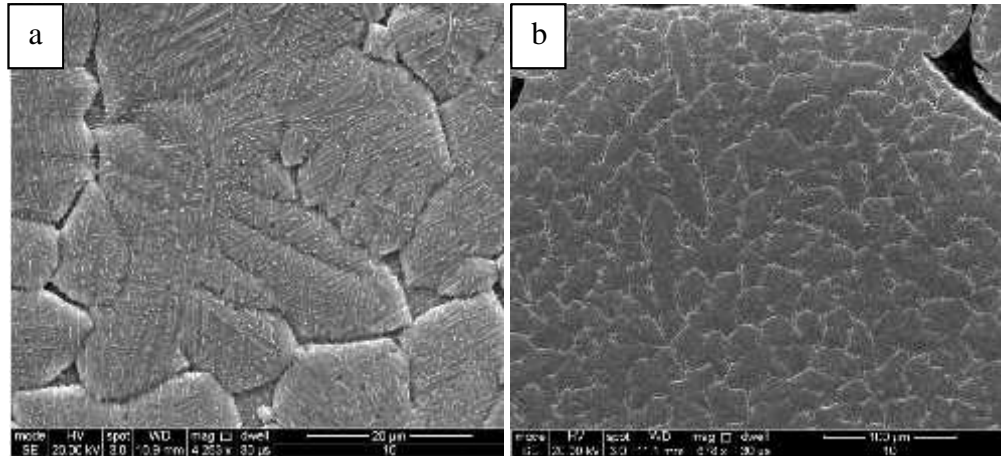


Figure 69: Microstructure obtained from hatch only setting in solid cube with a) Widmanstätten microstructure, and b) grain size arrangement

The hatch only setting produces large dendritic grains with the fine Widmanstätten structure overlay, much like the contour only cube. Although no segregation was found in these images, it is possible that segregation was present, but unobserved in this case. The edges of the hatch cube have smaller grains collecting at the edges of the cube, like seen in the contour only cube (Figure 70). Both cubes had evidence of porosity, and very similar microstructures. This is both expected, and unexpected. Considering the difficulties in building contour only lattices, with regards to the heat themes, it is a surprise that the extra heat input that caused so many problems when running the build, had very little effect, if any, on the microstructure of the solid cubes.

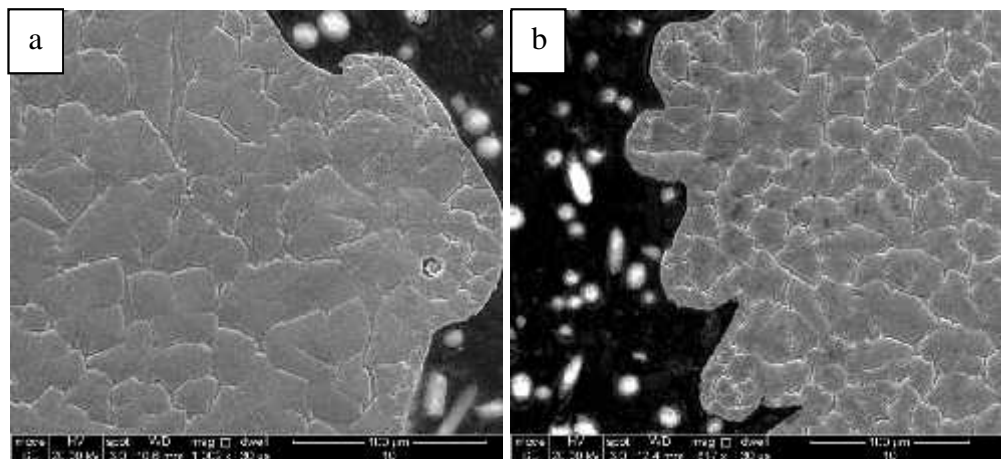


Figure 70: Grains at edges of a) contour only and b) hatch only solid cubes

## II. *As-built lattices*

Regarding the as-built lattice struts shown in Figure 72 on page 129, images a and b show contamination of the samples. This is likely caused by improper handling during the preparation of the samples for image analysis. These images have been included to demonstrate the large deviation in the shapes of the lattice struts, despite the design of the struts being identical.

Considering all the struts, at the edges, tightly packed, irregular grains accumulate. Away from the edge, regular dendritic grains can be seen. Some are closely packed while others are islands in a sea of melt. This is particularly clear in image c, with large, tightly packed dendrites across the strut. At these scales, microstructure cannot be seen, however higher magnification shows a very fine Widmanstätten microstructure overlapping the dendritic formations, as demonstrated in Figure 71.

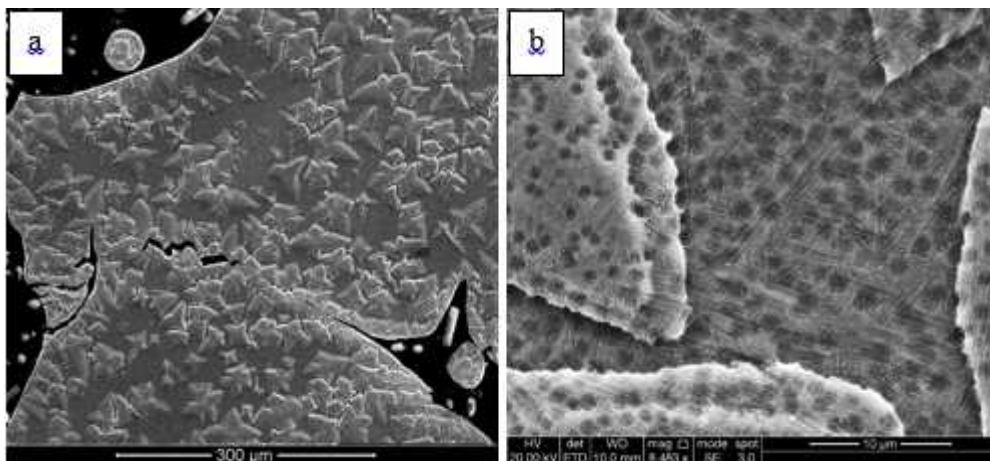
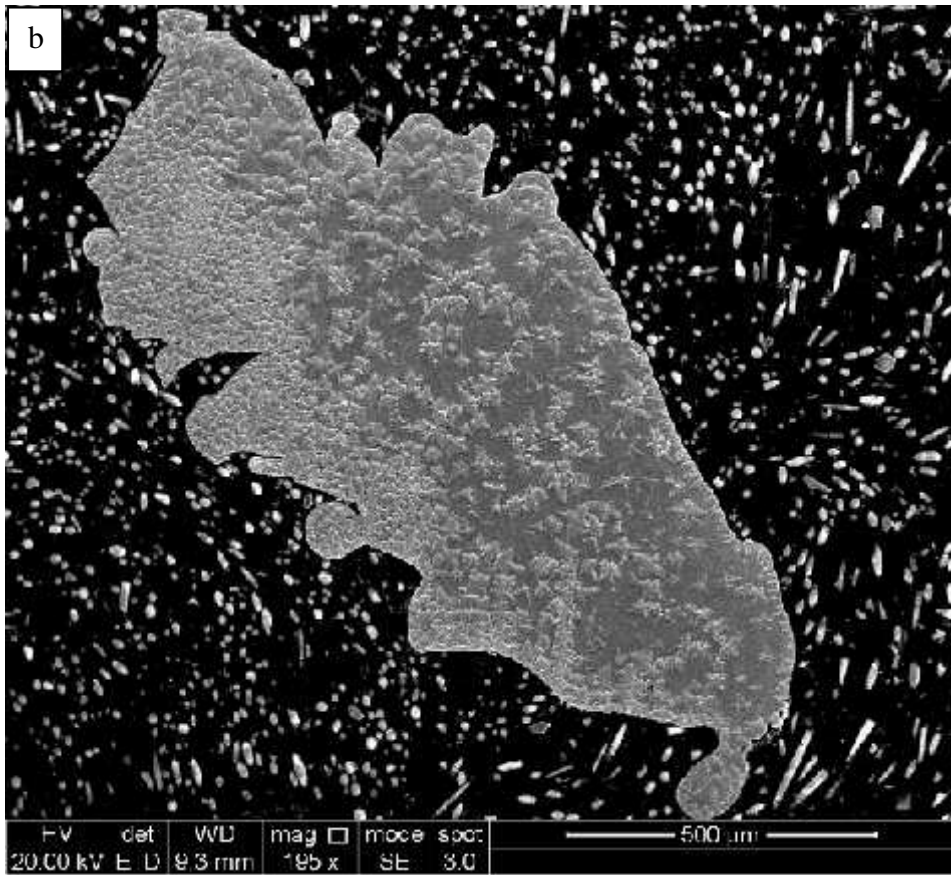
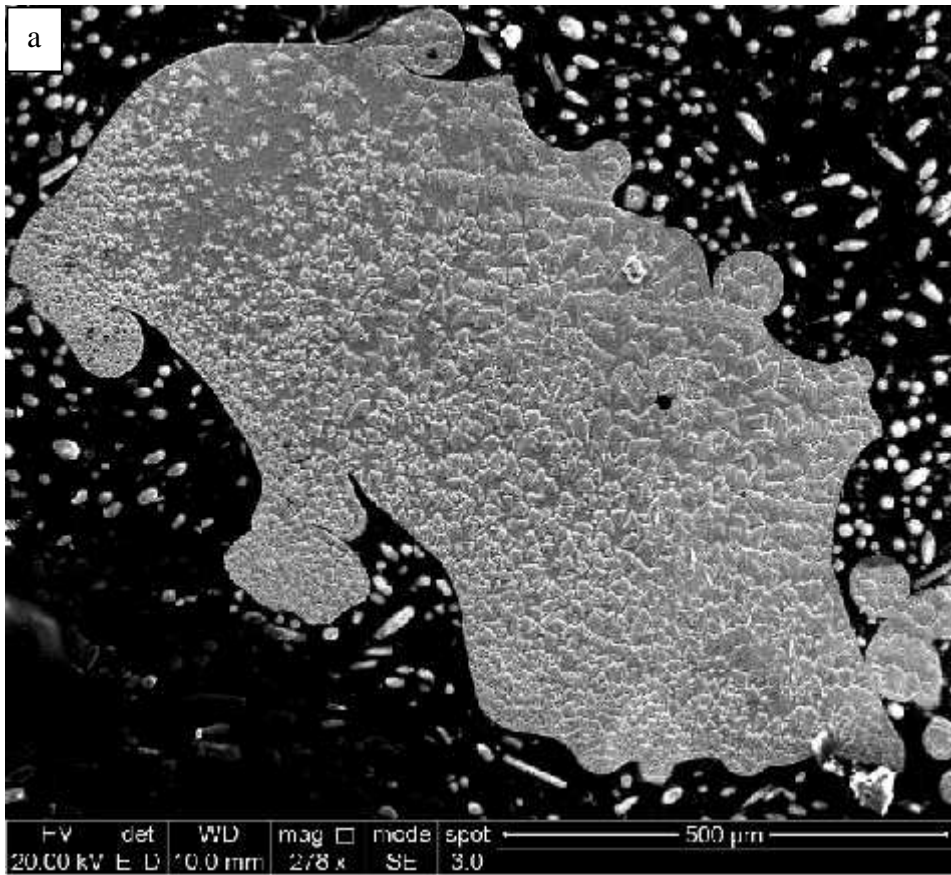


Figure 71: a) Lattice struts: in areas of densely packed small grains, gaps are observed, b) High magnification image of struts showing fine Widmanstätten pattern. Over-etching at the sample preparation stage has led to pitting





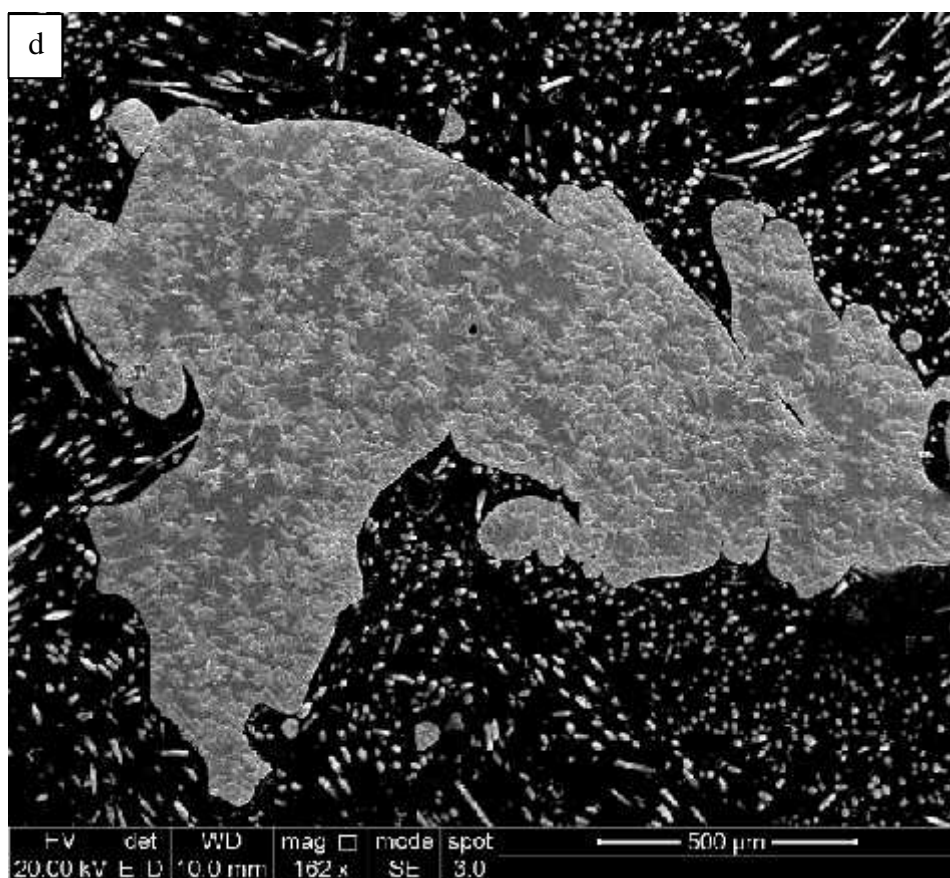
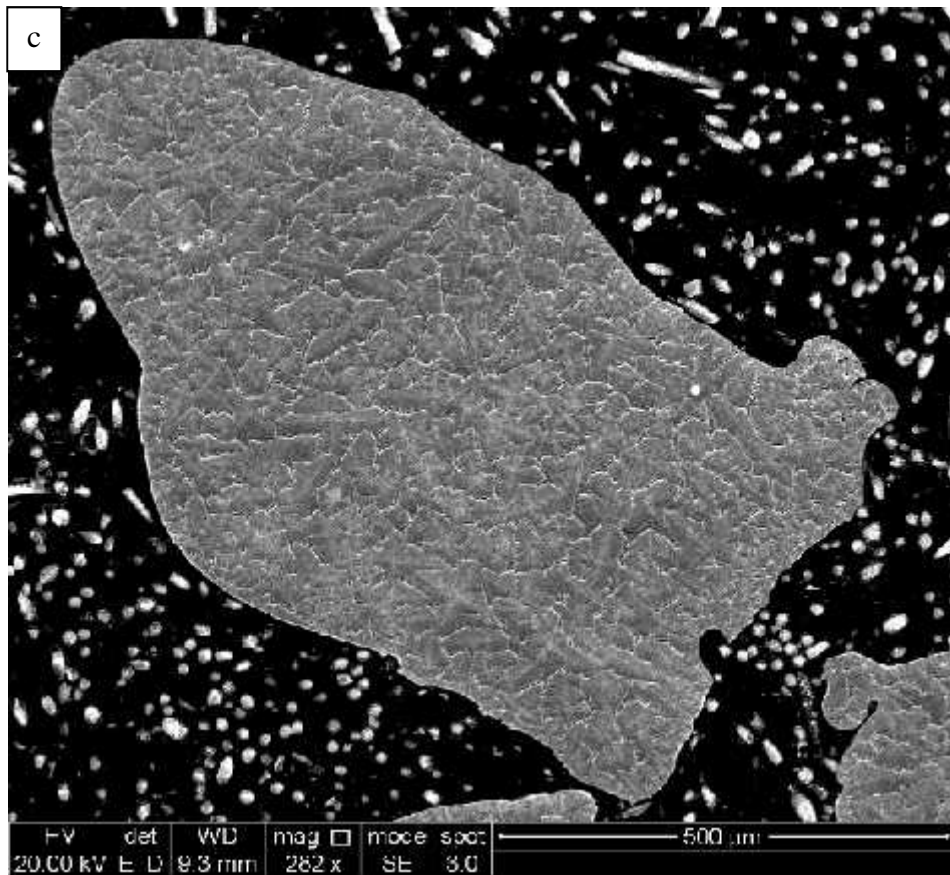
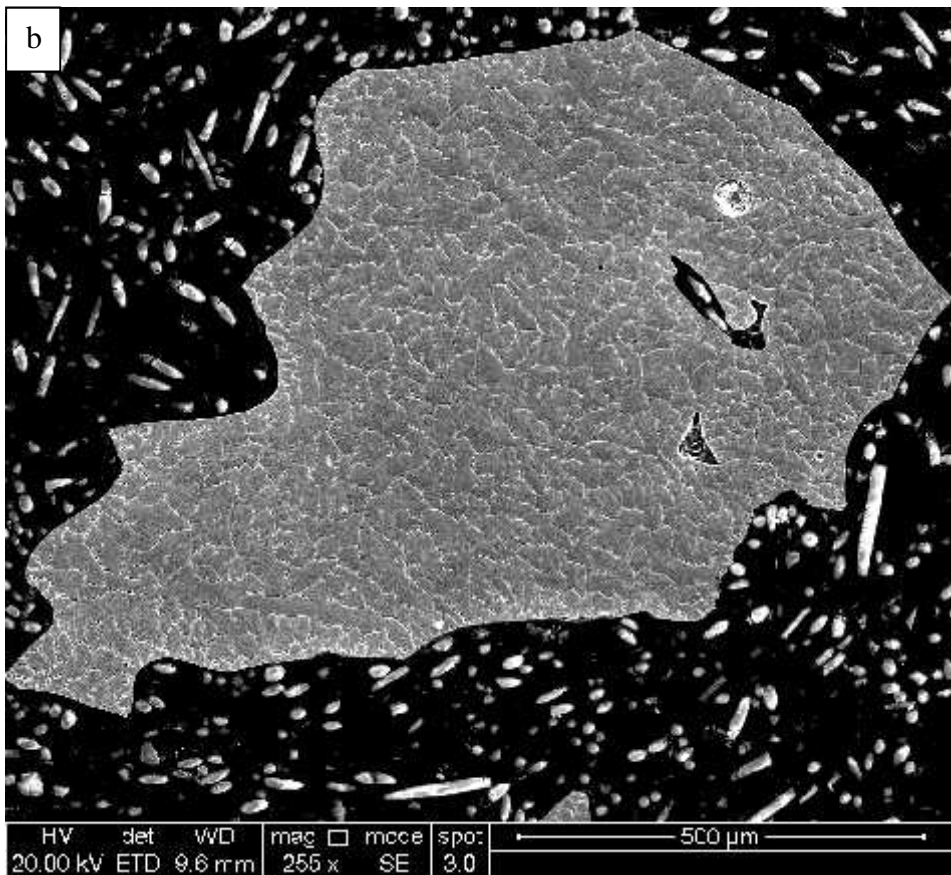
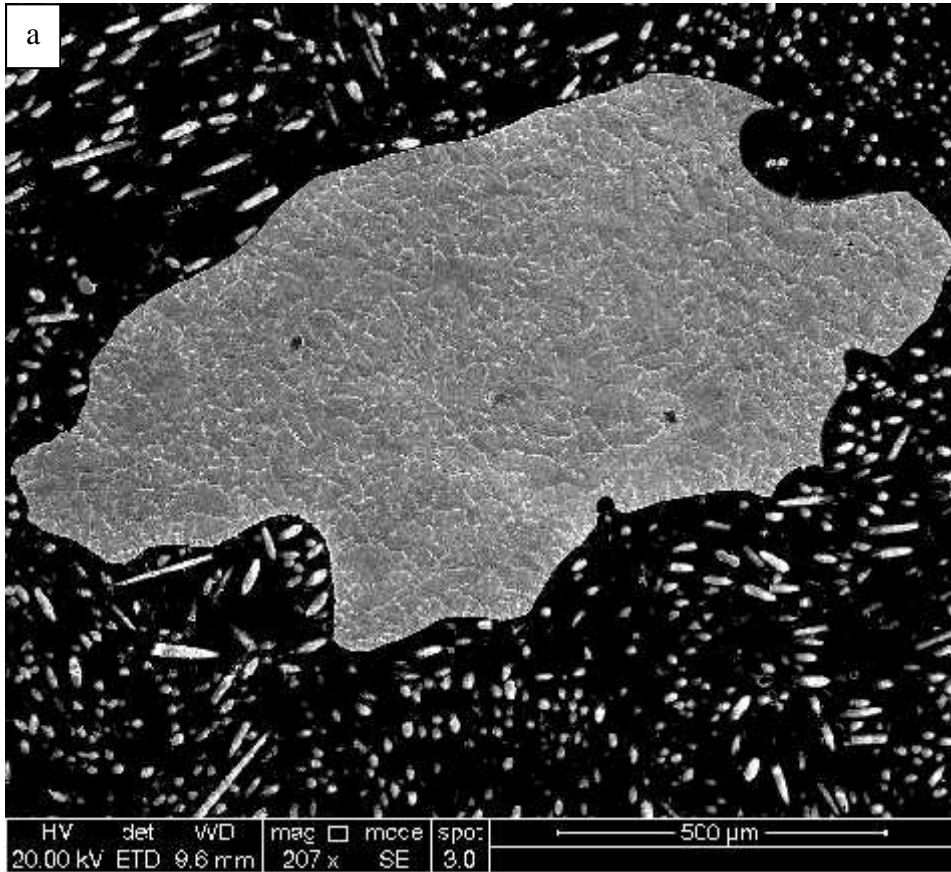


Figure 72: As built lattices, cross sections of four full struts

III. Etched lattices



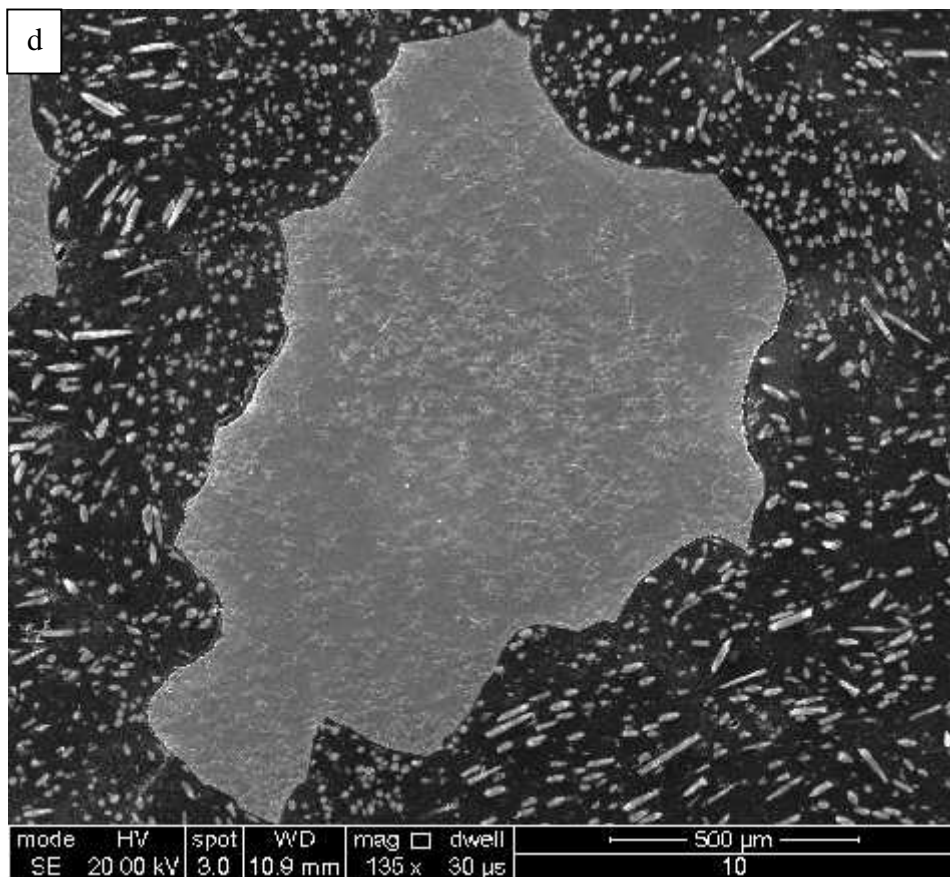
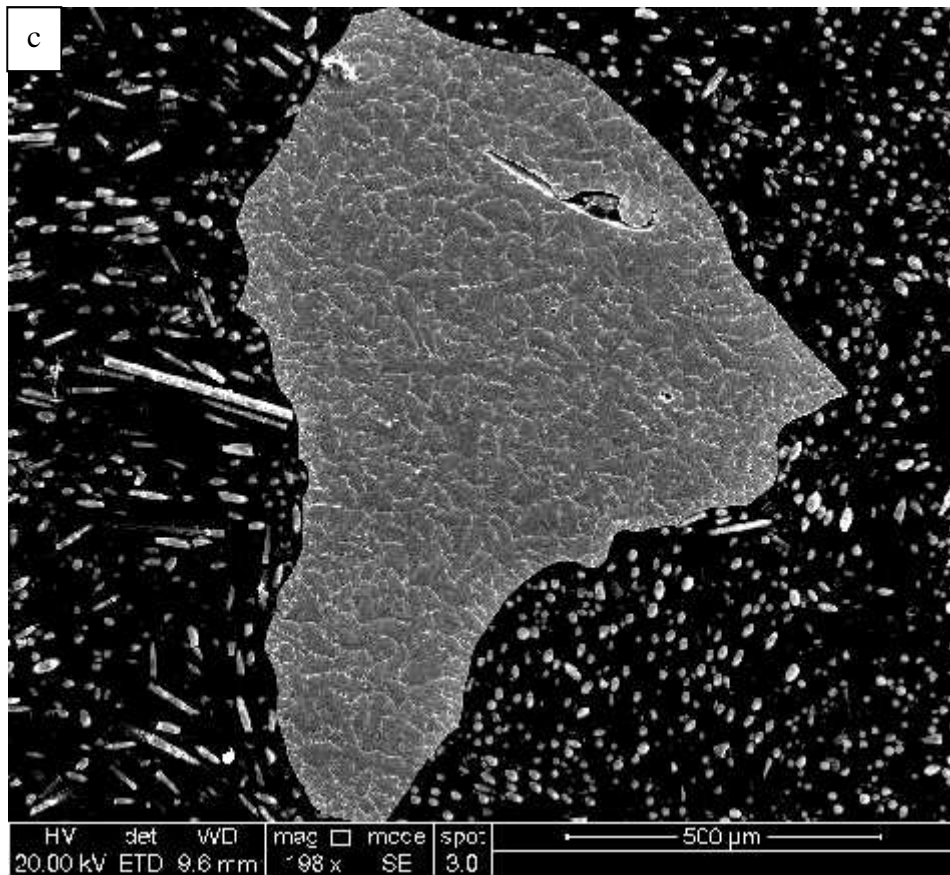


Figure 73: Lattice struts with surface removed by etchant

As before, all struts display a large deviation from the ideal cylindrical design. The most obvious difference between Figure 72 and Figure 73 is the surface of the lattice struts. As expected, the etchant has removed the outermost layer of the struts, smoothing the appearance. There is no evidence of sintered powder at the edges, and the smaller tightly packed grains at the edges have been minimised.

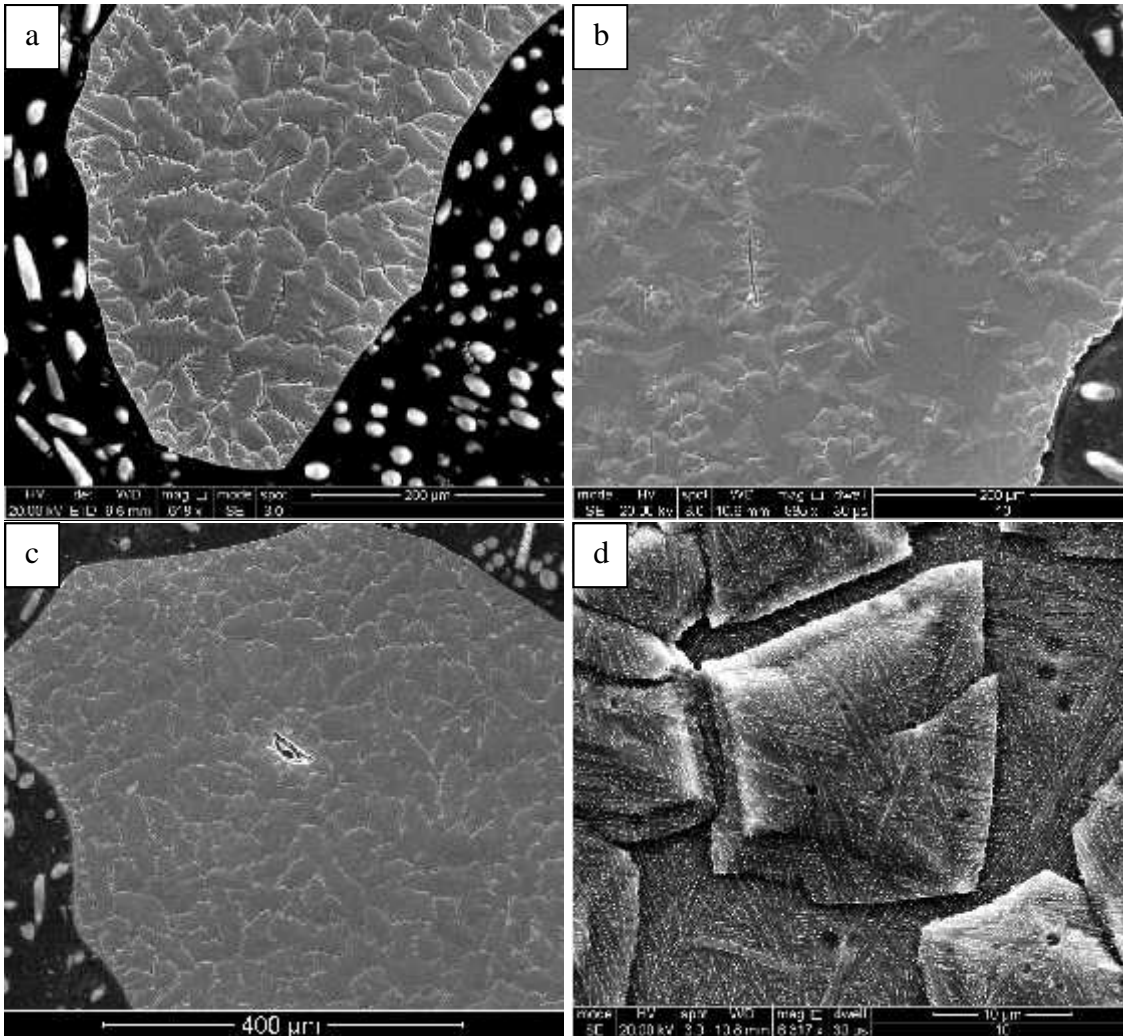


Figure 74: Dendritic-like grains within the lattice struts. a) smaller grain formations at edges, b) smaller grain formations at defects, c) smaller grain formation at pores, d) high magnification image showing very fine Widmanstätten pattern

The dendritic-like formations observed in the as-built samples appear here also, with the very fine Widmanstätten grain structure seen at the high resolution. Like the as-built struts, there are congregations of small grains around the pores and gaps, however there is not enough information to determine whether the gaps or the grains came first.

#### IV. HIP lattices

The original purpose of the HIP was to close internal porosity within the lattice struts, and comparing the porosity seen in the as-built struts in Figure 72 and Figure 73 to SEM images in Figure 76, the HIP process appears to have been effective. This is because it was very difficult to find pores within these images, and those found are small and misshapen.

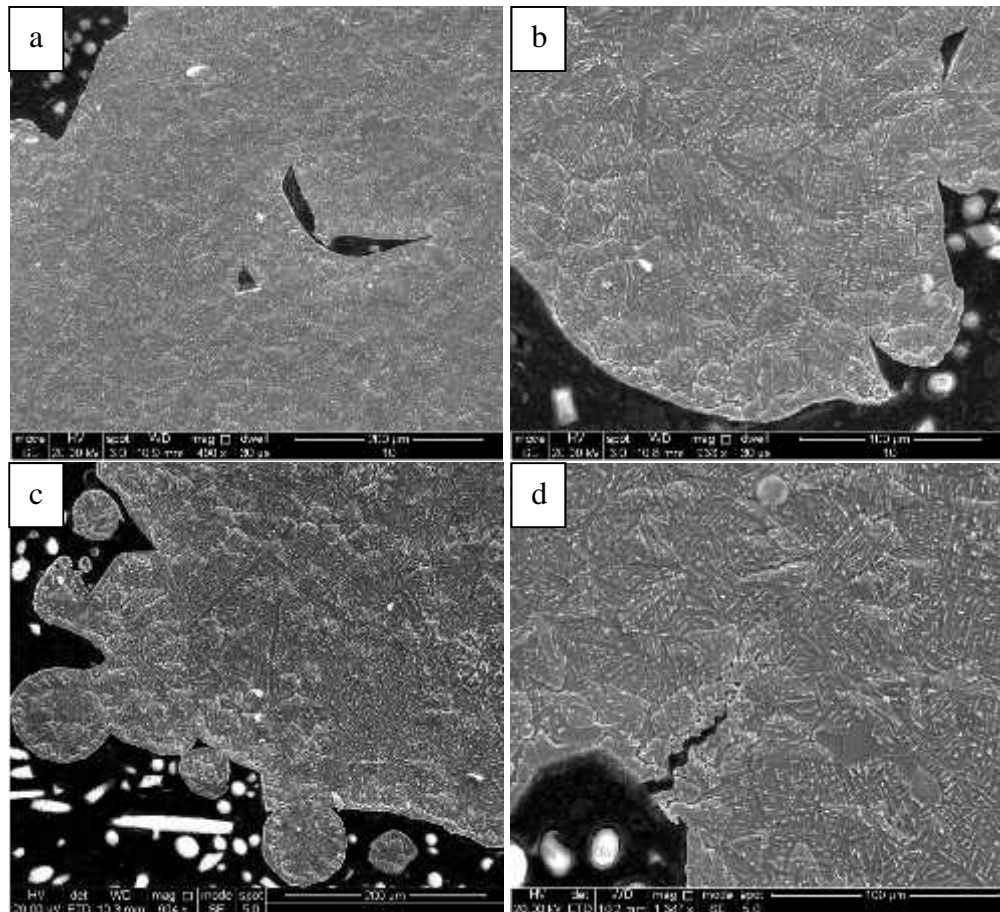
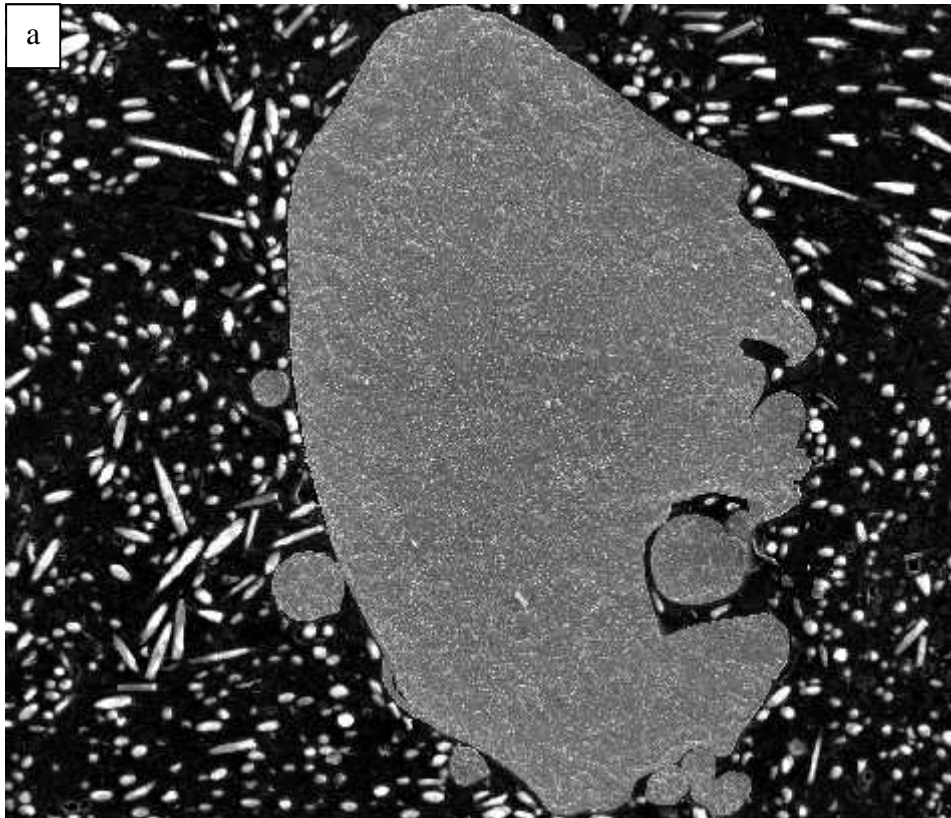
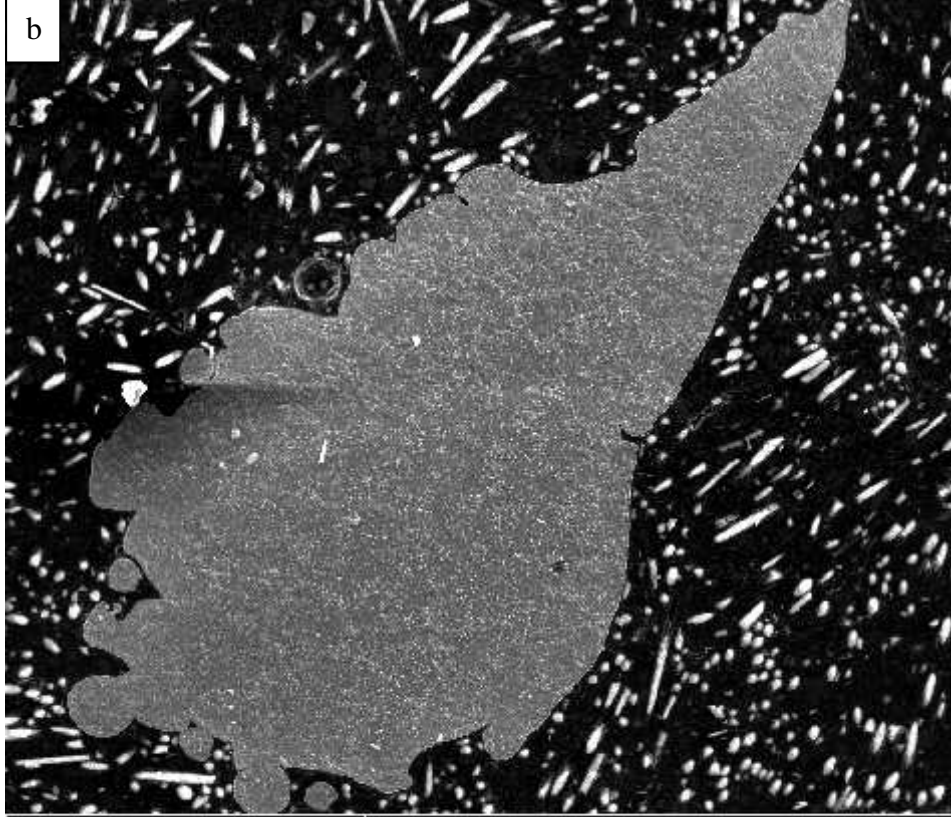


Figure 75: SEM images display dendritic grains with Widmanstätten pattern at lower magnification than as-built lattices, with a and b) show misshapen pores within lattice struts, c) small grains accumulating at edges, and d) small densely packed grains at crack site



HV	det	WD	mag	<input type="checkbox"/>	mode	spot	500 $\mu\text{m}$
20.00 kV	ETD	10.1 mm	251 x		SE	5.0	



HV	det	WD	mag	<input type="checkbox"/>	mode	spot	500 $\mu\text{m}$
20.00 kV	ETD	10.3 mm	207 x		SE	5.0	

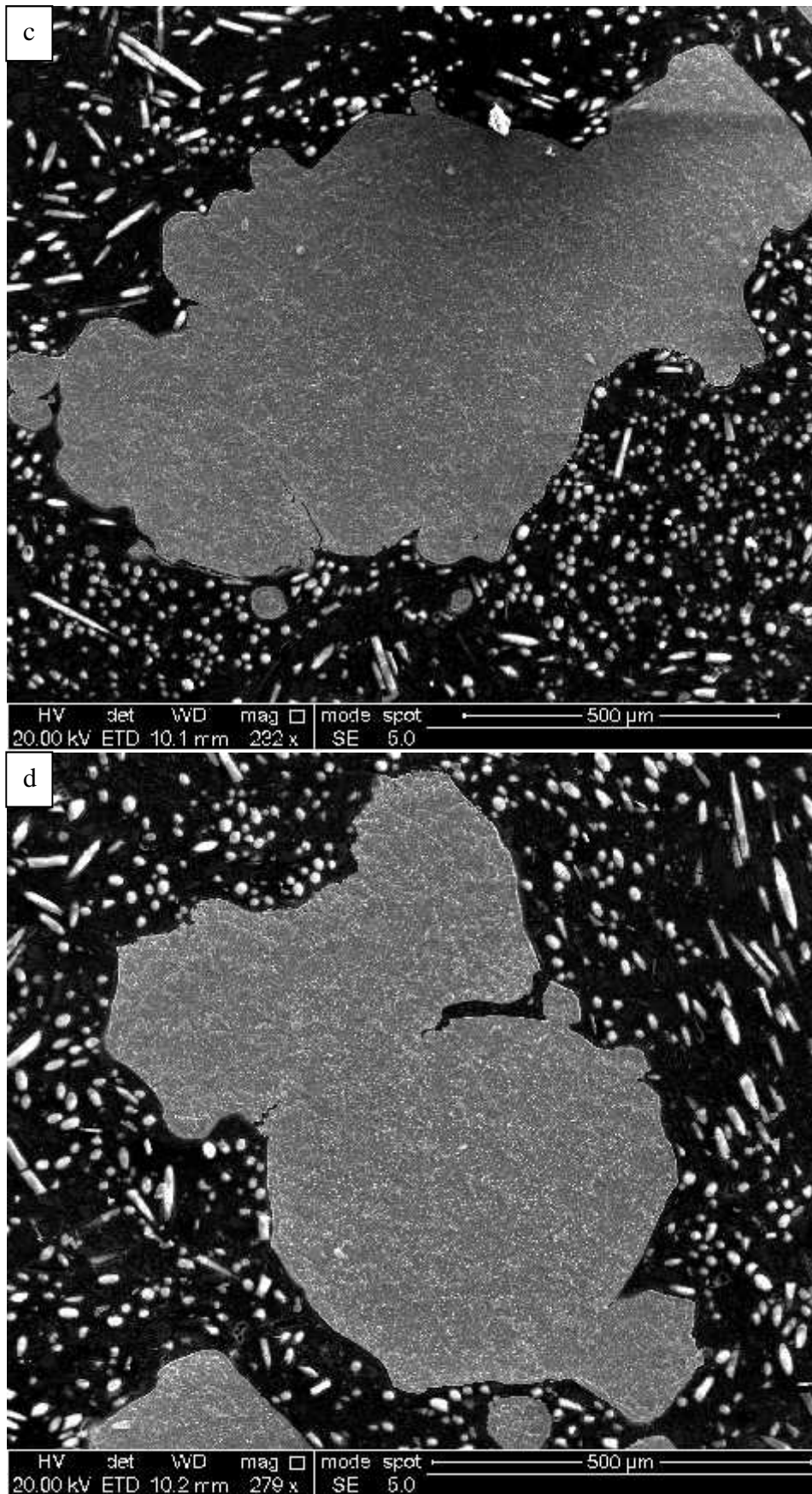


Figure 76: lattice struts of HIP post processed lattices

The HIP post processed lattices have a more uniform structure compared to the unprocessed lattices, with densely packed dendritic grains and no segregation seen. There is a clear Widmanstätten pattern, coarser than previous lattices, with fine lines overlaying the dendritic-like grains. Small grains accumulate at the edges of the struts, with larger grains closer to the centre. These smaller grains at the edges appear to be as numerous as in the unprocessed lattices, and, as before, these smaller grains accumulate at cracks and within gaps. It is clear that although the HIP treatment encourages a coarse basket-weave structure to form, it does not act to dissipate the dendrite-like grains, and has little to no effect on dendritic-like grain formations.

#### V. *HIP+etch lattices*

The lattice struts post processed with both HIP+etch displayed the highest strength, however there is clear porosity remaining within the struts (Figure 77). In these images, there appear to be more instances of porosity than in the lattices that were only post processed with the HIP, however the areas of porosity here are all seen very close to the edges, and containing un-melted powder within the pores. Due to this, it is possible that the HIP was less effective in these areas, however it may have worked to close air gaps deeper within the struts.

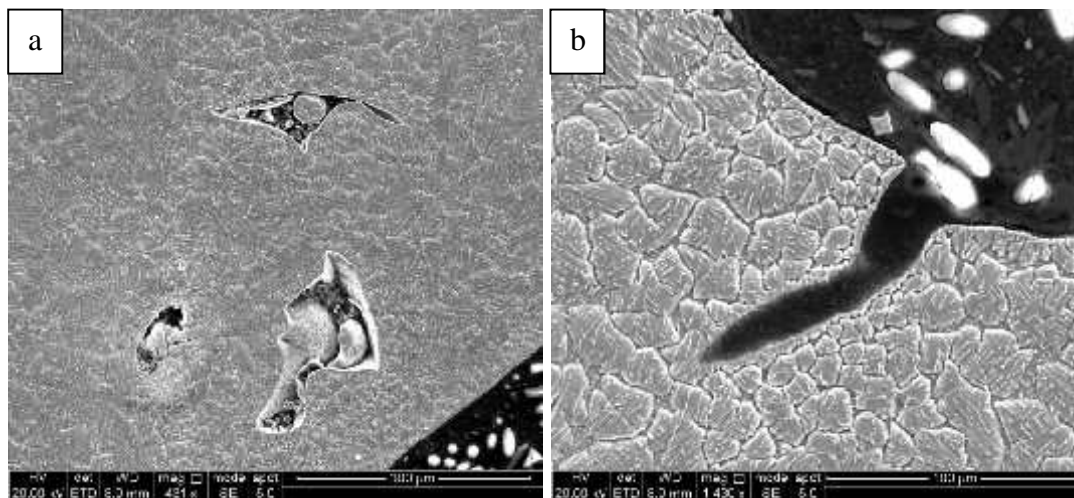
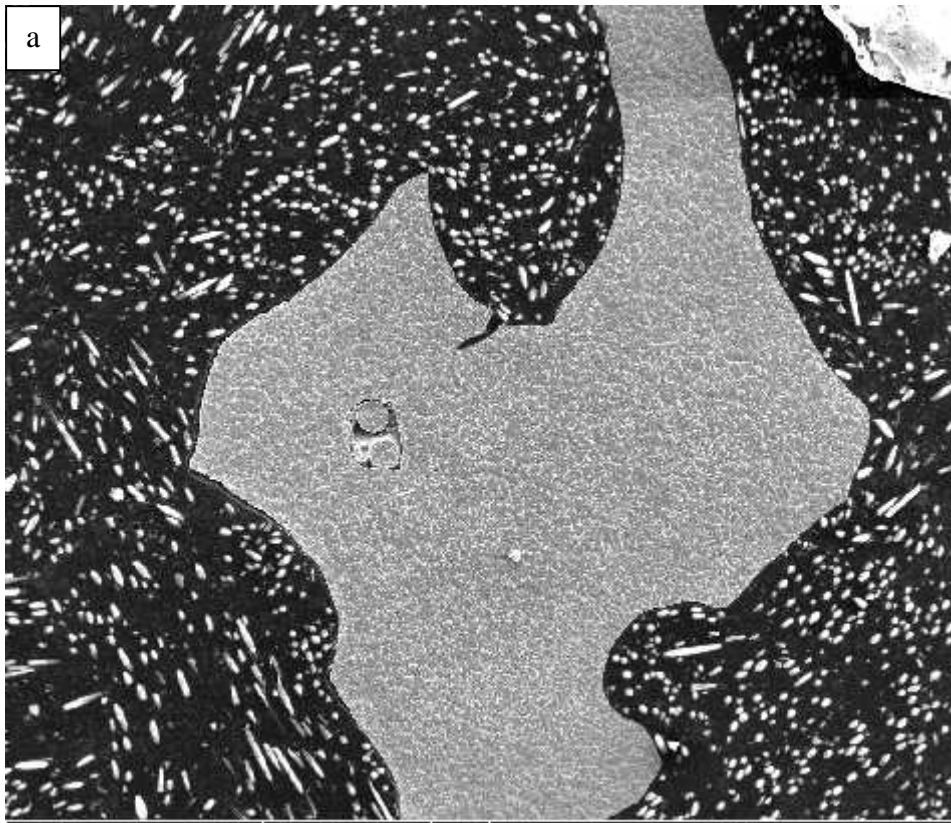


Figure 77: a) Porosity within HIP+etch struts b) Widmanstätten microstructure across dendrite grains in HIP+etch lattices, with small grains accumulating at edges and in cracks

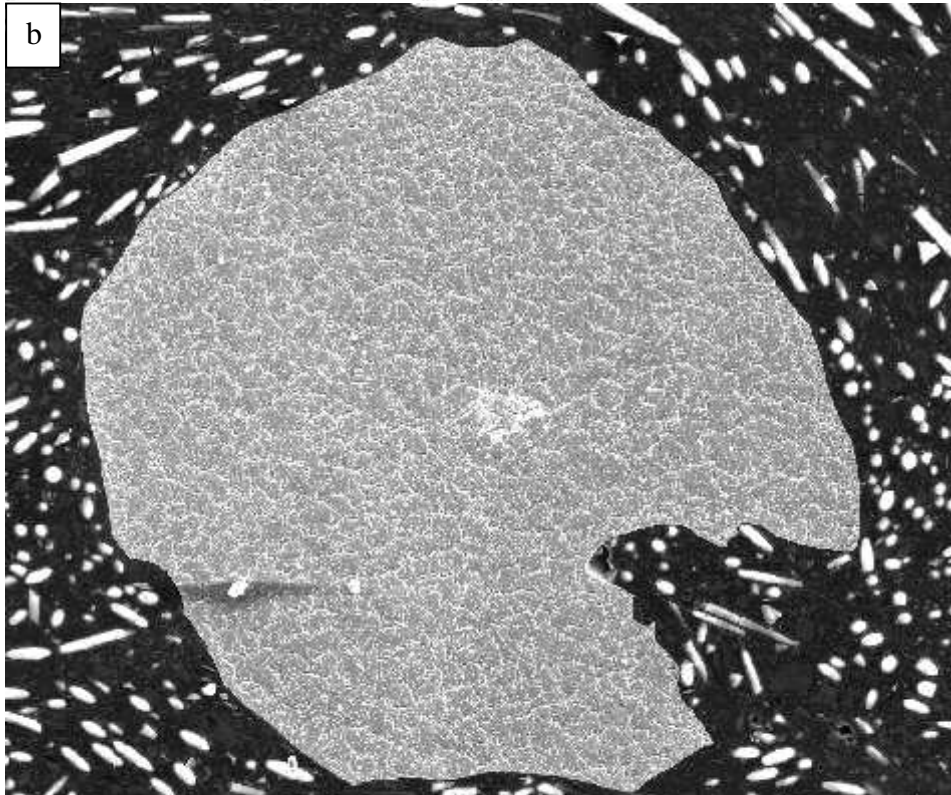
The microstructure in the HIP+etch is very similar to HIP lattices, with a coarse Widmanstätten structure visible. As seen previously, small grains accumulate at the edges and around cracks, with larger grains deeper within the lattice struts. It is clear that the etchant has worked to remove the smaller grains on the outside, smoothing the lattice surface and reducing the thickness of the fine grains.





HV	det	WD	mag	mode	spot
20.00 kV	ETD	8.9 mm	~56 x	SE	5.0

500  $\mu$ m



HV	det	WD	mag	mode	spot
20.00 kV	ETD	9.1 mm	281 x	SE	5.0

500  $\mu$ m

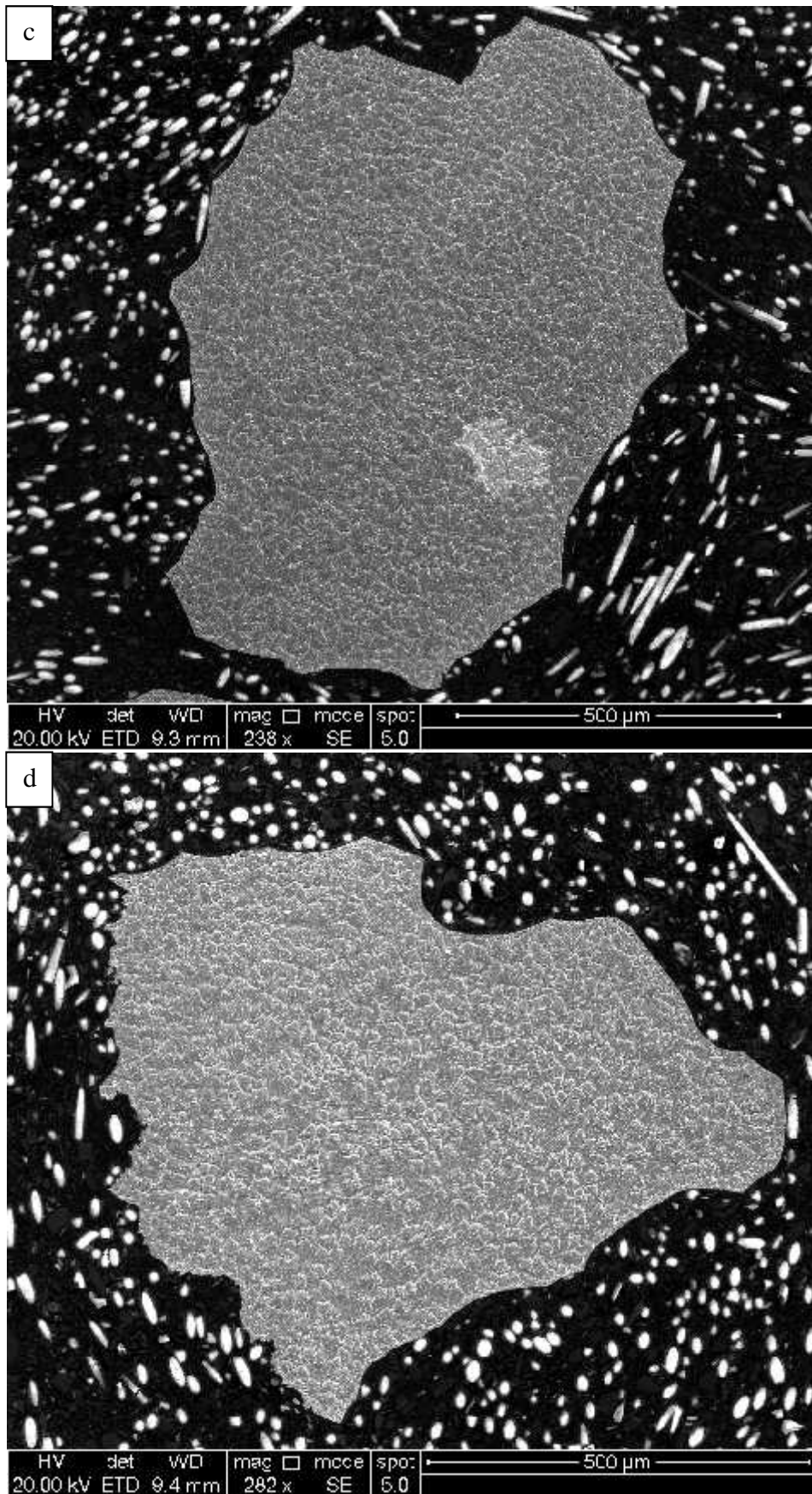


Figure 78: Lattice struts post processed with both HIP +etch

#### 4.4.4 Summary

The microstructure of as-built lattices is very similar to as-built solids, in the fine Widmanstätten pattern available. In lattice structures, the grains have a dendritic appearance, and the grains in the solids have similar shapes. Differences between as-built EBM solids compared to lattices could arise from the small grains at the edges of the build being more abundant in lattices due to the far greater surface area to volume ratio.

Current as-built lattices have smaller grains at the edges and larger grains towards the centre, much like EBM solids. In lattices, however, due to the large surface area to volume ratio, there are a great many more small grains than large ones. In solid parts, these smaller grains found at the edges are often removed in a polishing step. Etching the surfaces of the lattices has a smoothing effect, and leads to a reduction in the smaller grains at the edges. The lattices were not etched for long enough to remove all the smaller grains at the edges and leave larger grains to make up the microstructure (like a polishing step might in solid parts), therefore the etching alone had little to no effect on the properties of the lattices.

Initially, it appeared that the HIP post process may minimise internal strut porosity, however it is clear that internal porosity is not eliminated. It is likely that the pressures involved during the HIP process are not high enough to influence the minimal volume of the metal struts, as the hot gases will flow freely through the porous structure. As such, when manufacturing lattices, it is important to reduce porosity through the machine settings as far as possible.

As-built lattices have large dendrite shaped grains in the middle, and small densely packed grains at the edges. Sometimes there is segregation between the large grains, however what makes up these areas is not clear in this study. HIP appears to reduce segregation by filling these areas with large dendritic grains, however the biggest effect of the HIP is the coarsening of the Widmanstätten microstructure.

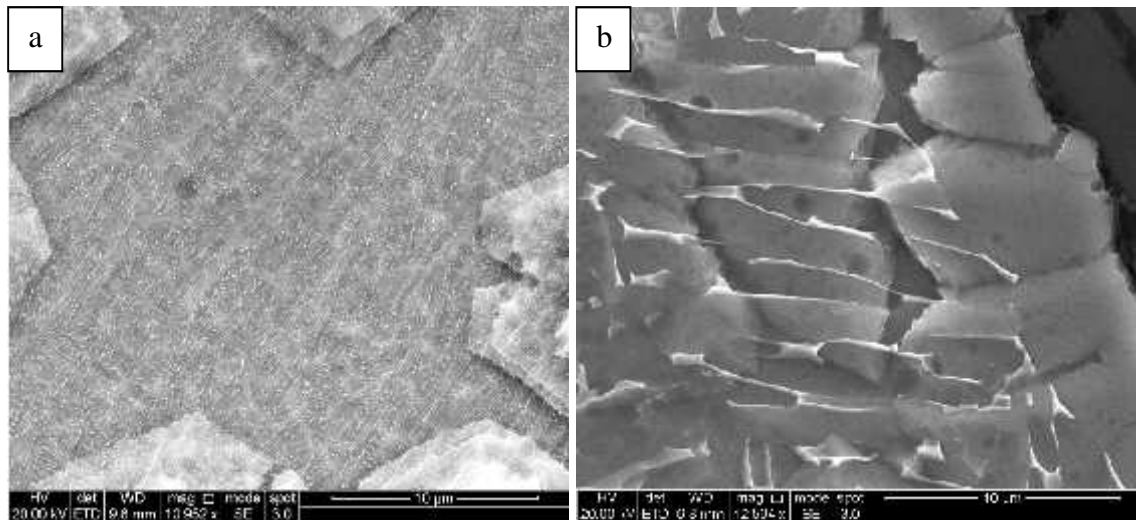


Figure 79: Widmanstätten pattern in a) as built, and b) HIP lattice struts

The as-built lattices have a finer Widmanstätten pattern, with the HIP treatment acting to widen the plates. As discussed previously, wider plates should mean lower strength. Considering the HIP+etch lattices had the highest strength, it would seem that this is not the case for lattices. Considering the literature on solid Ti6Al4V, small colonies and grains should increase the yield strength and elastic modulus (Table 1, page 21). Contrary to this, the lattices that did not undergo the HIP process had the finer microstructure, whereas the HIP+etch lattices had the higher yield strength and elastic modulus. In this case, the microstructural features played an unexpected role, as when determining mechanical properties HIP+etch produced the strongest lattices.

From this, the ideal lattice might have: large uniform grains, minimal segregation, minimal porosity, large, uniformly distributed grains of Widmanstätten microstructure, consisting of large plates.

## 4.5 Fatigue testing of as-built and further processed lattices

This section compares as-built lattices to HIP lattices through fatigue tests, to determine if using a HIP post process leads to changes in life. The samples utilised are the F series of samples, the methods for which testing was conducted are detailed in section 3.2.4.

### 4.5.1 Determination of viability of the fatigue test

The odd numbered fatigue samples from F1 were utilised to determine whether a fatigue test would be possible given the limitations of the equipment, and if so, to investigate the extension that could be achieved for the material to remain in its elastic range. A load/unload test was performed using the Zwick, where the sample was extended to 1% of its length before returning to its original length. The sample was then extended to 2% of its length, and this process repeated, with extension increasing each time in 1% increments until failure (see Figure 80).

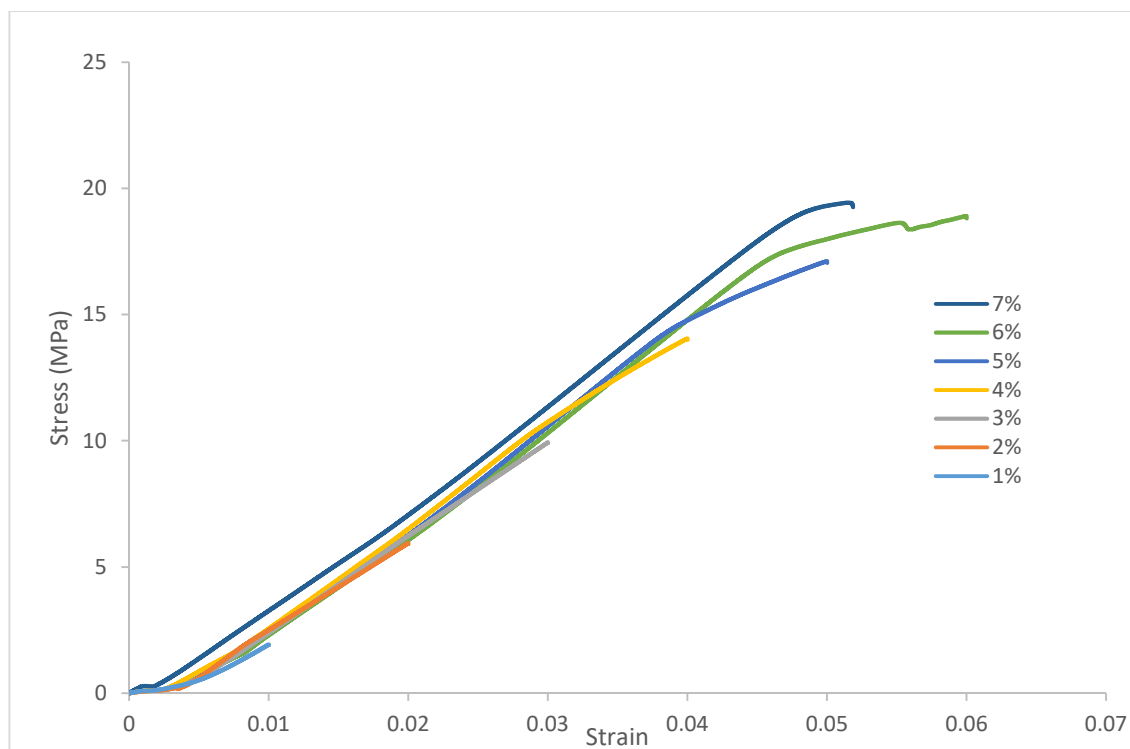


Figure 80: Example of plot produced from load/unload test of fatigue samples for different maximum values of elongation

In this case, the stress/strain curve follows the path of the elastic modulus fairly reliably until 5%, where plastic deformation appears to shift the elastic modulus. Although the 6% curve overlaps the elastic modulus of the previous elongations, there is a clear

buckling at around 0.04 strain, which leads to plastic deformation. This is particularly clear at 7% elongation, where the curve has shifted, before failure just after 0.05 strain.

By comparing the behaviour of the lattices during the load/unload test, and analysing the data after the test, it was predicted that during fatigue testing, specimens at 5% elongation or more would fail quickly, and therefore demonstrate low cycle fatigue (LCF) behaviour. To demonstrate high cycle fatigue (HCF), the samples would need to remain below their elastic limit, and therefore be under 3% elongation.

#### *4.5.2 Effect of position on the build plate on mechanical properties of samples*

Using the fatigue samples from F1, an investigation was conducted to find out whether position on the build plate led to different results. If true, this would mean that position on the build plate played a large role in the mechanical properties (see Figure 47 page 80). As discussed in 2.2.2, if the parts in the build did not have a sufficient heat sink, they would swell due to excess heat. Due to this, it was considered that the fatigue samples at the corner of the build with two exposed sides (1's) would have less insulation, therefore be more prone to swelling, than parts with one exposed side (2's and 4's) and even less than samples with no exposed sides (3's, 5's and 6's).

As there were only four of each odd numbered sample, the eight even numbered samples were selected to give more repeats. It was expected that if the position on the build plate was significant, there would be some difference in fatigue life when comparing the 2 and 4 samples to the 6's. After recording the fatigue life, the results were displayed using a box plot, and the numerical values displayed in a table for statistical analysis.

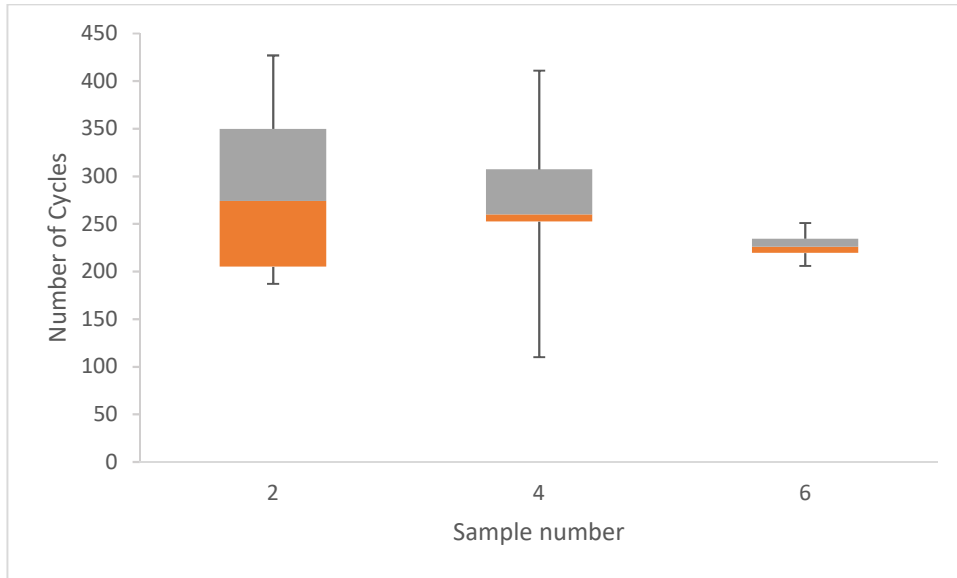


Figure 81: plot to compare lifetimes between samples for investigating potential mechanical property variation due to position of samples on the build plate

Table 9: values of lifetimes for investigating potential mechanical property variation due to position of samples on the build plate

Build	Number of cycles		
	2	4	6
mean	283	267	227
minimum	187	110	206
Q1	205	253	220
Median	274	260	226
Q3	350	307	235
Maximum	427	411	251

Considering these results, it was determined that the position on the build plate did not lead to a statistically significant difference in fatigue life.

There is a large spread of overlapping data, all of which lies within the other data sets. From this it was decided that when conducting dynamic tests on parts, it did not matter where in the build each part had resided, therefore when building samples, all parts manufactured could be used to produce results.

### 4.5.3 Fatigue analysis to determine SN and EN curves

Thirty six samples from build F2 were utilised in their as built condition to produce plots of stress life and strain life through fatigue testing, as defined in 3.7.

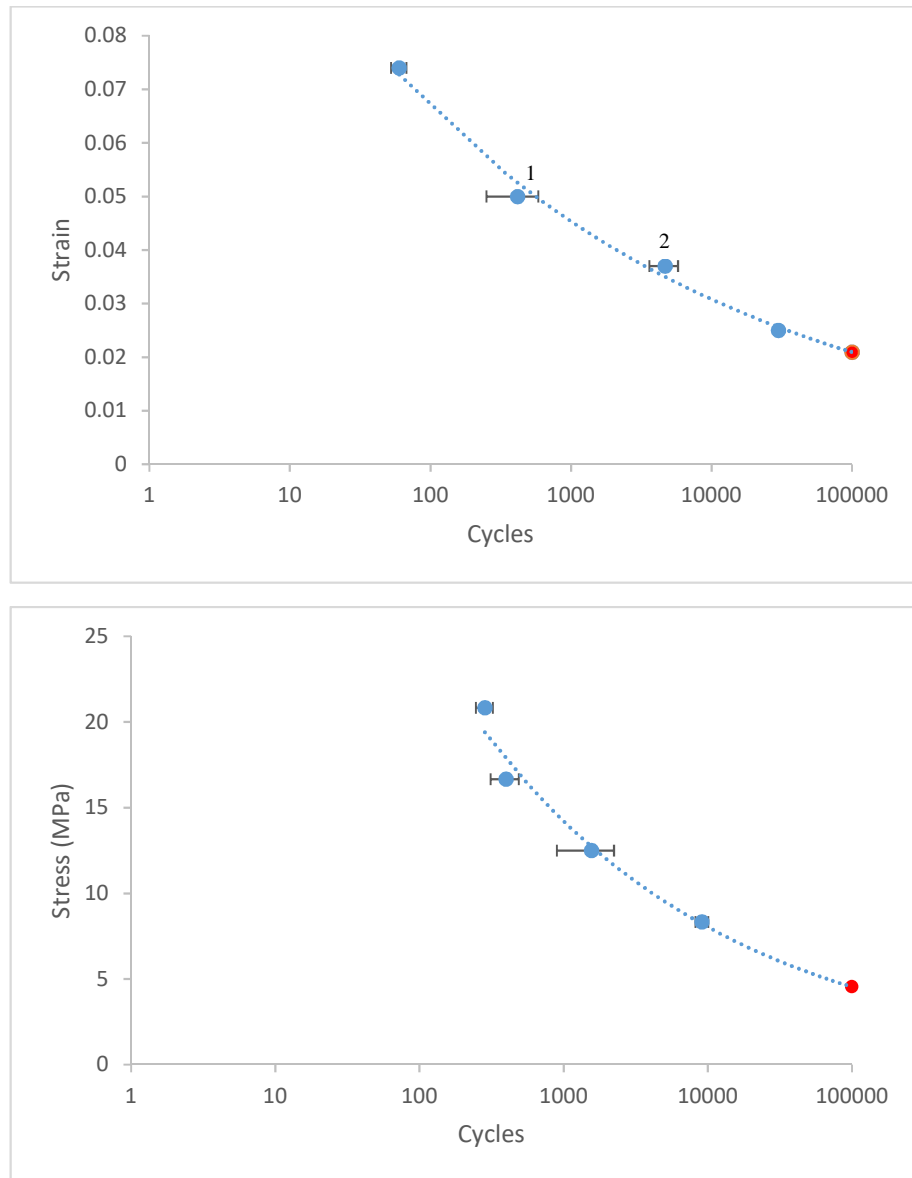


Figure 82: Results of fatigue testing, a) EN curve, b) SN curve

As expected, these curves have a correlation of higher forces leading to shorter lifetimes. Although fatigue is a test with high variation in results, the data provides a standard life curve.

Following the curve of the available points, an estimate for 100000 cycles has been plotted, as the single red point in Figure 82. For strain/cycles, this is estimated to occur

at around a strain of 0.021, whereas for stress/cycles, this is estimated to occur at a stress of around 4.54 MPa.

It appears that with this limited number of data points, a fatigue limit has not been established. According to Rafi et al. solid Ti6Al4V made by EBM reaches a fatigue limit of 340MPa at  $10^7$  cycles, after reaching  $10^6$  cycles at ~360MPa, and  $10^5$  cycles at ~410MPa [82]. Assuming this trend would apply to Ti6Al4V lattices, the curves can be extended to  $10^7$  cycles. Doing this suggests the fatigue limit for the stress/cycle curve to be around 3.77MPa, and the fatigue limit for the strain/cycle curve to be around 0.017.

Considering how lattice technology has a lot more in common with foams than their solid counterparts, this may not be the most accurate prediction. Indeed, when comparing fatigue of solid polymers to foams, Gibson and Ashby state that the inherent mechanism of fatigue in foams may differ from that of true solids.

At the time of writing, however, until more comprehensive studies surface on fatigue of Ti6Al4V porous metals, this is the most appropriate comparison available. Further work is required to support these findings.

#### 4.5.4 Fracture analysis

As is expected for Ti6Al4V, examining the fracture surface for both high cycle (HCF) and low cycle (LCF) fatigue revealed ductile fracture at the point of separation (Figure 83). During testing, it became clear that different mechanisms were at work depending on the forces involved (Figure 84).

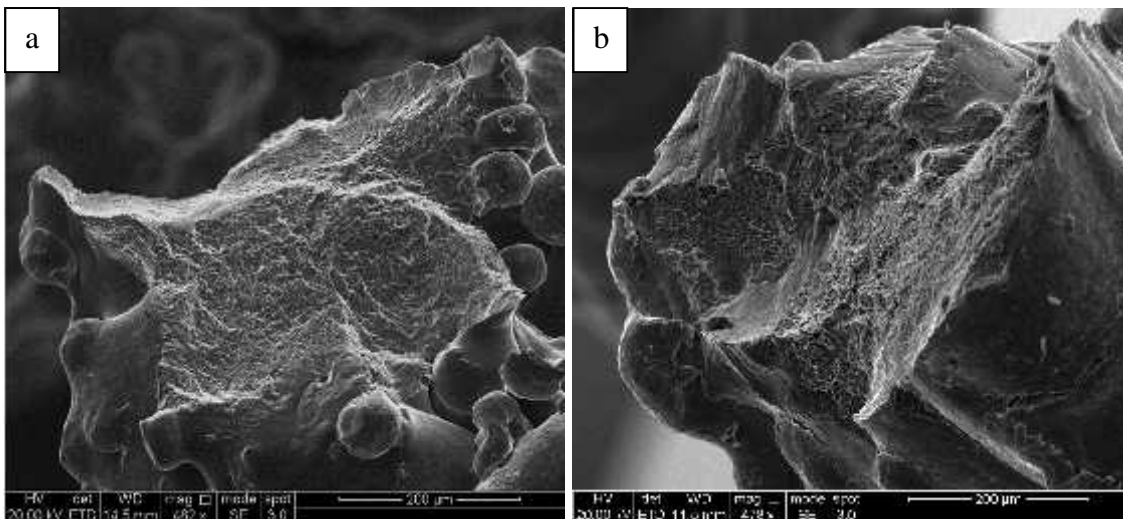


Figure 83: Representative ductile failure for lattices that were fatigue tested at: a) HCF, low stress, and b) LCF, high strain



Figure 84: Failure pathways for specimens subjected to HCF (low strain, left) and LCF (high strain, right).

During testing, it was observed that when the samples were subjected to a low stress or small strain, the crack pathway was at 45 degrees to the test direction, propagating in a pathway up the specimen from strut to strut, which aligns with recent findings in porous metals. Some specimens failed but did not separate, by displaying little resistance to the force, with sections remaining attached by few struts. Often these specimens displayed numerous regions of 45 degree damage.

Under a high stress or a large strain, the crack pathway was perpendicular to the test direction, and directly horizontal across the test specimen. This led to complete separation of the specimen as is common in solid materials.

Intermediate stress or strain show 45 degree crack pathways, however these propagate horizontally across the test specimen, keeping the damage contained to a two unit cell height region. Intermediate forces sometimes lead to separation at catastrophic failure; however, sometimes catastrophic failure was reached despite the sample remaining connected by a few struts. These observations suggest two different mechanisms at work during dynamic loading, depending on the size of the forces applied. With low forces, the stress concentration is not limited to one specific area of the part, and failure can occur simultaneously at different points. For high forces, the failure zones in on one particular area of weakness, where cumulative damage causes failure at one particular point.

#### 4.5.5 Fatigue analysis of HIP to as-built samples

Eighteen of the thirty six samples from build F3 were sent for HIP post processing. Upon their return, half of each set were tested at a strain of 0.037, and half were tested at a strain of 0.049.

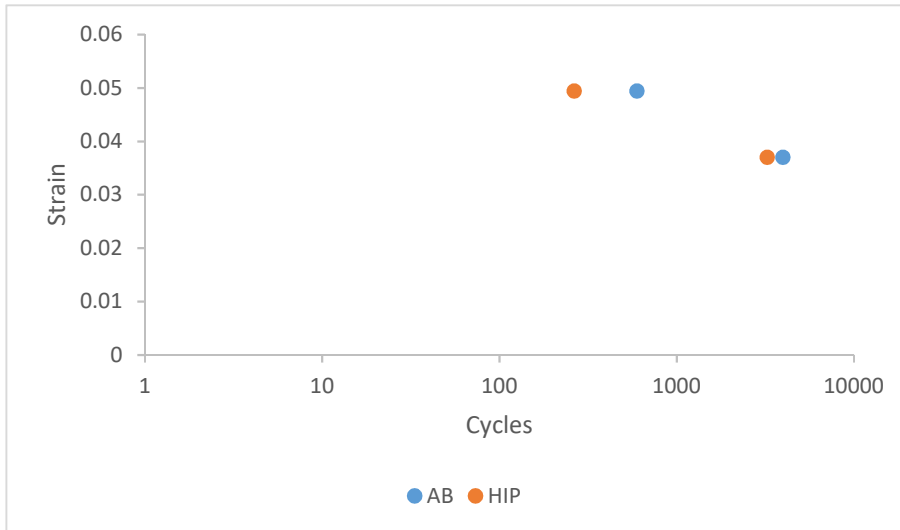


Figure 85: Position controlled fatigue test of as built lattices to samples that had also undergone a HIP post process

Due to the limited number of samples, only two strain values were investigated. These correspond to points numbered 1 and 2 on the EN curve in Figure 82a. From Figure 85, it would appear that the samples which underwent the HIP process failed at a lower number of cycles than the as-built samples.

This is of particular interest, as areas of porosity had been observed within the struts in SEM images. Intuitively the HIP process should work to close these gaps and lengthen the fatigue life. This is not the case here. It was therefore considered that due to the small sample size, perhaps there was no difference between the samples. Statistics were employed to determine the probability that the data sets were independent, as previously discussed in section 3.7.1.

Initially, a basic t test was performed to compare the mean of as-built to HIP for each strain rate. This gave p values for 0.037 strain as 0.103, and for 0.049 strain as  $1.52 \times 10^{-4}$ . This indicates an 89.7% and 99.9% confidence that the mean of the as-built samples is different to the mean of the HIP samples at a 0.037 and 0.049 strain respectively. Due to the p value of the 0.037 strain being above 0.05, the null hypothesis could not be ruled out for this strain, however, with the p value of the 0.049 strain being a great deal lower than 0.05 would suggest the null hypothesis could be ruled out. Due to these

contradictory results, it is not possible to say whether HIP has any effect on the fatigue life from comparing the means, therefore more information is needed from further statistical tests.

A generalised likelihood ratio test was performed assuming the data followed a Weibull distribution to find a p value. This test gave a p value of 0.0275 for the 0.037 strain, and a value of  $1.81 \times 10^{-5}$  for the 0.049 strain. This indicates a 97.2%, and a higher than 99.9% confidence that the as-built data set is different to the HIP data set.

Finally, a log-rank test was performed to consider the general shape of the data and determine a p value without the need for an assumption of the distribution function. A Kaplan-Meier plot was produced to view the probability of survival for a given number of cycles and these plots compared by the script (see Figure 86). This test gave a p value of 0.0195 for 0.037 strain, and 0.00047 for 0.049 strain. This indicates a 98.05% and 99.95% confidence that the as-built data set is different to the HIP data set.

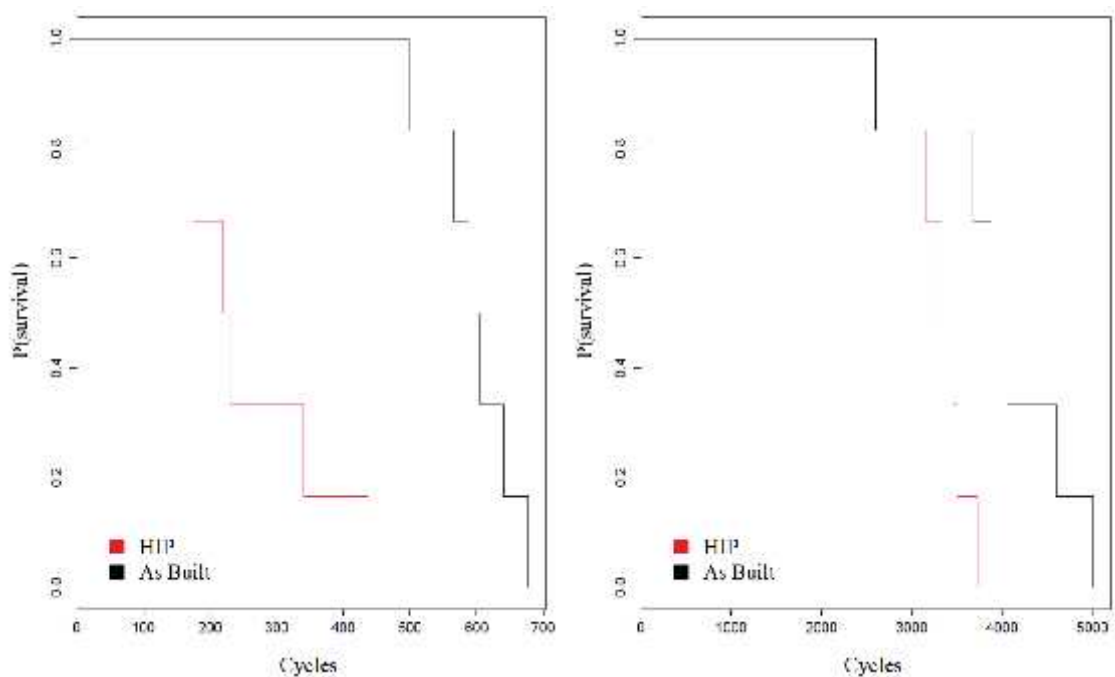


Figure 86: Kaplan-Meier plot produced by R of data for a) 0.037 strain and b) 0.049 strain

Table 10: Results from statistical tests, probability data sets are the same.  
 Statistically, a value of less than 0.05 leads to rejection of the null hypothesis

Test →	t test	GLRT	Log-rank
Strain ↓			
0.037	0.103	0.0275	0.0195
0.049	$1.52 \times 10^{-4}$	$1.81 \times 10^{-5}$	0.00047

The result for the 0.049 strain is a very strong one, with p values indicating a very high probability in the values at this strain being significantly different.

The p values for 0.037 are slightly less certain. It can be considered that the GLRT and log-rank tests hold greater weight than the t test, as the other statistical tests compare the overall data set as opposed to the means. Although the t test has a high p value, the p values produced for the GLRT and log-rank tests fall well below the 5% cut off. Therefore, these resulting p values suggest that the null hypothesis can be rejected, and that it is highly likely that the results between samples are different.

From this, it can be concluded that post processing lattices with a HIP treatment leads to a lower fatigue life.



## Chapter 5 Conclusions and future work

The original purpose of the thesis was to investigate the diamond lattice structure made from Ti6Al4V by the EBM process. During the course of the investigation, it became apparent that several questions would need to be answered in order to ensure optimal mechanical properties. Namely: Are lattices anisotropic? Does surface improvement translate to changes in mechanical properties? Can internal porosity be reduced to improve both static and dynamic properties? This thesis has drawn a series of conclusions. Some questions have been answered, and some results have led to speculative conclusions, which would require further work to confirm. These are given here.

### 5.1 Conclusions

A minimum number of four unit cells in every direction can give reliable mechanical properties for lattices. This is lower than the six found for foams in 2001. This could be because the structured nature of lattices leads to more reliable behaviour at smaller sizes, compared to the random nature of foams, where the different sizes of pores means a larger number is required to average out the effects.

When considering building lattices for applications, as long as the machine is calibrated in line with the manufacturer's guidelines, there does not appear to be any uneven heat distribution for lattice parts. As such, the position of lattice samples on the build plate does not affect mechanical properties.

Diamond structure lattices do not display the same anisotropic behaviour as solids built with EBM. This is at least true for diamond structure lattices with struts of around 1mm diameter, and at 30-60° angles, however it is possible that struts built parallel or perpendicular to the build direction (such as cubic lattices) may have more in common with solid parts. Lattice structures other than diamond may display anisotropic behaviour, and further work would be needed to investigate this possibility.

When best efforts for quality control are implemented with identical CAD models and machine settings, variations in product, and therefore mechanical properties of lattice occur. As such, comparisons of porous materials made by EBM in the literature should be made with caution. This is from the number of variables available at every stage of the process. Within the literature machine settings and parameters can be very different while being under the umbrella term "the EBM process". Differences in powder

composition seem to have less of an effect, although it is important that the powder be “in specification”.

The ideal EBM lattice for strength applications would have a coarse Widmanstätten structure, with large uniform grains and low porosity. Although this microstructure is in direct contradiction to the highest performing microstructure for solid Ti6Al4V. These conditions can be best achieved by making lattice struts a minimum of 20% thicker than required, post processed with a high pressure HIP treatment and then etched to remove the excess surface. Within this work, the actual increase in strength is moderate, and comes with a moderate increase in stiffness. To etch or HIP the lattices alone leads to brittle lattices with little to no increase in strength, and in the case of HIP, reduces the lattice life (whether the HIP+etch would improve the life of lattices is an area for further investigation). Therefore to improve the lattice, both processes need to be conducted. As these are costly and time consuming processes, it is important for the user to consider how beneficial this would be for the application.

Lattices have different fracture mechanisms at high stresses and large strains compared to low stresses and small strains. At high stresses and large strains, the lattice fractures perpendicular to the test direction, breaking at the nodes by following a horizontal path across the lattice. At low stresses and small strains, the lattice fractures at a 45° angle to the force direction, by accumulated damage at the nodes. Multiple fracture pathways may occur in the lattice.

Under all conditions, lattice struts are easily broken when the structure is exposed to any kind of damage. This is particularly true at high stresses and large strains where the forces can eject the struts from the structure at high speed. At low stresses and small strains, the lattice is more likely to maintain its integrity through uniform deformation, with failure occurring from a shear break 45° to the test direction, however this does not guarantee that individual struts will not break away. It is possible that by covering the strut surfaces with some elastic polymer, if the metal lattice struts would break, the polymer would prevent the metal from leaving the structure. In their current form, however, the ease at which the lattice struts become shrapnel is something to be aware of when considering the application.

## 5.2 Future work

Following the completion of the build, parts are left to cool within the machine. There will be a fast dissipation of heat immediately after the beam has swept over the surface, and then slow cooling over some hours, until the chamber can be opened at 100°C. The HIP process has a controlled period of cooling, where the part will be gradually cooled from high temperatures, although over a shorter time scale. The differences between these cooling rates have clearly led to differences in microstructure. Future work should focus on characterising the cooling times and temperatures in the EBM machine. This could be achieved by installing thermal cameras to monitor the heat input and dissipation on the build surface, and comparing this data to temperature readings from an array of thermocouples on the base plate.

Anisotropy occurs in bulk Ti6Al4V made by AM processes, however does not seem to be in lattices in this study (of 91% porosity). Other studies have observed anisotropy in lattices (with 81% porosity), therefore perhaps there is a transition point for lattices, where anisotropy becomes irrelevant, lying between 81-91% porosity. A study on lattices with graded struts should be conducted to confirm this, and investigate where the anisotropy-isotropy transition point lies.

During the project, despite attempts being made to control machine parameters through thorough discussions between collaborate partners, differences between the builds arose. As such, the method of how the EBM builds lattices has not been systematically investigated, therefore building lattices using different heat themes would lead to a fuller understanding of how the process works, and how the heat themes affect the macro and micro features of the lattices. This would lead to a greater control over the final lattice structures, and their mechanical properties, leading to a fully optimised process and a thorough specification, whereby lattices could be fully customised as required.

Solid parts made by the EBM process have a “skin” on the part surface, which has a different microstructural texture than the inner core of the part. This is often removed during the polishing post processing step which acts to smoothen the surface. For the thin lattice struts, it is possible that the entire lattice structure is comprised of this “skin”. To confirm or reject this hypothesis, energy dispersive X-ray Spectroscopy (EBSD) could be used to look at the texture of the lattice struts, and compare to EBSD from solid parts.

To more accurately define surface roughness, a profile could be made of the strut surface before and after different etching times, to determine a roughness profile. By looking at the amplitude of the peaks and valleys, a numerical value (such as the  $R_a$  value) can be determined to quantify surface roughness, to investigate the effect of etchant in an investigation to improve the surface of lattices by making the surface uniform. This could be used to quantify the effect of the etchant, to more closely link lattice strut surface features to the mechanical properties.

As touched upon in the conclusions, using the HIP alone reduces the life of the lattices, indicating that the microstructure of lattices has an effect on the lifetime, despite the expectation that macro features would dominate the behaviour. Polishing the surface by using an etching agent alone is not enough to make an impact on static strength, indicating that altering macro features alone does not go far enough to improve the mechanical properties. This is contradictory to the “hierarchy” of features expected to dominate lattice behaviour, which should be explored by further work.

While considering the SEM images obtained for the lattices which underwent the HIP treatment, the inherent microstructure that is beneficial for Ti6Al4V lattices (when coupled with a surface alteration by etching) appears to be contrary to the microstructure which improves the strength of Ti6Al4V solids. An investigation into microstructural alteration by HIP, or other heat treatments, is required to scrutinise this finding.

In general, a thorough investigation of fatigue life of metal lattices should be conducted, to consider how the different geometries, macro features and microstructures collate to fatigue life. From this, a database of optimised lattices for various applications could be established, to link which desirable features are obtained from which AM processes. This could be supported by the literature in order to advance lattice technology, and aim to fully understand the best method of manufacture for a given application.

## Chapter 6 References

- [1] R. Boyer, G. Welsch, and E. W. Collings, “Commercially Pure and Modified Titanium,” in *Materials properties handbook : titanium alloys*, ASM International, 2007, pp. 165–260.
- [2] G. Lutjering and J. C. Williams, *Titanium*, 2nd ed. Ohio: Springer, 2007.
- [3] J. Gambogi, “Titanium Mineral Concentrates,” in *U.S. Geological Survey*, 2010, pp. 172–173.
- [4] W. Zhang, Z. Zhu, and C. Y. Cheng, “A literature review of titanium metallurgical processes,” *Hydrometallurgy*, vol. 108, no. 3–4, pp. 177–188, Jul. 2011.
- [5] C. Woodford, *Titanium*. Benchmark Books, 2003.
- [6] J. Barksdale, *Titanium: its occurrence, chemistry, and technology - Jelks Barksdale - Google Books*, 2nd ed. New York: The Ronald Press Company, 1949.
- [7] M. J. Donachie, *Titanium : a technical guide*. ASM International, 2000.
- [8] K. Araci, D. Mangabhai, and K. Akhtar, “Production of titanium by the Armstrong Process®,” in *Titanium Powder Metallurgy*, Elsevier, 2015, pp. 149–162.
- [9] G. Z. Chen, D. Fray, and T. W. Farthing, “Direct Electrochemical Reduction of Titanium Dioxide to Titanium Molten Calcium Chloride,” *Nature*, vol. 407, no. 6802, pp. 361–364, 2000.
- [10] I. Mellor *et al.*, “Titanium powder production via the Metalysis process,” in *Titanium Powder Metallurgy*, Elsevier, 2015, pp. 51–67.
- [11] R. O. Suzuki, “Calciothermic reduction of TiO<sub>2</sub> and in situ electrolysis of CaO in the molten CaCl<sub>2</sub>,” *J. Phys. Chem. Solids*, vol. 66, no. 2–4, pp. 461–465, Feb. 2005.
- [12] D. S. van Vuuren, A. D. Engelbrecht, and T. D. Hadley, “Opportunities in the electrowinning of molten titanium from titanium dioxide,” *JOM*, vol. 57, no. 10, pp. 53–55, Oct. 2005.
- [13] D. Jewell, S. Jiao, M. Kurtanjek, and D. J. Fray, “Titanium Metal Production via Oxycarbide Electro-Refining,” *Int. Titan. Assoc.*, 2012.
- [14] J. K. Beddow, *The Production of Metal Powders by Atomization*. London: Heyden & Son, 1978.
- [15] “Our Technology - AP&C.” [Online]. Available: <http://advancedpowders.com/plasma-atomization-technology/our-technology/>. [Accessed: 24-Sep-2017].
- [16] ASTM International, “Standard Specification for Titanium and Titanium Alloy Strip, Sheet, and Plate,” B265-15, 2015.
- [17] A. Zhecheva, W. Sha, S. Malinov, and A. Long, “Enhancing the microstructure

- and properties of titanium alloys through nitriding and other surface engineering methods,” *Surf. Coatings Technol.*, vol. 200, no. 7, pp. 2192–2207, Dec. 2005.
- [18] E. W. Collings, *Materials Properties Handbook: Titanium Alloys*. Ohio, USA: ASM International, 2007.
- [19] “Titanium-Aluminum (Ti-Al) Phase Diagram.” [Online]. Available: <http://www.calphad.com/titanium-aluminum.html>. [Accessed: 21-Sep-2017].
- [20] P. J. Bania, “Beta titanium alloys and their role in the titanium industry,” *JOM*, vol. 46, no. 7, pp. 16–19, Jul. 1994.
- [21] B. Predel, “Ti-V (Titanium-Vanadium),” in *Subvolume J ‘Pu-Re – Zn-Zr’ of Volume 5 ‘Phase Equilibria, Crystallographic and Thermodynamic Data of Binary Alloys’ of Landolt-Börnstein - Group IV Physical Chemistry*, O. Madelung, Ed. Berlin/Heidelberg: Springer-Verlag, 1998.
- [22] ASTM International, “Standard Specification for Additive Manufacturing Titanium-6 Aluminum-4 Vanadium with Powder Bed Fusion,” F2924-14, 2014.
- [23] Z. Liu and G. Welsch, “Effects of Oxygen and Heat Treatment on the Mechanical Properties of Alpha and Beta Titanium Alloys,” *Metall. Trans. A*, vol. 19, no. 3, pp. 527–542, 1988.
- [24] E. Tal-Gutelmacher and D. Eliezer, “Hydrogen cracking in titanium-based alloys,” *J. Alloys Compd.*, vol. 404–406, pp. 621–625, 2005.
- [25] S. P. Lynch, “Hydrogen embrittlement (HE) phenomena and mechanisms,” in *Stresss Corrosion Cracking, Theory and Practice*, vol. 2011, Cambridge: Woodhead Publishing Limited, pp. 90–130.
- [26] J. B. Cotton, “The role of palladium in enhancing corrosion resistance of titanium,” *Platin. Met. Rev.*, vol. 11, no. 2, pp. 50–52, 1967.
- [27] I. Polmear, *Light Alloys-From Traditional Alloys to Nanocrystals*. London: Elsevier, 2006.
- [28] Y. Fan, P. H. Shipway, G. D. Tansley, and J. Xu, “The Effect of Heat Treatment on Mechanical Properties of Pulsed Nd:YAG Welded Thin Ti6Al4V,” *Adv. Mater. Res.*, vol. 189–193, pp. 3672–3677, Feb. 2011.
- [29] S. Patil *et al.*, “Effect of  $\alpha$  and  $\beta$  Phase Volume Fraction on Machining Characteristics of Titanium Alloy Ti6Al4V,” *Procedia Manuf.*, vol. 6, pp. 63–70, Jan. 2016.
- [30] C. Zheng *et al.*, “Failure mechanisms in ballistic performance of Ti–6Al–4V targets having equiaxed and lamellar microstructures,” *Int. J. Impact Eng.*, vol. 85, pp. 161–169, Nov. 2015.
- [31] R. J. Morrissey, D. L. McDowell, and T. Nicholas, “Frequency and stress ratio effects in high cycle fatigue of Ti-6Al-4V,” *Int. J. Fatigue*, vol. 21, no. 7, pp. 679–685, Aug. 1999.
- [32] L. Wanying, L. Yuanhua, C. Yuhai, S. Taihe, and A. Singh, “Effect of Different Heat Treatments on Microstructure and Mechanical Properties of Ti6Al4V Titanium Alloy,” *Rare Met. Mater. Eng.*, vol. 46, no. 3, pp. 634–639, Mar. 2017.

- [33] G. Lütjering, “Influence of processing on microstructure and mechanical properties of ( + ) titanium alloys,” *Mater. Sci. Eng. A*, vol. 243, no. 1–2, pp. 32–45, Mar. 1998.
- [34] M. R. Bache and W. J. Evans, “Impact of texture on mechanical properties in an advanced titanium alloy,” *Mater. Sci. Eng. A*, vol. 319–321, pp. 409–414, Dec. 2001.
- [35] S. Hémerly and P. Villechaise, “Influence of anisotropy on deformation processes operating in Ti-5Al-5Mo-5V-3Cr at room temperature,” *Acta Mater.*, vol. 141, pp. 285–293, Dec. 2017.
- [36] X. Sun, Y. Guo, Q. Wei, Y. Li, and S. Zhang, “A comparative study on the microstructure and mechanical behavior of titanium: Ultrafine grain vs. coarse grain,” *Mater. Sci. Eng. A*, vol. 669, pp. 226–245, Jul. 2016.
- [37] F. J. Gil, M. P. Ginebra, J. M. Manero, and J. A. Planell, “Formation of  $\beta$ -Widmanstätten structure: effects of grain size and cooling rate on the Widmanstätten morphologies and on the mechanical properties in Ti6Al4V alloy,” *J. Alloys Compd.*, vol. 329, no. 1–2, pp. 142–152, Nov. 2001.
- [38] M. T. Jovanović, S. Tadić, S. Zec, Z. Mišković, and I. Bobić, “The effect of annealing temperatures and cooling rates on microstructure and mechanical properties of investment cast Ti–6Al–4V alloy,” *Mater. Des.*, vol. 27, no. 3, pp. 192–199, Jan. 2006.
- [39] M. Žitňanský and L. Šaplóvič, “Effect of the thermomechanical treatment on the structure of titanium alloy Ti6Al4V,” *J. Mater. Process. Technol.*, vol. 157–158, pp. 643–649, Dec. 2004.
- [40] ASTM International, “Standard Specification for Wrought Titanium-6Aluminum-4Vanadium Alloy for Surgical Implant Applications,” F1472–14 (UNS R56400), 2014.
- [41] R. Schoenberger, “Taming titanium with technology, expertise,” *Aerospace Manufacturing and Design*, 2017. [Online]. Available: <http://magazine.aerospacemanufacturinganddesign.com/article/march-2017/taming-titanium-with-technology-expertise.aspx>. [Accessed: 13-Jun-2017].
- [42] V. N. Divakaren, G. V. V Ravikumar, and S. R. Patnala, “Aircraft Landing Gear Design and Development - How Advanced Technologies are helping to meet the challenges?,” 2017.
- [43] Transparency Market Research, “Titanium Alloys Market - Global Industry Analysis, Size, Share, Growth, Trends and Forecast 2017 - 2025.” [Online]. Available: <https://www.transparencymarketresearch.com/titanium-alloys-market.html>. [Accessed: 17-Aug-2017].
- [44] V. Zatkalíková, P. Palček, L. Markovičová, and M. Chalupová, “Analysis of Fractured Screw Shaped Ti6Al4V Dental Implant,” *Mater. Today Proc.*, vol. 3, no. 4, pp. 1216–1219, Jan. 2016.
- [45] D. G. Bansal, O. L. Eryilmaz, and P. J. Blau, “Surface engineering to improve the durability and lubricity of Ti–6Al–4V alloy,” *Wear*, vol. 271, no. 9–10, pp. 2006–2015, Jul. 2011.

- [46] C. W. Hull, "Apparatus for production of three-dimensional objects by stereolithography," US4575330 A, 1984.
- [47] K. P. Karunakaran, S. Suryakumar, V. Pushpa, and S. Akula, "Low cost integration of additive and subtractive processes for hybrid layered manufacturing," *Robot. Comput. Integr. Manuf.*, vol. 26, no. 5, pp. 490–499, Oct. 2010.
- [48] Sandia National Laboratories, "Laser Engineered Net Shaping Manufacturing Technologies." [Online]. Available: <http://www.sandia.gov/mst/pdf/LENS.pdf>. [Accessed: 18-Aug-2017].
- [49] R. Lancaster, G. Davies, H. Illsley, S. Jeffs, and G. Baxter, "Structural integrity of an electron beam melted titanium alloy," *Materials (Basel)*, vol. 9, no. 6, 2016.
- [50] Y. K. Ahn *et al.*, "Mechanical and microstructural characteristics of commercial purity titanium implants fabricated by electron-beam additive manufacturing," *Mater. Lett.*, vol. 187, pp. 64–67, Jan. 2017.
- [51] B. J. Merema *et al.*, "The design, production and clinical application of 3D patient-specific implants with drilling guides for acetabular surgery," *Injury*, vol. 48, no. 11, pp. 2540–2547, Nov. 2017.
- [52] M. Bram, T. Ebel, M. Wolff, A. P. Cysne Barbosa, and N. Tuncer, "Applications of Powder Metallurgy in Biomaterials," in *Advances in Powder Metallurgy*, I. Chang and Y. Zhao, Eds. Woodhead Publishing Limited, 2013, pp. 520–554.
- [53] I. Gibson, D. W. Rosen, and B. Stucker, *Additive manufacturing Technologies - 3D Printing, Rapid Prototyping and Direct Digital Manufacturing*, 2nd ed. New York: Springer, 2015.
- [54] ExOne, "ExOne Home." [Online]. Available: <http://www.exone.com/>. [Accessed: 12-Mar-2017].
- [55] Norsk Titanium, "Norsk Titanium – Forged Strength at the Speed of Innovation." [Online]. Available: [http://www.norsktitanium.com/#\\_technology](http://www.norsktitanium.com/#_technology). [Accessed: 29-Aug-2017].
- [56] BeAM S.A.S, "Technology." [Online]. Available: <http://beam-machines.fr/en/technology>. [Accessed: 14-Sep-2017].
- [57] J. DeLalio, "Electron beam or laser beam welding?," *The Fabricator*, 2016. [Online]. Available: <http://www.thefabricator.com/article/laserwelding/electron-beam-or-laser-beam-welding->. [Accessed: 13-Mar-2017].
- [58] J. K. Watson, K. M. Tamingler, R. A. Hafley, and D. D. Petersen, "Development of a Prototype Low-Voltage Electron Beam Freeform Fabrication system," in *Solid Freeform Fabrication Proceedings*, 2002, pp. 458–465.
- [59] L. Parry, I. A. Ashcroft, and R. D. Wildman, "Understanding the effect of laser scan strategy on residual stress in selective laser melting through thermo-mechanical simulation," *Addit. Manuf.*, vol. 12, pp. 1–15, 2016.
- [60] C. Li, J. F. Liu, and Y. B. Guo, "Prediction of Residual Stress and Part Distortion in Selective Laser Melting," *Procedia CIRP*, vol. 45, pp. 171–174, 2016.

- [61] H. Ali, L. Ma, H. Ghadbeigi, and K. Mumtaz, "In-situ residual stress reduction, martensitic decomposition and mechanical properties enhancement through high temperature powder bed pre-heating of Selective Laser Melted Ti6Al4V," *Mater. Sci. Eng. A*, vol. 695, no. February, pp. 211–220, 2017.
- [62] N. Kalentics *et al.*, "3D Laser Shock Peening – A new method for the 3D control of residual stresses in Selective Laser Melting," *Mater. Des.*, vol. 130, no. April, pp. 350–356, 2017.
- [63] A. Bandyopadhyay, B. V Krishna, W. Xue, and S. Bose, "Application of Laser Engineered Net Shaping (LENS) to manufacture porous and functionally graded structures for load bearing implants," *J. Mater. Sci. Mater. Med.*, vol. 20, no. S1, pp. 29–34, Dec. 2009.
- [64] Arcam AB, "History - Arcam AB." [Online]. Available: <http://www.arcam.com/company/about-arcam/history/>. [Accessed: 22-Sep-2017].
- [65] S. S. Al-Bermani, M. L. Blackmore, W. Zhang, and I. Todd, "The Origin of Microstructural Diversity, Texture, and Mechanical Properties in Electron Beam Melted Ti-6Al-4V," *Metall. Mater. Trans. A*, vol. 41A, pp. 3422–3434, 2010.
- [66] L. D. Bobbio, S. Qin, A. Dunbar, P. Michaleris, and A. M. Beese, "Characterization of the strength of support structures used in powder bed fusion additive manufacturing of Ti-6Al-4V," *Addit. Manuf.*, vol. 14, pp. 60–68, Mar. 2017.
- [67] D. Morgan, E. Agba, and C. Hill, "Support Structure Development and Initial Results for Metal Powder Bed Fusion Additive Manufacturing," *Procedia Manuf.*, vol. 10, pp. 819–830, Jan. 2017.
- [68] J. K. Algardh *et al.*, "Thickness dependency of mechanical properties for thin-walled titanium parts manufactured by Electron Beam Melting (EBM)®," *Addit. Manuf.*, vol. 12, pp. 45–50, Oct. 2016.
- [69] E. Hernandez-Nava *et al.*, "The effect of defects on the mechanical response of Ti-6Al-4V cubic lattice structures fabricated by electron beam melting," *Acta Mater.*, vol. 108, pp. 279–292, 2016.
- [70] H. P. Tang, M. Qian, N. Liu, X. Z. Zhang, G. Y. Yang, and J. Wang, "Effect of Powder Reuse Times on Additive Manufacturing of Ti-6Al-4V by Selective Electron Beam Melting," *JOM*, vol. 67, no. 3, pp. 555–563, Mar. 2015.
- [71] N. Hrabe, T. Gnäupel-Herold, and T. Quinn, "Fatigue properties of a titanium alloy (Ti-6Al-4V) fabricated via electron beam melting (EBM): Effects of internal defects and residual stress," *Int. J. Fatigue*, vol. 94, pp. 202–210, 2017.
- [72] Arcam AB, "Arcam Q20plus." [Online]. Available: <http://www.arcam.com/technology/products/arcam-q20/>. [Accessed: 22-Jul-2017].
- [73] M. Cronskär, M. Bäckström, and L. Rännar, "Production of customized hip stem prostheses – a comparison between conventional machining and electron beam melting (EBM)," *Rapid Prototyp. J.*, vol. 19, no. 5, pp. 365–372, Jul. 2013.
- [74] H. Huang *et al.*, "Surface characterization and in vivo performance of plasma-sprayed hydroxyapatite-coated porous Ti6Al4V implants generated by electron

- beam melting,” *Surf. Coatings Technol.*, vol. 283, pp. 80–88, Dec. 2015.
- [75] M. Sandomierski, T. Buchwald, B. Strzemieska, and A. Voelkel, “Modification of Ti6Al4V surface by diazonium compounds,” *Spectrochim. Acta Part A Mol. Biomol. Spectrosc.*, vol. 191, pp. 27–35, Feb. 2018.
- [76] S. Bruschi, R. Bertolini, F. Medeossi, A. Ghiotti, E. Savio, and R. Shivpuri, “Case study: The application of machining-conditioning to improve the wear resistance of Ti6Al4V surfaces for human hip implants,” *Wear*, vol. 394–395, pp. 134–142, Jan. 2018.
- [77] P. Lhuissier, C. de Formanoir, G. Martin, R. Dendievel, and S. Godet, “Geometrical control of lattice structures produced by EBM through chemical etching: Investigations at the scale of individual struts,” *Mater. Des.*, vol. 110, pp. 485–493, Nov. 2016.
- [78] M. Kahlin, H. Ansell, and J. J. Moverare, “Fatigue behaviour of additive manufactured Ti6Al4V, with as-built surfaces, exposed to variable amplitude loading,” *Int. J. Fatigue*, vol. 103, pp. 353–362, Oct. 2017.
- [79] C. De Formanoir, S. Michotte, O. Rigo, L. Germain, and S. Godet, “Electron beam melted Ti–6Al–4V: Microstructure, texture and mechanical behavior of the as-built and heat-treated material,” *Mater. Sci. Eng. A*, vol. 652, pp. 105–119, Jan. 2016.
- [80] M. Benedetti, M. Cazzolli, V. Fontanari, and M. Leoni, “Fatigue limit of Ti6Al4V alloy produced by Selective Laser Sintering,” *Procedia Struct. Integr.*, vol. 2, pp. 3158–3167, Jan. 2016.
- [81] H. Galarraga, R. J. Warren, D. A. Lados, R. R. Dehoff, M. M. Kirka, and P. Nandwana, “Effects of heat treatments on microstructure and properties of Ti-6Al-4V ELI alloy fabricated by electron beam melting (EBM),” *Mater. Sci. Eng. A*, vol. 685, pp. 417–428, Feb. 2017.
- [82] H. K. Rafi, N. V. Karthik, H. Gong, T. L. Starr, and B. E. Stucker, “Microstructures and Mechanical Properties of Ti6Al4V Parts Fabricated by Selective Laser Melting and Electron Beam Melting,” *J. Mater. Eng. Perform.*, vol. 22, no. 12, pp. 3872–3883, Dec. 2013.
- [83] X. Gong *et al.*, “Building direction dependence of corrosion resistance property of Ti–6Al–4V alloy fabricated by electron beam melting,” *Corros. Sci.*, vol. 127, pp. 101–109, Oct. 2017.
- [84] F. Wang, S. Williams, P. Colegrove, and A. A. Antonysamy, “Microstructure and Mechanical Properties of Wire and Arc Additive Manufactured Ti-6Al-4V,” *Metall. Mater. Trans. A*, vol. 44, no. 2, pp. 968–977, Feb. 2013.
- [85] P. Mengucci *et al.*, “Effects of build orientation and element partitioning on microstructure and mechanical properties of biomedical Ti-6Al-4V alloy produced by laser sintering,” *J. Mech. Behav. Biomed. Mater.*, vol. 71, pp. 1–9, Jul. 2017.
- [86] Y. Zhong *et al.*, “Additive manufacturing of 316L stainless steel by electron beam melting for nuclear fusion applications,” *J. Nucl. Mater.*, vol. 486, pp. 234–245, Apr. 2017.

- [87] S. H. Sun, Y. Koizumi, S. Kurosu, Y. P. Li, H. Matsumoto, and A. Chiba, "Build direction dependence of microstructure and high-temperature tensile property of Co-Cr-Mo alloy fabricated by electron beam melting," *Acta Mater.*, vol. 64, pp. 154–168, Feb. 2014.
- [88] D. Deng, J. Moverare, R. L. Peng, and H. Söderberg, "Microstructure and anisotropic mechanical properties of EBM manufactured Inconel 718 and effects of post heat treatments," *Mater. Sci. Eng. A*, vol. 693, pp. 151–163, May 2017.
- [89] A. A. Antonysamy, J. Meyer, and P. B. Prangnell, "Effect of build geometry on the  $\alpha$ -grain structure and texture in additive manufacture of Ti6Al4V by selective electron beam melting," *Mater. Charact.*, vol. 84, pp. 153–168, Oct. 2013.
- [90] X. Tan *et al.*, "Graded microstructure and mechanical properties of additive manufactured Ti-6Al-4V via electron beam melting," *Acta Mater.*, vol. 97, 2015.
- [91] Y. Zhai, H. Galarraga, and D. A. Lados, "Microstructure, static properties, and fatigue crack growth mechanisms in Ti-6Al-4V fabricated by additive manufacturing: LENS and EBM," *Eng. Fail. Anal.*, vol. 69, pp. 3–14, Nov. 2016.
- [92] H. K. Rafi, N. V Karthik, T. L. Starr, and B. E. Stucker, "Mechanical property evaluation of Ti-6Al-4V parts made using Electron Beam Melting," in *Annual International Solid Freeform Fabrication Symposium*, 2012, pp. 526–535.
- [93] J. Banhart, "Light-Metal Foams-History of Innovation," *Adv. Eng. Mater.*, vol. 15, no. 3, pp. 83–111, 2013.
- [94] M. A. De Meller, "Produit metallique pour l'obtention d'objets lamines, moules ou autres, et procedes pour sa fabrication," 615,147, 1925.
- [95] B. Sosnick, "Process of making foamlike mass of metal," 2,434,775, 1943.
- [96] J. C. Elliott, "Method of producing metal foam," 2,751,289,775, 1951.
- [97] J. C. Elliott, "Metal foaming process," 3,005,700, 1961.
- [98] J. Banhart, "Manufacture, characterisation and application of cellular metals and metal foams," *Prog. Mater. Sci.*, vol. 46, no. 6, pp. 559–632, Jan. 2001.
- [99] P. Lui and G. F. Chen, *Porous Materials Processing and Applications*. 2014.
- [100] J. Banhart, "Manufacturing Routes for Metallic Foams," *JOM*, vol. 52, no. 12, pp. 22–27, 2000.
- [101] R. Goodall and A. Mortensen, "Porous Metals," in *Physical Metallurgy: Fifth Edition*, Fifth Edit., vol. 1, no. Bâtiment MX, Elsevier, 2014, pp. 2399–2595.
- [102] C. Yan, L. Hao, A. Hussein, P. Young, J. Huang, and W. Zhu, "Microstructure and mechanical properties of aluminium alloy cellular lattice structures manufactured by direct metal laser sintering," *MatSciEngA*, vol. 628, pp. 238–246, 2015.
- [103] S. Arabnejad and D. Pasini, "Mechanical properties of lattice materials via asymptotic homogenization and comparison with alternative homogenization methods," *IntJMechSci*, vol. 77, pp. 249–262, 2013.
- [104] S. Kim and C. W. Lee, "A Review on Manufacturing and Application of Open-

- cell Metal Foam,” *Procedia Mater. Sci.*, vol. 4, pp. 305–309, Jan. 2014.
- [105] Y. Gaillard and J. Dairon, “Casting parts with metallic foam,” in *6th International Conference on Porous Metals and Metallic Foams*, 2009.
- [106] J. O. Osorio-Hernandez, M. A. Suarez, R. Goodall, G. A. Lara-Rodriguez, I. Alfonso, and I. A. Figueroa, “Manufacturing of open-cell Mg foams by replication process and mechanical properties,” *Mater. Des.*, vol. 64, pp. 136–141, 2014.
- [107] A. Jinnapat and A. Kennedy, “The Manufacture and Characterisation of Aluminium Foams Made by Investment Casting Using Dissolvable Spherical Sodium Chloride Bead Preforms,” *Metals (Basel)*, vol. 1, no. 1, pp. 49–64, 2011.
- [108] D. P. Haack, K. R. Butcher, T. Kim, H. P. Hoduston, and T. J. Lu, “Novel Lightweight Metal Foam Heat Exchangers,” *Proc. V.3 (PID-4B Heat Exch. Appl. Chang. Phase Media Fuel Cells Syst. B. No. I00548)*, pp. 1–7, 2001.
- [109] B. Ozmat, B. Leyda, and B. Benson, “Thermal Applications of Open-Cell Metal Foams,” *Mater. Manuf. Process.*, vol. 19, no. 5, pp. 839–862, 2004.
- [110] M. J. Campagna and R. J. Moffat, “Heat exchanger with conduit surrounded by metal foam,” 2011.
- [111] 강신왕 and 김태규, “Metal-foam catalyst for hydrogen generation from chemical hydride and method for manufacturing same,” WO 2013018993 A2, 2013.
- [112] 박만호, 류덕수, and 박미정, “Metal foam catalyst support having reaction point of 3d structure without increase in exhaust gas pressure.” Google Patents, 2014.
- [113] D. I. Park and T. G. Kim, “Hydrogen Generation from Sodium boro-hydride Hydrolysis on Co-Ni-P-B/Ni Foam Catalyst,” *Trans. Korean Hydrog. new energy Soc.*, vol. 21, no. 5, pp. 383–389, 2010.
- [114] H. T. Kim, “Filter device for reducing automobile exhaust fume,” US 8444738 B2, 2013.
- [115] F. Chi, D. P. Haack, and L. S. Aubrey, “Low expansion corrosion resistant ceramic foam filters for molten aluminum filtration,” US20120175804 A1, 2012.
- [116] L. S. Aubrey, “Porous reticulated metal foam for filtering molten magnesium,” US8202346 B1, 2012.
- [117] 李建坤, “Engine exhaust pipe silencer with tail gas purifying function, replaceable filter element and obvious silencing effect,” CN105587377 A, 2016.
- [118] A. J. Sherman, J. Brockmeyer, G. Peters, and R. H. Tuffias, “Flash suppressor,” US 6298764 B1, 2000.
- [119] S. Guinehut, “Energy-absorbing case for a motor vehicle bumper beam,” US7240932 B2, 2007.
- [120] T. D. Claar, H. H. Eifert, and C. J. Yu, “Use of metal foams in armor systems,” EP1078215 A1, 2001.

- [121] X. J. Wang *et al.*, “Topological design and additive manufacturing of porous metals for bone scaffolds and orthopaedic implants: A review,” *Biomaterials*, vol. 83, pp. 127–141, Mar. 2016.
- [122] L. E. Murr *et al.*, “Next-generation biomedical implants using additive manufacturing of complex, cellular and functional mesh arrays,” *Philos. Trans. A. Math. Phys. Eng. Sci.*, vol. 368, no. 1917, pp. 1999–2032, Apr. 2010.
- [123] L. E. Murr, S. M. Gaytan, E. Martinez, F. Medina, and R. B. Wicker, “Next Generation Orthopaedic Implants by Additive Manufacturing Using Electron Beam Melting,” *Int. J. Biomater.*, vol. 2012, pp. 1–14, 2012.
- [124] M. Regis, E. Marin, L. Fedrizzi, and M. Pressacco, “Additive manufacturing of Trabecular Titanium orthopedic implants,” *MRS Bull.*, vol. 40, no. 02, pp. 137–144, 2015.
- [125] N. W. Hrabe, P. Heintl, R. K. Bordia, C. Körner, and R. J. Fernandes, “Maintenance of a bone collagen phenotype by osteoblast-like cells in 3D periodic porous titanium (Ti-6Al-4 V) structures fabricated by selective electron beam melting,” *Connect. Tissue Res.*, vol. 54, no. 6, pp. 351–360, Nov. 2013.
- [126] Y. Bo, Z. Linxi, Y. Quanzhan, Z. Guirong, Z. Fangxin, and S. Gang, “Additive manufacturing technologies of porous metal implants,” *China Foundry*, vol. 11, no. 4, 2014.
- [127] R. Mueller, S. Soubielle, R. Goodall, F. Diologent, and A. Mortensen, “On the steady-state creep of microcellular metals,” *Scr. Mater.*, vol. 57, no. 1, pp. 33–36, 2007.
- [128] W. Van Grunsven, E. Hernandez-Nava, G. C. Reilly, and R. Goodall, “The effect of density and feature size on mechanical properties of isostructural metallic foams produced by additive manufacturing,” *Metals (Basel)*, vol. 4, pp. 401–409, 2014.
- [129] M. Mamun and V. Bindiganavile, “Specimen size effects and dynamic fracture toughness of cement based foams,” *J. Mater. Civ. Eng.*, vol. 26, no. 1, pp. 143–151, 2014.
- [130] C. Shin, S. Lim, H. Jin, P. Hosemann, and J. Kwon, “Specimen size effects on the weakening of a bulk metastable austenitic alloy,” *Mater. Sci. Eng. A*, vol. 622, pp. 67–75, 2015.
- [131] E. W. Andrews, G. Gioux, P. Onck, and L. J. Gibson, “Size effects in ductile cellular solids. Part II: experimental results,” *Int Jour Mech Sci*, pp. 701–713, 2001.
- [132] J. Parthasarathy, B. Starly, S. Raman, and A. Christensen, “Mechanical evaluation of porous titanium (Ti6Al4V) structures with electron beam melting (EBM),” *J. Mech. Behav. Biomed. Mater.*, vol. 3, pp. 249–259, 2010.
- [133] S. M. Ahmadi *et al.*, “Mechanical behavior of regular open-cell porous biomaterials made of diamond lattice unit cells,” *Mech. Behav. Biomed. Mater.*, vol. 34, pp. 106–115, 2014.
- [134] A. Herrera, A. Yáñez, O. Martel, H. Afonso, and D. Monopoli, “Computational study and experimental validation of porous structures fabricated by electron

- beam melting: A challenge to avoid stress shielding,” *Mater. Sci. Eng. C*, vol. 45, pp. 89–93, Dec. 2014.
- [135] X. P. Tan, Y. J. Tan, C. S. L. Chow, S. B. Tor, and W. Y. Yeong, “Metallic powder-bed based 3D printing of cellular scaffolds for orthopaedic implants: A state-of-the-art review on manufacturing, topological design, mechanical properties and biocompatibility,” *Materials Science and Engineering C*, vol. 76. Elsevier, pp. 1328–1343, 01-Jul-2017.
- [136] T. J. Horn, O. L. A. Harrysson, D. J. Marcellin-Little, H. A. West, B. D. X. Lascelles, and R. Aman, “Flexural properties of Ti6Al4V rhombic dodecahedron open cellular structures fabricated with electron beam melting,” *Addit. Manuf.*, vol. 1–4, pp. 2–11, Oct. 2014.
- [137] J. Kadkhodapour *et al.*, “Failure mechanisms of additively manufactured porous biomaterials: Effects of porosity and type of unit cell,” *J. Mech. Behav. Biomed. Mater.*, vol. 50, pp. 180–191, Oct. 2015.
- [138] M. Dumas, P. Terriault, and V. Brailovski, “Modelling and characterization of a porosity graded lattice structure for additively manufactured biomaterials,” *Mater. Des.*, vol. 121, pp. 383–392, May 2017.
- [139] V. Weißmann, R. Bader, H. Hansmann, and N. Laufer, “Influence of the structural orientation on the mechanical properties of selective laser melted Ti6Al4V open-porous scaffolds,” *Mater. Des.*, vol. 95, pp. 188–197, Apr. 2016.
- [140] A. Deschamps, G. Martin, R. Dendievel, and H. P. Van Landeghem, “Lighter structures for transports: The role of innovation in metallurgy,” *Comptes Rendus Phys.*, vol. 18, no. 7–8, pp. 445–452, Sep. 2017.
- [141] I. Maskery *et al.*, “Mechanical Properties of Ti-6Al-4V Selectively Laser Melted Parts with Body-Centred-Cubic Lattices of Varying cell size,” *Exp. Mech.*, vol. 55, no. 7, pp. 1261–1272, Sep. 2015.
- [142] M. Mazur, M. Leary, S. Sun, M. Vcelka, D. Shidid, and M. Brandt, “Deformation and failure behaviour of Ti-6Al-4V lattice structures manufactured by selective laser melting (SLM),” *Int. J. Adv. Manuf. Technol.*, vol. 84, no. 5–8, pp. 1391–1411, Sep. 2015.
- [143] M. T. Tilbrook, D. D. Radford, V. S. Deshpande, and N. A. Fleck, “Dynamic crushing of sandwich panels with prismatic lattice cores,” *Int. J. Solids Struct.*, vol. 44, no. 18–19, pp. 6101–6123, 2007.
- [144] T. George, V. S. Deshpande, and H. N. G. Wadley, “Mechanical response of carbon fiber composite sandwich panels with pyramidal truss cores,” *Compos. Part A Appl. Sci. Manuf.*, vol. 47, no. 1, pp. 31–40, 2013.
- [145] H. N. G. Wadley *et al.*, “Deformation and fracture of impulsively loaded sandwich panels,” *J. Mech. Phys. Solids*, vol. 61, no. 2, pp. 674–699, 2013.
- [146] J. M. Hundley, E. C. Clough, and A. J. Jacobsen, “The low velocity impact response of sandwich panels with lattice core reinforcement,” *Int. J. Impact Eng.*, vol. 84, pp. 64–77, 2015.
- [147] K. Wei, Y. Peng, K. Wang, F. Yang, S. Cheng, and T. Zeng, “High temperature mechanical properties of lightweight C/SiC composite pyramidal lattice core

sandwich panel,” *Compos. Struct.*, vol. 178, pp. 467–475, 2017.

- [148] M. F. Ashby, “The properties of foams and lattices,” *Philos. Trans. A. Math. Phys. Eng. Sci.*, vol. 364, no. 1838, pp. 15–30, Jan. 2006.
- [149] V. S. Deshpande, M. F. Ashby, and N. A. Fleck, “Foam topology: Bending versus stretching dominated architectures,” *Acta Mater.*, vol. 49, no. 6, pp. 1035–1040, 2001.
- [150] R. A. Rahman Rashid, J. Mallavarapu, S. Palanisamy, and S. H. Masood, “A comparative study of flexural properties of additively manufactured aluminium lattice structures,” *Mater. Today Proc.*, vol. 4, no. 8, pp. 8597–8604, 2017.
- [151] M. Kaur, T. G. Yun, S. M. Han, E. L. Thomas, and W. S. Kim, “3D printed stretching-dominated micro-trusses,” *Mater. Des.*, vol. 134, pp. 272–280, 2017.
- [152] C. Bonatti and D. Mohr, “Large deformation response of additively-manufactured FCC metamaterials: From octet truss lattices towards continuous shell mesostructures,” *Int. J. Plast.*, vol. 92, pp. 122–147, 2017.
- [153] F. Brenne, T. Niendorf, and H. J. Maier, “Additively manufactured cellular structures: Impact of microstructure and local strains on the monotonic and cyclic behavior under uniaxial and bending load,” *J. Mater. Process. Technol.*, vol. 213, no. 9, pp. 1558–1564, Sep. 2013.
- [154] S. McKown *et al.*, “The quasi-static and blast loading response of lattice structures,” *Int. J. Impact Eng.*, vol. 35, no. 8, pp. 795–810, Aug. 2008.
- [155] T. Tancogne-Dejean, A. B. Spierings, and D. Mohr, “Additively-manufactured metallic micro-lattice materials for high specific energy absorption under static and dynamic loading,” *Acta Mater.*, vol. 116, pp. 14–28, Sep. 2016.
- [156] H. D. Carlton *et al.*, “Mapping local deformation behavior in single cell metal lattice structures,” *Acta Mater.*, vol. 129, pp. 239–250, May 2017.
- [157] A. Desmoulins and D. M. Kochmann, “Local and nonlocal continuum modeling of inelastic periodic networks applied to stretching-dominated trusses,” *Comput. Methods Appl. Mech. Eng.*, vol. 313, pp. 85–105, 2017.
- [158] A. Vigliotti and D. Pasini, “Linear multiscale analysis and finite element validation of stretching and bending dominated lattice materials,” *Mech. Mater.*, vol. 46, pp. 57–68, 2012.
- [159] M. Galati and L. Iuliano, “A literature review of powder-based electron beam melting focusing on numerical simulations,” *Addit. Manuf.*, vol. 19, pp. 1–20, Jan. 2018.
- [160] A. Zargarian, M. Esfahanian, J. Kadkhodapour, and S. Ziaei-Rad, “Numerical simulation of the fatigue behavior of additive manufactured titanium porous lattice structures,” *Mater. Sci. Eng. C*, vol. 60, pp. 339–347, Mar. 2016.
- [161] S. Tammis-Williams, H. Zhao, F. Leonard, F. Derguti, I. Todd, and P. B. Prangnell, “XCT analysis of the influence of melt strategies on defect population in Ti-6Al-4V components manufactured by Selective Electron Beam Melting,” *Mater. Charact.*, vol. 102, pp. 47–61, 2015.

- [162] A. Safdar, H. Z. He, L. Y. Wei, A. Snis, C. de Paz, and L. Eduardo, "Effect of process parameters settings and thickness on surface roughness of EBM produced Ti-6Al-4V," *Rapid Prototyp. J.*, vol. 18, no. 5, pp. 401–408, 2012.
- [163] N. Béraud, F. Vignat, F. Villeneuve, and R. Dendievel, "Improving dimensional accuracy in EBM using beam characterization and trajectory optimization," *Addit. Manuf.*, vol. 14, pp. 1–6, Mar. 2017.
- [164] C. Qiu, N. J. E. Adkins, and M. M. Attallah, "Microstructure and tensile properties of selectively laser-melted and of HIPed laser-melted Ti-6Al-4V," *Mater. Sci. Eng. A*, vol. 578, pp. 230–239, 2013.
- [165] X. Zhao *et al.*, "Comparison of the microstructures and mechanical properties of Ti-6Al-4V fabricated by selective laser melting and electron beam melting," *Mater. Des.*, vol. 95, pp. 21–31, Apr. 2016.
- [166] O. Cansizoglu, O. Harrysson, D. Cormier, H. West, and T. Mahale, "Properties of Ti-6Al-4V non-stochastic lattice structures fabricated via electron beam melting," *Mater. Sci. Eng. A*, vol. 492, no. 1–2, pp. 468–474, Sep. 2008.
- [167] A. Ataee, Y. Li, D. Fraser, G. Song, and C. Wen, "Anisotropic Ti-6Al-4V gyroid scaffolds manufactured by electron beam melting (EBM) for bone implant applications," *Mater. Des.*, vol. 137, pp. 345–354, Jan. 2018.
- [168] E. Sallica-Leva, A. L. Jardini, and J. Fogagnolo, "Microstructure and mechanical behavior of porous Ti-6Al-4V parts obtained by selective laser melting," *J. Mech. Behav. Biomed. Mater.*, vol. 26, pp. 98–108, 2013.
- [169] L. J. Gibson and M. F. Ashby, *Cellular solids - Structure and Properties*, 2nd ed. Cambridge: Cambridge University Press, 2001.
- [170] I. Maskery *et al.*, "A mechanical property evaluation of graded density Al-Si10-Mg lattice structures manufactured by selective laser melting," *Mater. Sci. Eng. A*, vol. 670, pp. 264–274, Jul. 2016.
- [171] L. R. Meza *et al.*, "Reexamining the mechanical property space of three-dimensional lattice architectures," *Acta Mater.*, vol. 140, pp. 424–432, Nov. 2017.
- [172] S. Y. Choy, C. N. Sun, K. F. Leong, and J. Wei, "Compressive properties of Ti-6Al-4V lattice structures fabricated by selective laser melting: Design, orientation and density," *Addit. Manuf.*, vol. 16, pp. 213–224, Aug. 2017.
- [173] M. Mazur, M. Leary, M. McMillan, S. Sun, D. Shidid, and M. Brandt, "Mechanical properties of Ti6Al4V and AlSi12Mg lattice structures manufactured by Selective Laser Melting (SLM)," in *Laser Additive Manufacturing*, Elsevier, 2017, pp. 119–161.
- [174] Y. Kok *et al.*, "Anisotropy and heterogeneity of microstructure and mechanical properties in metal additive manufacturing: A critical review," *Mater. Des.*, vol. 139, pp. 565–586, Feb. 2018.
- [175] P. Heinl, L. Muller, C. Korner, R. F. Singer, and A. Muller, "Cellular Ti-6Al-4V structures with interconnected macro porosity for bone implants fabricated by selective electron beam melting," *Acta Biomater.*, vol. 4, pp. 1536–1544, 2008.

- [176] R. Wauthle *et al.*, “Effects of built orientation and heat treatment on the microstructure and mechanical properties of selective laser melted Ti6Al4V lattice structures,” *Addit. Manuf.*, vol. 5 SRC-Go, pp. 77–84, 2015.
- [177] M. F. Ashby, H. Shercliff, and D. Cebon, *Materials : engineering, science, processing and design*. Elsevier Butterworth-Heinemann, 2007.
- [178] R. I. Stephens, A. Fatemi, R. R. Stephens, and H. O. Fuchs, *Metal fatigue in engineering*, 2nd ed. Wiley, 2001.
- [179] J. D. Kalbfleisch and R. Prentice, *The Statistical Analysis of Failure Time*. John Wiley & sons, 1980.
- [180] D. Collett, *Modelling survival Data in Medical Research*, 3rd ed. London: Taylor & Francis Group, ., 2015.
- [181] R. L. Carlson, G. A. Kardomateas, and J. I. Craig, “Fatigue in Metals,” Springer, Dordrecht, 2012, pp. 19–39.
- [182] N. J. Dunne, J. F. Orr, M. T. Mushipe, and R. J. Eveleigh, “The relationship between porosity and fatigue characteristics of bone cements,” *Biomaterials*, vol. 24, no. 2, pp. 239–245, Jan. 2003.
- [183] C. Laird, “The fatigue limits of metals,” *Mater. Sci. Eng.*, vol. 22, pp. 231–236, 1976.
- [184] D. Kuhlmann-Wilsdorf and C. Laird, “Dislocation behavior in fatigue,” *Mater. Sci. Eng.*, vol. 27, no. 2, pp. 137–156, Feb. 1977.
- [185] P. Lukáš and L. Kunz, “Role of persistent slip bands in fatigue,” *Philos. Mag.*, vol. 84, no. 3–5, pp. 317–330, Jan. 2004.
- [186] P. C. Paris, M. P. Gomez, and W. E. Anderson, “A Rational Analytic Theory of Fatigue,” *Trend Eng.*, vol. 13, pp. 9–14, 1961.
- [187] S. S. Manson, “Behaviour of materials under conditions of Thermal Stress,” *Natl. Advis. Comm. Aeronaut.*, 1953.
- [188] L. F. Coffin, “A study of the effects of cyclic thermal stresses on a ductile metal,” *Trans. ASME*, vol. 76, pp. 931–950, 1954.
- [189] G. Q. Wu, C. L. Shi, W. Sha, A. X. Sha, and H. R. Jiang, “Effect of microstructure on the fatigue properties of Ti–6Al–4V titanium alloys,” *Mater. Des.*, vol. 46, pp. 668–674, Apr. 2013.
- [190] H. Gong, K. Rafi, H. Gu, G. D. Janaki Ram, T. Starr, and B. Stucker, “Influence of defects on mechanical properties of Ti-6Al-4V components produced by selective laser melting and electron beam melting,” *Mater. Des.*, vol. 86, 2015.
- [191] R. Kone ná, L. Kunz, A. Ba a, and G. Nicoletto, “Long Fatigue Crack Growth in Ti6Al4V Produced by Direct Metal Laser Sintering,” *Procedia Eng.*, vol. 160, pp. 69–76, Jan. 2016.
- [192] P. Edwards, A. O’Conner, and M. Ramulu, “Electron Beam Additive Manufacturing of Titanium Components: Properties and Performance,” *J. Manuf. Sci. Eng.*, vol. 135, no. 6, p. 061016, 2013.

- [193] P. Li, D. H. Warner, A. Fatemi, and N. Phan, "Critical assessment of the fatigue performance of additively manufactured Ti-6Al-4V and perspective for future research," *Int. J. Fatigue*, vol. 85, pp. 130–143, Apr. 2016.
- [194] E. Brandl, C. Leyens, and F. Palm, "Mechanical properties of additive manufactured Ti-6Al-4V using wire and powder based processes," *IOP Conf. Ser. Mater. Sci. Eng.*, vol. 26, no. 1, 2011.
- [195] U. Ackelid and M. Svensson, "Additive manufacturing of dense metal parts by electron beam melting," in *EURO PM, International Powder Metallurgy Congress & Exhibition. PM in Copenhagen - Linking Industry and Technology, 2009*, 2009, pp. 179–184.
- [196] T. Persenot, J. Y. Buffiere, E. Maire, R. Dendievel, and G. Martin, "Fatigue properties of EBM as-built and chemically etched thin parts," *Procedia Struct. Integr.*, vol. 7, pp. 158–165, 2017.
- [197] M. Kahlin, H. Ansell, and J. J. Moverare, "Fatigue behaviour of notched additive manufactured Ti6Al4V with as-built surfaces," *Int. J. Fatigue*, vol. 101, pp. 51–60, Aug. 2017.
- [198] S. Beretta and S. Romano, "A comparison of fatigue strength sensitivity to defects for materials manufactured by AM or traditional processes," *Int. J. Fatigue*, vol. 94, pp. 178–191, Jan. 2017.
- [199] M. Zhao, X. Fan, and T. J. Wang, "Fatigue damage of closed-cell aluminum alloy foam: Modeling and mechanisms," *Int. J. Fatigue*, vol. 87, pp. 257–265, Jun. 2016.
- [200] R. Hedayati, S. Amin Yavari, and A. A. Zadpoor, "Fatigue crack propagation in additively manufactured porous biomaterials," *Mater. Sci. Eng. C*, vol. 76, pp. 457–463, Jul. 2017.
- [201] S. Zhao, S. J. Li, W. T. Hou, Y. L. Hao, R. Yang, and R. D. K. Misra, "The influence of cell morphology on the compressive fatigue behavior of Ti-6Al-4V meshes fabricated by electron beam melting," *J. Mech. Behav. Biomed. Mater.*, vol. 59, pp. 251–264, Jun. 2016.
- [202] S. J. Li *et al.*, "Compression fatigue behavior of Ti-6Al-4V mesh arrays fabricated by electron beam melting," *Acta Mater.*, vol. 60, no. 3, pp. 793–802, Feb. 2012.
- [203] N. W. Hrabe, P. Heintl, B. Flinn, C. Körner, and R. K. Bordia, "Compression-compression fatigue of selective electron beam melted cellular titanium (Ti-6Al-4V)," *J. Biomed. Mater. Res. Part B Appl. Biomater.*, vol. 99B, no. 2, pp. 313–320, Nov. 2011.
- [204] B. Van Hooreweder and J. P. Kruth, "Advanced fatigue analysis of metal lattice structures produced by Selective Laser Melting," *CIRP Ann. - Manuf. Technol.*, vol. 66, no. 1, pp. 221–224, 2017.
- [205] S. J. N. Morrish, M. Pedersen, K. F. W. Wong, I. Todd, and R. Goodall, "Size effects in compression in Electron Beam Melted Ti6Al4V diamond structure lattices," *Mater. Lett.*, vol. 190, pp. 138–142, 2017.
- [206] L. G. Johnson, *The Statistical Treatment of Fatigue Experiments*. London:

Elsevier Publishing Company, 1964.

- [207] C. Körner, “Additive manufacturing of metallic components by selective electron beam melting — a review,” *Int. Mater. Rev.*, vol. 61, no. 5, pp. 361–377, Jul. 2016.
- [208] E. Marin, S. Fusi, M. Pressacco, L. Paussa, and L. Fedrizzi, “Characterization of cellular solids in Ti6Al4V for orthopaedic implant applications Trabecular titanium,” *J. Mech. Behav. Biomed. Mater.*, vol. 3, pp. 373–381, 2010.

# Chapter 7 Appendix

## Appendix 1 - Accuracy of powder analysis samples



Table of allowed tolerances when using QC Samples

Reg No: LAB/C/036Uncert  
 Sheet: 1 of 1  
 Issue: A Amd: 0  
 Date: 16/04/01

Authorised: *M. E. J. Burt*

QC Sample Value	Allowed Tolerance (+/-)	QC Sample Value	Allowed Tolerance (+/-)	QC Sample Value	Allowed Tolerance (+/-)
0.05	0.01	6.50	0.10	44.00	0.27
0.06	0.01	7.00	0.11	46.00	0.27
0.07	0.01	7.50	0.11	48.00	0.28
0.08	0.01	8.00	0.11	50.00	0.28
0.09	0.01	8.50	0.12	52.00	0.29
0.10	0.01	9.00	0.12	54.00	0.29
0.11	0.01	9.50	0.12	56.00	0.30
0.12	0.01	10.00	0.13	58.00	0.30
0.13	0.01	11.00	0.13	60.00	0.31
0.15	0.02	12.00	0.14	62.00	0.31
0.20	0.02	13.00	0.14	64.00	0.32
0.30	0.02	14.00	0.15	66.00	0.32
0.40	0.03	15.00	0.15	68.00	0.33
0.50	0.03	16.00	0.16	70.00	0.33
0.60	0.03	17.00	0.16	72.00	0.34
0.70	0.03	18.00	0.17	74.00	0.34
0.80	0.04	19.00	0.17	76.00	0.35
0.90	0.04	20.00	0.18	78.00	0.35
1.00	0.04	22.00	0.19	80.00	0.36
1.50	0.05	24.00	0.20	82.00	0.36
2.00	0.06	26.00	0.20	84.00	0.37
2.50	0.06	28.00	0.21	86.00	0.37
3.00	0.07	30.00	0.22	88.00	0.38
3.50	0.07	32.00	0.23	90.00	0.38
4.00	0.08	34.00	0.23	92.00	0.38
4.50	0.08	36.00	0.24	94.00	0.39
5.00	0.09	38.00	0.25	96.00	0.39
5.50	0.09	40.00	0.25	98.00	0.40
6.00	0.10	42.00	0.26	100.00	0.40

The wide range of materials analysed in the laboratory by XRF requires us to keep a very wide range of QC samples.

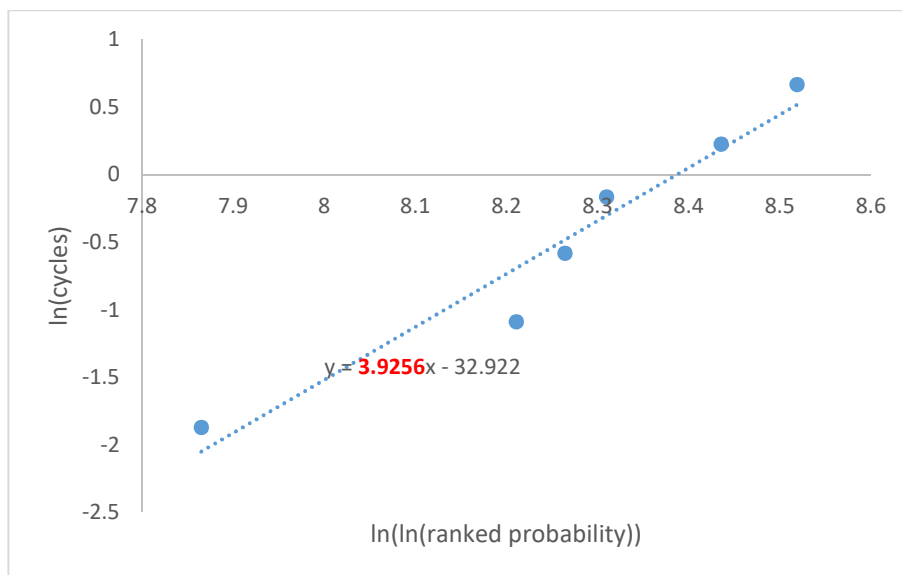
Where QC samples are not set up for automatic comparison by the XRF software the analyst will use:

- a the published inter laboratory uncertainty data where available
- b  $0.04\sqrt{c}$  if published data not available.

A table of  $0.04\sqrt{c}$  values at different levels of determinand is given above.

Appendix 2- Example of determination of Weibull modulus through ranking data. Data here from as-built samples at 0.037 strain:

Rank	Ranked cycles	P(Nf)	ln(cycles)	ln(ln(1/1-Nf))
1	2604	0.142857143	7.864804003	-1.869824714
2	3679	0.285714286	8.210396255	-1.08923964
3	3881	0.428571429	8.263848131	-0.580504824
4	4062	0.571428571	8.309430742	-0.165702981
5	4606	0.714285714	8.43511508	0.225351487
6	5006	0.857142857	8.518392472	0.665729811



Therefore Weibull modulus = 3.9256

Appendix 3 - Scripts from R and outputs for statistical analysis, reproduced from work by Dr Tim Heaton and Dr Eleanor Stillman at the Department of Mathematics and Statistics, University of Sheffield.

```

library(survival)
# 0.057 strain
nx <- 6
ny <- 6
x <- c(5006,4060,4606,2604,3881,3679)
y <- c(3325,3725,3507,2253,3154,3437)

# censoring information (1 means it is observed and 0 right censored)
censorx <- rep(1, nx)
censory <- rep(1, ny)

# combine the data
comb <- c(x,y)
censorcomb <- c(censorx, censory)

# Create survival objects
x.surv <- surv(x, censorx, type = "right")
y.surv <- Surv(y, censory, type = "right")
comb.surv <- Surv(comb, censorcomb, type = "right")

# Now fit the weibull distributions and find the log likelihood
x.weibullfit <- survreg(x.surv ~ 1)
y.weibullfit <- survreg(y.surv ~ 1)
comb.weibullfit <- survreg(comb.surv ~ 1)

# Find GLRT statistics, i.e.  $2 * (\loglik(alt) - \loglik(null))$ 
GLRTstat <- 2 * (x.weibullfits$loglik[1] + y.weibullfits$loglik[1] - comb.weibullfits$loglik[1])
GLRTstat
# we have gone from 4 parameters (different) to 2 (same) so we compare this with a chi-squared with dof = 2
# Find p value
1-pchisq(GLRTstat, df = 2)

# add group indicator
group1 <- rep(1, nx)
group2 <- rep(2, ny)
group <- c(group1, group2)

#assemble data into a data frame for analysis
lifedata<-data.frame(comb, censorcomb, group)

#Non-parametric test of whether groups have different life distns
survdiff(comb.surv~as.factor(group),data=lifedata)

#Plot of Kaplan Meier curves of survival
plot(survfit(comb.surv~as.factor(group),data=lifedata), lty=c(2,3))

```

~

```

> GLRTstat
7.187103

> 1-pchisq(GLRTstat, df = 2) (p-value for the GLRT test)
0.02750048

```

~

```
survdiff(formula = comb.surv ~ as.factor(group), data = lifedata)
```

	N	Observed	Expected	(O-E) <sup>2</sup> /E	(O-E) <sup>2</sup> /V
as.factor(group)=1	6	6	9.07	1.04	5.45
as.factor(group)=2	6	6	2.93	3.23	5.45

chisq= 5.5 on 1 degrees of freedom, p= 0.0195

```

library(survival)
# 0.045 strain
nx <- 6
ny <- 6
x <- c(605,677,589,563,499,611)
y <- c(340,220,175,231,438,175)

# censoring information (1 means it is observed and 0 right censored)
censorx <- rep(1, nx)
censory <- rep(1, ny)

# combine the data
comb <- c(x,y)
censorcomb <- c(censorx, censory)

# create survival objects
x.surv <- Surv(x, censorx, type = "right")
y.surv <- Surv(y, censory, type = "right")
comb.surv <- Surv(comb, censorcomb, type = "right")

# Now fit the weibull distributions and find the log-likelihood
x.weibullfit <- survreg(x.surv ~ 1)
y.weibullfit <- survreg(y.surv ~ 1)
comb.weibullfit <- survreg(comb.surv ~ 1)

# find GLRT statistics i.e.  $2 * (\loglik(\text{alternative}) - \loglik(\text{null}))$ 
GLRTstat <- 2 * (x.weibullfit$loglik[1] - y.weibullfit$loglik[1] - comb.weibullfit$loglik[1])
GLRTstat
# We have gone from 1 parameter (different) to 2 (same) so we compare this with a chi-squared with dof = 2
# find p value
1-pchisq(GLRTstat, df = 2)

# add group indicator
group1 <- rep(1, nx)
group2 <- rep(2, ny)
group <- c(group1, group2)

# assemble data into a data frame for analysis
lifedata <- data.frame(comb, censorcomb, group)

# Non-parametric test of whether groups have different life distrs
survfit1 <- survfit(comb.surv ~ as.factor(group), data = lifedata)

# Plot of Kaplan Meier curves of survival
plot(survfit1, lty=c(2,3))

```

~

```

> GLRTstat
] 21.83654

> 1-pchisq(GLRTstat, df=2) (p-value for the GLRT test)

1.812402e-05

```

~

```
survdifff(formula = comb.surv ~ as.factor(group), data = lifedata)
```

	N	Observed	Expected	(O-E) <sup>2</sup> /E	(O-E) <sup>2</sup> /V
as.factor(group)=1	6	6	9.87	1.52	12.2
as.factor(group)=2	6	6	2.13	7.06	12.2

chisq= 12.2 on 1 degrees of freedom, p= 0.00047